INTERFACIAL INTERACTIONS OF OLIGOANILINES WITH SOLID SURFACES

INTERFACIAL INTERACTIONS OF OLIGOANILINES WITH SOLID SURFACES

By AMIRMASOUD MOHTASEBI, B.SC., M.SC.(HONS)

A Thesis Submitted to the Scholl of Graduate Studies in Partial Fulfilment of the Requirements of the Degree of Doctor of Philosophy in Chemistry

McMaster University

McMaster University DOCTOR OF PHILOSOPHY (2017)
Hamilton, Ontario, Canada (Chemistry)

TITLE: Interfacial Interactions of Oligoanilines with Solid Surfaces

AUTHOR: Amirmasoud Mohtasebi, B.Sc. (Tehran Polytechnique), M.Sc. (Hons) (University of Erlangen-Nuremberg)

SUPERVISOR: Professor Peter Kruse

NUMBER OF PAGES: xx, 193

Abstract

It is known that organic monolayers on solid surfaces can enable electronic properties that are absent in the bulk of the solid materials. Often, once the organic film come into the contact with a solid surface, the established electronic interaction at their interface remains undisturbed. However, using a redox-active organic monolayer creates the possibility for modulating the extent and the direction of the interfacial charge transfer, establishing a switch at the interface.

The theme of this thesis is investigation of the interfacial interaction of different redox states of a molecular switch, phenyl-capped aniline tetramer (PCAT) with iron oxide and graphite surfaces and their potential application in electronic devices. The nucleation and growth of submonolayer films of different oxidation states of PCAT on iron oxide surface was studied. Using atomic force microscopy and scaling island size distribution method the surface diffusion parameters of these islands were evaluated. Using X-ray photoelectron spectroscopy (XPS) and Raman spectroscopy the changes in these organic monolayers before and after interaction with iron oxide were demonstrated. However, these techniques were unable to provide similar data from the solid surface side of the interface. Instead, we were able to demonstrate the changes in the iron oxide film as a result of interfacial charge transfer using electrical conductivity measurement techniques. Based on this information a microfluidic chemical sensor based on the interface of pencil film and PCAT for quantification of free chlorine in drinking water was constructed. Using XPS and UV-vis spectroscopy it was shown that the interaction the organic monolayer with

sodium hypochlorite solution leads to the development of positive charges on the backbone of PCAT. This electrostatic charge can affect the charge transport in the pencil film causing the modulation of electrical conductivity of the film. The presented work demonstrates alternative pathways for the design of novel hybrid electronic devices based on thin molecular film and solid surfaces.

Acknowledgments

I would like to thank my previous supervisors for giving me the opportunity to pursue scientific research. I thank all my colleagues during my time at McMaster: Dr. Yue Wang, Dr. Tanzina Chowdhury, Dr. Enamul Hoque, Andrew D. Broomfield, Omar Sharif. Alon Genkin, and Alan M. Awaz.

I am grateful to Prof. Peter Kruse for supervising me as a graduate student in his laboratory. I am thankful to Peter because of the freedom he gave me during my research. He provided me with his valuable suggestions and feedback on my reports and papers. I am also deeply grateful of his patience and support during these years.

I thank Prof. Gillian Goward and Prof. Andrew Kish for serving on my Ph.D. supervisory committee and their interest in my progress.

I am also thankful for financial support from McMaster University, Natural Science and Engineering Research Council of Canada, and Canadian Light Source.

I would like to thank our collaborators Dr. Mark C. Basinger from Surface Science Western, Prof. P. Ravi Selvaganapathy and his research group at McMaster University, Mechanical Engineering Department.

I would like to thank my friends Ian Duffy and Michael Son for their assistance in performing some of the experiments.

Finally, but most importantly, I thank my parents, Maryam and Mehdi. They are the rocks of my life. I thank my brothers, Amirhessam and Amirhossein who are always there for me.

The map is not the territory. -Alfred Korzybski

Table of Contents

Table of Figures

Chapter 5 Interfacial Charge Transfer between Phenyl-Capped Aniline Tetramer Films and Iron Oxide Surfaces

List of Schematics

List of Abbreviations

$A(\theta)$	Average Island Size
AFM	Atomic Force Microscope
B.E.	Binding Energy
CHEMFETs	Chemical Field Effect Transistors
CNTs	Carbon Nanotubes
CV	Cyclic Voltammetry
D	Diffusion Constant
D_0	Diffusion Prefactor
DPD	Diethyl-*p*-phenylenediamine
E_a	Diffusion Barrier Energy
EB	Emeraldine Base
ES	Emeraldine Salt
F	Flux
f(u)	Scaling Function
FETs	Field Effect Transistors
i	Critical Island Size

LB	Leocoemeraldine Base
LD	Leocoemeraldine Salt
N	Nucleaction Density
$N_a(\theta)$	Distribution of Islands of Size a per Unit Area
NaOCl	Sodium Hypochlorite
NaOH	Sodium Hydroxide
NMR	Nuclear Magnetic Resonance
PANI	Polyaniline
PB	Pernigraniline Base
PCAT	Phenyl-Capped Aniline Tetramer
PDMS	Poly(dimethylsilioxane)
PS	Pernigraniline Salt
QCM	Quartz Crystal Microbalance
R	Deposition Rate
SEM	Scanning Electron Microscopy
SWCNTs	Single Walled Carbon Nanotubes

T	Temperature
TBAP	Tetrabutylammonium Perchlorate
TGA	Thermogravimetric Analysis
UV-vis	Ultraviolate-Visible
XPS	X-ray Photoelectron Spectroscopy
θ	Surface Coverage
ν_0	Attempt Frequency
$(NH_4)_2S_2O_8$	Ammonium Persulfate

Declaration of Academic Achievement

Chapter 4 is based on a draft prepared for submission. The author contribution to this chapter is as follows. Amirmasoud Mohtasebi and Peter Kruse designed the study. A.M. performed the organic synthesis and its characterization. A.M. performed the organic deposition experiments. A.M. and Tanzania Chowdhury performed the atomic force microscopy (AFM) experiments. Mark C. Biesinger performed x-ray photoelectron spectroscopy. A.M. and M.B. analyzed the XPS data. A.M. performed the annealing experiments. A.M. analyzed all the data which led to all figures of this chapter. A.M. wrote the manuscript. This research has been carried out between 2016-2017.

Chapter 5 is based on a paper published in the Journal of Physical Chemistry C. (Mohtasebi, A.; Chowdhury, T.; Hsu, L.H.H.; Biesinger, M. C.; Kruse, P. *J. Phys. Chem. C.* 2016, 51, 29248-29263). The author contribution for this paper is as follows. A.M. and P.K. designed the study. A.M. and T.C. prepared the small organic molecules in different oxidation states. A.M. and T.C. performed all AFM experiments. A.M. and M.B. performed the XPS measurements. A.M. and M.B. analyzed the XPS data. A.M. reanalyzed the XPS data acquired by Mark T. Greiner which was published earlier in the Journal of Physical Chemistry (Greiner, M. T.; Festin, M.; Kruse, P. *J. Phys. Chem. C.* 2008, 112, 18991-19004). A.M. performed the Raman and UV-vis spectroscopy measurements. L.H.H.H fabricated the interdigitated gold electrodes on glass substrates. A.M. developed the procedure for preparation of thin iron oxide films on the interdigitated gold electrodes. A.M. fabricated the thin iron oxide film on the later substrate and prepared

and performed the microfluidic experiment. A.M. wrote the paper. This project has been carried out between 2015-2016.

Chapter 6 is based on the paper published in the journal of ACS Applied Materials and Interfaces (Mohtasebi, A.; Broomfield, A. D., Chowdhury, T., Selvaganapathy, P. R., Kruse, P. *ACS Appl. Mater. Interfaces*, **2017**, 9, 20748-20761). A.M., P.R.S., and P.K. designed the project. A.M. performed the colorimetry, absorptivity, and UV-vis experiments. A.M. and A.D.B performed the sensing experiments. A.M. and Mark. C. Biesinger performed the XPS experiments and the data analysis. A.M. performed the Raman and NMR experiments. A.M. and T.C. performed the AFM measurements. A.M. performed the scanning electron microscopy experiment. A.M. wrote the paper. This research has been carried out between 2015-2017

Chapter 1 Organic Layer-Solid Surfaces Interface

1.1 Organic Semiconductor-Metal Junction

It is known that certain organic monolayers on solid surfaces can enable electronic properties that are absent in the bulk of the solid materials. Often, once an organic film meets a solid surface, the established electronic interaction at their interface remains undisturbed. However, using a redox-active organic monolayer creates the possibility for modulating the extent and the direction of the interfacial charge transfer, establishing a switch at the interface. In this work, the interaction of phenyl-capped aniline tetramer (PCAT), a redox active tetraaniline, with various iron oxide and graphitic surfaces is studied. In case of charge transfer at such interfaces, the contact between the organic film and the substrate can be categorized as either ohmic contact or schottky junction (rectifying contact). The type of the contact at this interface can be determined by measuring the energy offset between the Fermi level of the metal and the conduction band minimum of n-type semiconductor or the energy offset of the metal and the valence band maximum of a p-type semiconductor. This energy offset is called Schottky barrier height (SBH). The magnitude of this potential energy barrier dictates whether the interface is rectifying or not. Therefore, the first step in understanding the charge transfer between PCAT and surfaces is understanding the general physics behind the electronic properties of organic semiconductors and metals interfaces. In this chapter, the basic physics of organic semiconductor and metal surfaces and different possibilities of these interactions are briefly

discussed. In addition, the basics of molecular self-assembly on surfaces are reviewed. Finally, the concept of molecular switches is introduced.

1.2 Interface Energy Balance

A common characteristic of all electronic devices is their interfaces. Material characteristics such as electrical resistivity are bulk attributes of the materials. In contrast, phenomena such as current rectification stem from the interfaces where the symmetry is broken. To this end, separation of electrons and holes at chemical interfaces become possible.[1] The chemical differences between the two sides of an interface will lead to an electrical potential gradient which is the basis of asymmetric charge transport.[1] The continuous miniaturization of electronic devices leads to the creation of high interface areas while the amount of bulk significantly diminished. Traditionally, it was assumed that there is an abrupt change in the properties of the two phases at an interface. However, the changes in the properties of the two phases across an interface is achieved through spatial gradients at their borders.[1] Traditionally, the majority of the work on heterojunctions have been carried at the interface of two semiconductors. In the last two decades, the interfaces between molecular layers and semiconductors gained significant attention due to their application in organic electronic devices.[2,3] Molecular layers can be used as a pathway for charge transport. In addition, they can act as a polarizable layer or a dielectric layer which enables the modulation of their electrostatic charge.[4] In this chapter some of the basics

about energy alignment between molecular layers and semiconductor surfaces are discussed.

1.2.1 Work-Function Balance

Energy levels of each component at an interface (metal, semiconductor, organic layer) is different before and after it comes in contact with other phases at the interface. Historically, several energy alignment theories have been used to describe the energy alignment between a metal and a semiconductor when their contact is not ohmic, which is termed as Schottky junction.[1] However, such theories can also be used to describe the energy alignment between an organic layer and a semiconductor. The main characteristic of a conventional Schottky junction is the Schottky barrier height (SBH) which is the energy required for an electron to transfer from the Fermi level (E_f) of the metal to an energy level at the semiconductor side. In the case of a n-type semiconductor, this latter energy level is the conduction band.[1] E_f is an energy level in which the chance to find an electron is 50%. The theory behind the energy level alignment at interfaces has been always under debate. One way to approach the issue is through electrochemical potential (μ_e) of each side of the junction. The μ_e consists of both chemical (μ) and electrical (Φ) potentials. This relationship can be written as equation 1.1, in which q is the electron charge.[1]

$$\mu_e = \mu + q\varphi \qquad 1.1$$

In solid state physics, it is assumed that the electrochemical potential is equal to the Fermi level of the solids.[5] Therefore, at equilibrium conditions the Fermi levels of both

sides of the Schottky junction become aligned. In addition, at equilibrium conditions, the energy required for removal of an electron from each side of the junction to the vacuum energy level (E_{vac}) is equal. The energy difference between the E_f and vacuum level is called work function (WF). Work function is often used for metal surfaces as the density of states at their fermi level is not zero. E_{vac} is an energy level in which the electron is not under the influence from the surface.[1] Therefore, E_{vac} can be used as a measure of averaged electrostatic potential of the surface. Figure 1.1 depicts the schematic illustration of two interface energy alignment at Schottky barrier of a metal and a semiconductor. The schematic in Figure 1.1A shows the Schottky barrier according to charging interface states while Figure 1.1B shows the same interface according to interface polarization. E_{vac} of each case is shown with a green continuous line. In Figure.1.1A this line shows as a smooth continuous line while in Figure 1.1B there is a fluctuation at the junction. The reason behind the fluctuation in the latter case is consideration of potential fluctuations due to atomic-scale charging at the junction. Upon contact of the two sides in Figures 1.1A or 1.1B, the Fermi level alignment is established. This can be performed either by flow of electrons from the material with lower WF to the one with a higher WF or by an electrical potential buildup at the interface.[1] The latter case has been shown by a step (Δ_0) in Figure 1.1. In the absence of an external applied potential, the charge buildup at the junction creates a gradual potential change, commonly refer to as band bending (BB_0). The BB_0 and the SBH can be related through the following equation, in which ξ is the difference between CB and the E_f of the semiconductor.

$$SBH = BB_0 + \xi \qquad 1.2$$

Equation 1.2 shows the importance of SBH in charge transport at a Schottky junction. Considering the metallic side of the junction in Figure 1.1A, the WF of the metal is equal to the Δ_0 plus the E_{vac} – CB, and SBH of the semiconductor. Therefore, for an n-type semiconductor the SBH is equal the following relationship, where $\chi = E_{vac}$ – CB in this equation is called electron affinity.[1,6] It should be noted that the equation 1.3 is written with respect to the semiconductor side of the metal-semiconductor junction in Figure 1.1. Since the density of states at the Fermi level of a semiconductor is equal to zero, often electron affinity is often used instead, similar to equation 1.3. Electron affinity of a semiconductor is defined as the difference in energy of the bottom of its conduction band and the vacuum level.[1]

$$SBH = WF - \chi - \Delta \qquad 1.3$$

The equation 1.3 is called Schottky-Mott rule which evaluates the SBH, based on the WF of the metal and the electron affinity of the semiconductor. Based on Schottky-Mott rule, when a metal and a semiconductor become in contact the band in the semiconductor rearrange in a way that its WF matches the WF of the metal.[1,7]

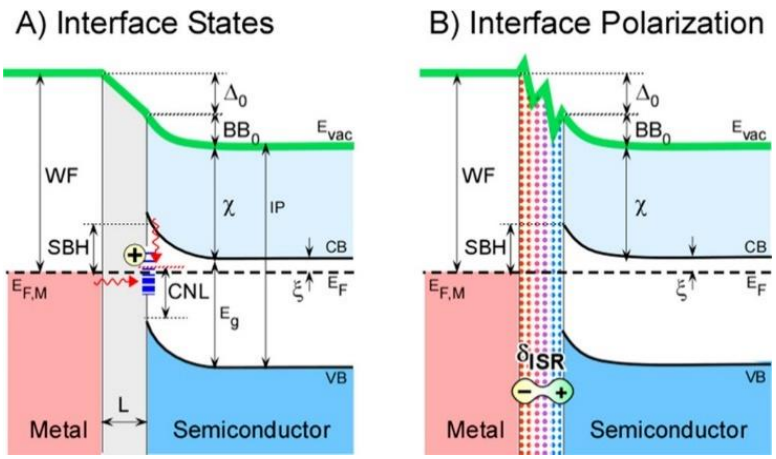

Figure 1.1. "Schematic illustration of interface energy alignment and creation of the Schottky barrier height (SBH), according to (A) charging of interface states or (B) interface polarization. Both panels show energy per electron (Y-axis) across an interface between a metal (left, red) and an n-type semiconductor (right, blue), with curved energy levels, depicting the surface charge region (SCR). The two panels illustrate two different views on the nature of the interface, the thickness of which is grossly exaggerated for clarity. The interface charging model (A) assumes a foreign layer (gray shade) with a density of interface states, marked by blue stripes, centered at a distance CNL (charge neutrality level) from the top of the valence band at the surface. The Fermi level is pinned nearly at the CNL, where the difference between them accounts for the net interface charge, QIS. In this case EF is below the CNL and therefore QIS is positive, with a counter negative charge on the metal edge, dictating $\Delta_0 > 0$. The red arrows in (A) mark possible electronic processes (see text). Panel (B) depicts the interface specific region (ISR) view, where even in the case of perfect, abrupt interface between two solids (no foreign substance) a transition region is developed (dotted in B). A net change in potential, Δ_0, emerges, emerges from the bond-polarization, δ_{ISR}, between the intrinsic atoms that make up the interface. In both panels, the electronic equilibrium state (0 V) is shown with a constant Fermi level (dashed line) across the interface, while the local vacuum level (green top line) varies across the interface. See list of symbols for other symbols."[1] Copyright 2017 by the American Chemical Society.

Although, the Schottky-Mott rule was true on predicating the band bending at the junction between a metal and a semiconductor, it was found to predict SBH values different from the experimentally measured values. This discrepancy was associated with the phenomenon called Fermi level pinning. In this case, the Fermi level of the semiconductor

is locked to a certain point of its band gap in which density of states exist (such as charge neutrality level, CNL in Figure 1.1A). This cause that the SBH has a constant value and be independent of metal WF and as a result, the $\Delta \neq 0$. This phenomenon was noted by Jon Bardeen and hence is referred to as Bardeen limit.[1]

1.2.2 Interface of Organic Films and Solid Substrates

It was argued that Fermi-level pining ($\Delta \neq 0$) requires some level of interface interactions. The two pathways suggested for this interfacial interaction are interface traps (Figure 1.1A) and interface bonds (Figure 1.1B). In the interface trap concept, the interface envisioned as a capacitor, in which the metal surface serves as one of the plates and the charges on the interface as another plate, while a thin foreign film serves as a dielectric.[1] On the other hand, the interface bond model is constructed based on the direct contact between the organic layer and the metal surface. At this junction, charge rearrangement will occur which leads to the polarization of the interface. This polarization region is depicted in Figure 1.1B.[8,9] The presence of traps at interfaces not only change the Δ and SBH, but also can interrupt the interfacial charge transfer. On the other hand, in the bond-polarization concept no interfacial trap state exists and therefore it does not interrupt the interfacial charge transfer. While the latter concept can explain the interface polarization, the former concept has been recognized as a closer theory to the behavior of molecular layers on metal and semiconductor surfaces as they block the interfacial bond polarization.[1] The interface specific region is regarded as a layer with its unique properties. However, it

can be formed by both physisorption and chemisorption of organic molecules on the metal or semiconductor surface.[6] Adsorbed organic molecules on surfaces add their own intrinsic dipole to the surface which originates from their closed electronic shell. Both electron donating or -withdrawing molecules can participate in this surface polarization.[1]

1.2.3 Charge Transfer into the Substrate

It has been reported that the adsorption of hydroquinone on the surface of hydrogen terminated Si will lead to an increase in the surface charge and as a result band bending.[10] Increasing of the surface charge lead to an increase in repelling of the electrons (majority charge carriers) in the silicon substrate which increases the lifetime of the minority charge carriers.[1,11] The coupling between majority of the organic molecules and substrates is not ideal which result the possibility for charge recombination at the interface.[11] Molecular layers are polarizable and as result can create static charges or dipoles on the surface which result in the band bending in the substrate. Both chemisorbed and physisorbed molecules can cause band bending and charge transfer to the substrate. Surface adsorbate can simply act as dopant of the substrate.[12] As an example, it has been shown that the adsorption of polyaniline (PANI) on the surface of single walled carbon nanotubes can cause doping of the substrate.[13]

It is known that the optimization of the organic electronic devices depends on the energy-level alignment between the organic layer and the metal or semiconducting substrates. It is known that for hole extraction or injection metallic electrodes the Fermi

level of the electrode should be aligned with the occupied states of the organic molecule.[14] It is also known that for electron injection or extraction metallic electrodes in contact with the organic layer, the unoccupied states of the organic molecule should be aligned with the Fermi level of the metal. In these situations the charge transfer at the interface can take place with an external applied potential.[2] In such scenarios, it is important to know whether a single molecule of the organic layer transfers a fraction of a charge to the substrate or an integer number of charges.[15] The former and latter assumptions are called fractional charge transfer and integer charge transfer, respectively.[14] In the case of fractional charge transfer (Figure 1.2a), the main debates is whether the excess charge of an organic molecule is transferred into its neighboring molecules thus there will be a homogenous fractional charge transfer across the interface.[14,16] On the other hand, the integer charge transfer is often discussed in the case of weakly interacting organic layer with the substrate which interrupts hybridization between the organic molecules orbitals and the substrate (Figure 1.2b).[16,17] This can be the case when the substrate is chemically inert or when an interlayer present at the interface (e.g. water molecules, dirt, oxides).[16,18] Using DFT calculations, it has been shown that the charge transfer between small organic acceptor tetracyanoethene (TCNE) adsorbed on the surface of cupper is fractional.[14] It is known that TCNE is weakly adsorbed on cupper surfaces but can undergo strong charge transfer with these substrates.[19'20] Previously, it has been shown that the formation of this complex leads to an increase in the work function which was used as a sign of charge transfer from Cu to TCNE.[21] The amount of this charge transfer depends on the alignment of the occupied orbitals of TCNE and the Fermi level of the cupper substrate and the physical distance

between the metal and organic layer.[14] However, introducing a dielectric layer between the organic film and the metal substrate cause their electronic decoupling and shifting the charge transfer mechanism from fractional to integer.[14]

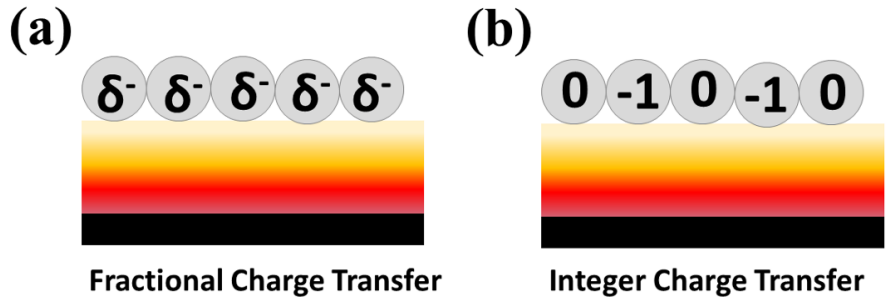

Figure 1.2. Fractional charge transfer at the interface of a weakly chemisorbed molecules on a metal surface. In this case the charge carriers spread homogenously between all organic molecules. (b) Integer charge transfer between physisorbed molecules on a metal surface. In this case, some molecules become charge while the rest remain neutral.

1.3 Molecular Monolayers on Surface

The monolayers can be zero-dimensional (0D), one-dimensional (1D), and two-dimensional (2D) molecular structures. The 0D molecular structure refers to individual molecules or small molecular clusters on surfaces.[22] Understanding of the interaction of these individual feature on surfaces are of great importance as it has been shown that their properties can be different from their molecular ensemble.[23] The final aim of such studies is the production of devices based on single molecules in which they act as molecular resistors, switches, or other components.[24] However, the production of these devices is challenging as the interface of a single molecule with the electrodes, substrate, and the

surrounding environment should be well engineered.[22'25] The 1D molecular structures on surfaces can be formed through various means. The first pathway is based on the anisotropy of molecules. Typically, most of the organic molecules used in molecular electronic application form either rodlike (1D, e.g. acenes, phenylenes) or platelike (0D, e.g. phthalocyanines, porphyrins) structures on surfaces.[26] Another pathway for the formation of 1D molecular structures on surface is through hydrogen bonding between individual organic molecules.[27] In addition, external forces such as electrical field and magnetic field can be used for alignment of these linear architectures.[28] In addition, the surface reconstruction of the substrate, a process to minimize the surface energy of the solids, can impose specific geometries to the molecular layer.[22] The surface features such as defects, step edges, and vacancies have different local electronic density of states from the rest of the surface and thus can influence the monolayer formation.[29] As an example, it has been shown that benzene molecules adsorb preferentially on step edges of Cu(111) surface.[30] An alternative route for the fabrication of 1D molecular structures on surfaces is through polymerization of self-assembled adsorbate molecules.[22,31]

Understanding the interaction of isolated single molecules or 1D assemblies with surfaces make it possible to understand how molecules relate to their environment. However, majority of the devices based on the interface between solid surfaces and molecular monolayers are based on ordered assembly of the molecules in 2D.[32] One of the possible outcomes from such arrangements is cooperativity between the molecules.23 This means that the coupled molecular systems are capable of performing complex actions which is not available from isolated or small ensemble of molecules. For example, it has been shown

that bundled phenylene ethynylene oligomers inserted in alkanethiolate host monolayer have higher persistence time against stochastic conductance switching in comparison to the its isolated oligomer in the same host matrices.[33] To this end, understanding the molecular structure, arrangement, and properties of molecules in ordered assemblies on surfaces is important for utilizing such interfaces in future devices.

1.3.1 Self-Assembled Monolayers

Self-assembled monolayers (SAMs) are nanostructured films with a molecular lattice that has optimized interactions with the substrate and within the molecular monolayer itself.[22] The typical thickness of SAMs are about 1-3 nm. The properties of the SAMs are majorly dictated by their interfaces due to the high proportion of atoms present at these locations.[22] The interaction of the molecules with the surface can have either covalent or non-covalent nature.[32] An example of covalent interaction is the Au-S bonds in SAMs of alkanethiols on gold surfaces. In this case, both interaction of Au-S and the packing within the thiol film determine the molecular lattice.[34] On the other hand, the π-stacking of conjugated organic molecules such as cyclodextrins on graphite is an example of non-covalent interaction.[35] SAMs on surfaces can be fabricated from either in vacuum or from solutions.[32] The later situation is more common when the substrate is not changed (e.g. get oxidized) under ambient conditions.[36] These films are dense and ordered and therefore suitable for characterization of the intermolecular interactions and intermolecular interactions with the surface. In addition, defects are important part of the monolayers.[22]

They can either originate from detect in the underlying substrates or from within the molecular film itself. An example of the former case is the presence of step edges in the substrate and an example of the latter case is the titling of the molecules in directions different the rest of the monolayer.[37]

1.3.2 Substrate Lattice

The monolayer formation on surfaces is dependent on the substrate atomic lattice and its electronic structure.[22] Much of the research on SAM formation has been performed on gold surfaces.[38] This is mainly because this surface does not form an oxide in ambient conditions and therefore it can be used for SAM formation from solutions.[34] Surfaces that have been used for SAM formation include Ag,[39] Cu,[40] Pd,[40] Pt,[41] Ni,[40] Fe,[40] Ti,[42] Te,[43] Hg,[44] GaIn,[45] GaN,[46] ZnSe,[47] HOPG,[48] Si.[49] Some of these surfaces such as Ag, Cu, Pt, Si, and Pd are prone to fast oxidation in ambient conditions. Therefore, the SAMs fabrication on these surfaces is better to be performed in vacuum conditions or in inert atmosphere.[22] In addition to the substrate composition, the substrate lattice also plays an important role in monolayer formation.[50] Surface reconstruction causes the minimization of surface energy. Change in the surface lattice provides different chemically non-equivalent binding sites. Different head groups of the molecules in the monolayers have different affinity to these sites.[22] In the following, some of the most common head groups used in SAMs are briefly reviewed.

1.3.3 Substrate Head Group Interface

The most common head groups among molecules used for SAMs are head groups with sulfur end. Due to the strong bond between Au and S, most of the studies on this group of molecules have been performed on Au surfaces such as Au(111).[51] Using scanning tunneling microscope (STM), it has been shown that the molecules with S head groups can lift this surface reconstruction. This is due the stronger bond between Au-S in comparison to Au-Au bonds.[22] It is believed that this process is carried out by these molecules through lifting of Au atoms and substitution at their sites.[52] Other common head groups are Si,[53] P,[46] Se,[54] carboxylic acids,[55] isocyanides.[56] In addition, molecules with head groups such as peptides,[57] pentacene,[58] and cyclodextrins[35] can lead to the noncovalent π-stacking of monolayers on graphitic surfaces. Amines, selonoles, and thioacetyls are also used for SAM on Au surface while Silanes and Silanoles are used for SAM on SiO_2.[32] Molecules with phosphorous head groups are also used for SAM on Au, Ti, TiO_2, ZrO_2, and SiO_2.[56]

1.3.4 Molecular Lattices

The molecular lattice of SAMs are under influence from the substrate and the packing within the monolayer. This translates to the bond between the SAM and substrate and intermolecular interactions within the SAM. The common molecular interaction in the lattice are van der Waals, dipole-dipole, and hydrogen bonding interactions.[22] These interactions can be modulated by the functional groups such as alkenes, alkynes,

diacetylene, oligo(phenylene ethynylene), sulfones, azobenzenes on the backbones of the molecules.[59,60,61,62]

1.3.5 Molecule-Environment Interface

Another important interface which can affect the characteristic and properties of the monolayer is its interface with the environment. Some of these properties are hydrophobicity, hydrophilicity of the monolayer or the possibility of the isomerization the molecules by visible or UV exposure. The properties of the SAMs can be achieved through engineering of their end group.[22,32] As an example, addition of methyl group to the end of alkanethiolates leads to a hydrophobic monolayer while addition of hydroxyl group to them lead to a hydrophilic layer.[63]

1.4 Molecular Switches

Molecular switches respond to an external stimuli by changing their properties13 or their molecular structures.[59] The external stimuli can be in various forms such electrical field,[64] chemical stimuli,[13] mechanical stimuli,[23] and optical stimuli.[62] To understand the switching behavior of these molecules they have been studied both as an isolated molecule on the surface and also when they are self-assembled on the surface.[32] As mentioned earlier, a SAM of molecular switch does not necessarily show the same behavior as when they are isolated. The common technique for fabrication of the SAMs of these molecules is through

solution processing. It should be noted that the solution is used for this process can itself affect the properties of the SAM.[32] For example some solvents can more strongly bind to the junction between the metal electrode and SAM layer, increasing the work function of the electrode surface and hence manipulating the energy alignment at the junction.[65]

Electronic switches are single or assembly of conductive molecules which can be switched from non-conductive or low conductive states to high conductive states. As an example, PANI or its oligomers can be protonically doped by acids like HCl. They are non-conductive or extremely poor conductive in their base state (undoped) but can reach high electrical conductance upon chemical doping.[66] They can be switched back to their initial state by exposure to basic solutions/vapors.[67] The contact between the SAMs and metal electrodes can significantly affect the electrical conductance of the monolayer. The main criteria for a successful charge transfer at this interface is the energy alignment between the SAM and the metal electrodes. In addition, the contact between at this junction can also significantly affect the SAM electrical conductance. The suitable functional groups that provides good contact between the molecules and the metal electrode are amines (-NH_2), thiols (-SH), nitriles (-CH), and selenols (-SeH).[32] Switching a molecule from OFF to ON state and vice versa can be carried out through reduction/oxidation of molecules,[13] change in the hybridization of metal-molecule bonds,[33] intermolecular interactions,[68] change in the conformation of the conjugated backbone or functional groups.[59]

Electronic switches can be used in various electronic devices such as field effect transistors13 and chemical sensors.[69] In addition, their application in corrosion inhibition of metals have been widely investigated.[32,70] Another type of molecular switches is

functioning based on photochromic switching. Exposure of these molecules to a certain wavelength of light lead to conformational changes in their structure. These processes can be reversed and the molecule can go back to its initial stage either by thermal relaxation or by its exposure to a light with another wavelength.[71] Common groups of photochromic switches are azobenzenes,[62] quinones, spiropyrans, spirooxazines.[72] An important aspect of these photoswitches is the fact they do not behave the same in solutions and on conductive surfaces. It has been noted that the contact of these molecules with conductive solid surfaces interrupts their isomerization. Several approaches have been found to overcome this problem. One approach is introducing a thin nonconductive barrier at the junction between the molecules and the conductive substrate. The other method is based on functionalization of the molecular switches with bulky legs. Finally, it has been shown that addition of an insulating SAM at the interface of the molecular switch and the substrate can solve the quenching of isomerization by the substrate.[32,73] Another route for isomerization of molecules such as azobenzenes on surfaces is by using electrons. This can be performed precisely using STM tip. A STM tip can be controlled with subnanometer precision. In the tunneling regime, tunneling electrons can be used to perform the switching of the molecule with high lateral precision. An example of electronic switching by tunneling electrons is irreversible switching of *trans*- to *cis*- configuration of 4-dimethylamineoazobenzene-4-sulfonic acid on Au(111).[74]

Isomerization of molecular switches can also be triggered using electric field. One way to induce electric field on a molecular island is through STM tip. For this purpose, the tip is positioned close to the islands, but not necessarily in the tunneling regime (e.g. 0.4-

3.6 nm) and electric pulses are applied between the tip and substrate.[32] It has been previously shown that SAM of TTB-functionalized azobenzene can be reversibly switched between its *cis* and *trans* configurations.[75] Another class of molecular switches is mechanically interlocked molecules (MIMs) which are based on noncovalent interaction of two or more functional groups with each other.[32] Using external stimuli these functional groups can be moved relative to each other. Some examples of such molecular switches are rotaxanes, catenanes, and their derivatives.[23] A Rotaxane is composed of a linear backbone with a cyclobis(paraquat-*p*-phenylene) ring ($CBPQT^+$) around it. The linear shaft is composed of two different stations of tetrathiafulvalene (TTF) and dioxynaphtalene (DNP) while the ring is a cyclobis(paraquat-*p*-phenylene). The electrostatic charge of TTF define the location of the $CBPQT^+$ ring. In neutral states of TTF, the ring docks at this station while in its charged state (oxidized) the ring docks at DNP station.[32] Catenanes, another well-known MIMs is composed of two interlocked rings interacting with each other via noncovalent interaction. The ultimate goal of the research on MIMs is the design of microscopic muscles in which the movement can be controlled by external stimulus.[23'76]

1.5 Structure of this Thesis

As described in previous sections, this work investigates the interfacial charge transfer of thin films of small organic molecules with solid surfaces. In addition, this work investigates the nucleation and growth of stable islands of these molecules on solid surfaces, which is the initial step toward thin organic films formation. Based on these two

points, the application of organic-solid interfaces in electronic devices such as chemical sensors have been explored. From a more general point of view, this thesis concerns how the fabrication of thin organic films on surfaces can unlock properties that the bulk of materials are not able to offer.

In the next chapter (chapter 2), the general concept of chemical sensors is briefly introduced. The focus of this chapter is the introduction of chemiresistive chemical sensors. Different architecture of chemiresistive sensors are introduced. In addition, the pioneering and the current states of this class of chemical sensors with respect to the materials used in these sensors are reviewed. In some cases, the fabrication of the active materials used in such sensors and their properties are discussed. Furthermore, the sensing mechanism, advantages, and limitation of each groups of chemiresistive sensors are briefly mentioned.

In chapter 3, the working principles of the primary techniques used in this thesis, including X-ray photoelectron spectroscopy (XPS), Raman spectroscopy, UV-vis spectroscopy, and atomic microscopy are briefly discussed. In addition, the theory of the scaled island size distribution model for nucleation and growth of thin films are presented and the most relevant mathematical formulas to this model are reviewed.

In chapter 4, the nucleation and growth of the fully reduced and the fully oxidized islands of PCAT on the surface of hematite single crystals are studied. The morphology of these islands as a function of substrate temperature is presented. In addition, using dynamic scaling, the critical island size for both reduced and oxidized PCAT islands are calculated. Furthermore, the activation barrier energy and diffusion prefactor for the reduced and

oxidized PCAT on hematite surface are estimated. To the best of my knowledge, this is the first time that the scaling island size distribution is applied to two different oxidation states of a molecule. The work shows the significance of small changes in the molecular structure of a molecule can cause in the film formation, and on the surface diffusion of the molecules. Thus, this work not only provides valuable information about the nucleation and growth of molecular switches, but can also provide valuable insights for applications in which the organic coating acts more than a mere encapsulation of the surface.

The charge transfer between different oxidation states of PCAT and iron oxide surfaces (hematite and low carbon steel) is demonstrated in chapter 5. The procedure for the fabrication of thin films of each state of PCAT on the surface of iron oxide is presented. The morphology and thickness of the fabricated films are investigated by atomic force microscopy. The XPS of the PCAT films before and after their fabrication on iron oxide is used to investigate the charge transfer at this interface. Raman spectroscopy is used to further validate these results. In addition, the in situ XPS data obtained from the step by step deposition of the fully reduced base PCAT on low carbon steel are reanalyzed to investigate the interfacial charge transfer in the absence of ambient conditions. Finally, using a microfluidic device, the effect of the fully reduced and the fully oxidized PCAT on iron oxide surface is demonstrated. Thus, the results of this study contribute to better understanding of the inhibitive corrosion protection of metal and metal oxide surfaces by redox-active organic molecules and polymers. In addition, this work demonstrates the potential of the interface of redox-active organic molecules and conductive surfaces for application in thin film electronic devices, in particular chemical sensors.

Chapter 7 is about using the concepts introduced in previous chapters and put them in action, developing an electronic device based on the interface of a thin PCAT film and a pencil film for quantification of free chlorine in drinking water. The fabrication procedure for the chemical sensor is discussed in details and the device is thoroughly characterized. Using various spectroscopy techniques, the reaction of sodium hypochlorite and PCAT is elucidated and the sensing mechanism of the sensor is explained. In addition, the effect of chlorination of PCAT on device sensitivity and stability of the device are discussed.

Finally, the results and findings of this thesis are summarized in the chapter 7 and a discussion about possible future works is presented.

1.6 References

(1) Vilan, A.; Cahen, D. Chemical Modification of Semiconductor Surfaces for Molecular Electronics. *Chem. Rev.* **2017**, *117*, 4624–4666.

(2) Koch, N. Organic Electronic Devices and Their Functional Interfaces. *Chemphyschem* **2007**, *8*, 1438–1455.

(3) Ruiz, R.; Nickel, B.; Koch, N.; Feldman, L.; Haglund, R.; Kahn, A.; Family, F.; Scoles, G. Dynamic Scaling, Island Size Distribution, and Morphology in the Aggregation Regime of Submonolayer Pentacene Films. *Phys. Rev. Lett.* **2003**, *91*, 136102.

(4) Klauk, H.; Zschieschang, U.; Pflaum, J.; Halik, M. Ultralow-Power Organic Complementary Circuits. *Nature* **2007**, *445*, 745–748.

(5) Gerischer, H.; Ekardt, W. Fermi Levels in Electrolytes and the Absolute Scale of Redox Potentials. *Appl. Phys. Lett.* **1983**, *43*, 393–395.

(6) Tung, R. T. The Physics and Chemistry of the Schottky Barrier Height. *Appl. Phys. Rev.* **2014**, *1*, 11304.

(7) Schottky, W. Zur Halbleitertheorie Der Sperrschicht- Und Spitzengleichrichter. *Z. Phys. C Part. Fields* **1938**, *26*, 367–414.

(8) Tung, R. T. Recent Advances in Schottky Barrier Concepts. *Mater. Sci. Eng. R Reports* **2001**, *35*, 1–138.

(9) Vázquez, H.; Flores, F.; Kahn, A. Induced Density of States Model for Weakly-Interacting Organic Semiconductor Interfaces. *Org. Electron. physics, Mater. Appl.* **2007**, *8*, 241–248.

(10) Peng, W.; Rupich, S. M.; Shafiq, N.; Gartstein, Y. N.; Malko, A. V.; Chabal, Y. J. Silicon Surface Modification and Characterization for Emergent Photovoltaic Applications Based on Energy Transfer. *Chem. Rev.* **2015**, *115*, 12764–12796.

(11) Har-Lavan, R.; Schreiber, R.; Yaffe, O.; Cahen, D. Molecular Field Effect Passivation: Quinhydrone/Methanol Treatment of N-Si(100). *J. Appl. Phys.* **2013**, *113*, 84909.

(12) Arthropods, C.; Lewis, O. T.; Godfray, H. C. J.; Webs, F.; Habitats, C. Surface Transfer Doping of Semiconductor. *Science* **2006**, *313*, 1057–1058.

(13) Klinke, C.; Chen, J.; Afzali, A.; Avouris, P. Charge Transfer Induced Polarity Switching in Carbon Nanotube Transistors. *Nano Lett.* **2005**, *5*, 555–558.

(14) Hofmann, O. T.; Rinke, P.; Scheffler, M.; Heimel, G. Integer versus Fractional Charge Transfer at Metal (/ Insulator)/ Organic Interfaces : Cu (/ NaCl)/ TCNE. *ACS Nano* **2015**, *9*, 5391–5404.

(15) Soos, Z. G.; Topham, B. J. Surface Dipole of F4TCNQ Films: Collective Charge Transfer and Dipole-Dipole Repulsion in Submonolayers. *Org. Electron.* **2011**, *12*, 39–44.

(16) Vazquez, H.; Oszwaldowski, R.; Pou, P.; Ortega, J.; Perez, R.; Flores, F.; Kahn, A. Dipole Formation at Metal/PTCDA Interfaces: Role of the Charge Neutrality Level. *Europhys. Lett.* **2004**, *65*, 802–808.

(17) Osikowicz, W.; De Jong, M. P.; Salaneck, W. R. Formation of the Interfacial Dipole at Organic-Organic Interfaces: C60/Polymer Interfaces. *Adv. Mater.* **2007**, *19*, 4213–4217.

(18) Hung, L. S.; Tang, C. W.; Mason, M. G. Enhanced Electron Injection in Organic Electroluminescence Devices Using an Al/LiF Electrode. *Appl. Phys. Lett.* **1997**, *70*, 152–154.

(19) Shabaka, A. A.; El-Behery, K. M.; Fadly, M. Infrared Spectroscopic Study of the Molecular Structure of Some Transition Metal TCNE Complexes. *J. Mater. Sci. Lett.* **1988**, *7*, 685–687.

(20) Webster, O. W.; Mahler, W.; Benson, R. E. Chemistry of Tetracyanoethylene Anion Radical. *J. Am. Chem. Soc.* **1962**, *84*, 3678–3684.

(21) Hofmann, O. T.; Egger, D. A.; Zojer, E. Work-Function Modification Beyond Pinning: When Do Molecular Dipoles Count? *Nano Lett.* **2010**, *10*, 4369–4374.

(22) Claridge, S. A.; Liao, W.; Thomas, J. C.; Zhao, Y.; Cao, H. H.; Cheunkar, S.; Serino, A. C.; Andrews, M.; Weiss, P. S. From the Bottom Up: Dimensional Characterization in Molecular Monolayers. *Chem. Soc. Rev.* **2013**, *42*, 2725–2745.

(23) Abendroth, J. M.; Bushuyev, O. S.; Weiss, P. S.; Barrett, C. J. Controlling Motion at the Nanoscale: Rise of the Molecular Machines. *ACS Nano* **2015**, *9*, 7746–7768.

(24) Metzger, R. M. Unimolecular Electronics and Rectifiers. *Synth. Met.* **2009**, *159*, 2277–2281.

(25) Claridge, S. A.; Castleman, A. W.; Khanna, S. N.; Murray, C. B.; Sen, A.; Weiss, P. S. Cluster-Assembled Materials. *ACS Nano* **2000**, *3*, 244–255.

(26) Potocar, T.; Lorbek, S.; Nabok, D.; Shen, Q.; Tumbek, L.; Hlawacek, G.; Puschnig, P.; Ambrosch-Draxl, C.; Teichert, C.; Winkler, A. Initial Stages of a Para-Hexaphenyl Film Growth on Amorphous Mica. *Phys. Rev. B* **2011**, *83*, 1–10.

(27) Udeh, C. U.; Rannou, P.; Brown, B. P.; Thomas, J. O.; Faul, C. F. J. Tuning Structure and Function in Tetra(aniline)-Based Rod–Coil–Rod Architectures. *J. Mater. Chem. C* **2013**, *1*, 6428–6437.

(28) Sereno, P. C.; Wilson, J. A.; Larsson, H. C. E.; Dutheil, D. B.; Sues, H. Alignment and Sensitive Detection of DNA by a Moving Interface. *Science* **2016**, *214*, 93–94.

(29) Buriak, J. M. Organometallic Chemistry on Silicon and Germanium Surface. *Chem. Rev.* **2002**, *102*, 1271–1307.

(30) Stranick, S. J.; Kamna, M. M.; Weiss, P. S. Atomic-Scale Dynamics of a Two-Dimensional Gas-Solid Interface. *Science* **1994**, *266*, 99–102.

(31) Andreev, A.; Matt, G.; Brabec, C. J.; Sitter, H.; Badt, D.; Seyringer, H.; Sariciftci, N. S. Highly Anisotropically Self-Assembled Structures of Para-Sexiphenyl Grown by Hot-Wall Epitaxy. *Adv. Mater.* **2000**, *12* (9), 629–633.

(32) Pathem, B. K.; Claridge, S. A.; Zheng, Y. B.; Weiss, P. S. Molecular Switches and Motors on Surfaces. *Annu. Rev. Phys. Chem.* **2013**, *64*, 605–630.

(33) Donhauser, Z. J.; B. A. Mantooth; K. F. Kelly; l. A. bUMM; J. D. Monnell; J. J. Stapleton; D. W. Price Jr.; A. M. Rawlett; D. L. Allara; J. M. Tour; P. S. Weiss. Conductance Switching in Single Molecules Through Conformational Changes. *Science* **2001**, *292*, 2303–2307.

(34) Hohman, J. N.; Claridge, S. A.; Kim, M.; Weiss, P. S. Cage Molecules for Self-Assembly. *Mater. Sci. Eng. R* **2010**, *70*, 188–208.

(35) Dorokhin, D.; Hsu, S.; Tomczak, N.; Reinhoudt, Ḱ. D. N.; Huskens, J.; Velders, A. H.; Vancso, G. J. Fabrication and Luminescence of Cyclodextrin Functionalized Quantum. *ACS Nano* **2010**, *4*, 137–142.

(36) Paloheimo, J.; Pal, A. J.; Stubb, H. Electrical Transport and Optical Properties of Tetraanilinobenzene Langmuir–Blodgett Films. *J. Appl. Phys.* **1996**, *79*, 7800–7808.

(37) Poirier, G. E. Characterization of Organosulfur Molecular Monolayers on Au(111) Using Scanning Tunneling Microscopy. *Chem. Rev.* **1997**, *97*, 1117–1128.

(38) Maksymovych, P.; Voznyy, O.; Dougherty, D. B.; Sorescu, D. C.; Yates, J. T. Gold Adatom as a Key Structural Component in Self-Assembled Monolayers of Organosulfur Molecules on Au(111). *Prog. Surf. Sci.* **2010**, *85*, 206–240.

(39) Laibinis, P. E.; Whitesides, G. M.; Allara, D. L.; Tao, Y. T.; Parikh, A. N.; Nuzzo, R. G. Comparison of the Structures and Wetting Properties of Self-Assembled Monolayers of N-Alkanethiols on the Coinage Metal Surfaces, Copper, Silver, and Gold. *J. Am. Chem. Soc.* **1991**, *113*, 7152–7167.

(40) Vericat, C.; Vela, M. E.; Benitez, G.; Carro, P.; Salvarezza, R. C. Self-Assembled Monolayers of Thiols and Dithiols on Gold: New Challenges for a Well-Known System. *Chem. Soc. Rev.* **2010**, *39*, 1805.

(41) Floridia Addato, M. A.; Rubert, A. A.; Benítez, G. A.; Fonticelli, M. H.; Carrasco, J.; Carro, P.; Salvarezza, R. C. Alkanethiol Adsorption on Platinum: Chain Length

Effects on the Quality of Self-Assembled Monolayers. *J. Phys. Chem. C* **2011**, *115*, 17788–17798.

(42) Mani, G.; Johnson, D. M.; Marton, D.; Dougherty, V. L.; Feldman, M. D.; Patel, D.; Ayon, A. A.; Mauli Agrawal, C. Stability of Self-Assembled Monolayers on Titanium and Gold. *Langmuir* **2008**, *24*, 6774–6784.

(43) Nakamura, T.; Miyamae, T.; Nakai, I.; Kondph, H.; Kawamoto, T.; Kobayashi, N.; Yasuda, S.; Yoshimura, D.; Ohta, T.; Nozoye, H.; Matsumoto, M. Adsorption States of Dialkyl Ditelluride Autooxidized Monolayers on Au(111). *Langmuir* **2005**, *21*, 3344–3353.

(44) Rampi, M. A.; Schueller, O. J. A.; Whitesides, G. M. Alkanethiol Self-Assembled Monolayers as the Dielectric of Capacitors with Nanoscale Thickness. *Appl. Phys. Lett.* **1998**, *72*, 1781–1783.

(45) Hohman, J. N.; Kim, M.; Wadsworth, G. A.; Bednar, H. R.; Jiang, J.; Lethai, M. A.; Weiss, P. S. Directing Substrate Morphology via Self-Assembly: Ligand-Mediated Scission of Gallium-Indium Microspheres to the Nanoscale. *Nano Lett.* **2011**, *11*, 5104–5110.

(46) Ito, T.; Forman, S. M.; Cao, C.; Li, F.; Eddy, C. R.; Mastro, M. A.; Holm, R. T.; Henry, R. L.; Hohn, K. L.; Edgar, J. H. Self-Assembled Monolayers of Alkylphosphonic Acid on GaN Substrates. *Langmuir* **2008**, *24*, 6630–6635.

(47) Noble-Luginbuhl, A. R.; Nuzzo, R. G. Assembly and Characterization of SAMs Formed by the Adsorption of Alkanethiols on Zinc Selenide Substrates. *Langmuir* **2001**, *17*, 3937–3944.

(48) Xue, Y.; Zimmt, M. B. Patterned Monolayer Self-Assembly Programmed by Side Chain Shape: Four-Component Gratings. *J. Am. Chem. Soc.* **2012**, *134*, 4513–4516.

(49) Schreiber, F. Structure and Growth of Self-Assembling Monolayers. *Prog. Surf. Sci.* **2000**, *65*, 151–256.

(50) Duke, C. B. Semiconductor Surface Reconstruction: The Structural Chemistry of Two-Dimensional Surface Compounds. *Chem. Rev.* **1996**, *96*, 1237–1260.

(51) Iski, E. V.; Jewell, A. D.; Tierney, H. L.; Kyriakou, G.; Sykes, E. C. H. Controllable Restructuring of a Metal Substrate: Tuning the Surface Morphology of Gold. *Surf. Sci.* **2012**, *606*, 536–541.

(52) Kowalczyk, P.; Kozlowski, W.; Klusek, Z.; Olejniczak, W.; Datta, P. K. STM Studies of the Reconstructed Au(111) Thin-Film at Elevated Temperatures. *Appl. Surf. Sci.* **2007**, *253*, 4715–4720.

(53) Allara, D. L.; Parikh, A. N.; Rondelez, F. Evidence for a Unique Chain Organization in Long Chain Silane Monolayers Deposited on Two Widely Different Solid Substrates. *Langmuir* **1995**, *11*, 2357–2360.

(54) Ulman, A. Formation and Structure of Self-Assembled Monolayer. *Chem. Rev.* **1996**, *96*, 1533–1554.

(55) Lim, M. S.; Feng, K.; Chen, X.; Wu, N.; Raman, A.; Nightingale, J.; Gawalt, E. S.; Korakakis, D.; Hornak, L. a; Timperman, A. T. Adsorption and Desorption of Stearic Acid Self-Assembled Monolayers on Aluminum Oxide. *Langmuir* **2007**, *23*, 2444–2452.

(56) Murphy, K. L.; Tysoe, W. T.; Bennett, D. W. A Comparative Investigation of Aryl Isocyanides Chemisorbed to Palladium and Gold: An ATR-IR Spectroscopic Study. *Langmuir* **2004**, *20*, 1732–1738.

(57) Clegg, R. S.; Reed, S. M.; Hutchison, J. E.; January, R. V; Am, C. E. D. J. Self-Assembled Monolayers Stabilized by Three-Dimensional Networks of Hydrogen Bonds. *J. Am. Chem. Soc.* **1998**, *7863*, 2486–2487.

(58) Hu, W. S.; Tao, Y. T.; Hsu, Y. J.; Wei, D. H.; Wu, Y. S. Molecular Orientation of Evaporated Pentacene Films on Gold: Alignment Effect of Self-Assembled Monolayer Molecular Orientation of Evaporated Pentacene Films on Gold: Alignment Effect of Self-Assembled Monolayer. *Langmuir* **2005**, *21*, 2260–2266.

(59) Zheng, Y. B.; Payton, J. L.; Chung, C. H.; Liu, R.; Cheunkar, S.; Pathem, B. K.; Yang, Y.; Jensen, L.; Weiss, P. S. Surface-Enhanced Raman Spectroscopy to Probe Reversibly Photoswitchable Azobenzene in Controlled Nanoscale Environments. *Nano Lett.* **2011**, *11*, 3447–3452.

(60) Kumar, A. S.; Ye, T.; Takami, T.; Yu, B. C.; Flatt, A. K.; Tour, J. M.; Weiss, P. S. Reversible Photo-Switching of Single Azobenzene Molecules in Controlled Nanoscale Environments. *Nano Lett.* **2008**, *8*, 1644–1648.

(61) Smith, R. K.; Lewis, P. A.; Weiss, P. S. Patterning Self-Assembled Monolayers. *Prog. Surf. Sci.* **2004**, *75*, 1–68.

(62) Kim, M.; Hohman, J. N.; Serino, A. C.; Weiss, P. S. Structural Manipulation of Hydrogen-Bonding Networks in Amide-Containing Alkanethiolate Monolayers via Electrochemical Processing. *J. Phys. Chem. C* **2010**, *114*, 19744–19751.

(63) Han, P.; Kurland, A. R.; Giordano, A. N.; Nanayakkara, S. U.; Blake, Ḱ. M. M.; Pochas, C. M.; Weiss, P. S. Heads and Tails: Simultaneous Exposed and Buried Interfaces Imaging of Monolayers. *ACS Nano* **2009**, *3*, 3115–3121.

(64) Lewis, P. A.; Inman, C. E.; Maya, F.; Tour, J. M.; Hutchison, J. E.; Weiss, P. S. Molecular Engineering of the Polarity and Interactions of Molecular Electronic Switches. *J. Am. Chem. Soc.* **2005**, *127*, 17421–17426.

(65) Quek, S. Y.; Venkataraman, L.; Choi, H. J.; Louie, S. G.; Hybertsen, M. S.; Neaton, J. B. Amine - Gold Linked Single-Molecule Circuits: Experiment and Theory. *Nano Lett.* **2007**, *7*, 3477–3482.

(66) Wang, Y.; Torres, J. A.; Stieg, A. Z.; Jiang, S.; Yeung, M. T.; Rubin, Y.; Chaudhuri, S.; Duan, X.; Kaner, R. B.; Al, W. E. T. Graphene-Assisted Solution Growth of Vertically Oriented Organic Semiconducting Single Crystals. *ACS Nano* **2015**, *9*, 9486–9496.

(67) Mohtasebi, A.; Chowdhury, T.; Hsu, L. H. H.; Biesinger, M. C.; Kruse, P. Interfacial Charge Transfer between Phenyl-Capped Aniline Tetramer Films and Iron Oxide Surfaces. *J. Phys. Chem. C* **2016**, *120*, 29248–29263.

(68) Seminario, J. M.; Zacarias, A. G.; Tour, J. M. Theoretical Interpretation of Conductivity Measurements of a Thiotolane Sandwich. A Molecular Scale Electronic Controller. *J. Am. Chem. Soc.* **1998**, *120*, 3970–3974.

(69) Hsu, L. H. H.; Hoque, E.; Kruse, P.; Ravi Selvaganapathy, P. A Carbon Nanotube Based Resettable Sensor for Measuring Free Chlorine in Drinking Water. *Appl. Phys. Lett.* **2015**, *106*, 63102-1-063102–063104.

(70) Rohwerder, M. Conducting Polymers for Corrosion Protection: A Critical View. *Int. J. Mat. Res.* **2009**, *219*, 1331–1342.

(71) Caldwell, W. B.; Campbell, D. J.; Chen, K.; Herr, B. R.; Mirkin, C. a; Malik, A.; Durbin, M. K.; Dutta, P.; Huang, K. G. A Highly Ordered Self-Assembled Monolayer Film of an Azobenzenealkanethiol on Au(111): Electrochemical Properties and Structural Characterization by Synchrotron in-Plane X-Ray Diffraction, Atomic Force Microscopy, and Surface-Enhanced Raman Spectroscopy. *J. Am. Chem. Soc.* **1995**, *117*, 6071–6082.

(72) Feringa, B. L.; Van Delden, R. a.; Feringa, B. L.; Delden, R. a Van; Koumura, N.; Koumura, N.; Geertsema, E. M.; Geertsema, E. M. Chiroptical Molecular Switches. *Chem. Rev.* **2000**, *100*, 1789–1816.

(73) Morgenstern, K. Switching Individual Molecules by Light and Electrons: From Isomerisation to Chirality Flip. *Prog. Surf. Sci.* **2011**, *86*, 115–161.

(74) Henzl, J.; Bredow, T.; Morgenstern, K. Irreversible Isomerization of the Azobenzene Derivate Methyl Orange on Au(1 1 1). *Chem. Phys. Lett.* **2007**, *435*, 278–282.

(75) Alemani, M.; Peters, M. V.; Hecht, S.; Rieder, K. H.; Moresco, F.; Grill, L. Electric Field-Induced Isomerization of Azobenzene by STM. *J. Am. Chem. Soc.* **2006**, *128*, 14446–14447.

(76) Juluri, B. K.; Kumar, A. S.; Liu, Y.; Ye, T.; Yang, Y.; Flood, Ḱ. A. H.; Fang, L.; Stoddart, J. F.; Weiss, P. S.; Huang, T. J. A Mechanical Actuator Driven Electrochemically by Artificial Molecular Muscles. *ACS Nano* **2009**, *3*, 291–300.

Chapter 2 Chemical Sensors Based on Surface Charge Transfer

2.1 Chemical Sensors

A chemical sensor is a device which can measure analytical parameters in real-time or semi real-time and convert the chemical data to measurable signal.[1] Each chemical sensor consists of two general parts, a detection agent, and a transducer. The detection agent (receptor part) transform the chemical information into a form of energy while the transducer transforms this energy to a measurable signal.[2] Transduction mechanism of chemical sensors is a criterion which can be used for their categorization. Based on this criterion, the most common groups of chemical sensors are optical sensors, electrochemical sensors, and electrical sensors. In optical sensors, the change in the optical properties of a reagent upon interaction with an analyte is measured. Some of these optical properties are absorption, fluorescence, light scattering, and decay time. The advances in optoelectronic industry in recent years assisted to the development of high quality light sources, photodetectors, and fiber optics which they can be used for developments of inexpensive and reliable optical sensors. These achievements have been made optical sensors a popular choice for various applications from water quality monitoring to biomedical applications. The most common optical sensor is pH papers in which a reagent has been covalently immobilized on a paper.

Another widely used group of chemical sensors are electrochemical sensors. The simple design of such sensors consists of two conductive electrodes and an electrolyte. The

most common use of electrochemical sensors is in pH measurement in which the activity of the hydronium ions is measured.[1,2] However, usually a reference electrode is also used in chemical sensors (Ag/AgCl electrode) to increase the precision of the measurements. Electrochemical sensors are designed based on various electrochemical techniques such as voltammetry, amperometry, potentiometry, and impedometry. The two former methods are more often used in chemical sensors. In voltammetry measurement, an applied potential to an electrode is linearly ramped to more negative potential and followed by ramping back to more positive potential while during this cycle the current is measured. In forward scan, the reduction of an analyte at any of the applied potential is monitored. Once the applied potential is equal to the reduction potential of the analyte the measured current increases. This follows by the reduction of the measured current as a result of the depletion of the analyte. In the reverse scan, at certain potential the analyte will be reoxidze to its initial form. This will appear as a peak with a reverse sign as the reduction peak. Theoretically, for a reversible process the difference between the reduction and oxidation peaks are about 59 mV. In amperometry measurement, a constant potential is applied and the change in measured current as a function of time is monitored. The value for this potential can be determined from the voltammogram of the analyte of interest.[2]

Chemical sensors operating based on electrical transduction are another group of chemical sensors. These sensors should not be mistaken for electrochemical signal because they do not have electrodes and do not necessarily require electrolyte solution. Therefore, these sensors can be used in liquids as well as in gas phase. Chemiresistive sensor are the main group of sensors based on electrical transduction. In these sensors, the changes in the

conductivity of an active layer is used to detect the presence of an analyte. Various types of interactions between the active material and the analyte can lead to change in the conductivity of the active layer. For example, the analyte can cause oxidation or reduction of the active layer or the analyte can undergo charge transfer with the active layer through processes such as surface doping.[3] More sophisticated sensors based on electrical transduction are sensor based on the architecture of field effect transistors. Therefore, this group of sensors are often called chemical field effect transistor (CHEMFET). Often in CHEMFETs, the interaction of analyte with the gate electrode is used to influence the charge transport in the conductive channel.[4] However, there are have reports that the direct interaction of the analyte with the conductive channel is used to influence the charge transport. The former architecture is simpler than the traditional CHEMFETs as the dielectric layer and the gate electrode have been removed.[5]

2.2 Chemiresistive Sensors

2.2.1 Metal Oxide Thin Film Chemical Sensors

Some of the earliest works on chemical sensors based on electrical transduction have been reported for chemiresistive sensors.[6,7] A simple description of the operating principle of these devices is that the adsorption of chemical species on the surface of a conductive/semiconducting materials leads to the changes in electrical properties of the substrate, mainly its electrical conductivity. The conductive substrate can be simply attached to conductive electrical leads connected to a source measurement unit.[7] More

sophisticated contact geometries include four-point electrical contacts or using interdigitated electrodes.[8] The chemical species can interact with the sensing film through various pathways such as physisorption, chemisorption, catalytic reactions, reaction at grain boundaries, and bulk reactions.[8] The change in the electrical properties of the sensing material by the adsorbed chemical species on its surface can be performed through different means such as oxidation/reaction of the surface or change in the surface work function.[8] Some of the earliest work on chemiresistive sensors have been performed using thin or thick oxide films such as tin oxide.[8] It was shown that the adsorption of oxygen molecules on this surface leads to the formation of O_2^- and O^-.[8] Since the tin oxide is an intrinsic n-doped semiconductor, the flow of electrons from this metal oxide electrode to these species leads to the decrease in its electrical conductivity. Up on exposure of this surface to a reducing gas (e.g. H_2, NH_3, CO) the electron transfer from the adsorbed gases to the metal oxide leads to the increase in the electrical conductivity of the substrate while the adsorption of an oxidizing gas such as NO_2 leads to an opposite response. In the latter situation, the direction of the charge transfer is opposite causing the formation of NO_2^- and thus reduction in the conductivity of the metal oxide.[6,7'9] Since the sensing depends on the surface adsorption/reactions, the surface structure of the sensing film (grain boundaries, defects, …) plays a key role in sensing.[8] Figure 2.1 demonstrates the schematic of reaction of different gases with different surface sites available in a thin film sensor and the direction of the charge transfer for each surface-analyte interface. Although the sensing step in these sensors often is performed at low temperatures (room temperature-100 ℃), the resetting step requires elevated temperatures in the range of 100-400 ℃.[8] These high temperatures

are essential for resetting the sensor as the thermal energy enhance the rate of the analyte desorption from the metal oxide surface.[10] However, the requirement for such step at high temperatures counts as the main drawback of these sensors and is the reason behind the limited application of such sensors. In addition, both sensing and/or resetting at elevated temperatures can cause sintering of the sensing film which can alter its reaction sites essential for chemical sensing. Some of these reaction sites are point and bulk defects, and grain boundaries.[8]

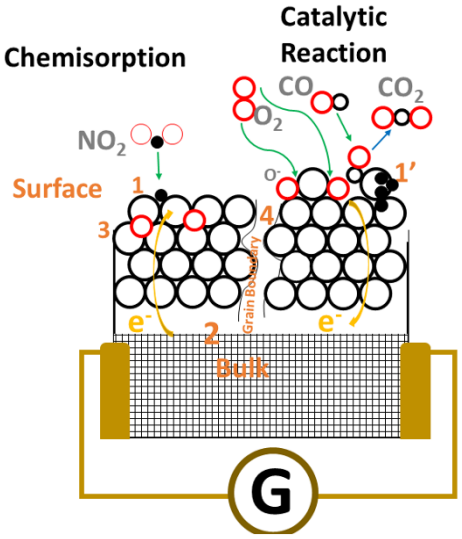

Figure 2.1. Schematic representation of detection of gas molecules by an active layer in chemiresistive sensor. Interaction of gas molecules lead to the change in the conductivity of the bulk and the surface of the active layer. Some of these reactions are from undoped (1) or doped surfaces (1´), from the bulk of the film (2), from the contacts (3), and from the grain boundaries (4).

2.2.2 Chemiresistor Sensors Based on Intrinsic Conductive Polymers

Another group of materials which have been widely used for chemical sensing applications are intrinsic conductive polymers (ICP) and their oligomers. The common structure of ICPs consist of repeating units of small organic monomers. Figure 2.2 shows some of these monomers such as acetylene, pyrrole, thiophene, and aniline.[7] The conductivity of the ICPs originates from the alternating single and double bonds which leads to the formation of delocalized electronic states.[11] These polymers in their neutral forms are not electrically conductive but can become conductive upon n-doping or p-doping reactions.[12] These processes lead to the generation of charge carriers on their backbone which transform them to one-dimensional conductors.[7] Such changes in their conductivity upon interaction with various chemical species (redox, basic/acidic) can be utilized for sensing applications. The adsorbed gas molecules on such polymers can act as secondary dopants, exchange charge carriers with polymers which can lead to the modulation of their electronic, optical, or magnetic properties.[11]

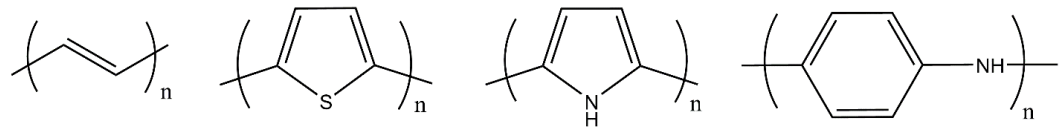

Polyacetylene (t-PA) Polythiophene (PT) Polypyrrole (ppy) Polyaniline (PANI)

Figure 2.2. Molecular structure of four intrinsic conductive polymer in their insulating state.

Most of the chemical sensors that have been developed based on ICPs are gas sensors. In these sensors, the polymer can be used as either the selective sensing material or as an interconnect component. The latter application is not desired as the change in the electrical conductivity of the interconnect component can interfere with the main sensing process.[11] Therefore, the ICPs or other organic small molecules should only be used as the selective sensing material. The simplest and most common measurement configuration for chemical sensors based on ICPs is the chemiresistor with two electrical leads (Figure 2.3a). In this configuration, the polymer film is deposited between two electrodes (commonly Au) and a constant current or voltage is applied between them (dc or ac).[12] The gaseous can interact with the ICP layer and act either as electron donor or electron acceptor. In the former case, the electrical conductivity of the film increases while in the latter case, it decreases.[11] Therefore, the common way to report the response from the ICP based sensors is in the form of $(R_1-R_0)/R_0$, where R_0 is the resistance of the system before the exposure to the analyte and R_1 is its resistance after exposure to the analyte.[7] This simple principle leads to the detection of the chemical species of interest present in the gas phase. The drawback of this configuration is the drop of the potential at the metal-polymer contacts. Such a change in the electrical conductivity at this junction is attributed to the modulation of the schottky barrier height which can be determined from the differences between the work function of the polymer and metal electrodes.[11] In addition the choices of the metal electrode can also influence the type of the contacts with the polymer film and as a result different magnitude of the response. It has been reported that the contact between gold and polyaniline (PANI) is ohmic while the contact between platinum (Pt) and PANI in the

presence of hydrogen is in the form of schottky contact. The latter system showed a greater response (65% increase in the resistance) to the presence of hydrogen gas in comparison to the former system (3% decrease in the resistance). The absence of hydrogen in the chemical sensor based on Pt-PANI sets back the contact between the metal and polymer film to the ohmic contact.[13] One way to avoid the contribution of the metal-polymer contact in the sensing response of a chemical sensor is through using four-point measurement configuration (Figure 2.3d). However, this technique does not provide any information regarding the contact resistance. This is not favorable in cases in which the contact resistance is higher than the sensing response. To be able to do both two- and four- point measurements the configuration in Figure 2.3e can be used. This configuration is also called as s24-configuration. This configuration enables the comparison of the delay time between the two- and four- measurement signal which can provide information regarding diffusion of the gas through the polymer layer. As it was mentioned earlier, most of the sensing measurements using these configurations are performed by application of constant potential or constant current. However, this can itself cause irreversible or reversible changes in the polymer layer.[12] Some of the measures to avoid such events are by application of ac technique (instead of dc) or by continuous switching of the dc pulses. In addition, the probe power should be limited as it can lead to self-heating of the polymer layer.[12] Some other common sensing configurations involving two- and/or four- point configurations are shown in Figures 2.3b, 2.3c, and 2.3f. Figure 2.3b shows the typical configuration which uses a conductive polymer layer in electrochemical systems. These configurations are based on organic field effect transistors in which the current between

the source and the drain electrodes is regulated by the gate voltage.[12] The details of the chemical sensors will be more discussed along with the discussion about CHEMFETs. In many chemical sensors based on conductive polymers, specifically in biosensor, the conductivity of the conductive polymer is low which results difficulties in measurement of its conductivity between two electrodes. In such cases the conductivity between the conductive polymer layer and an electrode in solution is used for sensing measurement.[12] Figure 2.3c shows a somewhat similar configuration to the set up in Figure 2.3b with the difference that in the latter case the purpose of the external electrode is fixation of the polymer potential. This is useful if the controlling the redox states of the polymer is required. This set up resembles the filed effect transistor (FET) architecture as the external electrode can control the potential of the polymer layer and thus it was termed as electrochemical transistor set up.[12]

Although chemiresistor sensors based on conductive polymers are simple, easy to fabricate, and can be prepared in various configurations, they have several drawbacks. First, the thickness of the organic film can greatly affect the response. Polymer films are porous and thus gas molecules of the analyte can diffuse through them.[14] However, the morphology of the polymer film (filament or dendritic, smooth, or compact) itself can change the sensitivity of device.[15,16] The interface between the polymer film and the insulating substrate of the sensor itself can affect the electrical response. Last but not the least, the copresence of different gases and moisture present in ambient environment can also interfere with the response from the analyte of interest.[11’17]

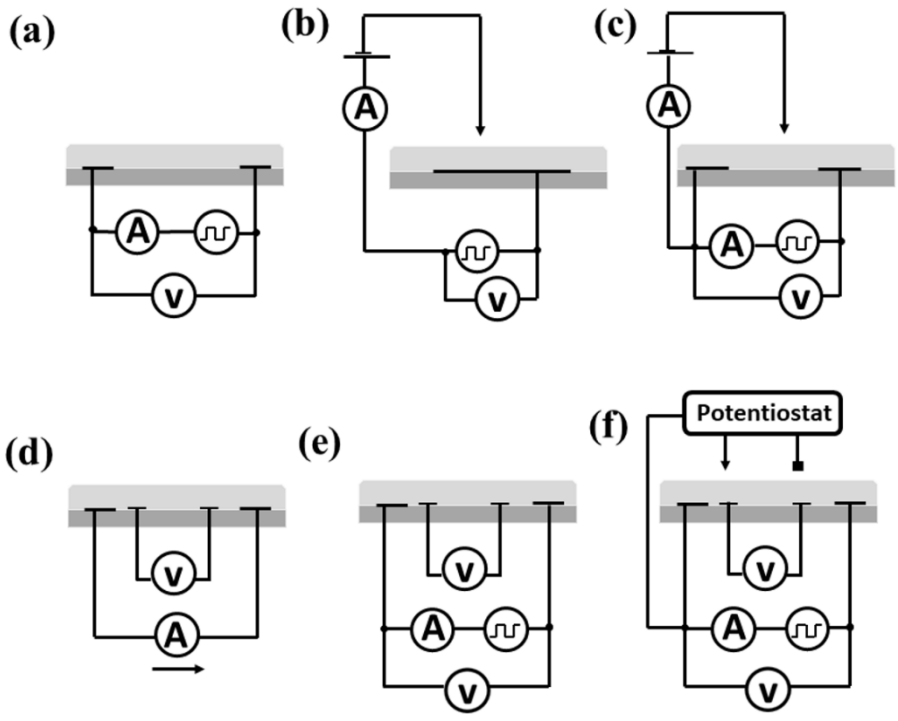

Figure 2.3. Common measurement configurations in chemiresistive sensors based on ICP selective layers. (a) Two-point measurement without fixation of the ICP layer, (b) typical set up used in electrochemical experiments, (c) Two-point measurement with fixation of the ICP layer, (d) Four-point technique, (e) Two- and Four- point measurement together without fixation of ICP potential, and (f) Two- and Four- point measurement together with fixation of ICP potential.

2.2.3 Chemiresistor Sensors Based on Nanocarbons

Another group of materials that have been extensively incorporated into the chemiresistor sensors are nanocarbons such as carbon nanotubes (CNTs),[18] graphene,[19] and even graphite or pencil lead.[20] Carbon based materials are often resistant to harsh chemical conditions and high temperatures.[18'20] In most cases, they are inexpensive or there is research underway for their mass production which will eventually reduce their production cost.[21] They are easy to fabricate on various substrates and can be prepared through various

fabrication methods such as CVD,[22] inkjet printing,[23] or drop-casting.[24] All of these parameters make them suitable materials for sensing applications. They have been both used for gas sensing18 and sensing in liquid phases.[24]

CNTs are one of the main group of nanocarbons which are used in chemiresistor sensors. The common form of CNTs used in electronic devices are single-walled carbon nanotubes (SWCNTs). They are used as the sensing materials and often suspended over Au or Pt electrodes. One of the unique characteristics of CNTs is their high surface area (~ 1600 m^2 g^{-1}).[18] In addition, they have superb electrical properties such as carrier mobility as high as ~10000 cm^2 V^{-1} s^{-1} which is better than silicon and electrical current density of ~ 4×10^9 A cm^{-1}, which is about thousand times higher than copper.[25] CNTs can be chemically doped (p- or n- doped) by wide range of chemical species.[26,27] Combination of these characteristics make SWCNTs a better choice than ceramics (e.g. SnO_2) or ICPs for sensing applications. In addition, in contrast to the sensors based on ceramics, they can operate at room temperature. The common sensing mechanism of chemical species by chemiresistive sensors based on CNTs are similar to what was described earlier for chemiresistive sensors based on ICPs/small molecules and metal oxides. The high surface area of CNTs allow good interaction with the analyte molecules. The analyte molecules adsorbed on this surface and can transfer charge with CNTs and as a result change the charge polarity (dope) of CNTs.[28] This will lead to change in the electrical conductivity of the CNTs and can be used for detection of analyte molecules.[29] Although, the presence of metallic CNTs is not crucial for chemiresistive sensors, it is more critical in the case FETs based on CNTs.[18] In addition, even in each batch of synthesized CNTs, the diameter of the

tubes is different. Since the bandgap of semiconducting CNTs have inverse relationship with their diameter, the bandgap of the tubes in each batch can vary over a broad range. As an example, it was reported that the SWCNTs produced via laser-ablation method have diameter over 11 to 16 Å which will lead to the variation of their bandgap from 0.65 to 0.95 eV.30 These variations in diameter, bandgap, and their electronic type (metallic/semiconducting) can cause reproducibility issues for mass production of such sensors.[18] Fortunately, in recent years the as synthesized CNTs (specially SWCNTs) can be sorted through various separation means in order to produce more homogenous batches of tubes.[30] Another issue with application of CNTs in electronic devices including chemiresistor sensors is based on the high contact resistance between the metallic electrodes and the CNTs. Suspending CNTs over electrodes often cause unreliable contacts between the electrodes and CNTs. This issue can be circumvented by new techniques such as creating end-bonded contacts between CNTs and molybdenum to form carbide.[31] Although, chemiresistive sensors based on CNTs are often more sensitive than the ones based one ICPs, both suffer from similar problems associated with the effects of interfering molecules present in uncontrolled environments such as ambient conditions. It is known that humidity, hydrogen bonding with oxygen defects, and direct water adsorption can greatly affect the baseline resistance of the sensor. Such cross sensitivity between interfering molecules and the analyte of interest makes the process of stablishing a calibration curve for these sensors challenging.[18] Another popular nanocarbon for use in chemical sensors is graphene. Graphene is a flat monolayer of carbon atoms arranged in the form of two-dimensional (2D) honeycomb lattice. Graphene is the basic building blocks

of many carbon allotropes such as graphite (3D), CNT (1D), and fullerenes (0D).[32] The pioneering reports on the concept of graphene set back to sixty years ago and related to the theoretical studies on the band structure of graphite.[33,34,35] For a long time, it was believed that the 2D crystals are thermodynamically unstable and as the lateral size increases the 2D crystal transform to a stable 3D structure.[36] The reason for such argument was that the thermal fluctuations in low-dimensional crystals lead to displacement of atoms over distances as large as their interatomic distances at any finite temperature. However, advances in fabrication and characterization of graphene showed the possibility of the existence of 2D crystals.[37] Graphene can be produced by several approaches such as mechanical exfoliation of graphite, chemical exfoliation of graphite, and epitaxial growth.[32,38,39]

The s, p_x, p_y of each carbon atom in a graphene sheet hybridized to form strong covalent sp^2 bonds leading to the chicken-wire-like arrangements. The p_z atomic orbital of each carbon atom overlaps with the other p_z orbitals forming filled π orbitals (valance band) and empty π^* orbitals (conduction band). This means three out four valance electrons of each carbon atom form σ bonds while the fourth electron participate in π bonding.[40,41] The superior electronic properties of graphene are mainly due to its high quality 2D crystal. Although graphite is made of AB stack of graphene sheets, their electronic structure is not similar. It is known that graphite is a semimetal while a single layer graphene is known as a zero-band gap semiconductor. The conduction band (CB) and valance band (VB) of graphene are cone-shaped which meet each other at Dirac point.[42,43] By increasing the number of sheets in graphene, crystal shows more semimetallic behavior and for the stack

of 11 or higher number of sheets, the band overlap is less than 10% different from graphite.[43] Another unique electrical property of graphene is its high charge carrier mobility (as high as 20,000 cm^2/Vs for Si/SiO_2 supported graphene sheets under the ambient conditions).[32]

Similar to CNTs, graphene can become both p-doped or n-doped through various means such as electric filled effect or by chemical dopants. The former method is based on the possibility to tune charge carriers between electrons and holes by changing the polarity of gate voltage (V_g). This means when V_g is negative the Fermi level is below the Dirac point and the VB is full of holes and when the V_g is positive the Fermi level is above the Dirac point and the CB is filled with electrons.[32] The latter method (chemical doping) is similar to the doping of CNTs as described earlier. Therefore, it is not surprising that one of the first electronic devices developed based on graphene was chemical sensor.[44] In fact, some of the most sensitive gas sensors ever developed are based on graphene which can detect adsorption/desorption of an individual gas molecule.[19] Up on adsorption of an individual gas molecule on graphene, the local carrier concentration in this substrate will change, which will appear as a step in the resistance. The reason behind the possibility to detect such a small change is the unique and extremely low-noise characteristic of graphene. Thus, the possibility of chemical doping of graphene is one of the basis of using this material in sensing devices.[19] In addition, graphene has high surface area (>2000 m^2/g) which is an important aspect in sensing applications. It has an advantage over CNTs in which it can be prepared in high quality with very low defect sites.[45] Graphene has been incorporated in both chemiresistor configuration[46] as well as chemical field-effect

transistor (CHEMFET) configuration.[47] These sensors have been used for both gas sensing and sensing in liquids.[46'47] Graphene, similar to CNTs, suffers from high sensitivity to many interfering adsorbates (humidity, oxygen,…) present in liquids or in ambient conditions and decrease the sensitivity of the device.[46]

2.3 CHEMFET

Another configuration for chemical sensing is based on the field-effect transistors (FETs) architecture. The general idea behind these sensors is that the interaction of the analyte with the gate electrode affect the charge transport properties in the conductive channel of the FET. This is different than the general scheme of FETs in which the gate electrode is insulated from the surrounding environment (Insulated Gate FET (IGFET)). Therefore, the gate electrode acts as the selective layer. The same technology which is used in semiconductor technology for fabrication of FETs can be used for fabrication of these sensors. Therefore, they can be miniaturized since in CHEMFETs the signal does not depend on the size of the sensing area. However, the signal from these type of sensors is small and required high input impedance amplifier.[4]

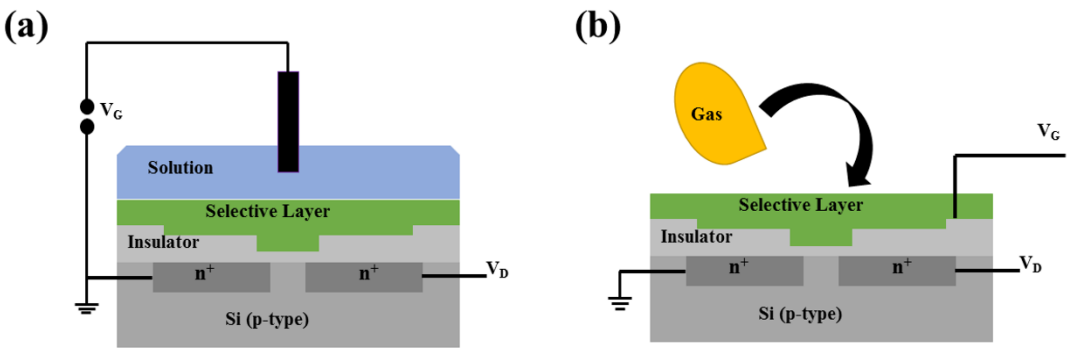

Figure 2.4. Schematic representation of two common architecture of CHEMFET. (a) ion sensitive (ISFET) sensor. (b) Work function sensor (WF-FET), in which no external reference electrode is required.

Traditionally, CHEMFETs have been categorized under two main configurations; ion-sensitive FET (ISFET, Figure 2.4a) and work function FET (WF-FET, Figure 2.4b). ISEF function based on the selective separation of ionic charge present in the analyte sample at its interface with the selective layer (e.g. ion selective membrane). Therefore, the interfacial potential follows the Nernst equation. Since the potential of a single electrode is not measurable, a second reference electrode is used to measure the potential difference between this electrode and the selective layer.[4] This design has been mostly used for pH measurements. Based on the analyte of interest, the selective layer of ISFET can be fabricated from either semiconducting inorganic or organic materials (e.g. ICP).[48] WF-FET resembles the working principle of Kelvin probes (vibrating capacitor).[49] The schematic of this configuration is depicted in Figure 2.4b. Since this configuration does not require the presence of an external electrode (unlike ISFET), they are suitable for miniaturization. It has been argued that the gate electrode in FETs is part of a capacitor consisting of the gate

electrode (here selective layer), the dielectric layer, and the conductive channel (often Si in FETs). The two plates of this capacitor (selective layer and the channel) have different chemical potential. Their connection leads to equalization of their fermi levels which results in formation of an electric field. Since in FETs the channel is sealed from the surrounding environment its work function remains unchanged during the sensing events. Therefore, it can be used as a reference electrode.[4] The gate electrode in WF-FET can be fabricated from ICPs.[48] The interaction of analyte molecules with this electrode leads to the charge transfer between them and the formation of a donor/acceptor complexs.[50] The extent of this charge transfer depends on the electron affinity of the host material (selective layer) and charge donacity of the analyte species.[4]

2.3.1 Chemical Sensing Based on Electrostatically Charged Selective Layer

CHEMFETs show many advantages such as the possibility to scale down their size or use current semiconducting fabrication technology for their mass production while maintaining uniform quality across devices.[4] The main difference between the chemiresistive sensors and CHEMFETs is the absence of the dielectric layer and gate electrode. This makes chemiresistive sensors simple, inexpensive, and allow easy incorporation of carbon nanotubes, graphene, and other 2D materials in these sensors. It has been recently reported that the electrostatic gating of semiconducting materials such as CNTs through chemical surface adsorbates can be used to create CHEMFETs without the need of dielectric layer and gate electrode.[5] The architecture of the reported sensor is

similar to chemiresistive sensors but the function and the response of the sensor is similar to CHEMFETs. It has been shown that the increase in the functional density of the negatively charged adsorbed receptors on CNTs can modulates the charge transport in the tube (charge transport layer). Based on this observation, it was concluded that the sensing mechanism of the device is based on chemically driven electrostatic gating. Therefore, the field effect created through electrostatic gating is similar to the effect of gate voltage in FETs (CHEMFETs).[5]

In this chapter, the typical transduction mechanism in chemical sensors were introduced. The working principle of different variations of chemiresistor sensor were described and the most common materials used in each one was mentioned. The advantages and disadvantages of each architecture was briefly mentioned. The CHEMFET and its most common configurations were briefly introduced. In addition, it was concluded that some variations of chemiresistor can be counted as CHEMFET, which have several advantages over traditional CHEMFET such as no need of gate electrode and dielectric layer.

2.4 References

(1) Wencel, D.; Abel, T.; McDonagh, C. Optical Chemical pH Sensors. *Anal. Chem.* **2014**, *86*, 15–29.

(2) Rahman, M. A.; Kumar, P.; Park, D.-S.; Shim, Y.-B. Electrochemical Sensors Based on Organic Conjugated Polymers. *Sensors* **2008**, *8*, 118–141.

(3) Janata, J.; Josowicz, M. Conducting Polymers in Electronic Chemical Sensors. *Nat. Mater.* **2003**, *2*, 19–24.

(4) Janata, J. Thirty Years of CHEMFETs - A Personal View. *Electroanalysis* **2004**, *16*, 1831–1835.

(5) Ng, A. L.; Chen, C.; Kwon, H.; Peng, Z.; Lee, C. S.; Wang, Y. Chemical Gating of a Synthetic Tube-in-a-Tube Semiconductor. *JACS* **2017**, *139*, 3045–3051.

(6) Seiyama, T.; Fujiishi, K.; Nagatani, M.; Kato, A. A New Detector for Gaseous Components Using Zinc Oxide Thin Films. *J. Soc. Chem. Ind. Japan* **1963**, *66*, 652–655.

(7) Albert, K. J.; Lewis, N. S.; Schauer, C. L.; A, G.; Stitzel, S. E.; Vaid, T. P.; Walt, D. R. Cross-Reactive Chemical Sensor Arrays. *Chem. Rev.* **2000**, *100*, 2595–2626.

(8) Göpel, W.; Schierbaum, K. D. SnO2 Sensors: Current Status and Future Prospects. *Sensors and Actuators B: Chem.* 1995, 1–12.

(9) Yamazoe, N.; Miura, N. Environmental Gas Sensing. *Sensors Actuators B. Chem.* **1994**, *20*, 95–102.

(10) Cho, B.; Hahm, M. G.; Choi, M.; Yoon, J.; Kim, A. R.; Lee, Y.-J.; Park, S.-G.; Kwon, J.-D.; Kim, C. S.; Song, M.; Jeong, Y.; Nam, K.-S.; Lee, S.; Yoo, T. J.; Kang, C. G.; Lee, B. H.; Ko, H. C.; Ajayan, P. M.; Kim, D.-H. Charge-Transfer-Based Gas Sensing Using Atomic-Layer MoS2. *Sci. Rep.* **2015**, *5*, 8052.

(11) Janata, J.; Josowicz, M. Conducting Polymers in Electronic Chemical Sensors. *Nat. Mater.* **2003**, *2*, 19–24.

(12) Lange, U.; Mirsky, V. M. Chemiresistors Based on Conducting Polymers: A Review on Measurement Techniques. *Anal. Chim. Acta* **2011**, *687*, 105–113.

(13) Fowler, J. D.; Virji, S.; Kaner, R. B.; Weiller, B. H. Hydrogen Detection by Polyaniline Nanofibers on Gold and Platinum Electrodes. *J. Phys. Chem. C* **2009**, *113*, 6444–6449.

(14) Huang, J.; Virji, S.; Weiller, B. H.; Kaner, R. B. Polyaniline Nanofibers: Facile Synthesis and Chemical Sensors. *J. Am. Chem. Soc.* **2003**, *125*, 314–315.

(15) Xue, M.; Li, F.; Chen, D.; Yang, Z.; Wang, X.; Ji, J. High-Oriented Polypyrrole Nanotubes for Next-Generation Gas Sensor. *Adv. Mater.* **2016**, *28*, 8265-8270.

(16) Virji, S.; Huang, J. X.; Kaner, R. B.; Weiller, B. H. Polyaniline Nanofiber Gas Sensors: Examination of Response Mechanisms. *Nano Lett.* **2004**, *227*, 491–496.

(17) Virji, S.; Kaner, R. B.; Weiller, B. H. Hydrogen Sensors Based on Conductivity Changes in Polyaniline Nanofibers. *J. Phys. Chem. B* **2006**, *110*, 22266–22270.

(18) Meyyappan, M. Carbon Nanotube-Based Chemical Sensors. *Small* **2016**, *12*, 2118–2129.

(19) Schedin, F.; Geim, A. K.; Morozov, S. V; Hill, E. W.; Blake, P.; Katsnelson, M. I.; Novoselov, K. S. Detection of Individual Gas Molecules Adsorbed on Graphene. *Nat. Mater.* **2007**, *6*, 652–655.

(20) Kurra, N.; Kulkarni, G. U. Pencil-on-Paper: Electronic Devices. *Lab Chip* **2013**, *13*, 2866–2873.

(21) Wakeland, S.; Martinez, R.; Grey, J. K.; Luhrs, C. C. Production of Graphene from Graphite Oxide Using Urea as Expansion-Reduction Agent. *Carbon* **2010**, *48*, 3463–3470.

(22) Bianco, G. V; Losurdo, M.; Giangregorio, M. M.; Capezzuto, P.; Bruno, G. Exploring and Rationalizing Effective N-Doping of Large Area CVD-Graphene by NH3. *Phys. Chem. Chem. Phys.* **2014**, *16*, 3632–3639.

(23) Qin, Y.; Kwon, H. J.; Subrahmanyam, A.; Howlader, M. M. R.; Selvaganapathy, P. R.; Adronov, A.; Deen, M. J. Inkjet-Printed Bifunctional Carbon Nanotubes for pH Sensing. *Mater. Lett.* **2016**, *176*, 68–70.

(24) Hsu, L. H. H.; Hoque, E.; Kruse, P.; Selvaganapathy, P. R. A Carbon Nanotube Based Resettable Sensor for Measuring Free Chlorine in Drinking Water. *Appl. Phys. Lett.* **2015**, *106*, 63102.

(25) Hong, S.; Myung, S. Nanotube Electronics: A Flexible Approach to Mobility. *Nat. Nanotechnol.* **2007**, *2*, 207–208.

(26) Moonoosawmy, K. R.; Kruse, P. Cause and Consequence of Carbon Nanotube Doping in Water and Aqueous Media. *J. Am. Chem. Soc.* **2010**, *132*, 1572–1577.

(27) Moonoosawmy, K. R.; Moonoosawmy, K. R.; Kruse, P.; Kruse, P. To Dope or Not to Dope: The Effect of Sonicating Single- Wall Carbon Nanotubes in Common Lab Solvents on Their Electronic Structure SI. *J. Am. Chem. Soc.* **2009**, *130*, 4522–4525.

(28) Klinke, C.; Chen, J.; Afzali, A.; Avouris, P. Charge Transfer Induced Polarity Switching in Carbon Nanotube Transistors. *Nano Lett.* **2005**, *5*, 555–558.

(29) Li, J.; Lu, Y.; Ye, Q. L.; Han, J.; Meyyappan, M. Carbon Nanotube Based Chemical Sensors for Gas and Vapor Detection. *Nano Lett.* **2003**, *3*, 929-933.

(30) Arnold, M. S.; Green, A. A.; Hulvat, J. F.; Stupp, S. I.; Hersam, M. C. Sorting Carbon Nanotubes by Electronic Structure Using Density Differentiation. *Nat. Nano.* **2006**, *1*, 60.

(31) Cao, Q.; Han, S.; Tersoff, J.; Franklin, A. D.; Zhu, Y.; Zhang, Z. End-Bonded Contacts for Carbon Nanotube Transistors with Low, Size-Independent Resistance. *Science* **2015**, *350*, 68–71.

(32) Geim, A. K.; Novoselov, K. S. The Rise of Graphene. *Nat. Mater.* **2007**, *6*, 183–191.

(33) McCurle, J. W. Diamagnetism of Graphite. *Phys. Rev.* **1956**, *104*, 666–671.

(34) Slonczewski, J. C.; Weiss, P. R. Band Structure of Graphite. *Phys. Rev.* **1958**, *330*, 272–279.

(35) Wallace, P. R. The Band Theory of Graphite. *Phys. Rev.* **1947**, *71*, 622–634.

(36) Mermin, N. D. Crystalline Order in Two Dimensions. *Phys. Rev.* **1968**, *176*, 250–254.

(37) Novoselov, K. S.; Geim, A. K.; Morozov, S. V; Jiang, D.; Zhang, Y.; Dubonos, S. V; Grigorieva, I. V; Firsov, A. A. Electric Field Effect in Atomically Thin Carbon Films. *Science* **2004**, *306*, 666–669.

(38) Levendorf, M. P.; Ruiz-Vargas, C. S.; Garg, S.; Park, J. Transfer-Free Batch Fabrication of Single Layer Graphene Transistors. *Nano Lett.* **2009**, *9*, 4479–4483.

(39) Geim, A. K. Graphene: Status and Prospects. *Science* **2009**, *324*, 1530–1534.

(40) Allen, M. J.; Tung, V. C.; Kaner, R. B. Honeycomb Carbon: A Review of Graphene. *Chem. Rev.* **2010**, *110*, 132–145.

(41) Denis, P. a.; Iribarne, F. Comparative Study of Defect Reactivity in Graphene. *J. Phys. Chem. C* **2013**, *117*, 19048–19055.

(42) Guo, B.; Fang, L.; Zhang, B.; Gong, J. R. Graphene Doping: A Review. *Insciences J.* **2011**, *1*, 80–89.

(43) Partoens, B.; Peeters, F. From Graphene to Graphite: Electronic Structure around the K Point. *Phys. Rev. B* **2006**, *74*, 75404.

(44) Liu, J.; Liu, Z.; Barrow, C. J.; Yang, W. Molecularly Engineered Graphene Surfaces for Sensing Applications: A Review. *Anal. Chim. Acta* **2015**, *859*, 1–19.

(45) Rutter, G. M.; Crain, J. N.; Guisinger, N. P.; Li, T.; First, P. N.; Stroscio, J. a. Scattering and Interference in Epitaxial Graphene. *Science* **2007**, *317*, 219–222.

(46) Varghese, S. S.; Lonkar, S.; Singh, K. K.; Swaminathan, S.; Abdala, A. Recent Advances in Graphene Based Gas Sensors. *Sensors Actuators, B Chem.* **2015**, *218*, 160–183.

(47) Ang, P. K.; Chen, W.; Thye, A.; Wee, S.; Loh, K. P. Solution-Gated Epitaxial Graphene as pH Sensor Solution-Gated Epitaxial Graphene as pH Sensor. *J. Am. Chem. Soc.* **2008**, *130*, 14392–14393.

(48) Qin, Y.; Kwon, H.-J.; Howlader, M. M. R.; Deen, M. J. Microfabricated Electrochemical pH and Free Chlorine Sensors for Water Quality Monitoring: Recent Advances and Research Challenges. *RSC Adv.* **2015**, *5*, 69086–69109.

(49) Zhang, T.; Petelenz, D.; Janata, J. Temperature-Controlled Kelvin Microprobe. *Sensors Actuators B* **1993**, *12*, 175–180.

(50) Li, J.; Petelenz, D.; Janata, J. Suspended Gate Field-Effect Transistor Sensitive to Gaseous Hydrogen Cyanide. *Electroanalysis* **1993**, *5*, 791–794.

Chapter 3 Characterization Techniques

3.1 Raman Spectroscopy

Raman spectroscopy is a type of vibrational spectroscopy of materials, in which the change in the polarizability of a molecule is detected by incident light and used for characterization purposes. When a material is exposed to monochromatic light, most of the scattered light has exactly the same energy as the incident light (elastic scattering, Rayleigh scattering). However, a fraction of the scattered light has different energy from the incident light due the absorption by the material. In Rayleigh scattering, the incident photons excite the electrons of the molecule to higher energy levels, called virtual energy levels. However, the electrons do not stay at these energy levels and decay back to their initial energy level called ground state. In the case that the scattered light does not have the same energy as the incident light, the decayed electrons end up to energy levels different than their initial energy state. Based on the position of the final state of these electrons the inelastic scattering is called Stokes or anti-Stokes scattering. In both cases the interaction of photons with the electric dipole of a molecule can be regarded as a modulation of the molecule's electric field. Figure 3.1 shows these two types of inelastic scattering processes in addition to the Rayleigh scattering.[1]

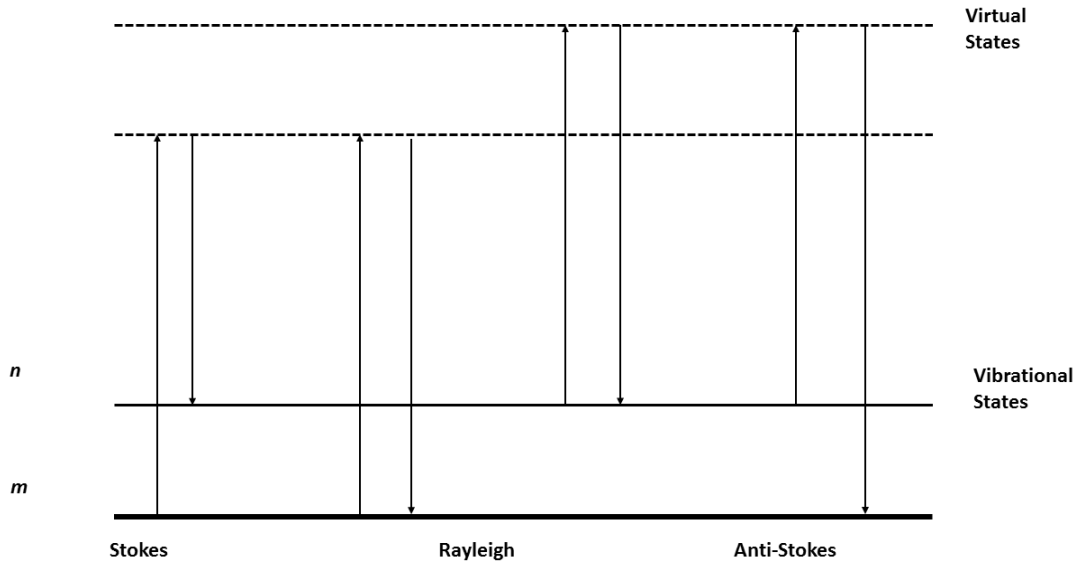

Figure 3.1. Schematic diagram of Stokes, Rayleigh, and anti-Stokes scattering. The upward and downward arrows mean excitation and scattering processes, respectively.

Both inelastic spectra have similar information and can be used in Raman spectroscopy. However, the Stokes spectrum is stronger than the anti-Stokes spectrum and therefore is commonly used in Raman spectroscopy. The difference between the initial and final vibrational levels ($\Delta\nu$) can be calculated using equation 3.1, where $\lambda_{incident}$ and $\lambda s_{cattered}$ are the wavelengths of the initial incident light and the scattered light, respectively. Based on this equation, the Raman spectrum of a molecule is reported as chemical shift (cm^{-1}) versus intensity. Raman spectrum has a good signal to noise ratio and can be used as a fingerprint of a compound. In addition, since the Raman spectrum of water is weak, it can also be used in aqueous media.

$$\Delta\nu = \frac{1}{\lambda_{\text{incident}}} - \frac{1}{\lambda_{\text{scattered}}} \qquad 3.1$$

Vibrational Raman spectroscopy has been traditionally used for characterizations of molecules. However, it can also be used for characterization of crystal lattice vibrations in semiconductors. In the past decade Raman spectroscopy has been used alongside electrical measurements for characterization of graphitic materials such as graphite,[2] graphene,[3] and carbon nanotubes (CNTs).[4,5] This technique can provide unique information with regards to defects, stacking of graphene layers, finite size of crystallites, and numbers of sheets (in graphene or graphite samples).[2,6] In addition, it has been proven to be a powerful tool for study of the charge transfer and chemical doping in graphitic materials.[3,6,7] Few bands are common in the Raman spectra of most graphitic materials. A G-band at around 1573-1579 cm^{-1} is present in all samples containing sp^2 carbon network. D (1330 cm^{-1}) and D´ (1850-2100 cm^{-1}) bands are characteristic of sp^3 and sp carbon networks, respectively. All graphitic materials also show a second order band called 2D around 2500-2800 cm^{-1} as a result of overtones of the D band.[6] One way to dope graphene or graphite is through surface transfer doping in which electron exchange takes place between adsorbed dopants and the substrate.[3] This type of doping does not disrupt the structure of the graphene or graphite and can be reversed. The position, full width at half maximum (FWHM), and ratios of intensities of these bands (e.g. 2D to G) are a common way to study the doping events.[8] It has been reported that for n-type chemical doping of graphene or adsorption of molecules with electron-donating groups on it, the G band shifts to lower frequency with a decrease in its FWHM. For p-type doping or adsorption of molecules with electron-withdrawing

groups on graphene, the G band shifts to higher frequency and its FWHM increases.[7] Another reported effect of adsorbed molecules on Raman spectrum of graphene is based on G band splitting or asymmetry of its peak shape.[9] In addition change in the ratio of intensities of 2D to G band (I_{2D}/I_G) is another indication of doping.[10] However not all of these changes have reported at the same time and different methods of doping (electrical doping, chemical doping) could create different response to the same type of doping (p-doping or n-doping).[6,7]

3.2 UV-vis-NIR Spectroscopy

Ultraviolet and visible radiation has been widely used for identification and determination of organic and inorganic compounds in liquids, gases, and solids. Absorption of radiation in this energy range by molecules can cause an excitation of an electron from a ground energy state to one of the excited electronic energy states. Two types of electrons are commonly responsible for absorption in this range, the shared electrons directly participating in the bond formation in a molecule and unshared outer electrons. Therefore, the absorption of electromagnetic radiations by compounds depend strongly on how electrons are arranged in their structure. The shared electrons in single bonds are tightly bound and therefore for excitation of such states deep ultraviolet radiation is required. Due to the difficulties to suffice such experimental requirement, UV-vis spectroscopy is not commonly used for studying single bonds in organic or inorganic compounds. In contrast, UV-vis is a powerful tool for studying the double bonds and triple bonds since the electrons

participating in these bonds can be readily excited using common ultraviolet or visible light sources available in UV-vis instruments.[11]

Based on Figure 3.2, the absorbance of a compound can be calculated based on the intensity of the incoming beam (I_0) and outcoming beam (I). In addition, the absorbance of a compound (A) is proportional to path length (l) and its concentration (c) through the Beer-Lambert law. Equation 3.2 shows this relationship where ε is the molar absorptivity.

$$A = \varepsilon c l = -\log\left(\frac{I}{I_0}\right) \qquad 3.2$$

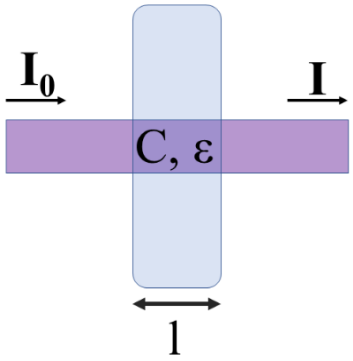

Figure 3.2. Schematic of Beer-Lambert absorption of a beam traveling through a cuvette with the thickness of l.

3.3 X-ray Photoelectron Spectroscopy

X-ray photoelectron spectroscopy (XPS) is based on the principles of photoelectric effect. When an atom is subjected to a photon source with sufficient energy, electrons can be ejected from the atom (photoelectrons). Based on the Einstein relationship (equation. 3.3), the binding energy (B.E.) of the photoelectrons can be calculated if the kinetic energy of the photoelectrons is measured and the energy of the photon source and the surface work

function are known. Here, E_K is the kinetic energy of the photo-ejected electron, hν is the energy of the photon source, E_B is the B.E. of the photo-ejected electron, and Φ is the surface work function.[12] In addition, other correction factors such as the work function of the spectrophotometer can be added to the following equation to increase the precision. Therefore, often XPS instruments get calibrated against clean gold or graphite surfaces.[13]

$$E_K = h\nu - E_B - \varphi \qquad 3.3$$

The photoelectrons are filtered using a hemispherical energy analyzer before the intensity for each electron energy is measured by a detector. Commonly in XPS, a monochromatic photon source with photon energies above 1200 eV (e.g. Al Kα, 1486 eV) is used. Such energies are sufficient for ejection of electrons from both valence and core atomic energy levels. Electrons in valence levels are involved in chemical bonding and have very small B.E.s (~0–10 eV). Although these electrons are the most sensitive to the bonding environment of the atom, they are not commonly used in XPS analysis. This is because the spectra obtain from these electrons are highly convoluted and therefore difficult to interpret. Electrons from the core levels have higher B.E.s (~20-115000 eV) and do not participate in chemical bonding but still under influence from the chemical surrounding of the atom. Their energies are quantized, and thus their spectra can be deconvoluted. Hence, XPS is commonly used to probe the core level electrons of atoms.[14]

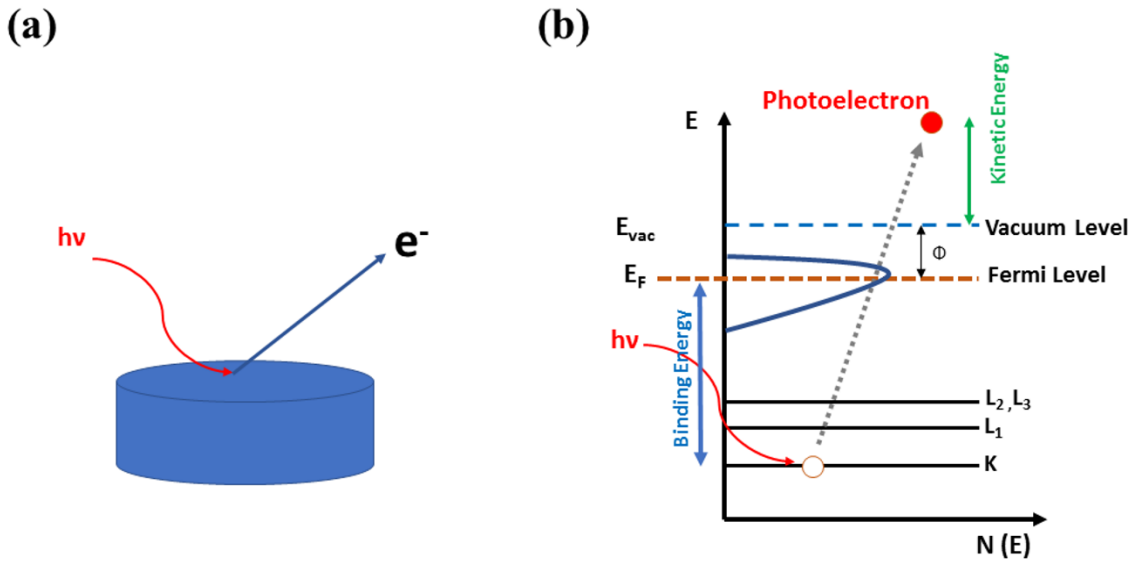

Figure 3.3. (a) Schematic diagram of photoelectric effect. The exposure of a solid substrate to an electromagnetic beam with energy of hν results in a photoejection of an electron from the surface to vacuum level. (b) Energy level diagram of a solid surface showing the photoejection process.

Figure 3.3 shows a typical energy level diagram of a metal surface. Core levels located at higher B.E.s while the valence and conduction bands lie at lower B.E.s. The fermi level is used as a reference energy level of the system. The vacuum level is the boundary level between the unbound and bound electrons of the system. The B.E.s of the electrons depend on their core level states in addition to their chemical states of the element. The dependence of B.E. to the latter property is called chemical shift.[12] Since XPS is capable of probing the electronic structure of atoms, it has been widely used in the studying of doping and charge transfer at interfaces.[15] One way to detect these processes by photoelectron spectroscopy is by monitoring the fermi level shift of the compounds involved in the charge transfer process. This method has been used to assess the doping

efficiency of N,N,N´,N´-tetrakis(4-methoxyphenyl)-benzidine by $C_{60}F_{36}$ and 2,2´-(perfluoronaphthalene-2,6-diylidine)dimalononitrile.[16] One way to detect the Fermi level shift is by monitoring the shift in the high resolution XPS spectra of species participating in the doping process, before and after contact with each other. For example, the shift of the Mo 3d and S 2p peaks of MoS_2 to higher binding energy after contact with TiO_2 layer is a sign of fermi level shift to conduction band and n-type doping.[17] Another feature that might indicate doping/charge transfer at an interface between two compounds is the appearance of shoulder features in their high resolution XPS spectra. As an example, it has been shown that the charge transfer between Mn^{3+} - Ni^{3+} → Mn^{4+} - Ni^{2+} at the interface between $La_{0.7}Ca_{0.3}MnO_3/LaNiO_3$ leads to the evolution of a shoulder feature in the Mn 2p core level spectrum.[18] It has been also shown that the appearance of charge on the backbone of polymers or small molecule after their interaction with dopant is a sign of doping/charge transfer.[19] Xu et al. have been reported that the appearance of charge on amine groups in the N 1s XPS spectrum of polyaniline in contact with graphene oxides is a result of interfacial doping.[20] In this work, CASA XPS software is used for data analysis.[21] The details of XPS data analysis is discussed thoroughly in chapters 4, 5, and 6.

3.4 Atomic Force Microscopy

Atomic force microscopy is a technique for probing the surface morphology using a sharp tip. The radius of the apex of this tip is usually about 10 nm. The tip is located at the end of a cantilever. The tip is brought close to the surface and the force between the tip

and the surface can bend the cantilever. In majority of AFMs a laser beam is used to measure the deflection of the tip. For this purpose, a laser beam is focused at the back of the cantilever. The reflection of the laser beam is measured by a position sensitive photodetector (PSPD). Once the tip rasters all the surface, a map of surface topography can be constructed. However, in AFM the tip is not moving laterally and instead the sample is moved under the tip by a piezo scanner (PZT scanner). The schematic details of AFM are depicted in Figure 3.4a. Van der Waals force is the major force which contributes to the deflection of a cantilever. As it is shown in Figure 3.4b, the extent of this force strongly depends to the distance between the sample and the tip. This force-distance curve can be divided into two parts; contact regime and non-contact regime. In the contact regime, the tip is held just few angstroms above the sample. The force between the sample and the tip in this regime is repulsive. In the non-contact regime, the tip is held tens to hundreds of nanometers above the sample. The force between the tip and the sample in this mode is attractive. Both modes (contact and non-contact modes) are used in probe microscopy. A variation of non-contact mode is the tapping mode (intermittent-contact mode). In this mode, the tip is brought closer to the sample in comparison to the non-contact mode. It is almost like if the bottom of the tip taps on the surface. The intermittent contact mode is shown on Figure 3.4b. This mode is preferred when the damage to the sample from the tip is a concern as the friction between the surface and the tip is eliminated in this mode. For analysis of AFM images, Gwyddion software is used and its details can be found in chapter 4, 5, and 6.[22]

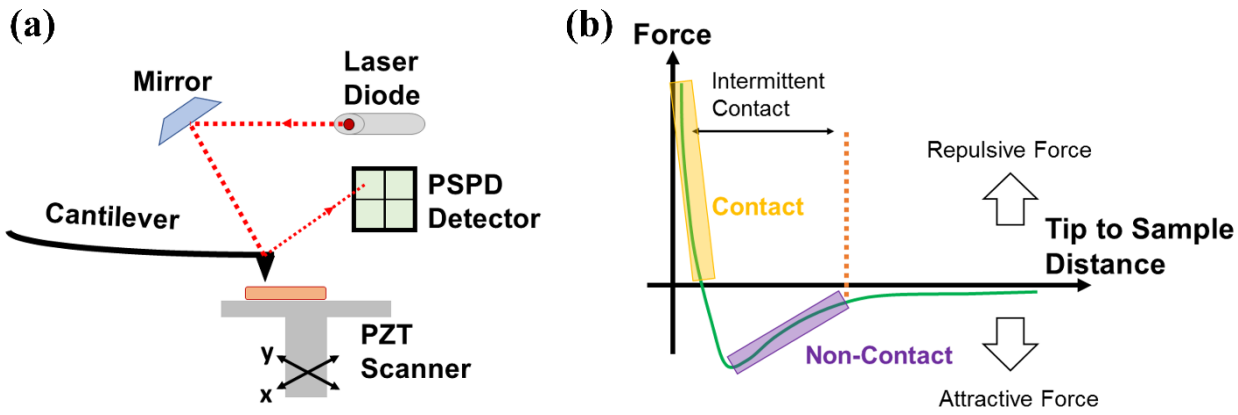

Figure 3.4. (a) Detection of the deflection of AFM cantilever by a focused laser beam. (b) Interatomic force between the tip and the sample in AFM.

3.5 Scaled Island Size Distribution of Phenyl-Capped Aniline Tetramer

3.5.1 Introduction

Thin organic films are important for applications in organic electronic devices, such as organic thin film transistors (OFETs), organic photovoltaics (OPVs), and organic light emitting diodes (OLEDs).[23-26] Models for inorganic film growth, particularly those of metallic compositions, have been studied since the 1980's.[27-29] While in theory these models were assumed to be also applicable to the organic thin films, it was only a decade ago that their applicability to organic thin films have been studied experimentally.[30-32] Film growth through diffusion on surfaces takes place in four distinct stages; initially, singular particles come into contact with the substrate on which the film is to form. Once a few of them meet (defined as the critical island size plus one) a stable nucleus, or island, is formed. Upon addition of more particles they may form their own individual islands, or may start adding to the existing nuclei. After a significant number of islands have been formed,

additional particles only add to the existing islands, in an aggregation regime. Over time surface diffusion results in the coalescence of the islands.[29] The rate of the diffusion mediated growth (R) can be obtained from the ratio between the diffusion constant (D) and the incoming flux (F). Equation 3.4 shows this relationship;

$$R = \frac{D}{F} \qquad 3.4$$

Ruiz et al.[30] have argued that several system specific properties such as nucleation density (N) and the average island size (A(θ)) can be obtained from this relationship through the following proportionality;

$$N = C R^{-\chi} \cong \frac{\theta}{A(\theta)} \qquad 3.5$$

Where θ is the coverage, C is a proportionality constant, and χ= i/i+2 (i is the critical island size, expressed as the number of monomers, $1/3 \leq \chi < 1$). Critical island size, i, is the largest unstable island that can be transformed to a stable island by addition of a single (i+1).[32] The critical island size depends on the interatomic and intermolecular forces between particles of the over layer film and the substrate atoms.[32] It was shown that the distribution of islands of size "a" per unit area ($N_a(\theta)$) scales with the average island size A(θ), according to the following relationship;

$$N_a(\theta) = \theta A(\theta)^{-2} f(u) \qquad 3.6$$

While u defined u = a/A(θ), f(u) is a dimensionless scaling function independent of coverage, and A(θ) can be calculated from the following equation;

$$A(\theta) = \frac{[\sum a\, N_a(\theta)]}{\sum N_a(\theta)} \qquad 3.7$$

In addition, A(θ) can be also calculated directly by averaging the area of islands obtained through images analysis of AFM images. Based on the numerical simulations it has been shown that the distribution of the scaling function can be correlated to the critical island size (i) by the following empirical expression;

$$f_i(u) = c_i\, u^i \exp\left(-b_i\, i\, u^{1/b_i}\right) \qquad 3.8$$

Here, C_i and b_i are fixed by absolute geometrical equations 3.9 and 3.10 which assure normalization behavior of f(u).[30]

$$\frac{\{\Gamma[(i+2)b_i]\}}{\{\Gamma[(i+1)b_i]\}} = \left(i\, b_i\right)^{b_i} \qquad 3.9$$

$$c_i = \frac{\left[\left(i\, b_i\right)^{(i+1)b_i}\right]}{\{b_i\, \Gamma[(i+1)b_i]\}} \qquad 3.10$$

The above equations are normally applied to the surface coverage of 0.1 to 0.5 (aggregation regime) because it shows the scaling behavior of the organic island size distribution in 2-dimentional and thus a fingerprint of diffusion-mediated growth can be extracted from them. In other word, aggregation regime is where the island density remains unchanged during deposition. The constants C_i and b_i for i = 1-6 can be found elsewhere.[32] It is known that the film formation and the critical island size depend on several factors such as the substrate temperature and the deposition rate. However, it was further shown that the former one has greater effect than the later one.[32] The deposition rate of the organic layer was shown to have a much more classical trend with the peak area of islands, increasing in a nearly linear fashion to the amount that was deposited per given unit of time.[32] The effect of temperature of the substrate is of importance to the size and shape of

island formation. It was noted that the dependence of the island's morphology on temperature follows two different trends for organic and metallic islands. Organic islands are compact at low substrate temperature and dendritic at higher temperatures. For metallic islands this trend is opposite, at low substrate temperatures the islands are dendritic while at higher temperatures they are compact. For metal islands, this behavior was explained based on diffusion-limited aggregation (DLA) model. At low temperatures, the adatoms hit and stick to the existing islands. As the temperature increases, the adatoms can diffuse along the rim of the islands, changing the shape of the island to a compact structure. Islands formation of large organic molecules on substrates have showed a reverse dependency to the temperature.[32,33] Therefore, the growth mechanism of the large organic molecules such as hexaphenyl are associated to models other than DLA.[33]

3.5.2 Calculation of Diffusion Barrier Energy

The diffusion barrier of an organic island on a substrate can be derived from its diffusion coefficient (equation 3.11), where D_0, E_a ($kJmol^{-1}$), T, and R are diffusion constant, diffusion barrier energy, the substrate's temperature, and the gas constant.

$$D = D_0 \exp(\frac{-E_a}{RT}) \qquad 3.11$$

By fixing F in equation 3.4, at a unchanged θ, and using equations 3.4 and 3.5, the equation 3.11 can be rewritten as follow:[33]

$$N = C\,R^{-\chi} = C\left(\frac{D}{F}\right)^{-\chi} \propto \left(\frac{-E_a}{RT}\right)^{-\chi} \propto \exp\left(\frac{\chi E_a}{RT}\right) \qquad 3.12$$

The equation 3.12 can be then written in linear form as follow:

$$\ln N = \ln C + \frac{\chi E_a}{RT} \qquad 3.13$$

Therefore, the E_a can be calculated using i, and the island density at various substrate's temperature.

3.6. Image Analysis

Image analysis is the first step toward extracting statistical and qualitative information from microscopy images (optical, probe, and electron microscopy). In this work, GIMP freeware (GNU Image Manipulation Program) was used for basic image manipulations and ImageJ freeware (NIH, USA) was used for more sophisticated image analysis.[34] Since the basic analysis principle of the ImageJ freeware is based on the contrast between the particles and their background, the image needs to have an appropriate contrast. In addition, common microscopy images contain large number of particles. Therefore, in order to that the program can distinguish particles from each other, it is important that they have sufficient distance from each other. However, since this is not always possible, a preliminary manipulation of the microscopy image is required. The basic manipulation step is separating particles with no or little space from each other with black/dark lines using GIMP software.[34] This will create sufficient contrast for the software to distinguish neighboring particles from each other.

3.6.1 Island Size Distribution Analysis

To perform the island size distribution on AFM images used in this work the following steps were followed.

- Open ImageJ freeware (version 1.51j8).
- Select the image through File and then Open menu.
- Set the scale bar by following the following step.
- Select the straight line from the tool bar, then draw on the scale bar of the image or along a known distance of it.
- Next, from the Analysis menu select Set Scale icon. Enter the known distance and select the appropriate unit, then press Ok.
- If there is a printed scale bar on the image, crop it using the Crop option from the Image menu.
- Select the Threshold Color icon from the Image, then Adjust menu. Set the thresholding method as Huang, threshold color as B&W, and color space as RGB.
- Select the Set Measurement icon through the Analysis menu. Select the information you would like from the image (Area, Standard deviation, Feret's diameter, …). Then set the number of decimal and press Ok.
- Select Analysis Particles from the Analysis menu. Enter the range of the size you expect to have in your figure. Select whether the particles at the edges of the frame be included or excluded. Select Outline in the Show menu. By pressing Ok, two spreadsheets contain the summary of the analysis and the requested parameters for each individual

particle will be generated. In addition, the outline figure of the analysis will be provided. Using the outline image, you can eliminate the erroneous outcomes. Figure 3.4 shows some of these steps to achieve the outcome.

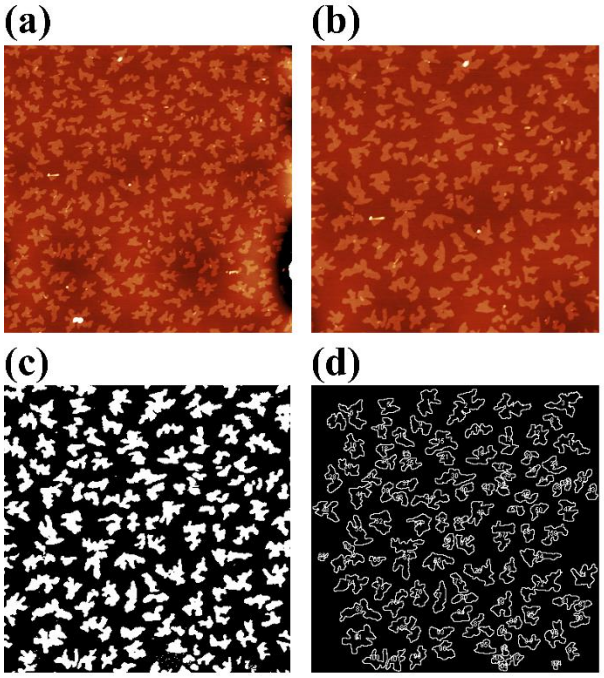

Figure 3.5. (a) AFM image of fully reduced PCAT on hematite (1000) single crystal surface. (b) cropped area of the (a), suitable for particle size analysis. (c) setting the color threshold to black and white version of (b). (d) the output of ImageJ software after particle analysis of (c)

3.7 References

(1) Smith, E.; Dent, G. *Modern Raman Spectroscopy - A Practical Approach*; John Wiley & Sones, Ltd: West Sussex, 2005.

(2) Nacken, T. J.; Damm, C.; Walter, J.; Rüger, A.; Peukert, W. Delamination of Graphite in a High-Pressure Homogenizer. *RSC Adv.* **2015**, *5*, 57328–57338.

(3) Liu, H.; Liu, Y.; Zhu, D. Chemical Doping of Graphene. *J. Mater. Chem.* **2011**, *21*, 3335.

(4) Meyyappan, M. Carbon Nanotube-Based Chemical Sensors. *Small* **2016**, *12*, 2118–2129.

(5) Klinke, C.; Chen, J.; Afzali, A.; Avouris, P. Charge Transfer Induced Polarity Switching in Carbon Nanotube Transistors. *Nano Lett.* **2005**, *5*, 555–558.

(6) Pimenta, M. A.; Dresselhaus, G.; Dresselhaus, M. S.; Can?ado, L. G.; Jorio, A.; Saito, R. Studying Disorder in Graphite-Based Systems by Raman Spectroscopy. *Phys. Chem. Chem. Phys.* **2007**, *9*, 1276.

(7) Das, B.; Voggu, R.; Rout, C. S.; Rao, C. N. R. Changes in the Electronic Structure and Properties of Graphene Induced by Molecular Charge-Transfer. *Chem. Commun.* **2008**, No. 41, 5155–5157.

(8) Dong, X.; Fu, D.; Fang, W.; Shi, Y.; Chen, P.; Li, L.-J. Doping Single-Layer Graphene with Aromatic Molecules. *Small* **2009**, *5*, 1422–1426.

(9) Dong, X.; Shi, Y.; Zhao, Y.; Chen, D.; Ye, J.; Yao, Y.; Gao, F.; Ni, Z.; Yu, T.; Shen, Z.; Huang, Y.; Chen, P.; Li, L. J. Symmetry Breaking of Graphene Monolayers by Molecular Decoration. *Phys. Rev. Lett.* **2009**, *102*, 1–4.

(10) Das, A; Pisana, S.; Chakraborty, B.; Piscanec, S.; Saha, S. K.; Waghmare, U. V; Novoselov, K. S.; Krishnamurthy, H. R.; Geim, A. K.; Ferrari, A. C.; Sood, a K. Monitoring Dopants by Raman Scattering in an Electrochemically Top-Gated Graphene Transistor. *Nat. Nanotechnol.* **2008**, *3*, 210–215.

(11) Skoog, D. A.; West, D. M.; Holler, F. J. *Fundamentals of Analytical Chemistry*, 6th ed.; Saunders College Publishing: Fort Worth, 1992.

(12) Sarma, D. D.; Santra, P. K.; Mukherjee, S.; Nag, A. X-Ray Photoelectron Spectroscopy: A Unique Tool to Determine the Internal Heterostructure of Nanoparticles. *Chem. Mater.* **2013**, *25*, 1222–1232.

(13) Fadley, C. S. X-Ray Photoelectron Spectroscopy: Progress and Perspectives. *J. Electron Spectros. Relat. Phenomena* **2010**, *178–179*, 2–32.

(14) Greiner, M. T. Investigation of Polyaniline Oligomer Thin Films on Iron Using Photoelectron Spectroscopy for Understanding Corrosion Inhibition, McMaster University, M.Sc. Thesis, 2008.

(15) Lee, J. H.; Kim, J. J. Interfacial Doping for Efficient Charge Injection in Organic Semiconductors. *Phys. Status Solidi A* **2012**, *209*, 1399–1413.

(16) Tietze, M. L.; Burtone, L.; Riede, M.; Leo, K. Fermi Level Shift and Doping Efficiency in P-Doped Small Molecule Organic Semiconductors: A Photoelectron Spectroscopy and Theoretical Study. *Phys. Rev. B* **2012**, *86*, 35320.

(17) Kaushik, N.; Karmakar, D.; Nipane, A.; Karande, S.; Lodha, S. Interfacial n-Doping Using an Ultrathin TiO2 Layer for Contact Resistance Reduction in MoS2. *ACS Appl. Mater. Interfaces* **2016**, *8*, 256–263.

(18) Ca, L.; Lanio, M.; Ning, X.; Wang, Z.; Zhang, Z. Fermi Level Shifting, Charge Transfer and Induced Magnetic Coupling at La0.7Ca0.3MnO3/LaNiO3 Interface. *Sci. Rep.* **2015**, *5*, 1–8.

(19) Mohtasebi, A.; Chowdhury, T.; Hsu, L. H. H.; Biesinger, M. C.; Kruse, P. Interfacial Charge Transfer between Phenyl-Capped Aniline Tetramer Films and Iron Oxide Surfaces. *J. Phys. Chem. C* **2016**, *120*, 29248–29263.

(20) Xu, D.; Xu, Q.; Wang, K.; Chen, J.; Chen, Z. Fabrication of Free-Standing Hierarchical Carbon Nanofiber/Graphene Oxide/Polyaniline Films for Supercapacitors. *ACS Appl. Mater. Interfaces* **2014**, *6*, 200–209.

(21) Fairley, N. *Casa XPS, Revision 2.3.17;* Casa Software Ltd: Teignmouth, Devon 2016.

(22) Nečas, D.; Klapetek, P. Gwyddion: An Open-Source Software for SPM Data Analysis. *Open Phys.* **2012**, *10*, 181–188.

(23) Venables, J. A.; Spiller, G. D. T.; Hansbücken, M. Nucleation and Growth of Thin Films. *Reports Prog. Phys.* **1984**, *47*, 399.

(24) Katz, H. E.; Huang, J. Thin-Film Organic Electronic Devices. *Annu. Rev. Mater. Res.* **2009**, *39*, 71–92.

(25) Mishra, A.; Bäuerle, P. Small Molecule Organic Semiconductors on the Move: Promises for Future Solar Energy Technology. *Angew. Chemie Int. Ed.* **2012**, *51*, 2020–2067.

(26) Lin, Y.; Li, Y.; Zhan, X. Small Molecule Semiconductors for High-Efficiency Organic Photovoltaics. *Chem. Soc. Rev.* **2012**, *41*, 4245–4272.

(27) Vicsek, T.; Family, F. Dynamic Scaling for Aggregation of Clusters. *Phys. Rev. Lett.* **1984**, *52*, 1669–1672.

(28) Family, F. Scaling of Rough Surfaces: Effects of Surface Diffusion. *J. Phys. A Math. Gen* **1986**, *19*, 441–446.

(29) Amar, J. G.; Family, F. Dynamic Scaling of the Island-Size Distribution and Percolation in a Model of Submonolayer Molecular-Beam Epitaxy. *Physical Rev. B* **1994**, *50* (12).

(30) Ruiz, R.; Nickel, B.; Koch, N.; Feldman, L. C.; Haglund, R. F.; Kahn, A.; Family, F.; Scoles, G. Dynamic Scaling, Island Size Distribution, and Morphology in the

Aggregation Regime of Submonolayer Pentacene Films. *Phys. Rev. Lett.* **2003**, *91*, 136102.

(31) Ruiz, R.; Nickel, B.; Koch, N.; Feldman, L.; Haglund, R.; Kahn, A.; Scoles, G. Pentacene Ultrathin Film Formation on Reduced and Oxidized Si Surfaces. *Phys. Rev. B* **2003**, *67*, 1–7.

(32) Potocar, T.; Lorbek, S.; Nabok, D.; Shen, Q.; Tumbek, L.; Hlawacek, G.; Puschnig, P.; Ambrosch-Draxl, C.; Teichert, C.; Winkler, A. Initial Stages of a Para-Hexaphenyl Film Growth on Amorphous Mica. *Phys. Rev. B - Condens. Matter Mater. Phys.* **2011**, *83*, 1–10.

(33) Yang, J.; Wang, T.; Wang, H.; Zhu, F.; Li, G.; Yan, D. Ultrathin-Film Growth of Para-Sexiphenyl (I): Submonolayer Thin-Film Growth as a Function of the Substrate Temperature. *J. Phys. Chem. B* **2008**, *112*, 7816–7820.

(34) The GIMP team, GIMP 2.8.10, www.gimp.com, 1997-2017, retrieved on 01/07/2017.

Chapter 4 Surface Mobility and Nucleation of a Molecular Switch: Tetraaniline on Hematite

4.1 Abstract

We have studied the nucleation and growth of the reduced and the oxidized states of phenyl-capped aniline tetramer (PCAT) deposited on hematite(1000) surface by physical vapor deposition. The fully reduced PCAT molecules form two-dimensional islands on the surface while the fully oxidized molecules form three-dimensional islands. Through scaled island size distribution, it was found that critical island size for the reduced and the oxidized molecules are i = 4-5 and i = 5-6 respectively. Furthermore, through studying the island density as a function of substrate temperature, the range of diffiusion energy barrier, E_a, for the reduced and the oxized molecules were evaluated to be 1.22-1.30 eV and 0.52-0.55 eV, respectively. At low temperatures, the reduced and the oxidized PCAT molecules form compact islands on the surface. At higher temperatures, the reduced islands become dendritic while the oxidized islands become slightly dendritic. In addition, the range of attempt frequencies for surface diffusion of the reduced and the oxidized islands were calculated to be 8×10^{22} - 5×10^{25} s^{-1} and 4×10^{11} - 8×10^{13} s^{-1}, respectively. The former value is in line with the high degree of surface wetting by the reduced PCAT while the latter value shows the higher degree of intermolecular interction in the fully oxidized PCAT and the low degree of its interaction with the iron oxide surface. Finally,

the effect of the substrate oxidation state on the nucleation and growth of each of these two molecules is discussed.

4.2 Introduction

Organic thin films are key components of variety of electronic devices. They function as the donor/acceptor layer in organic photovoltaic device,[1] as conductive channel in thin film transistors,[2] and as sensing material in chemical sensors.[3,4] The molecular orientation and packing plays an important role in the function of these devices as the quality of the organic thin films influence properties such as electrical conductivity or charge mobility.[2,5] Therefore, understanding the organic thin film formation is important for the design of better organic electronic devices and smart coatings. One of the primary steps in an organic or inorganic film formation is nucleation and growth of the submonolayer films.[6] Various studies have shown that the nucleation and growth of the organic thin films follow different behaviors than the metallic thin films. Generally, the metallic submonolayer islands on surfaces held at room temperature forms dendritic morphologies and at higher temperatures transform to compact islands. On the other hand, the submonolayer islands of many large organic molecules form compact morphologies when the substrate is at low temperature and form dendritic islands at higher temperatures.[7,8] Thus, the models commonly used to describe the latter case[9] are unable to fully describe the early stages of nucleation and growth of the organic films.[8] One of the proposed reasons for these opposite trends is different intermolecular

interactions in the organic films in comparison to the metallic films can account for such differences in growth modes.[10] Another reason is the intrinsic anisotropy associated with the organic molecules in comparison to the isotropy of the metal atoms.[10] In addition, even different oxidation states of an organic molecule can adsorb on a surface with different conformations.[11,12] This becomes important considering the application of such layers in novel set ups such organic electronic devices which requires a thin and homogenous molecular layer.[8] As an example, it has been shown that for a vertical crystal of a tetraaniline can reach an electrical conductivity of 12.3 S/cm while its horizontally oriented crystal shows electrical conductivity values as low as 10^{-4} S/cm.[5]

One of these organic molecules is Phenyl-capped aniline tetramer (PCAT), a redox-active oligomer of polyaniline (PANI) which mimics many characteristics of this polymer.[13] Similar to PANI it has three oxidation states and becomes electrically conductive through chemical doping.[5] The reversible conversion of different oxidation states of PCAT (or PANI) to each other makes it attractive for different applications such as carbon nanotube FETs with switchable polarity[14] or resettable chemical sensors.[4] In all these applications and their many others,[15] the interaction of the thin organic film with a substrate is crucial for the device performance and thus requires a high quality of the organic coating. The structure of the tetraaniline films on surfaces prepared through drop-casting or vapor-infiltration has been studied previously.[5,16] It has been shown that the solvent, substrate, and the doping/undoping of the oligoaniline can significantly change the morphology, packing, and electrical conductivity of the final organic films.[5,16] Another application of PCAT molecular layers is its use as an active coating against corrosion of

metals, particularly iron based alloys.[17,18] This is based on the idea that redox-active molecules in their oxidized form while in contact with the metallic substrate can provide sufficient polarization potential to form a passive oxide layer at the interface with metallic substrate.[19] As a result of this process, the organic molecule is reduced, and the oxide layer protects the metal from corrosion. The reoxidation of these molecules under ambient condition maintains the passive metal oxide film for prolonged protection of the substrate.[17] This reemphasizes that the key to the success of such applications is the quality of the thin film formation on the substrate.

To understand the film formation of small organic molecules (including PCAT) on solid surface, the early stages of this process which is the nucleation and growth of submonolayer organic islands should be understood. These islands are in direct contact with the underlying substrate and dictate the growth and morphology of the next monolayers.[11] A common method to obtain nucleation and growth parameters on the surface is through thermal desorption spectroscopy.[8,11] An alternative method for finding such parameters is through determination of island size distribution by scanning probe microscopy.[20] This is followed by the determination of scaling island size distribution through a scaling law. Based on the scaling law the critical number of monomers for the formation of a stable island can be evaluated. More diffusion properties such as diffusion prefactor and diffiusion energy barrier (E_a) can be found through study of islands form on the surface at different substrate temperature.[8]

The motivation behind this study is the ever-growing applications of redox-active small molecules in smart coatings and organic electronic devices.[4,14] In this work, the

nucleation and growth of submonolayer films of PCAT in two oxidation states (fully reduced (LB) and fully oxidized (PB)) on the surface of hematite is studied. This system is used as a model system of the commercial system based on redox-active organic thin films on metal oxide surface. Using island size distribution and scaling island size distribution, the critical island sizes for reduced and oxidized oxidation states of PCAT were determined. The shape, morphology, surface coverage, and nucleation density of each states at various substrate temperature were demonstrated. Using these series of data, the diffusion energy barrier, and the frequency factor of the diffusion of each oxidation states was determined. These values can be used as a quantitative measure of mobility and wetting of the surface of iron oxide by different oxidation states of PCAT. Using a flat hematite single crystal provides an opportunity to evaluate the diffusion parameters with minimum influence from the surface roughness or the grain boundaries. Finally, the chemistry of the surface of the substrate was modified through vacuum annealing without effecting the surface roughness. This was used to investigate the effect of oxidation states of the substrate on the critical island size of each oxidation states of PCAT.

4.3 Experimental Details

PCAT was synthesized based on a literature procedure.[21] The preparation of the fully reduced and the fully oxidized forms of base PCAT was performed using the reducing and the oxidizing agents as described previously.[17] Natural sourced hematite(1000) single crystals were obtained from SurfaceNet GmbH. The single crystals are chemical-mechanical polished to have a final RMS better than 6 Å over 20 × 20 μm^2. Submonolayer

organic thin films were deposited on substrates in a homemade vacuum chamber with a base pressure better than 4×10^{-6} Torr using a low temperature Knudsen cell with a glass crucible. The sample holder can be cooled or heated in the range of 0-70 ℃. Single crystal substrates were clamped between two sapphire washers in a commercial sample holder (RHK Inc.) equipped with a heater made of tungsten wire. The substrate temperature was controlled using temperature controller (Lake shore Cryotronics Inc.) using a Ni-NiCr thermocouple clamped between the sample and a copper sheet placed underneath the sample. Using X-ray photoelectron spectroscopy (XPS), it was previously shown that the vacuum deposition under these conditions does not impact the oxidation states of PCAT (LB and PB) nor does it cause degradation of the organic films.[17] The deposition rate was monitored using a quartz crystal microbalance (Inficon, XTC) which is positioned next to the sample holder. In all experiments, the deposition rates were kept close to ~ 0.01 nm/s. All samples were transferred to an ex situ atomic force microscope (AFM, Veeco Enviroscope with a MultiMode IIIa controller) within five minutes of the deposition of the organic thin films. All AFM measurements were performed under dry nitrogen environment and in tapping mode using antimony doped Si cantilevers (Bruker, model NCHV-A) with 320 kHz resonance frequency and maximum tip radius of 10 nm. All AFM images were analyzed using Gwyddion software.[22] In all AFM images the false color ruler is shown beside the topography image. Using this software, for all images the data was leveled by mean plane subtraction. The polynomial background of all images was removed with horizontal and vertical polynom degree of 2. If necessary, scares in images were removed using the "correct horizontal scares" function of the software. Raman spectra of

PCAT powders were acquired using a Renishaw inVia Raman spectrometer with a spectra resolution of 2 cm^{-1} and an Ar^{+} ion laser at 514 nm (2.41 eV). The powders were dispersed in methanol and drop cast and dried on clean silicon wafers.

XPS was performed using a Kratos Axis Ultra DLD spectrometer with a monochromatic Al Kα X-ray source (15 mA, 1486.6 eV). The approximate analysis areas for both survey and high resolution spectra were 300 × 700 μm^2. For the former and the later measurements, pass energies of 160 eV and 20 eV were used, respectively. The in situ annealing of the hematite single crystal was performed in the XPS analysis chamber with a base pressure better than 1×10^{-8} Torr. The sample was heated radiatively and the annealing process was dynamically monitored by XPS. For each cycle of annealing the temperature was ramped to 350 ℃ and kept at this temperature for five minutes. Then, the sample was cooled down in vacuum and was stored in dry argon environment for 24 hours before it was load locked back into the XPS analysis chamber for further measurements. For each step, in addition to the survey spectra, the high resolution (0.1 eV resolution) C 1s, O 1s, and Fe 2p spectra were acquired. CasaXPS software (version 2.3.17) was used for analysis of XPS spectra.[23] Shirley-type background and line-shape of GL(30) were used for all peak integrations. All spectra were charge corrected to the binding energy (B.E.) of 284.8 eV for C-C and C-H.

4.4 Results and Discussion

PCAT in its base form (undoped) can be prepared in three different oxidation states; fully reduced, half-oxidized, and fully oxidized.[17] The molecular structure of each state is

depicted in Figures 4.1a, 4.1b, and 4.1c, respectively. The fully reduced and the fully oxidized forms of PCAT can be quantitatively achieved using excess amount of a reducing agent (e.g. L-ascorbic acid) and an oxidizing agent (e.g. ammonium persulfate), respectively. Commonly, the preparation of the half-oxidation state of PCAT is performed through addition of 1:1 molar ratio of ammonium persulfate to fully reduced PCAT with the hope to create an exact half-oxidation state of the oligoaniline.[17] However, it is known that there is a poor control over the final oxidation states of the molecules achieved through this procedure.[24] In addition, using scanning tunneling microscopy it has been shown that the monolayers of vacuum deposited half-oxidized PCAT on the surface of Cu(110) shows disordered structures.[25] This behavior has been attributed to the multiple isomers of this oxidation state of PCAT.[25] The same conclusion also reported using nuclear magnetic resonance spectroscopy of this oxidation state.[26] Therefore, the focus of this work is only on the nucleation and growth of the fully reduced and the fully oxidized PCAT which can be prepared with high precision. The oxidation states of the former and the latter oligoanilines prepared through chemical redox processes were examined by Raman spectroscopy. Raman spectrum of the fully reduced form (Figure 4.1e) shows the main bands at 1179, 1221, and 1622 cm^{-1}, an indication of a successful reduction process. The Raman spectrum of the oxidized form (Figure 4.1d) shows the bands at 1165, 1216, 1500, and 1589 cm^{-1} in agreement with the Raman bands of the fully oxidized PCAT.[27]

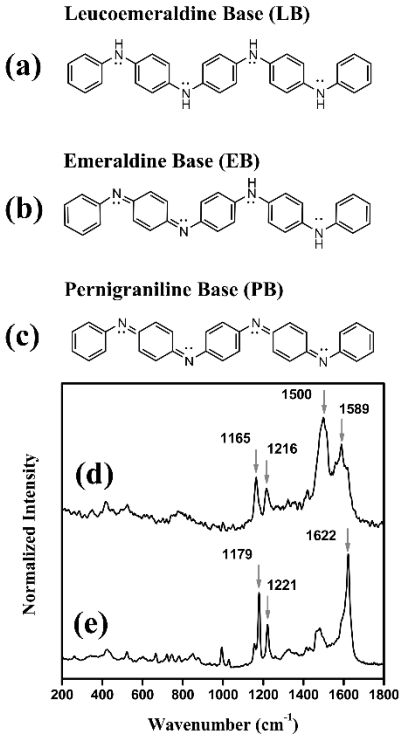

Figure 4.1. Molecular structure of different oxidation states of base PCAT; fully reduced (a), half-oxidized (b), and fully oxidized (c) states. Raman spectra of the oxidized (d) and the fully reduced (e) base PCAT.

Figure 4.2 shows the evolution of the morphologies of the fully reduced and the fully oxidized PCAT on the surface of a hematite(1000) single crystal as a function of surface temperature. At low substrate temperature (278 K), high densities of the reduced and the oxidized islands with nearly compact morphologies can be found on the surface. By increasing the substrate temperature, the density of the reduced islands decreases while the islands become more dendritic but with smooth corners. Regardless of the temperature, for all fully reduced islands their cross-section profiles show the island height of about 3 nm (Figure 4.2). At surface temperatures above 323 K, the main dendritic islands are

surrounded by small islands/nuclei with identical sizes. The same behavior has been previously reported for hexaphenyl (6P) islands on amorphous mica and was attributed to the existence of not well amorphized areas of the substrate or possible surface impurities.[8] At higher substrate temperature (338 K), the number of these small islands decrease. This may be due to the sufficient thermal energy present for their diffusion to the larger dendritic islands. Another reason might be the transition from a complete condensation into an incomplete condensation of the incoming flux to the surface at around 338 K.[10] The growth of the fully oxidized islands on hematite surfaces as a function of temperature shows a similar trend to the fully reduced islands. However, at any temperature the density of the fully oxidized islands is lower than that of the fully reduced islands. In addition, the effect of temperature on the change in the island density of the fully oxidized islands is far less than on the fully reduced islands. At temperatures between 278 K - 308 K, islands are nearly globular. Above these temperatures, their shape starts to become slightly dendritic. The cross-section height profiles of the fully oxidized islands at different surface temperatures show somewhat similar heights, which fluctuate between 110-130 nm. This behavior is an indication of far less wetting of the hematite surface by this oxidation state of PCAT in contrast to the well wetting of the same surface with LB islands. This growth mechanism in which the islands shape is compact at lower temperatures and become more dendritic at higher temperatures is opposite of what has been reported for the growth of metallic islands.[28] This behavior has been previously reported for other large organic molecules such as 6P[10] and hexathiophene.[7] In the latter case, at low temperatures the islands are dendritic and an increase in the temperature makes them more compact. It is

known that the metallic island growth follows the classical diffusion-limited aggregation model.[29] Based on this model, at low temperature, atoms stick to the nearest stable islands.[10] These atoms do not have enough energy to diffuse along the rim of the island which hinders the formation of compact morphologies. However, an increase in the temperature provides enough energy for diffusion of atoms which causes the formation of compact islands which are more thermodynamically stable.[8]

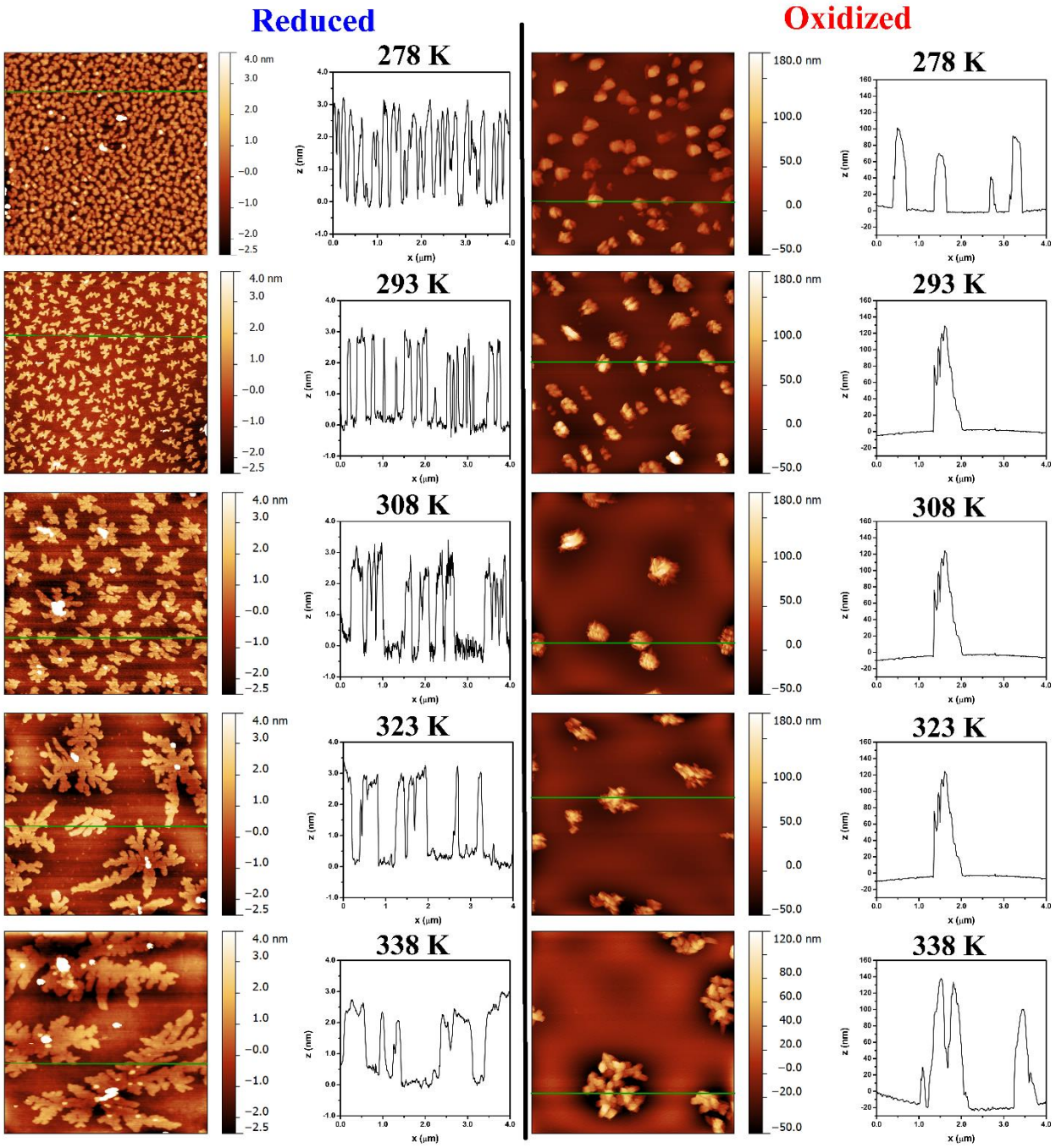

Figure 4.2. AFM images (4 μm × 4 μm) of the reduced (left column) and the oxidized (right column) PCAT molecules on hematite surface at different substrate temperatures (278, 293, 308, 323, and 338 K). The height cross-section of each figure extracted along the green line is represented next to each AFM micrograph.

4.4.1 Substrate Temperature Dependence of the Fully Reduced and the Fully Oxidized PCAT

The kinetic of diffusion of atoms and molecules on surfaces is defined by the ratio of the diffusion constant (D) to the incoming flux to the surface (F, R = D/F). Through these parameters, other parameters of a surface diffusion such as nucleaction density (N) can be calculated.20 These paramters are related to each other through equation 4.1, where θ is the surface coverage, A(θ) is the average island size, C is a proportionality constant, and $\chi = i/i/i+2$ ($1/3 \leq \chi < 1$, $i \geq 1$) where i is the critical island size.[10'20] The critical island size is the smallest number of particles (atoms/molecules) required that by addition of one extra particle, a stable island can be formed.[8] Once an island becomes stable, it will not undergo dissociation.[20]

$$N = CR^{-\chi} \cong \frac{\theta}{A(\theta)} \qquad 4.1$$

It was shown that in the aggregation regime (typically $0.1 \leq \theta \leq 0.5$), the island size distribution shows a scaling behaviour.[30] The aggregation regime by definition is a range of surface coverages in which the island density remains unchanged.[8] This means that the interisland length scale is the only determental length and thus is a sign of diffision-mediated growth.[20] In diffusion-mediated growth, the distribution of islands of size a per unit area ($N_a(\theta)$) scales with A(θ) through the equation 4.2.[30]

$$N_a = \theta\, A(\theta)^{-2} f(u) \qquad 4.2$$

In this equation, f(u) is a dimensionless scaling function dependent on i while u = a/A(θ). This function defines based on equation 4.3, in which C_i and b_i are only funtions of i and can be obtained numerically.[8]

$$f(u) = C_i\, u^{i} \exp\left(-b_i\, i\, u^{1/b}i\right) \qquad 4.3$$

Other diffiusion parameters such as the diffusion energy barrier (E_a) can be obtained through combination of above equations (4.1 and 4.2) with the equation 4.4, where T and R are the temperature and the gas constant (8.314 kJ/mol), respectively.

$$D = D_0 \exp\left(\frac{-E_a}{RT}\right) \qquad 4.4$$

Assuming the situation in which F and θ are constant, N_a and E_a can be related as N_a α $\exp(-E_a/RT)^{-\chi}$ α $\exp(\chi E_a/RT)$. Thus, $N_a = a_0 \exp(\chi E_a/RT)$, where a_0 is the proportionality constant which can be related to N_a and E_a through the following linear equation:

$$\ln N_a = \ln a_0 + \frac{\chi E_a}{RT} \qquad 4.5$$

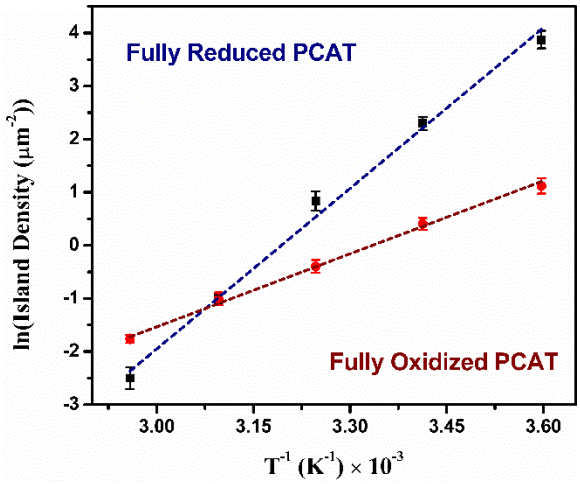

Figure 4.3. Island density of the fully reduced and the fully oxidized on hematite(1000) single crystal as a function of surface temperature.

In order to obtain diffiusion parameters of the reduced and the oxidized PCAT on hematite surface, the nucleation density of these two states at various temperatures should be measured. Figure 4.3 shows the island density as a function of temperature (278 K to 338 K) for these two types of PCAT islands on hematite surface in the form of $\ln N_a$ versus 1/T. Data points of each oxidation states of PCAT can be fitted with a linear line. The adjusted R-square values for the fitted line to the reduced PCAT data points and the oxidized PCAT data posints are 0.993 and 0.998, respectively. The absence of any bent in these two lines at this temperature range indicates that only one growth mechanism is dominate.[8,10] Based on equation 4.5, the activation energies of both the reduced and the oxidized PCAT islands can be calculated using the slope of the linear fitted lines ($\chi E_a/R$). Thus, to obtain E_a values for each oxidation state of PCAT islands, the evaluation of χ values is necessary. Since $\chi = i/i+1$, the i value for each oxidation state of PCAT should be

measured. Therefore, the island size distribution of both reduced and oxidzed islands at 293 K and at different surface coverages were measured. For each coverage, the N_a has a maxium which is located at $A(\theta)$.[20] In order to find i for each type of the islands, each island size distrubution is converted to f(u) by multiplying the N_a by A^2/θ and dividing the a by $A(\theta)$. This way, for each specific molecule, the island density curves at different surface coverages scaled down to a single curve of f(u).[20] The maximum of such curve is located around a/A = 1. Comparison of the experimentally obtaind f(u) curves with f(u) curves obtained numerically for different i values through equation 4.3 is used to assess i values of the islands. Figure 4.4a and 4.4c show the island size distribution of the reduced and the oxidized islands, respectively, each at two different surface coverages. The best fit of the two curves based on a least square method lead to i values between 4 and 5 (Figure 4.4b). Based on the same analysis the i value for the oxidized islands is evaluated to be between 5 and 6. Using the range of critical island sizes of the reduced and the oxidized islands, the χ values for both states of islands can be evaluated (4/6 and 5/7 for the reduced and 5/7 and 6/8 for the oxidized islands). Based on these information and the slope of the linear fits in Figure 4.3, the range of activation energies for the reduced and the oxidized islands are estimated to be about 1.22-1.30 eV (115-125 kJ/mol) and 0.52-0.55 eV (50-53 kJ/mol), respectively.

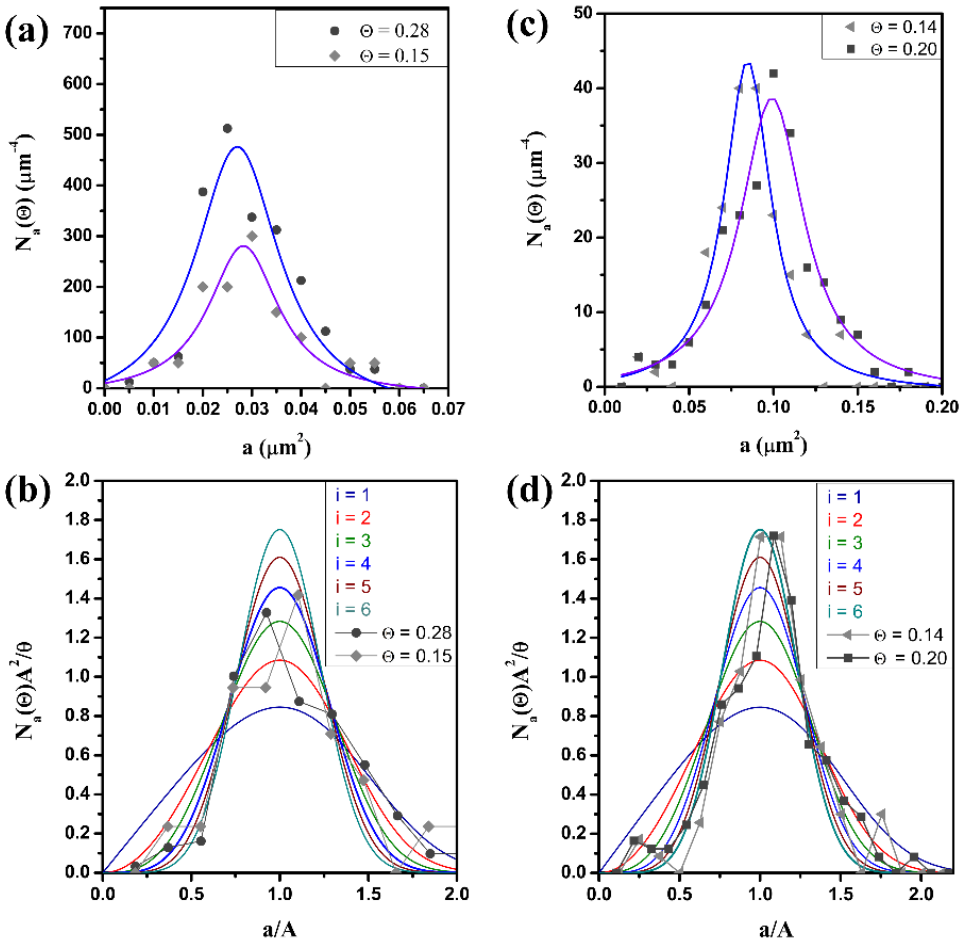

Figure 4.4. Island size distribution $N_a(\theta)$ of reduced (a) and oxidized (c) PCAT islands at different surface coverages. (b) Scaled island size distribution of the island size distribution in (a). (d) Scaled island size distribution of the island size distribution in (c). In both (b) and (d) the scaling function f(u) for critical cluster sizes of i=1–6 are shown along the experimentally measured data.

In addition to the information obtained earlier, the range of attempt frequencies (ν_0) for surface diffusion of the reduced and the oxidized islands can be calculated. This paprameter can be evaluted using equation 4.6,[8] where y_{0T} is the intercept of fittings in Figure 4.3 with the y axis, η is a weak function of θ and i, N_0 is the number of surface sites

per unit area, and F is the deposition rate. Equation 4.6 is a number value equation and the units of cm^2 and s should be used for evaluation of attempt frequency using Figure 4.3.[31]

$$y_{0T} = \ln(\eta N_0) + \frac{i}{i+2}\ln\left(\frac{4}{N_0}\right) - \frac{i}{i+2}\ln \nu_0 + \frac{i}{i+2}\ln F \qquad 4.6$$

The main information required for evaluation of these parameters can be obtained from Figure 4.3 in addition to critical island size i of each oxidation state of PCAT. The N_0 was estimated to be about 4.8×10^{14} PCAT molecules.cm^{-2}. Considering that the the reduced islands are two dimentional and the oxidized islands are three diemntional in shape, the value of η for both of these islands was estimated to be around about 2.5.[9] Therefore, based on these information the ranges of attempt frquencies for the reduced and the oxidized islands on the surface of hematite(1000) was estimated to be between 8×10^{22} - 5×10^{25} s^{-1} and between 4×10^{11} - 8×10^{13} s^{-1}, respectively. The attempt frequencies for the reduced islands are siginificantly higher than the typical attempt frequency values for surface diffusion of atoms (~ 10^{11} – 10^{13}).[9] However, such large attempt frequency value is not unrealistic as similar values has been reported for other small organic moleucles with similar molecular weight (6P on Au(111) and mica).[8,32] The high attempt frequency of 6P was explained through transition state theory based on the fact that large organic moeclues have many more translational, vibrational, and rotational modes to be excited in comparsion to a single atom on the surface.[8] On the other hand, the obtained attempt frequencies for the oxidized PCAT islands are lower than the typical attempt frequency values reported for atoms one surface.[9] These low frequencies explain the low tendency of the oxidized PCAT to grow on hematite surface by increasing the temperature.

4.4.2 Nucleation and Growth of PCAT on Thermally Reduced Hematite

In order to partially reduce the surface of a hematite single crystal, the hematite substrate was annealed in a vacuum environment. It has been shown that vacuum annealing of hematite at tempertures above 350 ℃ leads to the transformation of hematite to magnetite.[33,34] Therefore, the hematite substrate was annealed in two cycles under vacuum conditions (base pressure $< 1 \times 10^{-8}$ Torr). The progress of the reduction process was monitored in situ by XPS. The Fe $2p_{1/2}$ and Fe $2p_{3/2}$ peaks of the pristine hematite substrate in Figure 4.5a are located at 724.7 eV and 710.8 eV while its Fe $2p_{1/2}$ and Fe $2p_{3/2}$ shake-up satellite peaks are located at 733.1 eV and 724.7 eV. The location of these peaks in addition to the absense of the metalic Fe 2p is an indication of the presense of pure phase of hematite on the surface of this sample.[34] Generally, the position of sattellite peaks are monitored during the reduction or oxidation process of hematite. This is due to the more distinct shift of these peaks in comparision to Fe $2p_{1/2}$ and Fe $2p_{3/2}$ peaks.[34] The Fe 2p spectrum of this sample after the fisrt vacuum annealing cycle shows the shift of the two pairs of peaks mentioned above to lower B.E.s which is an indication of transformation of Fe^{3+} to Fe^{2+}. These peaks shift further to lower B.E.s after the second annealing cycle which is A sign of partial reduction of hematite by loosing oxygen atoms from the surface. This is evident based on the continous decrease in the instensity of the O 1s spectra of the annelead surfaces (Figure 4.5b, spectra 2 and 3) in comparsion to the pristine hematite (Figure 4.5b, spectra 1). The organic deposition chamber used in this work is not attached to the preperation (annealing) chamber which requires the transfer of the partially reduced

sample in an inert atmosphere (dry argon) between the two vacuum chambers. Therefore, it is necessary to examin the stability of the partially reduced hematite surface against oxidation in absense of high vacuum conditions. Thus, the sample was kept in dry argon environment for twenty four hours before acquiring O 1s, Fe 2p, C 1s, and survey spectra of the sample. As it is evident in Figure 4.5a, the Fe 2p spectrum of this sample slightly shifted to the higher B.E.s which is an indication of partial oxidation of the surface but not its fully oxidation. The same conclusion can be deduced from the O 1s spectrum of this sample (Figure 4.5b), which shows a slight increase in its intensity in comparison to the partially reduced hematitie surface obtained after the second vacuum annealing cycle.

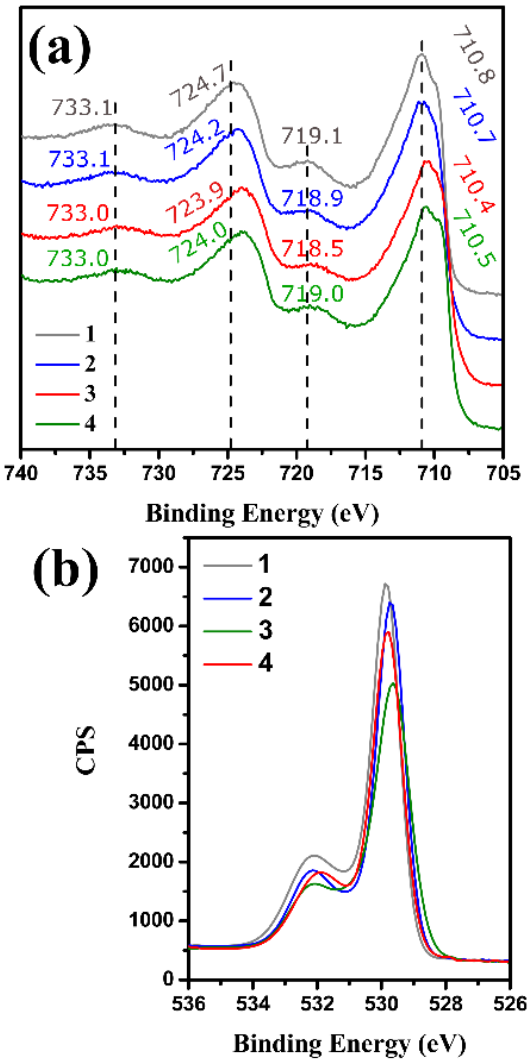

Figure 4.5. Partial reduction of hematite surface through vacuum annealing. High resolution Fe 2p and O 1s XPS spectra of prisitine hematite (1), 1st cycle of vacuum annealing (2), 2nd cycle of vacuum annealing (3), and after storage of the sample out of vacuum condition in dry Ar environemnt for 24 hours (4).

To examine the effect of the substatre's oxidation state on PCAT islands growth, hematite single crystal was annealed based on the above recepie. For each experiment the hematite single crysal was lossly clamped between two saphire washers to avoid any thermal stress of the substrate which could possibly change its surface roughness. The base

pressure of the system was about 2×10^{-7} Torr. After two cycles of annealing at 350 ℃ (5 minutes each), the sample was removed from the preperation chamber and quickly trasnfered into the deposition chamber under dry nitrogen environment.

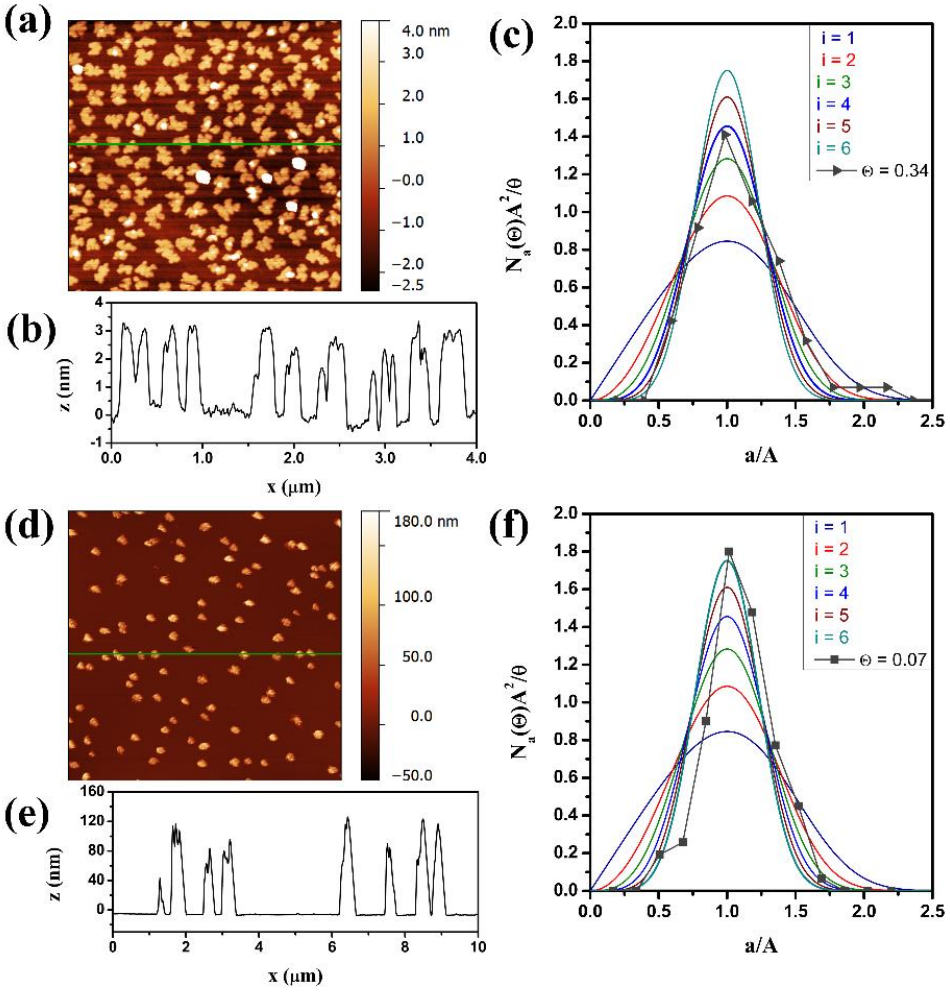

Figure 4.6. AFM images of LB (a, 4 μm × 4 μm) and PB (d, 10 μm × 10 μm) islands on partially reduced hematite surface at 293 K. The cross-section of the heights of the LB and PB islands along the green lines in (a) and (d) are shown in (b) and (e), respectively. (c) and (d) show the scaling island size distribution of LB and PB islands on partially reduced hematite, respectively.

Figure 4.6a shows the AFM images of the reduced islands on paritally reduced hematite surface. The morphology of the islands does not show any noticeable difference from the reduced islands on prisitine hematite surface at 293 K (Figure 4.2). The cross-section of the heights of the reduced islands on the partially reduced surface (Figure 4.6b) shows islands with heights about 3 nm which is comparable with the heights of the reduced islands on pristine hematite surface (Figure 4.2). The effect of the oxidation state of the hematite substrate on the nucleation and growth of the reduced islands can be studied through their scaling islands size distirbution analysis. The scaling islands size distribution of the reduced islands on partially reduced hematite located in proximity of f(u) for i = 4, which indicates the critical island size for this system is close to four. This is the same number of molecules (five molecules) required for the formation of a stable reduced island on pristine hematite surface. The same analysis was repeated for the oxidized islands on partially reduced hematite surface at 293 K. The AFM image of this sample (Figure 4.6d) does not show any differences in the morphology of these islands from the oxidized islands formed on prisitine hematite surface at 293 K. The cross-section heights of these islands have maximum heights about 120 nm (Figure 4.6e) comparible with the heights of islands on prisitine hematite surface. The scaling size distribution of the oxidized islands on the partially reduced surface of hematite (Figure 4.6f) fits best with f(u) for i = 6 which is the same critical island size (seven molecules) for the oxidized islands on pristine hematite surface. Therefore, it is concluded that the partial reduction of the hematite substrate by removing the oxygen atoms from its surface sites does not effects the nucleation and growth of different oxidation states of PCAT.

4.5 Conclusion

Submonolayers of two different oxidation states of PCAT on hematite(1000) single crystal surfaces were grown. The nucleation and growth of the fully reduced and the fully oxidized PCAT as a function of substrate temperature (278 – 338 K) have been studied. The nucleation density as a function of the substrate temperature has been evaluated for each of the two oxidation states of PCAT which resulted in two linear fits. The absence of any bend in these two fits was deduced as the dominance of a single growth mode. At low substrate temperatures (<293 K) both types of oligoanilines formed compact islands on the surface. Increasing the substrate temperatures to 338 K significantly affect the growth of the reduced islands leading to dendritic islands on the surface. However, high temperatures had minimal effect on the growth of the oxidized islands. In addition, at these substrate temperatures the height of the reduced islands was about 3 nm while for the oxidized molecules this value was on average about 120 nm. This significant difference between the height of the islands of two oxidation states of an oligoaniline indicates better wetting of the iron oxide surface by the reduced state of PCAT and dewetting of the same surface by the oxidized form of this molecule. Using the scaled island size distribution of the reduced and oxidized molecules at room temperature, the critical island size values for the reduced molecules and the oxidized molecules was evaluated. Five or six fully reduced molecules and six or seven fully oxidized molecules are required for the formation of their stable islands, respectively. Furthermore, the range of diffusion barrier energies for the reduced and the oxidized islands on hematite surface were evaluated to be about 1.22-1.30 eV and 0.52-0.55 eV, respectively. This significant difference between the diffusion barrier

energies of the two oxidation states of PCAT on hematite surface indicates higher mobility of the reduced forms of this oligoaniline on this surface. This is in line with the growth of the reduced islands on this surface as a function of substrate temperature which was demonstrated by AFM in Figure 4.2. In addition, the range of the attempt frequencies of the fully reduced and the fully oxidized islands on hematite surface were evaluated to be between 8×10^{22} - 5×10^{25} s^{-1} and between 4×10^{11} - 8×10^{13} s^{-1}, respectively. The latter range is close to the attempt frequencies for the surface diffusion of atoms (~ 10^{11} – 10^{13}). However, the former range is several orders of magnitude larger than the common attempt frequencies for surface diffusion. These rather large values have been previously explained using transition-state theory and was attributed to numerous rotational and vibration modes available for diffusion of such islands.[8] Finally, it was shown that the change in the oxidation states of the substrate through partial reduction of the hematite surface does not affect the nucleation and growth of the reduced and the oxidized PCAT.

The findings of this work are important considering the application of PCAT in corrosion inhibition coating.[18] The dewetting of the iron oxide surface by the oxidized PCAT hinders appropriate coupling between the organic phase and the metal oxide surface while it is an essential prerequisite for efficient charge transfer and polarization of iron oxide surface. In addition, the dewetting of the surface by the oxidized PCAT create a breach in the coating film, increasing the exposure of the surface to corrosion media. The different wetting of surfaces by PCAT can be problematic for other applications such chemiresistive sensors based on PCAT-graphite layer.[4] This can result in alteration of the interface between PCAT

and graphite which was described as an essential part in the sensing mechanism of such sensor.

4.6 AUTHOR INFORMATION

Corresponding Author

E-mail: pkruse@mcmaster.ca. Phone: (905) 525-9140 ext23480. Fax: (905) 522-2509.

4.7 Funding Sources

The National Science and Engineering Research Council of Canada provided financial support through the Discovery Grant program.

4.8 Notes

The authors declare no competing financial interest.

4.9 References

(1) Mishra, A.; Bäuerle, P. Small Molecule Organic Semiconductors on the Move: Promises for Future Solar Energy Technology. *Angew. Chemie Int. Ed.* **2012**, *51*, 2020–2067.

(2) Wang, H.; Zhu, F.; Yang, J.; Geng, Y.; Yan, D. Weak Epitaxy Growth Affording High-Mobility Thin Films of Disk-Like Organic Semiconductors. *Adv. Mater.* **2007**, *19*, 2168–2171.

(3) Xue, M.; Li, F.; Chen, D.; Yang, Z.; Wang, X.; Ji, J. High-Oriented Polypyrrole Nanotubes for Next-Generation Gas Sensor. *Adv. Mater.* **2016**, *28*, 8265–8270.

(4) Mohtasebi, A.; Broomfield, A. D.; Chowdhury, T.; Selvaganapathy, P. R.; Kruse, P. Reagent-Free Quantification of Aqueous Free Chlorine via Electrical Readout of Colorimetrically Functionalized Pencil Lines. *ACS Appl. Mater. Interfaces* **2017**, *9*, 20748–20761.

(5) Wang, Y.; Torres, J. A.; Stieg, A. Z.; Jiang, S.; Yeung, M. T.; Rubin, Y.; Chaudhuri, S.; Duan, X.; Kaner, R. B.; Al, W. E. T. Graphene-Assisted Solution Growth of Vertically Oriented Organic Semiconducting Single Crystals. *ACS Nano* **2015**, *9*, 9486–9496.

(6) Hlawacek, G.; Puschnig, P.; Frank, P.; Winkler, A.; Ambrosch-Draxl, C.; Teichert, C. Characterization of Step-Edge Barriers in Organic Thin-Film Growth. *Science* **2008**, *321*, 108-111.

(7) Campione, M.; Caprioli, S.; Moret, M.; Sassella, A. Homoepitaxial Growth of α-Hexathiophene. *J. Phys. Chem. C* **2007**, *111*, 12741–12746.

(8) Potocar, T.; Lorbek, S.; Nabok, D.; Shen, Q.; Tumbek, L.; Hlawacek, G.; Puschnig, P.; Ambrosch-Draxl, C.; Teichert, C.; Winkler, A. Initial Stages of a Para-Hexaphenyl Film Growth on Amorphous Mica. *Phys. Rev. B* **2011**, *83*, 1–10.

(9) Venables, J. A.; Spiller, G. D. T.; Hansbücken, M. Nucleation and Growth of Thin Films. *Reports Prog. Phys.* **1984**, *47*, 399.

(10) Yang, J.; Wang, T.; Wang, H.; Zhu, F.; Li, G.; Yan, D. Ultrathin-Film Growth of Para-Sexiphenyl (I): Submonolayer Thin-Film Growth as a Function of the Substrate Temperature. *J. Phys. Chem. B* **2008**, *112*, 7816–7820.

(11) Chowdhury, T.; Mohtasebi, A.; Kruse, P. Nature of the Interaction of N, N ′-Diphenyl-1,4-Benzoquinonediimine with Iron Oxide Surfaces. *J. Phys. Chem. C* **2017**, *121*, 2721–2729.

(12) Chowdhury, T.; Mohtasebi, A.; Kruse, P. Nature of the Interaction of N, N ′-Diphenyl-1,4-Benzoquinonediimine with Iron Oxide Surfaces and Its Mobility on the Same Surfaces. *J. Phys. Chem. C* **2017**, *121*, 2294–2302.

(13) Shao, Z.; Rannou, P.; Sadki, S.; Fey, N.; Lindsay, D. M.; Faul, C. F. J. Delineating Poly(Aniline) Redox Chemistry by Using Tailored Oligo(Aryleneamine)s: Towards Oligo(Aniline)-Based Organic Semiconductors with Tunable Optoelectronic Properties. *Chem. - A Eur. J.* **2011**, *17*, 12512–12521.

(14) Klinke, C.; Chen, J.; Afzali, A.; Avouris, P. Charge Transfer Induced Polarity Switching in Carbon Nanotube Transistors. *Nano Lett.* **2005**, *5*, 555–558.

(15) Manseki, K.; Yu, Y.; Yanagida, S. A Phenyl-Capped Aniline Tetramer for Z907/tert-Butylpyridine-Based Dye-Sensitized Solar Cells and Molecular Modelling of the Device. *Chem. Commun.* **2013**, *49*, 1416–1418.

(16) Dane, T. G.; Cresswell, P. T.; Bikondoa, O.; Newby, G. E.; Arnold, T.; Faul, C. F. J.; Briscoe, W. H. Structured Oligo(aniline) Nanofilms via Ionic Self-Assembly. *Soft Matter* **2012**, *8*, 2824–2832.

(17) Mohtasebi, A.; Chowdhury, T.; Hsu, L. H. H.; Biesinger, M. C.; Kruse, P. Interfacial Charge Transfer between Phenyl-Capped Aniline Tetramer Films and Iron Oxide Surfaces. *J. Phys. Chem. C* **2016**, *120*, 29248–29263.

(18) Wei, Y.; Jamasbi, H.; Cheng, S.; Jansen, S. A.; Sein, L. T.; Zhang, W.; Wang, C. Corrosion Protection Properties of Coating of the Epoxy-Cured Aniline Oligomers Based on Spray and UV-Salt Fog Cyclic Tests. *ASC symp. Ser.* **2003**, *843*, 208–227.

(19) Weßling, B. Passivation of Metals by Coating with Polyaniline: Corrosion Potential Shift and Morphological Changes. *Adv. Mater.* **1994**, *6*, 226–228.

(20) Ruiz, R.; Nickel, B.; Koch, N.; Feldman, L.; Haglund, R.; Kahn, A.; Family, F.; Scoles, G. Dynamic Scaling, Island Size Distribution, and Morphology in the Aggregation Regime of Submonolayer Pentacene Films. *Phys. Rev. Lett.* **2003**, *91*, 136102.

(21) Wang, W.; Macdiarmid, A. G. New Synthesis of Phenyl / Phenyl End-Capped Tetraaniline in the Leucoemeraldine and Emeraldine Oxidation States. **2002**, *129*, 199–205.

(22) Nečas, D.; Klapetek, P. Gwyddion: An Open-Source Software for SPM Data Analysis. *Open Phys.* **2012**, *10*, 181–188.

(23) Fairley, N. Casa XPS. *CasaXPS*, 2016.

(24) Heeger, A. J. Semiconducting and Metallic Polymers: The Fourth Generation of Polymeric Materials (Nobel Lecture). *Angew. Chem. Int. Ed. Engl.* **2001**, *40*, 2591–2611.

(25) Thomas, J. O.; Andrade, H. D.; Mills, B. M.; Fox, N. a.; Hoerber, H. J. K.; Faul, C. F. J. Imaging the Predicted Isomerism of Oligo(aniline)s: A Scanning Tunneling Microscopy Study. *Small* **2015**, *11*, 3430–3434.

(26) Rebourt, E.; Joule, J. a.; Monkman, A. P. Polyaniline Oligomers; Synthesis and Characterisation. *Synth. Met.* **1997**, *84*, 65–66.

(27) Boyer, M.-I.; Quillard, S.; Rebourt, E.; Louarn, G.; Buisson, J. P.; Monkman, A.; Lefrant, S. Vibrational Analysis of Polyaniline: A Model Compound Approach. *J. Phys. Chem. B* **1998**, *102*, 7382–7392.

(28) Brune, H. Microscopic View of Epitaxial Metal Growth: Nucleation and Aggregation. *Surf. Sci. Rep.* **1998**, *31*, 125–229.

(29) T. A. Witten, J.; Sander, L. M. Diffusion-Limited Aggregation, a Kinetic Critical Phenomenon. *Phys. Rev. Lett.* **1981**, *47*, 1400–1403.

(30) Amar, J.; Family, F. Critical Cluster Size: Island Morphology and Size Distribution in Submonolayer Epitaxial Growth. *Phys. Rev. Lett.* **1995**, *74*, 2066–2069.

(31) Winkler, A. Institute of Solid State Physics, TU Graz, Graz. Personal communication, September 2017.

(32) Müllegger, S.; Winkler, A. Hexaphenyl Thin Films on Clean and Carbon Covered Au(1 1 1) Studied with TDS and LEED. *Surf. Sci.* **2006**, *600*, 1290–1299.

(33) Schlueter, C.; Lübbe, M.; Gigler, A. M.; Moritz, W. Growth of Iron Oxides on Ag(111) — Reversible Fe2O3/Fe3O4 Transformation. *Surf. Sci.* **2011**, *605*, 1986–1993.

(34) Xue, M.; Wang, S.; Wu, K.; Guo, J.; Guo, Q. Surface Structural Evolution in Iron Oxide Thin Films. *Langmuir* **2011**, *27*, 11–14.

Chapter 5 Interfacial Charge Transfer between Phenyl-Capped Aniline Tetramer Films and Iron Oxide Surfaces

This chapter investigates the interaction of iron oxide surfaces with different oxidation states of phenyl-capped aniline tetramer (PCAT) through changes in organic layer or the metal oxide film. While photoelectron spectroscopy and vibrational spectroscopy techniques could elucidate the changes in the organic films, they were unable to provide similar information from the oxide film. Therefore, a method for elucidating the latter case based on conductivity measurements was presented. Based on these results the mutual doping and the direction of charge transfer at these interfaces are demonstrated.

Reprinted with permission from the Journal of Physical Chemistry C, **2016**, 120, 29248-29263, Amirmasoud Mohtasebi, Tanzina Chowdhury, Leo H. H. Hsu, Mark C. Biesinger, and Peter Kruse. DOI: 10.1021/acs.jpcc.6b09950

THE JOURNAL OF PHYSICAL CHEMISTRY C

Article

pubs.acs.org/JPCC

Interfacial Charge Transfer between Phenyl-Capped Aniline Tetramer Films and Iron Oxide Surfaces

Amirmasoud Mohtasebi,[†] Tanzina Chowdhury,[†] Leo H. H. Hsu,[‡] Mark C. Biesinger,[§] and Peter Kruse*[,†]

[†]Department of Chemistry and Chemical Biology, McMaster University, 1280 Main Street West, Hamilton, Ontario L8S 4M1, Canada

[‡]Department of Mechanical Engineering, McMaster University, Hamilton L8S 4L8, Canada

[§]Surface Science Western, Room LL31, 999 Collip Circle, London, Ontario N6G 0J3, Canada

Supporting Information

ABSTRACT: Redox-active organic compounds have been studied as corrosion inhibitors for steel. Even though it is clear that chemical interactions at the organic−metal oxide interface are behind this inhibitive process, the detailed mechanism is not yet fully understood. Using phenyl-capped aniline tetramer (PCAT), we have elucidated the interactions at the interface with iron oxide. We demonstrate the partial reduction of fully oxidized PCAT and the partial oxidation of fully reduced PCAT upon interaction with iron oxide. X-ray photoelectron spectroscopy reveals the appearance of charged nitrogen structures in PCAT deposited on hematite. Iron oxide films in contact with reduced PCAT show a higher conductance due to the introduction of defects, resulting in n-doping. In contrast, the iron oxide film in contact with oxidized PCAT shows a lower conductance, indicating that defects in the film are removed via oxidation, thus reducing the doping level. This is consistent with accepted models for corrosion inhibition, in which PCAT assists in the formation of a passive oxide film. These results are indicative of interfacial charge transfer between PCAT and iron oxide. The extent of the charge transfer and the direction of redox processes depend on the oxidation state of the molecules, enabling the construction of redox-active devices, including sensors and switches.

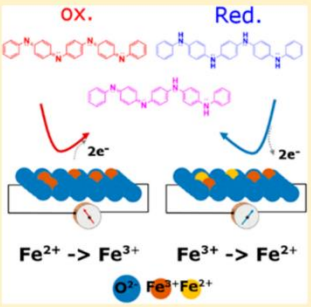

INTRODUCTION

Redox-active organic compounds are known to protect transition metals against corrosion.[1] Their weak performance under practical corrosion conditions has prevented their widespread use in commercial settings. Therefore, a better understanding of the chemical and electronic interactions at the interface between metal oxides and redox-active organic molecules is crucial to the design of better organic corrosion inhibitor coatings. Furthermore, transition metal oxide−organic interfaces have important applications in organic electronic devices, such as photovoltaics,[2] light-emitting diodes,[3] and thin-film transistors.[4] All of these devices function on the basis of the charge transfer at the interface between a metal oxide and an organic layer. Metal oxides can be used in conjunction with a broad range of organic materials because their chemical and electronic properties can be tuned in order to create a desirable alignment with the energy levels of the organic layer.[5]

It was discovered in 1985 that polyaniline (PANI) electrodeposited on steel can inhibit corrosion.[6] PANI acts as more than a simple barrier coating in this case as it was shown that breaching the organic layer does not necessarily initiate corrosion in steel presumably as a result of an electrochemical interaction between the polymer layer and the surface of iron oxide.[1,7,8] The mechanism that has been proposed to explain the corrosion inhibition of steel by redox-active organic molecules is based on the assumption that by applying these organic molecules in their oxidized states to metal surfaces they can act as an oxidizers, improving the oxide layer structure by creating a passive oxide.[1,8] The metal oxide layer remains passivated as long as the organic layer can provide a large enough shift of the corrosion potential. This mainly relies on two conditions: the presence of a sufficient number of active redox-active compounds and the regeneration of reduced organic molecules back into their active form through reoxidation by ambient oxygen.[1]

It was recently suggested that limiting the extent of the percolation network present in the organic layer is the key to successful corrosion inhibition, even in the presence of large defects in the organic layer. Rohwerder[1] concluded that an effective redox-active layer should form a microscopic percolation network at the interface rather than a macroscopic one. This means that although good electric contact between the organic film and the passive metal surface is essential,[9] it is the redox activity of the organic film that is vital for corrosion

Received: October 3, 2016
Revised: December 11, 2016
Published: December 12, 2016

Scheme 1. Chemical Structure and Protonic Doping Process for PCAT[a]

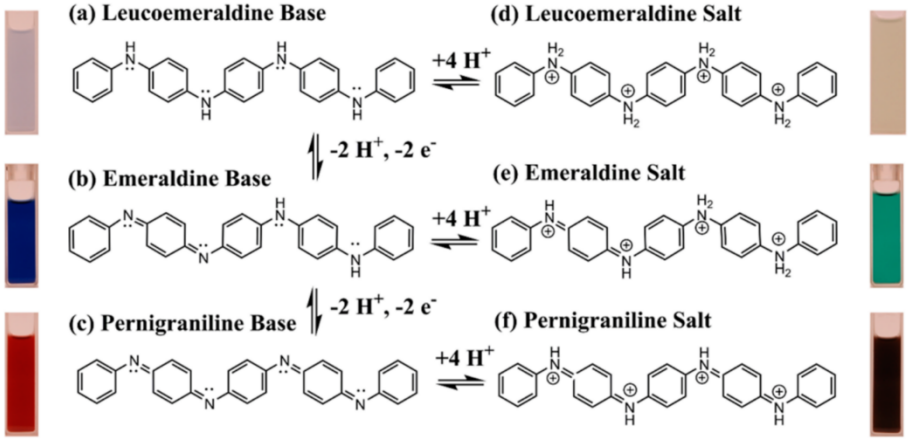

[a]Doping the base states of oligomers (left) with HCl gas results in the salt state (right). The color of the methanolic solution of each state is visible in the photograph beside each chemical structure.

inhibition and not its electrical conductivity. Instead a macroscopic network of the redox-active polymers leads to fast cation incorporation into the polymer, which results in its fast reduction and thus breakdown of the coating.[1,10] In addition, the organic layer needs to provide enough passivation current to polarize the surface in order to create a passive oxide layer. Otherwise, the corrosion process would be accelerated more than in the absence of an organic coating.[1] This condition can be achieved through the careful choice of organic molecules. Oligoanilines have emerged as promising substitutes for PANI in corrosion inhibition applications.[11] They show the same redox properties, higher solubility, and better processability than PANI. In addition, there is plenty of room for tailoring their structure to achieve the desired properties.[12] It has also been reported that oligoanilines can show superior corrosion inhibition to PANI.[13] The phenyl-capped aniline tetramer (PCAT, Scheme 1) is the smallest oligomer with at least three oxidation states: leucoemeraldine base (LB, fully reduced state), emeraldine base (EB, half-oxidized state), and pernigraniline base (PB, fully oxidized state).[14]

Temperature-programmed desorption mass spectrometry, UV−vis absorption spectroscopy, and X-ray photoelectron spectroscopy (XPS) have already shown the possibility of the vacuum deposition of PCAT on a quartz substrate under high vacuum conditions.[15] In addition to the superior processability, PCAT is reported to lack order in its monolayers because of the number of isomers available for each of its oxidation states.[16] This disordered structure could fulfill the prerequisite for an organic coating with a microscopic percolation network, in the absence of a macroscopic one.[1]

Iron naturally forms several different oxide and (oxy)-hydroxide phases when exposed to ambient air and humidity. The oxide layer is not passive and consists of an inner layer of Fe_3O_4 (magnetite) and an outer layer of Fe_2O_3 (hematite or maghemite).[17,18] The structure of this top layer is of great importance when trying to fully understand the corrosion inhibition of steel by redox-active organic molecules. On occasion, it has been wrongly assumed that the organic coating is in direct contact with the metal phase rather than the native oxide film.[19,20] However, a thin oxide film consisting of a mixture of magnetite and maghemite was shown to form on an iron surface at room temperature upon exposure to oxygen at pressures of as low as 10^{-4} Torr for only 120 s.[21]

Here we report the impact of the interaction of iron oxide on the redox chemistry and electronic properties of different oxidation states of PCAT. The hematite single-crystal (1000) surface was considered to be a model system. The charge transfer and extent of doping were quantified using X-ray photoelectron spectroscopy (XPS). Changes in the oxidation states of oligoaniline were characterized using Raman spectroscopy. We also investigated the impact of protonic doping on the doping level of base oligoanilines films at an interface with iron oxide. Finally, we examined these interaction/charge-transfer processes between iron oxide and different oxidation states of PCAT through $I-V$ measurements made by employing an array of interdigitated gold electrodes covered with a thin layer of iron oxide placed inside a microfluidic channel carrying a flow of PCAT solution. The details of these interfacial interactions are crucial pieces in the puzzle of corrosion inhibition and allow for the design of redox-active electronic devices such as chemical sensors.

■ EXPERIMENTAL DETAILS

PCAT in the leucoemeraldine oxidation state (PCAT LB) was synthesized according to a literature procedure.[14] PCAT in its half-oxidized (PCAT EB) and fully oxidized (PCAT PB) states were prepared using ammonium persulfate $(NH_4)_2S_2O_8$ (Sigma-Aldrich) as an oxidizing agent. For the preparation of PCAT PB, an excess amount of ammonium persulfate was used. Although the preparation of an exactly half-oxidized state of the oligomers is not possible through chemical doping,[8] a 1:1 molar ratio of $(NH_4)_2S_2O_8$ to PCAT LB was used to approximately prepare this oxidation state. To remove the excess amount of oxidizing agent, both solutions were filtered and washed several times with Millipore water (18.2 MΩ cm) under vacuum suction. To ensure that PCAT LB is also in the fully reduced state, the as-synthesized PCAT LB powder was mixed with an excess amount of L-ascorbic acid (Caledon Laboratories Ltd.). The same purification and filtration process applied to PCAT EB and PCAT PB powders was applied to

this sample. Finally, all samples were suspended in a dilute solution of NH_4OH (0.1 mol/L) in order to ensure that they are in the base state. All particles were collected by vacuum filtration using an air aspirator.

Hematite single crystals (natural source, one-side epi polished, SurfaceNet GmbH) with a surface orientation of (1000) were washed with methanol (MeOH, HPLC, Caledon Laboratories Ltd.) and Millipore water. All crystals were exposed to UV−air plasma under low vacuum for 2 min. None of the iron oxide substrates were sputter cleaned prior to deposition of the organic film, as this can cause the reduction of iron oxide.[22] Iron(III) oxide nanoparticles (Sigma-Aldrich) with an average particle size of 50 nm were used for Raman measurements. Nanoparticles were annealed in an air atmosphere at 440 °C for 14 h in order to form a hematite phase and remove any organic residue (Figure S5). All organic thin film depositions were performed in a home-built vacuum deposition chamber equipped with a low temperature K-cell, stage cryostat, and deposition monitor (QCM). To minimize cross contamination, the vacuum chamber was thoroughly baked prior to each deposition process. The base pressure of the chamber was better than 5×10^{-6} Torr during all depositions. All samples were stored in a dry nitrogen atmosphere prior to transfer to the UHV analysis chamber. NaCl (reagent grade, Caledon Laboratories Ltd.) was exposed to sulfuric acid (reagent grade, 98.5%, Caledon Laboratories Ltd.) in order to create water-free high-purity HCl vapor used for the protonic doping of PCAT base films on the hematite substrates.

XPS probes the surface of the sample to a depth of 7−10 nm and has detection limits ranging from 0.1 to 0.5 atom %, depending on the element. A Kratos Axis Ultra spectrometer with a monochromatic Al Kα X-ray source (15 mA, 1486.6 eV) was used to record the photoelectron spectra of the powders and coated organic films fabricated on glass or a hematite substrate. The PCAT base powders were pressed onto double-sided adhesive tape for XPS analysis. The bare hematite samples were charge corrected to a binding energy (B.E.) of 284.8 eV for C−C and C−H. All of the other samples had the main line of the carbon being mostly C═C, and as such they were charge corrected to the B.E. of 284.5 eV. High-resolution (0.1 eV) spectra were obtained using a 20 eV pass energy and an analysis area of 300×700 μm^2. All acquired spectra were analyzed using CasaXPS software (version 2.3.17).[23] For peak integration, a Shirley-type background and a line shape of GL(30), which is 30% Lorentzian and 70% Gaussian, were used. Standard deviations of XPS peak areas were calculated using a built-in procedure in Casa XPS software to estimate the precision error of output quantities by optimizing a set of peak parameters.[23]

A Renishaw inVia laser Raman spectrometer was used to acquire spectra over a range of 100−1800 cm^{-1}, with a spectral resolution of 2 cm^{-1}, using a 20× objective excited with an Ar^+ ion laser at 514 nm (2.41 eV) or a solid-state laser at 785 nm (1.57 eV). All samples were cast and dried on glass substrates. Data was collected on multiple locations on each sample and recorded with fully focused 1 or 5% laser power having a field of view of 50×50 μm^2. This will introduce less than 0.4 $\mu W/\mu m^2$ for the 514 nm laser beam and 6 $\mu W/\mu m^2$ for the 785 nm laser beam into the sample, which minimizes sample damage.[24] All Raman spectra were normalized on the basis of their most intense peaks.

Atomic force microscopy was performed in a dry nitrogen atmosphere in tapping mode using a Veeco Enviroscope with a Nanoscope IIIa controller. Typical line scan rates were 0.5 Hz. Care was taken to ensure that the tip was not modifying the surface during image acquisition. For all images, the background was subtracted and the lines were corrected by matching median height levels using Gwyddion data analysis software.[25]

The microfluidic devices are fabricated by first sputter depositing a 200 nm gold film on a glass slide. Then an array of 500 interdigitated electrodes with 100 μm spacing was photolithographically patterned. Next, a 14.2 nm iron oxide film was deposited on the gold electrodes under high-vacuum conditions (base pressure $\sim 5 \times 10^{-6}$). The iron source was a clean iron wire (0.99%, diameter = 0.01 cm, OMEGA Engineering) wrapped tightly around a clean tantalum wire. To form iron oxide, pure oxygen gas (oxygen 2.6 grade, BOC Canada Limited) was introduced into the vacuum chamber through a leak valve ($P = 5 \times 10^{-4}$ Torr) during the slow evaporation of the Fe source (~1 nm/min), as monitored by QCM. Subsequently, the substrate was exposed to hydrogen peroxide vapor for over an hour to ensure that the deposited film was oxidized. A poly(dimethylsilioxane) (PDMS) microchannel (length/width/depth = 50 mm:5 mm:100 μm) was fabricated by soft lithography. Subsequently, the PDMS microchannel was bonded on top of interdigitated electrodes by air plasma. Conductivity measurements were carried out using a Keithley 2636 source measuring unit.

RESULTS

Film Fabrication Method. Prior to studying the interaction of oligoanilines with iron oxide surfaces, it is crucial to know the possible effects of the organic layer's fabrication methods on its chemical state. Two common fabrication methods for small-molecule thin films are drop casting[12,26] and vacuum deposition.[15] Vacuum deposition has the benefit of controlling the film thickness with subnanometer precision, but the process involves expensive instrumentation.[15,27] On the other hand, drop casting is simple, and the morphology and crystallinity of the film can be altered on the basis of the choice of the solvent, nonsolvent, and substrate; however, there is poor control over the thickness of the film.[26]

High-resolution XPS was utilized to examine the impact of the deposition method on the chemical state of the organic films as well as pristine powders. The LB (Scheme 1a) and PB (Scheme 1c) states of PCAT contain only benzenoid nitrogen (amine structure) and quinonoid nitrogen (imine structure), respectively, whereas the EB state of PCAT (Scheme 1b) consist of equal amounts of these structures. Thus, the oxidation states of PCAT can be assessed on the basis of the percentage of amine and imine groups. Therefore, the N 1s XPS spectra of the pristine PCAT LB, PCAT EB, and PCAT PB powders were obtained to use as reference spectra for this work.

The N 1s spectrum of the pristine PCAT LB powder (Figure 1a) exhibits only a symmetrical peak at 399.5 eV. This peak is characteristic of neutral amine nitrogen (−NH− structure)[28,29] and shows that the powder is in the fully reduced state as expected. The XPS N 1s envelope peak of PCAT EB powder (Figure 1b) at ~399 eV is asymmetric with a distinct shoulder at lower B.E. Deconvolution of this peak yields an amine nitrogen peak at 399.6 eV and an imine nitrogen peak at 398.5 eV. On the basis of the area under these two peaks (65.9%

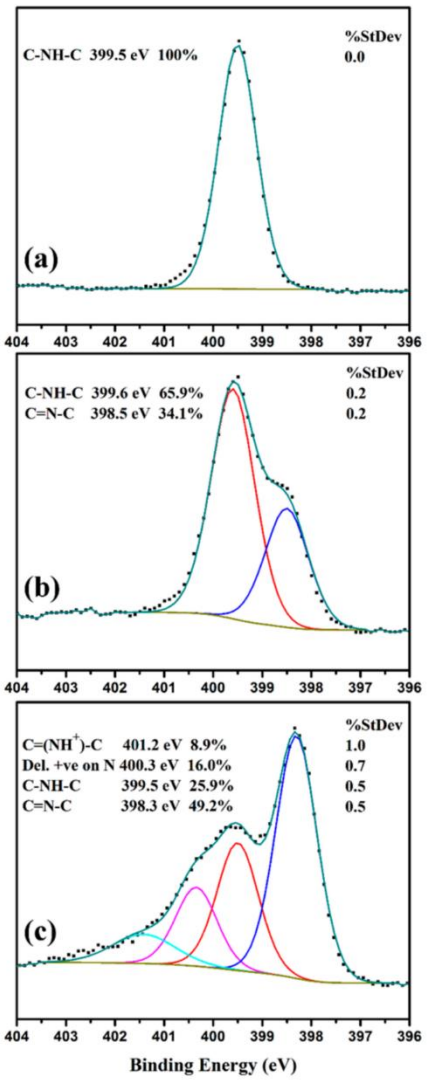

Figure 1. High-resolution N 1s XPS spectra of (a) pristine PCAT LB powder, (b) PCAT EB powder, and (c) PCAT PB powder.

amine nitrogen, 34.1% imine nitrogen), this powder is not exactly half oxidized. Although the EB state should be theoretically 50% oxidized, this result is consistent with previous literature reports for PANI EB[8] because chemical modification of the organic molecules to an exact intermediate oxidation state is difficult to control.[30] The N 1s peak of PCAT PB powder was fitted by four peaks at 398.3, 399.5, 400.3, and 401.4 eV (Figure 1c). The peaks at 398.3 and 399.5 eV are in agreement with the B.E.[29] of the nitrogen atoms in imine and amine structures, respectively. On the basis of the previous reports, the other two peaks at higher B.E.s can be assigned to charged nitrogen species.[3,32] The peak at 400.3 eV was attributed to the nitrogen atom with delocalized positive charge,[31] and the one at higher B.E. (401.4 eV) was assigned to the N^+ atom in C═(NH^+)−C.[31−33] On the basis of the area under the amine peak, the powder was less than three-quarters oxidized. The presence of two peaks associated with positively charged nitrogen atoms is presumably due to the incomplete washing of sulfate or persulfate from the product after the oxidizing step. This argument is supported by the presence of S 2s and S 2p signals in the survey spectra of the PCAT PB powder (Figure S7b) as an indication of a residual amount of sulfate still present in this sample. No such signals have been detected for the PCAT LB powder (Figure S7a).

To minimize the effect of the substrate on the chemical state of the deposited film, glass slides were used as neutral substrates. For the preparation of drop cast films, pristine PCAT LB powder was sonicated in MeOH (~7.9 mM) for 2 min and was cast on glass slides at room temperature. Figure 2a,b shows the N 1s core-level XPS spectra of vacuum-

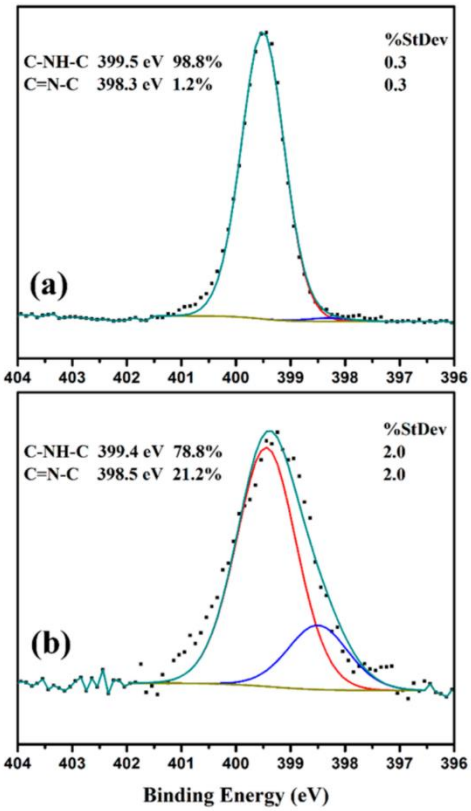

Figure 2. High-resolution N 1s XPS spectra of (a) the PCAT LB film vacuum deposited on a glass substrate and (b) the PCAT LB film drop cast on a glass substrate.

deposited and drop-cast films on glass substrates. The N 1s spectrum of the PCAT LB thin film fabricated by vacuum deposition on glass was deconvoluted into two peaks (Figure 2a). The major peak is an amine peak (399.5 eV). The other fitted peak is a low-intensity imine peak (398.3 eV). This peak makes only about a 1% contribution to the envelope peak. It is also possible to fit the N 1s spectrum of the organic film drop cast on glass (Figure 2b) by an amine (399.4 eV) and an imine peak (398.5 eV). In contrast to the vacuum-deposited film, the

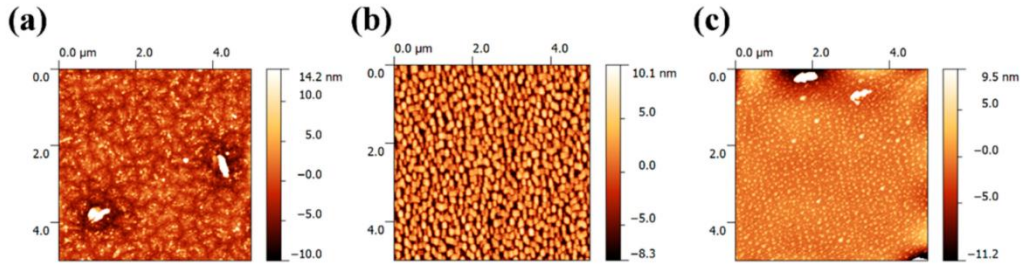

Figure 3. (a) The PCAT LB film (2.5 nm thick) on hematite single crystal (5 μm × 5 μm), (b) the PCAT EB film (2.5 nm thick) on hematite single crystal (5 μm × 5 μm), and (c) the PCAT PB film (2.3 nm thick) on a hematite single crystal (5 μm × 5 μm).

contribution of the imine peak to the envelope peak was increased to more than 20%. This partial oxidation may be due to the prolonged exposure of the PCAT film to ambience during the sonication, deposition, and drying process. A comparison of the deconvoluted N 1s XPS spectra shows that vacuum deposition has a negligible effect on the oxidation states of the pristine PCAT powder whereas drop casting can cause a considerable change in the oxidation state of the precursor. Therefore, on the basis of this experiment and because the thickness of the deposited film can be more precisely controlled through vacuum deposition, this technique was used as the method of choice for the rest of this study, unless stated otherwise.

Morphology of the Oligoaniline Films. There have been several reports on XPS of redox-active organic compounds deposited on steel and iron oxide substrates, attempting to understand the interaction at this interface.[8,34,35] However, to the best of our knowledge all of these studies used organic films with thicknesses in the range of hundreds of nanometers to micrometers. Because XPS is capable of probing only a few nanometers from the surface, all of these studies are in fact probing the interaction at the interface of the organic compounds and the ambient surroundings or the interactions in the bulk of the organic film. Thus, to ensure that the XPS data includes the signal from the interface of iron oxide and the organic layer, the thickness of the organic layer must be limited to a few nanometers. The deposition conditions (substrate temperature and deposition rate) were optimized in order to fabricate thin and uniform organic films. The thickness and morphology of each layer were studied by AFM. Vacuum-deposited PCAT, in its fully reduced state, on a hematite (1000) surface tends to wet the surface and form dendritic islands that are less than 7 nm thick (Figure 3a). The same quality films can be achieved for the PCAT EB film (Figure 3b), although in this case the islands are more globular in shape. Deposition of PCAT PB on the substrate kept at room temperature (~25 °C) led to the formation of two types of island morphology; small, thin, globular islands and long, thick, needle-shape islands (Figure S8). By keeping the substrate at lower temperatures during the deposition (9−10 °C), the number of needle-shaped islands decreases (Figure 3c). Thus, the latter condition is preferable, as it leads to the formation of a more uniformly thin organic layer. This variation in the morphology of the islands is an indication that PCAT PB molecules tend to dewet the surface more than PCAT LB and EB molecules do, likely because of weaker interactions with the surface.

The higher dewetting of the metal oxide surface by PCAT molecules in higher oxidation states differs from the trend predicted for the aggregation of PANI in organic solutions.[36] Zhang et al. reported that the highest extent of self-association is observed for the EB state because of the possibility of interchain hydrogen bonding between imine and amine nitrogen sites. Because of the fact that the LB and PB states consist only of purely amine or purely imine groups, respectively, no such aggregation should be expected. Island formation of oligoanilines on solid metal oxide surfaces depends on the balance of molecule−surface and molecule−molecule interactions. Water adsorption and dissociation on iron oxide surfaces, including hematite, leads to the formation of hydroxyl groups at different surface sites,[37−39] aiding the interaction with the PCAT molecules through their amine and imine groups. For PCAT LB, the lone pair electrons of amine nitrogen can interact with the hydrogen of the surface hydroxyl groups, in addition to the interaction between the lone pair of electrons of the oxygen in the hydroxyl groups and the hydrogen in the amine group. In the case of PCAT PB, the lone pair of the imine nitrogen can interact with the hydrogen in the hydroxyl group. This decrease in the interaction pathways between the oxidized molecules and the substrate can account for the lesser degree of surface wetting by PCAT PB and PCAT EB films.

Interaction of PCAT LB with the Hematite Surface. Thin films of PCAT LB were vacuum-deposited on hematite single-crystal substrates. A bare hematite substrate was used as a reference sample for the Fe 2p spectra. For all samples, high-resolution Fe 2p, O 1s, C 1s, and N 1s XPS peaks were collected. Deconvolution of the N 1s envelope peak of PCAT LB-coated hematite shows three peaks (Figure 4): a primary amine peak at 399.5 eV and two minor peaks at 398.3 and 401.2 eV. The component at 398.3 eV can be assigned to imine (=N− structure).[29] As previously reported for PANI,[32,33] the higher B.E. component of the N 1s envelope peak was attributed to the most positively charged nitrogen sites (C=(NH$^+$)−C structure). On the basis of this peak assignment, the N 1s envelope peak consists of approximately 93% amine nitrogen, 5% positively charged nitrogen, and 2% imine. A comparison of these spectra with the N 1s XPS spectra of PCAT LB powder as a reference sample (Figure 1a) indicates the partial oxidation of PCAT LB on hematite. In addition, even though there are reports on the X-ray-induced reduction of materials in UHV,[40,41] no such reduction was observed in the case of PCAT LB on hematite by comparison to the N 1s XPS spectra of PCAT LB powder.

Raman spectroscopy is an alternative tool to characterize the interaction between these oligoanilines and iron oxide surfaces. Under ambient conditions, it is a powerful tool to qualitatively determine the oxidation states of PANI and its oligomers.[42]

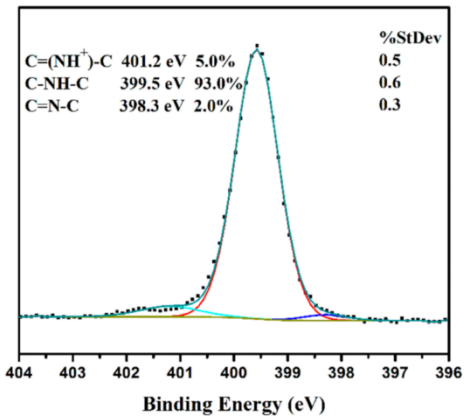

Figure 4. High-resolution N 1s XPS spectra of PCAT LB deposited on a hematite surface.

Because normal Raman spectroscopy lacks the surface sensitivity of XPS, acquiring a strong Raman signal from the few monolayers in direct contact with the hematite surface is nontrivial. One way to amplify this signal is by increasing the surface area of the interface between the organic layer and the metal oxide. Therefore, instead of using a flat single-crystal surface, small iron oxide nanoparticles with a mean diameter of 50 nm were used. PCAT LB powder was mixed with the annealed hematite nanoparticles (1:5 by weight) using a vortex mixer. Both pristine PCAT LB powder and the mixture were sonicated in MeOH for 10 min and were cast onto glass slides. Because Raman features are known to be sensitive to many parameters including temperature and laser power,[24,43] the lowest possible laser power (below 0.4 $\mu W/\mu m^2$) was utilized during spectra acquisition. For comparison, the most intense peak of each spectrum was normalized to 1. The PCAT LB film showed the three main signature Raman bands of the reduced state of PCAT at 1179, 1221, and 1622 cm^{-1} (Figure 5a).[44,45] No bands indicating the presence of the other oxidation states of PCAT are observed. For the mixture of hematite nanoparticles with PCAT LB, all three bands observed for the pristine PCAT LB disappeared and instead five bands at 1162, 1216, 1493, 1586, and 1612 cm^{-1} emerged (Figure 5b). These bands are associated with the oxidization of PCAT.[44] The coexistence of these bands and the low-intensity bands of PCAT LB proves the partial oxidation of PCAT LB at the surface of hematite particles.

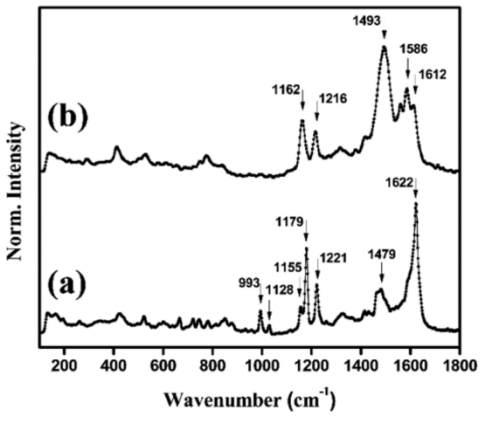

Figure 5. Raman spectra of (a) the PCAT LB film and (b) the composite film of PCAT LB and hematite nanoparticles.

Both Raman spectroscopy under ambient conditions and XPS in vacuum indicate the partial oxidation of PCAT on hematite. Scheme 2 depicts different pathways for oxidation/reduction and doping/dedoping of PCAT. On the basis of this scheme, one route for the oxidation of PCAT LB is losing two electrons and two protons, and thus the product of this process remains in the base state (Scheme 2c). The other possibility is the oxidation of the oligoanilines mediated by the hematite surface. The removal of electrons from a base form of amine nitrogen through charge transfer to hematite and the formation of a positivity charged amine nitrogen is also an oxidation process. The result of such a process is the salt form of the molecule (Scheme 2a). Hence, the hematite surface can oxidize PCAT LB as an alternative process to the oxidation of the leucoemeraldine state under ambient conditions.[8] It has been known that polyaniline can be oxidized on the surface of iron oxide by oxygen.[46] Although extreme care has been taken to minimize the exposure of the sample to air, this could be an alternative source of oxidation of PCAT LB, as the sample has been exposed to the laboratory atmosphere for a short amount of time during the transfer from the deposition chamber to the XPS chamber.

In Situ Deposition and Spectroscopy of PCAT LB on Low-Carbon Steel. To examine whether the oxidation of the PCAT LB film on hematite was induced by the interfacial interactions, the previously reported high-resolution XPS spectra of the in-situ-deposited LB on a sputtered clean steel substrate were reanalyzed.[15] The layer-by-layer deposition of LB had been performed in three different thicknesses with the final thickness of approximately 5 nm. The N 1s XPS spectrum of the sputtered cleaned steel shows a low-intensity spectrum of nitrogen species at around 396.8 and 400.5 eV (Figure 6a). The former peak is attributable to nitride compounds formed as a result of the sputtering process of the steel. The latter peak is indicative of an unknown organic nitrogen, possibly amide.[15] After the first deposition of LB (Figure 6b), two additional peaks appear, an amine peak at 399.4 eV (53.89%) and an imine peak at 398.2 eV (17.75%). After further deposition of LB, the N 1s spectrum still can be deconvoluted into the same three peaks (Figure 6c). The contribution of the amine peak to the envelope peak increases (64.48%), and the contribution of the imine peak decreases (13.98%). Finally, after the deposition of approximately 5 nm of LB on steel, the N 1s envelope peak can be deconvoluted only to a major amine peak (99.13%) and a minor imine peak (0.87%) (Figure 6d).

Because the deposition and XPS analysis had been performed in two interconnected vacuum chambers, the sample had not been exposed to ambient conditions prior to data acquisition. These results indicate that the partial oxidation of the thin LB film on steel is mediated by iron oxide. It also confirms that the LB film was indeed partially oxidized through interaction with iron oxide (Figure 4). In addition, using ultraviolet photoelectron spectroscopy, it has been shown that the deposition of a thin film of fully reduced PCAT on steel causes band bending and a decrease in the work function of the metal oxide surface by 0.5 eV.[15] This makes it easier for LB to be oxidized on the surface of iron oxide. This observation is consistent with our

Scheme 2. Conversion between Different Base and Salt States of PCAT at the Interface with Hematite

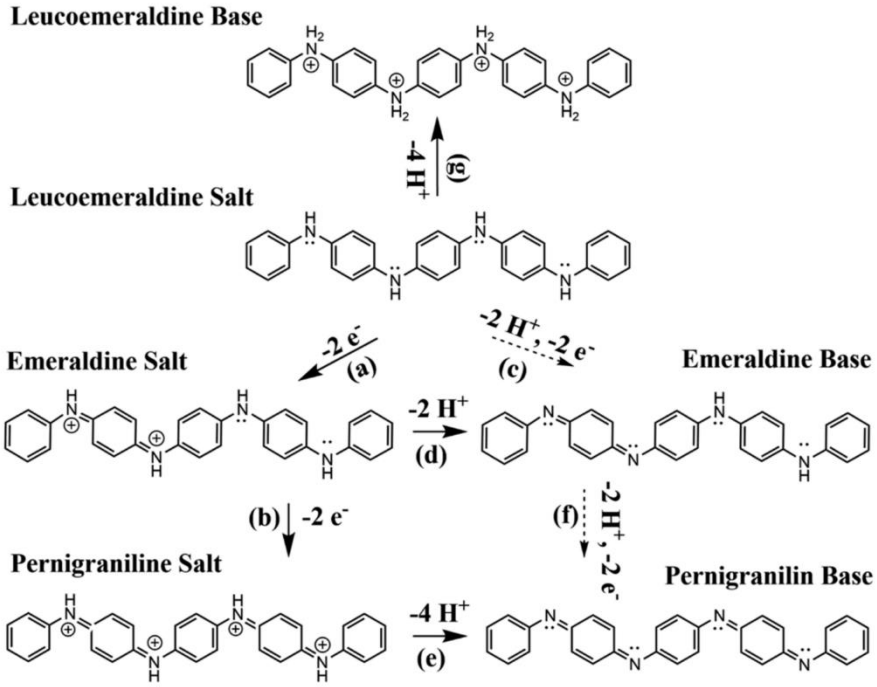

results regarding the oxidation of PCAT LB on hematite as obtained by XPS and Raman spectroscopy. As the thickness of the LB film reaches approximately 5 nm, the contribution of the imine to the N 1s peak decreases. The imine species remain localized at the interface. Further deposition of PCAT results in the attenuation of the signal from the interface. The nitrogen in the newly deposited layer retains its amine character.

This shows that the interface-mediated charge transfer by the iron oxide is limited to the proximity of the interface in comparison to air oxidation, which can act on the bulk organic film. The comparison of the N 1s spectra of the LB film on steel with the same film on a hematite single crystal shows the absence of charged nitrogen peaks at higher B.E. in the former sample. One possible reason behind this discrepancy could be the differences in the chemical and electronic properties of the low-carbon steel and hematite single crystal. The other major difference between these two samples is the adsorbed water film on their surfaces. The hematite single crystal had been exposed to the ambient environment, which allows for the formation of a water film on the substrate. The presence of such a film on this particular steel substrate is less likely due to oxidation under dry nitrogen flow.

Interaction of PCAT EB and PCAT PB with the Hematite Surface. The same characterization methodology applied to the PCAT LB-hematite interface was repeated for other oxidation states of PCAT. Thin films of PCAT EB and PCAT PB fabricated on hematite single-crystal substrates were studied by XPS. The N 1s XPS spectrum obtained from the interface of a PCAT EB film and hematite can be fitted by three peaks (Figure 7a). The peaks at 399.56 and 398.3 eV were assigned to amine and imine nitrogen, respectively, and the peak at 401.2 eV was assigned to positively charged nitrogen as previously reported for PANI in contact with graphene.[32,33] As for the interface between PCAT LB and hematite, this peak is a sign of charge transfer between the PCAT EB film and hematite. A comparison of the area under these fitted peaks with the deconvoluted spectra of the PCAT EB powder (Figure 1b) shows that the interaction of the PCAT EB molecules with hematite leads to the partial reduction of PCAT.

Deconvolution of the N 1s peak for the PCAT PB-coated hematite (Figure 7b) leads to the same four peaks that were previously fitted for the N 1s XPS spectrum of PCAT PB powder (Figure 1c). However, the contribution of each peak to the envelope peak has changed significantly. Figure 8b shows that the intensity of the amine peak increased drastically at the expense of the imine peak in the PCAT PB powder (Figure 1c). This demonstrates a significant reduction of the fully oxidized oligomers in contact with the hematite phase. However, the number of charged nitrogen atoms was slightly decreased. Therefore, the deconvoluted N 1s XPS spectra of PCAT EB and PCAT PB films on hematite substrates show the partial reduction of the small molecules in addition to the interfacial charge transfer at the interface.

Raman spectroscopy of PCAT EB and PB powders mixed with hematite nanoparticles confirmed the results obtained from XPS. Raman spectra of pristine PCAT EB (Figure 8a) and a mixture of PCAT EB and hematite nanoparticles (Figure 8b) look almost identical, and both show Raman bands at approximately 1162, 1214, 1496, and 1585 cm^{-1}. These bands are associated with PCAT in its half-oxidized state.[44]

The Raman spectra of PCAT PB powder (Figure 8c) and the composite film of PCAT PB and hematite nanoparticles (Figure 8d) show several bands of oxidized PCAT. However, the transformation of the shoulder of the bands at 1589 and

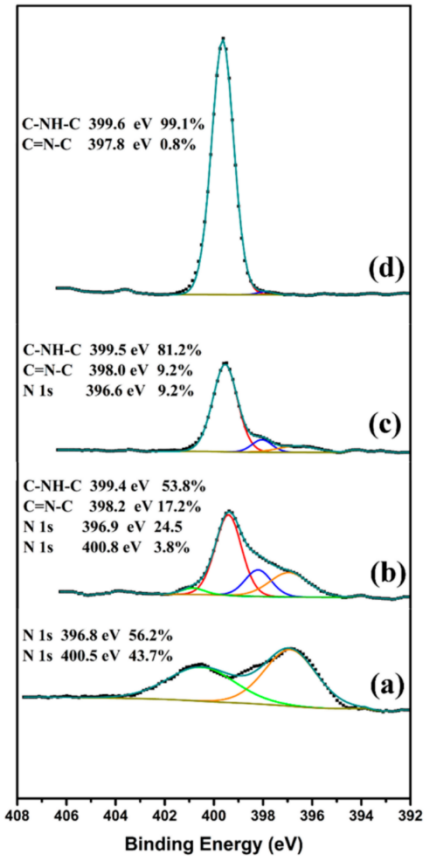

Figure 6. High-resolution N 1s XPS spectra of (a) sputtered, cleaned low-carbon steel, (b) PCAT LB first deposition, (c) PCAT LB second deposition, and (d) PCAT LB third deposition on steel.

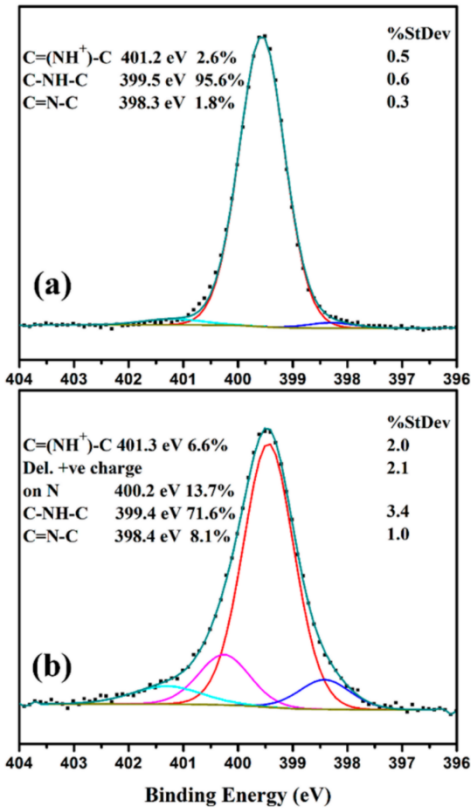

Figure 7. High-resolution N 1s XPS spectra of (a) PCAT EB deposited on a hematite surface and (b) PCAT PB deposited on a hematite surface.

1500 cm^{-1} in the PCAT PB powder spectrum to the separate bands at 1619 and 1488 cm^{-1} in the mixture of PCAT PB with hematite, respectively, can be interpreted as the sign of the partial reduction of PCAT.[44] One reason behind the greater similarity between the Raman spectra of the PCAT PB and its mixture with hematite nanoparticles is the fact that the measurement has been performed in air and thus there is a possibility of air-exposed oxidation. In addition, the observation of this reduction event by both XPS and Raman spectroscopy is an indication that this reduction was not induced by the X-ray beam used in XPS.

The XPS spectra presented here (Figure 7a,7b) indicate that the thin films of PCAT EB and PB will be reduced by hematite surfaces. The presence of N 1s signals at higher B.E. indicates the possibility of charge transfer at the interface between oxidized molecules (PCAT EB or PB) and the hematite substrate. Raman spectroscopy, under ambient conditions, also shows a partial reduction of PCAT PB molecules in contact with hematite nanoparticles. No such reduction was observed for PCAT EB molecules. These results are consistent with the previously assumed mechanism for corrosion protection of steel by redox-active organic compounds.[8] It has been argued that these compounds, if applied in their oxidized states, can act as an oxidizer, improving the underneath metal oxide layer and inhibiting the corrosion. However, these reports assumed EB to be the oxidized form whereas it is only half-oxidized.[8,34] In addition, the organic films used in those cases were several micrometers thick.[8] The base forms of PANI and its oligoanilines are known to be extremely poor electrical conductors. Therefore, it is expected that most of these measurements benefit not only from corrosion inhibition induced by redox-active organic compounds in proximity to the interface but also from other mechanisms such as barrier coating protection. Our results expand the understanding of corrosion inhibition by redox-active organic compounds by using the fully oxidized PCAT (PB) instead of half-oxidized PCAT (EB). In addition, using only very thin films for the organic coatings ensures that the observed change in the organic phase was indeed induced by the underlying metal oxide surface.

Interaction of PCAT Salt with Hematite Surfaces. Even though there are reports on effective corrosion inhibition using redox-active organic compounds in their base form,[42,47,48] most of the research to date is focused on the application of the salt form of these compounds.[49−51] This is based on the assumption that the higher conductivity of the salt films will assist with better integration of the entire organic layer and thus more effectively passivate any exposed metal.[19,52] Kinlen et

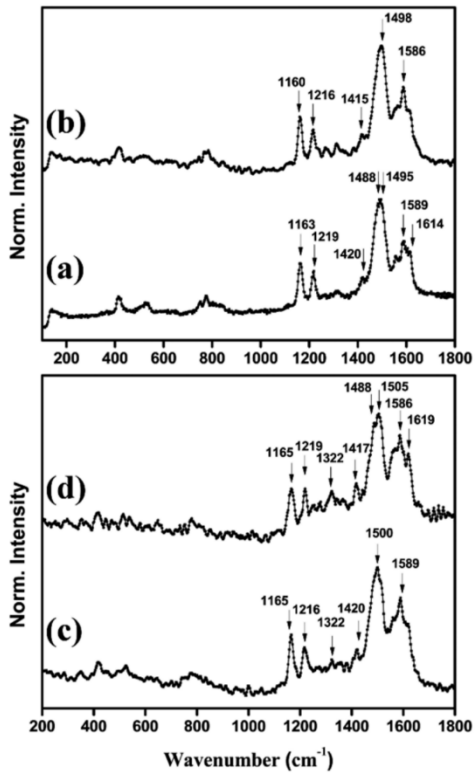

Figure 8. Raman spectra of (a) the PCAT EB film, (b) the composite film of PCAT EB and hematite nanoparticles, (c) the PCAT PB film, (d) the composite film of PCAT PB and hematite nanoparticles.

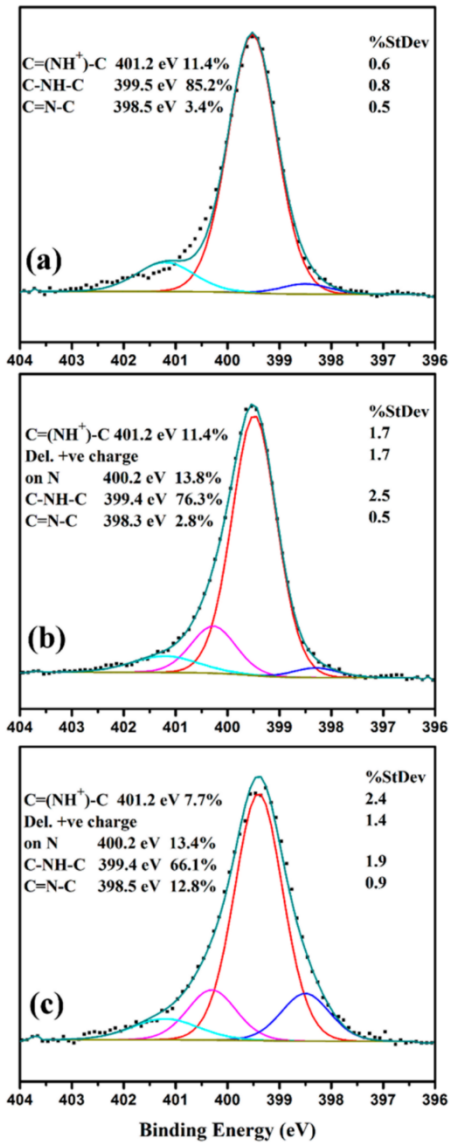

Figure 9. N 1s XPS spectra of salt PCAT on hematite for (a) PCAT LS, (b) PCAT ES, and (c) PCAT PS.

al.[42,46] have suggested that the conversion of ES state films fabricated on steel to LS state films is done through redox chemistry and to EB state films though acid−base means. It is not possible to directly deposit the salt form of PCAT in vacuum. Therefore, to fabricate thin and uniform films of PCAT salt, all of the previously analyzed PCAT base films on hematite were exposed to gaseous HCl for 30 s and load-locked back to the XPS chamber. The N 1s XPS spectra of PCAT LS (Figure 9a) still can be properly fit by three peaks of an imine (398.5 eV), an amine (399.5 eV), and a positively charged amine (−NH^+−, 401.2 eV). Although the quantitative comparison of these peaks with the N 1s spectra of PCAT LB on hematite shows only a slight increase in imine content, there is a more than a 2-fold increase in the number of charged amines. This expected increase in the amount of cationic nitrogen in PCAT salt is due to protonic doping by HCl gas. The Cl 2p XPS peak from this sample (Figure S17) can be decomposed into a $2p_{3/2}$ peak at 198.4 eV and a $2p_{1/2}$ peak at 200.0 eV. These peaks are attributed to the presence of chloride species in the vicinity of nitrogen atoms in the structure of PCAT. The absence of any peaks at higher B.E.s is a sign that no covalently bonded chlorine was formed upon exposure to HCl gas and thus is proof of the successful protonic doping of PCAT.[53]

A comparison of N 1s XPS spectra of the PCAT EB film on hematite before (Figure 7a) and after (Figure 9b) exposure to HCl gas shows the appearance of a fourth peak at 400.2 eV. On the basis of a previous report on PANI, this peak was assigned to the delocalized positive charge on the backbone of the oligomer.[29] This new peak has the second highest contribution to the envelope peak after the peak of the benzenoid nitrogen. Although protonic doping does not lead to a significant increase in the amount of imine nitrogen, the amount of positively charged nitrogen tripled.

The same number of fitted peaks, with the same trend between the doped (Figure 9c) and undoped (Figure 7b) organic films on hematite, has been observed for the fully oxidized form of PCAT. On the basis of the previous reports on the interaction of PANI and graphene,[32,33] the N 1s XPS signals

at higher B.E.s such as 400.4 and 402.0 eV are associated with the electronic interaction between the two materials and were considered to be a sign of the protonic doping process at the interface.

Because all three PCAT base films (LB, EB, PB) fabricated on the hematite substrate have been exposed to the same amount of HCl gas for the same period of time, the only difference between the salt films is the starting base structure from which they are derived (imine and amine content). The amount of amine and imine structure between the base PCAT LB and EB films on hematite and their corresponding salt films (LS and ES, respectively) stayed nearly constant, whereas the content of charged nitrogen has been significantly increased. Although the comparison of the PB and PS films on hematite shows only a slight increase in the amount of imine after exposure to HCl gas, the amount of charged nitrogen stayed the same in both samples. This comparison between the base and salt films shows that the PCAT films exposed to excess HCl gas do not show more than an ~20% cationic nitrogen N 1s signal. One way to determine the protonic doping level of each films is through the ratio of Cl/N atomic percentages, derived from the area under their peaks. On the basis of this method, PCAT LB and PB are doped to almost the same level (25.0 and 25.9%, respectively), whereas PCAT EB was doped to a lesser degree (18.9%). Another way to determine the extent of protonic doping is by considering the ratio of charged nitrogen atoms to the total amount of nitrogen. On the basis of this method, the PCAT EB and PB films are doped almost twice as much (20.8 and 21.1%, respectively) as the LB film (11.4%). The results from the later method are in better agreement with the expected structures in Scheme 2, which shows the increase in protonic doping by moving toward oxidized states. This is due to the fact that the ratio of Cl/N atomic percentages includes all Cl^- ions, some of which might not participate in the protonic doping process.

Impact on the Substrate. In the case of the protonation of the PCAT LB organic layer and its partial oxidation by hematite, a partial reduction of iron oxide and the alteration of its oxidation state should be observed. The B.E. of O 1s is independent of the Fe oxidation states and thus cannot be used to monitor the effect of charge transfer on the hematite substrate (Figure S8).[54,55] Different iron oxide and hydroxide phases are commonly distinguished by their Fe 2p XPS spectra.[54] However, the analysis of Fe 2p spectra is challenging because of issues such as peak asymmetry, complex multiplet splitting, and overlapping B.E.s.[22] The Fe 2p spectra of both the bare hematite surface (Figure 10a) and the hematite surface coated with PCAT LB (Figure 5b) exhibit two sets of peaks, $2p_{1/2}$ (~724 eV) and $2p_{3/2}$ (~711 eV), as a result of spin−orbit coupling. They also show Fe $2p_{3/2}$ and Fe $2p_{1/2}$ shake-up satellite peaks with B.E.s of around 719 and 733 eV, respectively. On the basis of ref 22, the satellite peaks were omitted from the fitting performed for the $2p_{3/2}$ part of the spectrum using a Shirley background. For each sample, the envelope peak at ~711 eV was deconvoluted into five peaks. The positions, fwhm's, and areas of these peaks confirm the presence of a single hematite phase.[22] The absence of a peak at around 706 eV confirms that there is no metallic iron present in either of the samples, as expected in the case of a hematite single crystal.

The Fe 2p satellite peaks can in principle be used to identify if any reduction of Fe^{3+} to Fe^{2+} occurring upon adsorption of PCAT LB Fe^{3+} satellite peaks appear at ~719 and 733 eV, in contrast to Fe^{2+} satellite peaks that are typically found at ~716 and 730 eV.[54,55] Despite a slight shift being observed between the positions of the satellite peaks of the bare hematite and PCAT LB-coated hematite samples, the spectra look largely identical and the shift is possibly due to the uncertainty of using C 1s as a charge-correction reference. The following calculation will demonstrate how this subtle expected change in the hematite phase due to the absorption of an organic layer is below the sensitivity of the XPS instrument used in this work. The Fe 2p and N 1s photoemissions contribute only 11.3 and 5.8% to the XPS survey spectra of the PCAT LB-coated hematite surface (Figure 10c), respectively. From this share of N 1s, only 2.8% of it is associated with the charged nitrogen peak (C═N^+−C) giving an overall 0.15%. If we assume that all eight nitrogen atoms present in each triclinic unit cell of PCAT are projected onto the interface with the hematite surface in a plane and the α-Fe_2O_3(1000) single crystal has a completely Fe-terminated surface, then there will be an approximately 1:1 interaction between surface Fe atoms and the cationic charged nitrogen.[56−58] This could lead to about a 1.3% change in the Fe 2p spectra (0.15/11.3: N^+/Fe 2p). This subtle change is very unlikely to be detectable considering that the data used for such a calculation is not truly coming from an interface but from a few nanometers to each side of it. In addition, the presence of an overlayer (organic layer) results in a background slope

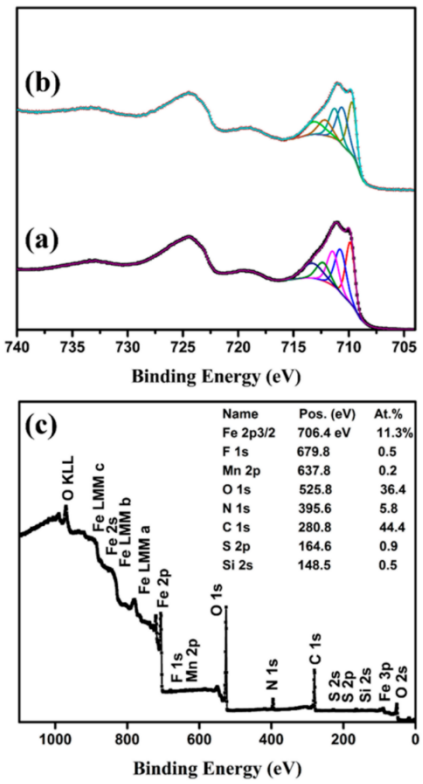

Figure 10. High-resolution Fe 2p XPS spectra of the bare hematite surface (a) before and (b) after vacuum deposition of 2.5-nm-thick PCAT LB film. Both spectra indicate the presence of a hematite phase. (c) XPS survey spectra of the PCAT LB-coated hematite interface.

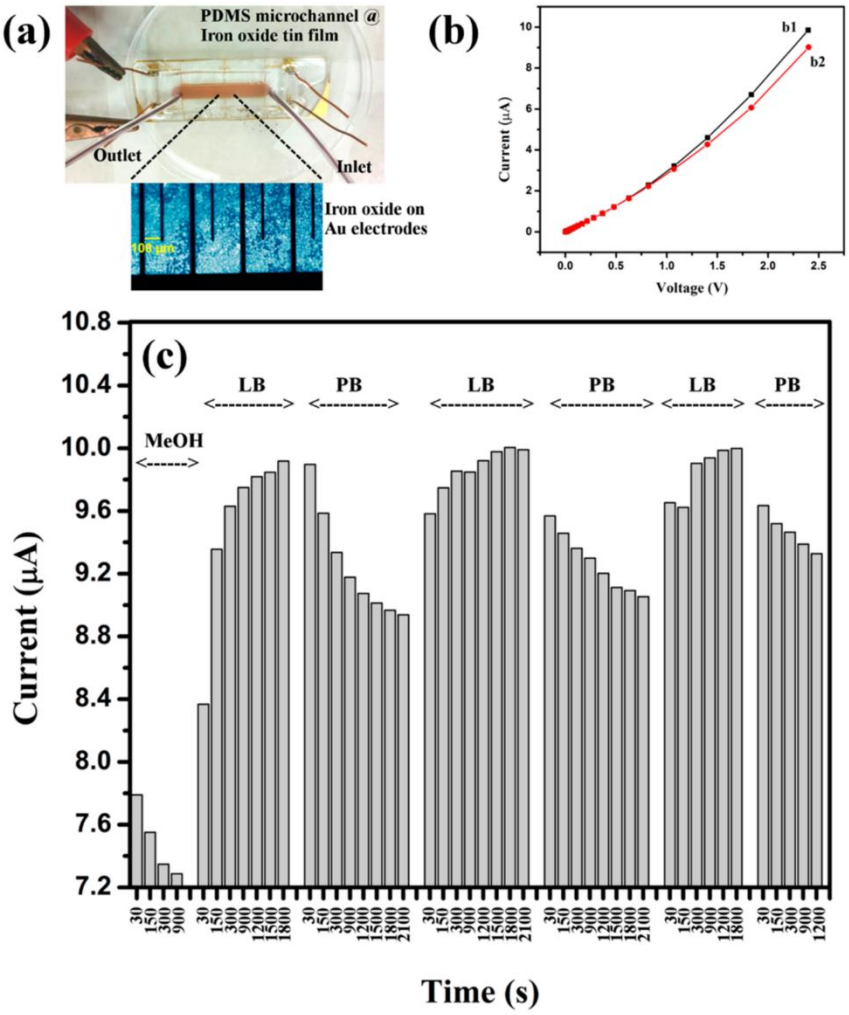

Figure 11. (a) Microfluidic channel fabricated on top of the 14.2 nm iron oxide-coated interdigitated gold electrodes. (b) Plot of current vs voltage of the iron oxide-coated gold electrode after 1500 s of flowing PCAT LB in MeOH (b1) and PCAT PB in MeOH (b2) into the microchannel. (c) Plot of current vs time by applying a bias voltage of 2.4 V to the iron oxide-coated gold electrodes while flowing MeOH, PCAT LB in MeOH, and PCAT PB in MeOH in the microchannel for three consecutive measurements.

change and makes the comparison between the intensity of the satellite and $2p_{3/2}$ peaks of each samples impossible.

Conductivity Measurement of Iron Oxide by a Microfluidic Device. An alternative path for better understanding the interaction of PCAT with iron oxide is through monitoring the change in conductivity of iron oxide while in contact with different oxidation states of PCAT (reduced and oxidized). Thus, we have fabricated a microfluidic device to sense these expected variations (Figure 11a). Because the thin fabricated iron oxide film (14.2 nm thick) has a high resistivity, we have used an array of closely packed interdigitated gold electrodes. Current−voltage curves were acquired by sweeping the bias logarithmically from 1 mV to 2.4 V in 5 min intervals while each analyte was flowing through the channel over the iron oxide film (flow rate = 0.2 mL/min). In the first run, pure MeOH was pushed through the channel. Subsequently, the same measurement was repeated three times while PCAT LB and PCAT PB solutions (3 mg/mL in MeOH) were flowing through the channel. Figure 11b shows the $I-V$ curves of the iron oxide film upon exposure to flows of PCAT LB and PCAT PB solutions. Both curves are nonlinear, which is characteristic of semiconducting materials. By flowing MeOH through the channel, the measured current starts to slowly decrease, indicating an increase in the electrical resistance of the iron oxide (Figure 11c). This indicates that the fabricated iron oxide film is not in its most oxidized form. However, when PCAT LB starts to flow, the current starts to increase quickly until reaching the stable value of 9.91 μA after 1800 s of exposure to this analyte. The trend reverses when flowing PCAT PB through the channel as the current starts to decrease to 8.99 μA after 2100 s of exposure.

This observation is in agreement with the results from our XPS, Raman spectroscopy, and previous reports,[7,8] which suggest that upon adsorption of oxidized PCAT on iron oxide the organic molecules will be reduced by oxidizing the metal oxide substrate. This will lead to an increase in the electrical resistance of the iron oxide, and thus the current will decrease. On the other hand, the adsorption of reduced PCAT on iron oxide will result in the oxidation of PCAT and a slight reduction in the iron oxide, making it less electrically resistive. The reproducibility of this experiment was confirmed using a second fabricated device (Figure S18).

■ DISCUSSION

Although a majority of previous studies indicate that polyaniline coatings in their EB state are unable to protect steel against corrosion, some reports argue otherwise.[8,59] PANI EB consists of 50% electron donor groups (secondary amines) and 50% electron acceptor groups (imines). It has previously been shown that half-oxidized PANI coatings are unable to induce a change in the polarity of the CNT substrate.[60] Despite the possibility of charge transfer to the substrate (e.g., native oxide on steel), because of its equal number of amine and imine groups the total net of the transferred charge at the interface is equal to zero. Therefore, a PANI EB coating is not able to change the potential of the underlying steel substrate and is not able to provide the overpotential necessary to form a passive iron oxide barrier layer. Our results showed that whereas an exact amount of oxidizing agent was employed for the preparation of PCAT EB, the result was not the half-oxidized state (Figure 1b). To the best of our knowledge, all of the synthesis routes for the preparation of PANI and its oligomers lead to the LB state.[14,61,62] The lack of control over the chemical oxidation process during the preparation of the EB state leads to deviations from the structure consisting of exact 50% amine and 50% imine groups. Therefore, it is believed that the discrepancy in the results from the corrosion inhibition involving EB is related to the challenges associated with the preparation of the exact half-oxidized state of redox-active organic compounds. Our results indicate that under ambient conditions PCAT EB will be further oxidized on the surface of iron oxide (Figures 7a and 8a). This also provides another explanation for the previous reports on the ineffectiveness of EB in the corrosion inhibition of steel.[63,64] Instead, we have shown that for the less-studied base state of redox-active oligoanilines, PB can withdraw electrons from the iron oxide substrate (Scheme 2f). All nitrogen atoms in the fully oxidized PCAT are in the sp^2-hybridized imine form. Charge transfer from the steel substrate to the electron-accepting imine groups leads to the formation of a passive iron oxide film, whereas the PB film will be reduced to the lower oxidation states (Figure 7b). Because the base states of PCAT are not conductive, only the few first monolayers at the interface with the metal oxide will participate in the charge transfer. Therefore, a thin redox-active coating can be sufficient for the application in corrosion inhibition. Thus, to assess the success of a redox-active coating in corrosion inhibition, one has to consider the extent of charge transfer at the interface.

XPS has proven to be one of the most useful analytical tools for surface and interface studies. However, its limitation to the surface layers limits its use in studying the buried interfaces involved in the corrosion protection of metal/metal oxides by redox-active organic compounds. Most of the fabricated organic coatings used in previous studies are too thick for XPS to allow access to the organic/oxide interface and have instead monitored the changes in the bulk of the top organic coatings.[8,65] To avoid this issue, other reports have tried to study the metal oxide film instead by either chemically removing the organic coatings prior to the introduction of the sample to the XPS analysis chamber or by in situ sputtering.[35,66] By removing the organic film, it was possible to study the surface of iron oxide surface, but it has been shown that sputtering of iron oxide can be destructive, causing the reduction of iron oxide.[22] To tackle this issue, the organic coating was kept on the surface and instead the bare side of the steel substrate was analyzed by XPS.[34] However, because of the limitation of XPS to top surface layers, the measured data was only a representative of the bulk of the oxide layer and not the oxide surface in contact with the top organic coating. This is an important issue considering the layered structure of iron oxide.

We have demonstrated that oligoanilines such as PCAT are suitable redox-active compounds for studying the corrosion inhibition mechanism. PCAT has three oxidation state similar to those in PANI but can be deposited in a well-defined fashion via vacuum deposition. This provides the possibility for the fabrication of thin organic films, enabling the study of the top organic coating, the underlying metal oxide, and their interface at the same time (Figures 4, 6, and 7). In addition, the thin organic film minimizes bulk contributions to the inhibition process. XPS data on the interface between PB and iron oxide showed the expected reduction of the organic phase. In addition, it showed the appearance of charged nitrogen species. The appearance of these structures is associated with charge transfer at the interface. Under ambient conditions, the fully reduced PCAT coating on the iron oxide surface was quickly oxidized. Although the effect of ambient conditions in this oxidation process was previously suggested, we have observed the oxidization when the experiment was performed under high vacuum (Figure 6d). Even though the rate of oxidation was noticeably slower, it proved the contribution of the surface to this process. Although our XPS results showed that the changes in the organic coating fabricated on the metal oxide surface can be used as a gauge to indirectly monitor the changes in the underlying metal oxide, we were unable to observe such changes directly via XPS (Figure 10c). Therefore, we have used an alternative method to directly characterize these changes induced by a redox-active coating. For this purpose, changes in the resistivity of an ultrathin film of iron oxide through dynamic exposure to fully reduced and fully oxidized oligoanilines were monitored (Figure 11c). Even though this measurement is unable to provide any information about the structure of the iron oxide film, it has demonstrated the charge transfer at this interface. The resistivity of the iron oxide film during exposure to fully oxidized oligoaniline will increase because of the removal of defects (Fe^{2+}) from the iron oxide thin film via oxidation by oligoanilines. The reverse effect was observed while exposing the iron oxide thin film to the fully reduced oligoaniline. This process is associated with the oxidation of the organic film by the iron oxide at the expense of the reduction of the oxide film.

Charge transfer between organic thin films and metal oxide films (or other substrates) is of relevance not only in corrosion protection but also in organic electronics,[3,5] sensor devices,[67,68] and photocatalysis.[69,70] Iron oxides (hematite in particular) have been studied for photocatalytic applications in water splitting for the hydrogen economy.[69,71−73] The tuning of dopant levels plays an important role in preparing suitable

hematite photocatalysts,[74] but so far doping has been seen as a static, irreversible process. Here we have shown that the doping of iron oxide (hematite) films can be adjusted in situ via the redox state of adsorbed organic molecules. These molecules function to stabilize the iron oxide films and modulate their electronic structure (doping level, conductivity) reversibly. Although the label of interfacial doping has been applied to situations where the dopants were initially introduced at the interface and then allowed to diffuse into the bulk,[75] that scenario does not lend itself to switchable doping. What we demonstrate here is a modulation of the electronic structure of a semiconductor strictly through interfacial effects.[76] The electrochemical notion of a shift in corrosion potential[1,7] is most compatible with the idea of redox potential doping (shift in band edge potentials regardless of charge-carrier transfer) rather than electronic doping.[77] Modifications to the band structure in the near-interface region (including but not limited to band bending) are commonly discussed in semiconductor physics,[76] but in nanoparticles and thin films, they can actually be considered to be a bulk phenomenon. Although indications of band structure modification (or maybe band bending) in the case of reduced PCAT on native iron oxide were found in an earlier study from our group,[15] our results presented here are indicative of actual charge transfer, i.e., electronic doping, although we have not attempted to elucidate possible changes in the iron oxide band structure. Ways of distinguishing these different cases have been proposed,[77] but further work will be required on the PCAT/hematite system. Both doping mechanisms result in desirable changes in the electronic structure for electronic devices, sensors, and (photo)catalysts. Of particular interest are configurations where the doping level can be externally controlled. Electric field switchable devices (a.k.a. field-effect transistors, FETs) and photoswitchable devices, e.g., based on azo-benzenes,[78] are well-known, but we can now add redox-switchable dopants to our toolbox.

■ CONCLUSIONS

We have demonstrated the effect of iron oxide surfaces on redox-active PCAT molecules and vice versa. High-resolution XPS measurements have shown the partial reduction of fully and partially oxidized PCAT molecules at the interface with hematite (1000) single-crystal surfaces. Partial oxidation of fully reduced PCAT on an iron oxide surface has been reported for the first time. In situ deposition and XPS spectroscopy of the thin films of PCAT LB on steel have confirmed that this oxidation is truly mediated by the iron oxide substrate and not only by ambient conditions. These conclusions were confirmed through the use of Raman spectroscopy under ambient conditions. However, because of air oxidation, the degree of oxidation of PCAT LB is higher than what is observed in vacuum. This confirms the previous theory of the role of redox-active organic compounds in their oxidized states as oxidizers of the native iron oxide film.[1,8] It also indicates the additional importance of air-exposed oxidation,[19] in addition to the role of hematite in the completion of the redox cycle.

To understand why an organic molecule could experience both reduction and oxidation at the interface of a transition-metal oxide, it is important to consider that PCAT, in its base form, has three main oxidation states. It is known that PCAT, in its half-oxidized form, is in its most stable state. Although PCAT EB can be found in both asymmetrical and symmetrical isomers, in regard to their quinoid ring position it has been shown that the symmetrical form is thermodynamically more stable than the asymmetrical form.[79,80] This means that fully reduced PCAT (LB) at the interface with iron oxide (Fe^{2+} or/and Fe^{3+}) will be oxidized in order to reach the equilibrium half-oxidized state (EB). On the other hand, fully oxidized PCAT (PB) at the same interface will experience partial reduction in order to reach the half-oxidized state (EB).

We also showed that the conversion of PCAT base to its salt form by exposure to HCl does not lead to a considerable change in the oxidation states of PCAT but causes a drastic increase in the number of cationic nitrogen structures. It was also found that the PB and EB forms of PCAT can be doped approximately twice as much as the LB form through gas-phase protonic doping.

An important feature in the N 1s XPS spectra is the appearance of charged nitrogen structures in all oxidation states of PCAT at the interface with hematite. This is indicative of interfacial charge transfer between hematite and PCAT, which increases with the degree of oxidation of PCAT. Consistent with previous reports,[32,33] this interfacial charge transfer can be considered to be a mutual interfacial doping process between the organic and the metal oxide phases. Further evidence for this interpretation comes from the possibility to detect the oxidation and reduction of ultrathin films of iron oxide using conductivity measurements on the iron oxide films.

Because of the close interactions of the redox states of both PCAT and iron oxide, modifications of the PCAT layer through acid–base or redox reactions can easily be detected through conductivity measurements. This can be utilized in the design of chemical sensing devices based on inexpensive iron oxide films. Molecular switches are an old concept, but practical examples of the facile detection of their state with a thin film sensor are less common. The facile doping and dedoping of iron oxide films in contact with different PCAT oxidation states is an example of interfacial doping with a switchable dopant, i.e., a molecular switch. The idea that a small local change in carrier concentration (in this case, due to a modification of the doping state) results in a large change in resistivity is somewhat reminiscent of (but not identical to) a chemical field-effect transistor (in which case the electric field is modulated by the creation of electric charges) in that it also constitutes an active sensor. In addition to applications in sensors, PCAT can also find use in the stabilization of iron oxide nanoparticles[81] for biomedical applications, smart coatings (anticorrosion, controlled release),[82,83] switchable membranes, and controlled adsorption.[84] PCAT and iron oxide form a fine-tuned system because of the alignment of the energy levels, but similar interactions could also apply to other surfaces if suitable ring substitutions for energy-level alignment are made. Although PCAT is a good model system by itself, polyaniline or other oligoanilines could be modified to also benefit from these interactions with iron oxide surfaces.

■ ASSOCIATED CONTENT

Supporting Information

The Supporting Information is available free of charge on the ACS Publications website at DOI: 10.1021/acs.jpcc.6b09950.

Additional data (mass spectrometry, UV–vis spectra, AFM, SEM, XPS spectra, and Raman spectroscopy) (PDF)

AUTHOR INFORMATION

Corresponding Author

*E-mail: pkruse@mcmaster.ca. Phone: (905) 525-9140 ext 23480. Fax: (905) 522-2509.

ORCID

Peter Kruse: 0000-0003-4051-4375

Notes

The authors declare no competing financial interest.

ACKNOWLEDGMENTS

We acknowledge technical assistance from and helpful discussions with P. Ravi Salvaganapathy, Andrew Broomfield, Steven A. Kornic, Kirk Green, James Britten, Jim Garrett, Leah Allan, Karen Neumann, Victoria Jarvis, and Enamul Hoque at McMaster University. Financial support was provided by the National Science and Engineering Research Council of Canada through the Discovery Grant program.

REFERENCES

(1) Rohwerder, M. Conducting Polymers for Corrosion Protection: A Review. *Int. J. Mater. Res.* **2009**, *100*, 1331−1342.

(2) Li, J.; Bao, Q.-Y.; Wei, H.-X.; Xu, Z.-Q.; Yang, J.-P.; Li, Y.-Q.; Lee, S.-T.; Tang, J.-X. Role of Transition Metal Oxides in the Charge Recombination Layer Used in Tandem Organic Photovoltaic Cells. *J. Mater. Chem.* **2012**, *22*, 6285−6290.

(3) Kim, S. Y.; Baik, J. M.; Yu, H. K.; Lee, J.-L. Highly Efficient Organic Light-Emitting Diodes with Hole Injection Layer of Transition Metal Oxides. *J. Appl. Phys.* **2005**, *98*, 093707.

(4) Chu, C.-W.; Li, S.-H.; Chen, C.-W.; Shrotriya, V.; Yang, Y. High-Performance Organic Thin-Film Transistors with Metal Oxide/Metal Bilayer Electrode. *Appl. Phys. Lett.* **2005**, *87*, 193508.

(5) Greiner, M. T.; Helander, M. G.; Tang, W. M.; Wang, Z. B.; Qiu, J.; Lu, Z. H. Universal Energy-Level Alignment of Molecules on Metal Oxides. *Nat. Mater.* **2011**, *11*, 76−81.

(6) DeBerry, D. W. Modification of the Electrochemical and Corrosion Behavior of Stainless Steels with an Electroactive Coating. *J. Electrochem. Soc.* **1985**, *132*, 1022−1026.

(7) Wessling, B. Passivation of Metals by Coating with Polyaniline: Corrosion Potential Shift and Morphological Changes. *Adv. Mater.* **1994**, *6*, 226−228.

(8) Beard, B. C.; Spellane, P. XPS Evidence of Redox Chemistry between Cold Rolled Steel and Polyaniline. *Chem. Mater.* **1997**, *9*, 1949−1953.

(9) Rohwerder, M.; Isik-Uppenkamp, S.; Amarnath, C. A. Application of the Kelvin Probe Method for Screening the Interfacial Reactivity of Conducting Polymer Based Coatings for Corrosion Protection. *Electrochim. Acta* **2011**, *56*, 1889−1893.

(10) Michalik, A.; Rohwerder, M. Conducting Polymers for Corrosion Protection: A Critical View. *Z. Phys. Chem.* **2005**, *219*, 1547−1559.

(11) Wei, Y.; Jamasbi, H.; Cheng, S.; Jansen, S. A.; Sein, L. T.; Zhang, W.; Wang, C. Corrosion Protection Properties of Coating of the Epoxy-Cured Aniline Oligomers Based on Salt Spray and UV-Salt Fog Cyclic Tests. *ASC symp. Ser.* **2003**, *843*, 208−227.

(12) Brown, B. P.; Picco, L.; Miles, M. J.; Faul, C. F. J. Conductive-AFM Patterning of Organic Semiconductors. *Small* **2015**, *11*, 5054−5058.

(13) Zhang, W.; Yu, Y.; Chen, L.; Mao, H.; Wang, C.; Wei, Y. Synthesis and Study of Phenyl-Capped Tetraaniline as an Anti-corrosion Additive. *ACS Symp. Ser.* **2003**, *843*, 156−165.

(14) Wang, W.; MacDiarmid, A. G. New Synthesis of Phenyl/phenyl End-Capped Tetraaniline in the Leucoemeraldine and Emeraldine Oxidation States. *Synth. Met.* **2002**, *129*, 199−205.

(15) Greiner, M. T.; Festin, M.; Kruse, P. Investigation of Corrosion-Inhibiting Aniline Oligomer Thin Films on Iron Using Photoelectron Spectroscopy. *J. Phys. Chem. C* **2008**, *112*, 18991−19004.

(16) Thomas, J. O.; Andrade, H. D.; Mills, B. M.; Fox, N. A.; Hoerber, H. J. K.; Faul, C. F. J. Imaging the Predicted Isomerism of Oligo(Aniline)s: A Scanning Tunneling Microscopy Study. *Small* **2015**, *11*, 3430−3434.

(17) Kruger, J.; Yolken, H. T. Room Temperature Oxidation of Iron at Low Pressures. *Corrosion* **1964**, *20*, 29t−33t.

(18) Kraljić, M.; Mandić, Z.; Duić, L. Inhibition of Steel Corrosion by Polyaniline Coatings. *Corros. Sci.* **2003**, *45*, 181−198.

(19) Kinlen, P. J.; Silverman, D. C.; Jeffreys, C. R. Corrosion Protection Using Polyaniline Coating Formulations. *Synth. Met.* **1997**, *85*, 1327−1332.

(20) Zhong, L.; Zhu, H.; Hu, J.; Xiao, S.; Gan, F. A Passivation Mechanism of Doped Polyaniline on 410 Stainless Steel in Deaerated H_2SO_4 Solution. *Electrochim. Acta* **2006**, *51*, 5494−5501.

(21) Grosvenor, A. P.; Kobe, B. A.; McIntyre, N. S. Activation Energies for the Oxidation of Iron by Oxygen Gas and Water Vapour. *Surf. Sci.* **2005**, *574*, 317−321.

(22) Biesinger, M. C.; Payne, B. P.; Grosvenor, A. P.; Lau, L. W. M.; Gerson, A. R.; Smart, R. S. C. Resolving Surface Chemical States in XPS Analysis of First Row Transition Metals, Oxides and Hydroxides: Cr, Mn, Fe, Co and Ni. *Appl. Surf. Sci.* **2011**, *257*, 2717−2730.

(23) Fairley, N. *CasaXPS*, Revision 2.3.17; Casa Software Ltd: Teignmouth, Devon, U.K., 2016.

(24) Moonoosawmy, K. R.; Kruse, P. Ambiguity in the Characterization of Chemically Modified Single-Walled Carbon Nanotubes: A Raman and Ultraviolet-Visible-Near-Infrared Study. *J. Phys. Chem. C* **2009**, *113*, 5133−5140.

(25) Nečas, D.; Klapetek, P. Gwyddion: An Open-Source Software for SPM Data Analysis. *Open Phys.* **2012**, *10*, 181−188.

(26) Wang, Y.; Torres, J. A.; Stieg, A. Z.; Jiang, S.; Yeung, M. T.; Rubin, Y.; Chaudhuri, S.; Duan, X.; Kaner, R. B.; Al, W. E. T. Graphene-Assisted Solution Growth of Vertically Oriented Organic Semiconducting Single Crystals. *ACS Nano* **2015**, *9*, 9486−9496.

(27) Poncet, M.; Corraze, B.; Quillard, S.; Wang, W.; Macdiarmid, A. G. Elaboration and Characterizations of Oligoaniline Thin Films. *Thin Solid Films* **2004**, *458*, 32−36.

(28) Kang, E. T.; Neoh, K. G.; Tan, K. L. The Intrinsic Redox States in Polypyrrole and Polyaniline: A Comparative Study by XPS. *Surf. Interface Anal.* **1992**, *19*, 33−37.

(29) Chen, Y.; Kang, E. T.; Neoh, K. G.; Lim, S. L.; Ma, Z. H.; Tan, K. L. Intrinsic Redox States of Polyaniline Studied by High-Resolution X-Ray Photoelectron Spectroscopy. *Colloid Polym. Sci.* **2001**, *279*, 73−76.

(30) Heeger, A. J. Semiconducting and Metallic Polymers: The Fourth Generation of Polymeric Materials (Nobel Lecture). *Angew. Chem., Int. Ed.* **2001**, *40*, 2591−2611.

(31) Yue, J.; Epstein, A. J. Xps Study of Self-Doped Conducting Polyaniline and Parent Systems. *Macromolecules* **1991**, *24*, 4441−4445.

(32) Bai, S.; Zhao, Y.; Sun, J.; Tian, Y.; Luo, R.; Li, D.; Chen, A. Ultrasensitive Room Temperature NH_3 Sensor Based on Graphene-Polyaniline Hybrid Loading on PET Thin Film. *Chem. Commun.* **2015**, *51*, 7524−7527.

(33) Xu, D.; Xu, Q.; Wang, K.; Chen, J.; Chen, Z. Fabrication of Free-Standing Hierarchical Carbon Nanofiber/graphene Oxide/polyaniline Films for Supercapacitors. *ACS Appl. Mater. Interfaces* **2014**, *6*, 200−209.

(34) Fahlman, M.; Jasty, S.; Epstein, A. J. Corrosion Protection of Iron/Steel by Emeraldine Base Polyaniline: An X-Ray Photoelectron Spectroscopy Study. *Synth. Met.* **1997**, *85*, 1323−1326.

(35) Talo, A.; Passiniemi, P.; Forsén, O.; Yläsaari, S. Polyaniline/Epoxy Coatings with Good Anti-Corrosion Properties. *Synth. Met.* **1997**, *85*, 1333−1334.

(36) Zheng, W.; Angelopoulos, M.; Epstein, A. J.; MacDiarmid, A. G. Experimental Evidence for Hydrogen Bonding in Polyaniline: Mechanism of Aggregate Formation and Dependency on Oxidation State. *Macromolecules* **1997**, *30*, 2953−2955.

(37) Jones, F.; Rohl, A. L.; Farrow, J. B.; van Bronswijk, W. Molecular Modeling of Water Adsorption on Hematite. *Phys. Chem. Chem. Phys.* **2000**, *2*, 3209−3216.

(38) Leist, U.; Ranke, W.; Al-Shamery, K. Water Adsorption and Growth of Ice on Epitaxial $Fe_3O_4(111)$, FeO(111) and Fe_2O_3(biphase). *Phys. Chem. Chem. Phys.* **2003**, *5*, 2435−2441.
(39) Joseph, Y.; Ranke, W.; Weiss, W. Water on FeO (111) and Fe_3O_4 (111): Adsorption Behavior on Different Surface Terminations. *J. Phys. Chem. B* **2000**, *104*, 3224−3236.
(40) Baer, D. R.; Engelhard, M. H.; Lea, A. S. Introduction to Surface Science Spectra Data on Electron and X-Ray Damage: Sample Degradation during XPS and AES Measurements. *Surf. Sci. Spectra* **2005**, *10*, 47−56.
(41) Heister, K.; Zharnikov, M.; Grunze, M.; Johansson, L. S. O.; Ulman, A. Characterization of X-Ray Induced Damage in Alkanethiolate Monolayers by High-Resolution Photoelectron Spectroscopy. *Langmuir* **2001**, *17*, 8−11.
(42) Kinlen, P. J.; Menon, V.; Ding, Y. A Mechanistic Investigation of Polyaniline Corrosion Protection Using the Scanning Reference Electrode Technique. *J. Electrochem. Soc.* **1999**, *146*, 3690−3695.
(43) Heller, D. A.; Barone, P. W.; Swanson, J. P.; Mayrhofer, R. M.; Strano, M. S. Using Raman Spectroscopy to Elucidate the Aggregation State of Single-Walled Carbon Nanotubes Using Raman Spectroscopy to Elucidate the Aggregation State of Single-Walled Carbon Nanotubes. *J. Phys. Chem. B* **2004**, *108*, 6905−6909.
(44) Boyer, M.-I.; Quillard, S.; Rebourt, E.; Louarn, G.; Buisson, J. P.; Monkman, A.; Lefrant, S. Vibrational Analysis of Polyaniline: A Model Compound Approach. *J. Phys. Chem. B* **1998**, *102*, 7382−7392.
(45) Lindfors, T.; Kvarnström, C.; Ivaska, A. Raman and UV-Vis Spectroscopic Study of Polyaniline Membranes Containing a Bulky Cationic Additive. *J. Electroanal. Chem.* **2002**, *518*, 131−138.
(46) Kinlen, P. J.; Ding, Y.; Silverman, D. G. Corrosion Protection of Mild Steel Using Sulfonic and Phosphonic Acid-Doped Polyanilines. *Corrosion* **2002**, *58*, 490−497.
(47) Li, P.; Tan, T. C.; Lee, J. Corrosion Protection of Mild Steel by Electroactive Polyaniline Coatings. *Synth. Met.* **1997**, *88*, 237−242.
(48) Sathiyanarayanan, S.; Muthukrishnan, S.; Venkatachari, G.; Trivedi, D. C. Corrosion Protection of Steel by Polyaniline (PANI) Pigmented Paint Coating. *Prog. Org. Coat.* **2005**, *53*, 297−301.
(49) Armelin, E.; Meneguzzi, A.; Ferreira, C. A.; Alemán, C. Polyaniline, Polypyrrole and poly(3,4-Ethylenedioxythiophene) as Additives of Organic Coatings to Prevent Corrosion. *Surf. Coat. Technol.* **2009**, *203*, 3763−3769.
(50) Meroufel, A.; Deslouis, C.; Touzain, S. Electrochemical and Anticorrosion Performances of Zinc-Rich and Polyaniline Powder Coatings. *Electrochim. Acta* **2008**, *53*, 2331−2338.
(51) Paliwoda-Porebska, G.; Rohwerder, M.; Stratmann, M.; Rammelt, U.; Duc, L. M.; Plieth, W. Release Mechanism of Electrodeposited Polypyrrole Doped with Corrosion Inhibitor Anions. *J. Solid State Electrochem.* **2006**, *10*, 730−736.
(52) Holness, R. J.; Williams, G.; Worsley, D. A.; McMurray, H. N. Polyaniline Inhibition of Corrosion-Driven Organic Coating Cathodic Delamination on Iron. *J. Electrochem. Soc.* **2005**, *152*, B73−B81.
(53) Aldissi, M.; Armes, S. P. X-Ray Photoelectron Spectroscopy Study of Bulk and Colloidal Polyaniline. *Macromolecules* **1992**, *25*, 2963−2968.
(54) Xue, M.; Wang, S.; Wu, K.; Guo, J.; Guo, Q. Surface Structural Evolution in Iron Oxide Thin Films. *Langmuir* **2011**, *27*, 11−14.
(55) Weiss, W.; Ranke, W. Surface Chemistry and Catalysis on Well-Defined Epitaxial Iron-Oxide Layers. *Prog. Surf. Sci.* **2002**, *70*, 1−151.
(56) Evain, M.; Quillard, S.; Corraze, B.; Wang, W.; MacDiarmid, A. G. A Phenyl-End-Capped Tetramer of Aniline. *Acta Crystallogr., Sect. E: Struct. Rep. Online* **2002**, *58*, o343−o344.
(57) Lemire, C.; Bertarione, S.; Zecchina, A.; Scarano, D.; Chaka, A.; Shaikhutdinov, S.; Freund, H. J. Ferryl (Fe═O) Termination of the Hematite α-Fe_2O_3(0001) Surface. *Phys. Rev. Lett.* **2005**, *94*, 166101.
(58) Tang, Y.; Qin, H.; Wu, K.; Guo, Q.; Guo, J. The Reduction and Oxidation of Fe_2O_3(0001) Surface Investigated by Scanning Tunneling Microscopy. *Surf. Sci.* **2013**, *609*, 67−72.
(59) Spinks, G. M.; Dominis, A. J.; Wallace, G. G.; Tallman, D. E. Electroactive Conducting Polymers for Corrosion Control: Part 2. Ferrous Metals. *J. Solid State Electrochem.* **2002**, *6*, 85−100.
(60) Klinke, C.; Chen, J.; Afzali, A.; Avouris, P. Charge Transfer Induced Polarity Switching in Carbon Nanotube Transistors. *Nano Lett.* **2005**, *5*, 555−558.
(61) Sun, Z. C.; Jing, X. B.; Wang, X. H.; Li, J.; Wang, F. S. Synthesis and Characterisation of Phenyl-Capped Oligoanilines. *Synth. Met.* **2001**, *119*, 399−400.
(62) Lu, F. L.; Wudl, F.; Nowak, M.; Heeger, A. J. Phenyl-Capped Octaaniline (COA): An Excellent Model for Polyaniline. *J. Am. Chem. Soc.* **1986**, *108*, 8311−8313.
(63) Williams, G.; Gabriel, A.; Cook, A.; McMurray, H. N. Dopant Effects in Polyaniline Inhibition of Corrosion-Driven Organic Coating Cathodic Delamination on Iron. *J. Electrochem. Soc.* **2006**, *153*, B425−B433.
(64) Gabriel, A.; Laycock, N. J.; Mcmurray, H. N.; Williams, G.; Cook, A. Oxidation States Exhibited by In-Coating Polyaniline during Corrosion-Driven Coating Delamination on Carbon Steel. *Electrochem. Solid-State Lett.* **2006**, *9*, B57−B60.
(65) Affrossman, S.; Comrie, R. F.; MacDonald, S. M. Interaction of a Model Epoxy Resin Compound, Diethanolamine, with Aluminium Surfaces Studied by Static SIMS and XPS. *J. Chem. Soc., Faraday Trans.* **1998**, *94*, 289−294.
(66) Virtanen, S.; Moser, E. M.; Böhni, H. XPS Studies on Passive Films on Amorphous Fe-Cr-(B,P)-C Alloys. *Corros. Sci.* **1994**, *36*, 373−384.
(67) Capone, S.; Manera, M. G.; Taurino, A.; Siciliano, P.; Rella, R.; Luby, S.; Benkovicova, M.; Siffalovic, P.; Majkova, E. Fe_3O_4/γ-Fe_2O_3 Nanoparticle Multilayers Deposited by the Langmuir-Blodgett Technique for Gas Sensor Application. *Langmuir* **2014**, *30*, 1190−1197.
(68) Hsu, L. H. H.; Hoque, E.; Kruse, P.; Ravi Selvaganapathy, P. A Carbon Nanotube Based Resettable Sensor for Measuring Free Chlorine in Drinking Water. *Appl. Phys. Lett.* **2015**, *106*, 063102.
(69) Liu, Y.; Yu, Y.-X.; Zhang, W.-D. Photoelectrochemical Properties of Ni-Doped Fe_2O_3 Thin Films Prepared by Electrodeposition. *Electrochim. Acta* **2012**, *59*, 121−127.
(70) Zhang, Y.; Cao, Y.; Wang, C.; Gao, J.; Xie, T.; Bai, Y. Study of Charge Transition Between Interfaces of Hetero-Structured Assemblies Based on Phenyl-Capped Aniline Tetramer/n(p)-Silicon. *J. Photochem. Photobiol., A* **2001**, *139*, 175−179.
(71) Chatman, S.; Pearce, C. I.; Rosso, K. M. Charge Transport at Ti-Doped Hematite (001)/Aqueous Interfaces. *Chem. Mater.* **2015**, *27*, 1665−1673.
(72) Toroker, M. C. Theoretical Insights into the Mechanism of Water Oxidation on Nonstoichiometric and Titanium-Doped Fe_2O_3(0001). *J. Phys. Chem. C* **2014**, *118*, 23162−23167.
(73) Kumar, P.; Sharma, P.; Shrivastav, R.; Dass, S.; Satsangi, V. R. Electrodeposited Zirconium-Doped α-Fe_2O_3 Thin Film for Photoelectrochemical Water Splitting. *Int. J. Hydrogen Energy* **2011**, *36*, 2777−2784.
(74) Liao, P.; Toroker, M. C.; Carter, E. A. Electron Transport in Pure and Doped Hematite. *Nano Lett.* **2011**, *11*, 1775−1781.
(75) Ye, L.; Pujari, S. P.; Zuilhof, H.; Kudernac, T.; de Jong, M. P.; van der Wiel, W. G.; Huskens, J. Controlling the Dopant Dose in Silicon by Mixed-Monolayer Doping. *ACS Appl. Mater. Interfaces* **2015**, *7*, 3231−3236.
(76) Cahen, D.; Kahn, A. Electron Energetics at Surfaces and Interfaces: Concepts and Experiments. *Adv. Mater.* **2003**, *15*, 271−277.
(77) Schimpf, A. M.; Knowles, K. E.; Carroll, G. M.; Gamelin, D. R. Electronic Doping and Redox-Potential Tuning in Colloidal Semiconductor Nanocrystals. *Acc. Chem. Res.* **2015**, *48*, 1929−1937.
(78) Basuki, S. W.; Schneider, V.; Strunskus, T.; Elbahri, M.; Faupel, F. Light-Controlled Conductance Switching in Azobenzene-Containing MWCNT-Polymer Nanocomposites. *ACS Appl. Mater. Interfaces* **2015**, *7*, 11257−11262.
(79) Yanagida, S.; Manseki, K.; Segawa, H. Theoretical Evaluation of Electron Transport in Aniline Tetramer-Based Dye-Sensitized Solar Cells. *Electrochim. Acta* **2015**, *179*, 169−173.
(80) Manseki, K.; Yu, Y.; Yanagida, S. A Phenyl-Capped Aniline Tetramer for Z907/tert-Butylpyridine-Based Dye-Sensitized Solar

Cells and Molecular Modelling of the Device. *Chem. Commun.* **2013**, *49*, 1416−1418.
(81) Wei, W.; Wang, G.; Yang, S.; Feng, X.; Müllen, K. Eficient Coupling of Nanoparticles to Electrochemically Exfloited Graphene. *J. Am. Chem. Soc.* **2015**, *137*, 5576−5581.
(82) LV, L.; Zhao, Y.; Vilbrandt, N.; Gallei, M.; Vimalanandan, A.; Rohwerder, M.; Landfester, K.; Crespy, D. Redox Responsive Release of Hydrophobic Self-Healing Agents from Polyaniline Capsules. *J. Am. Chem. Soc.* **2013**, *135*, 14198−14205.
(83) Vimalanandan, A.; Lv, L.; Tran, T.; Landfester, K.; Crespy, D.; Rohwerder, M. Redox-Responsive Self-Healing for Corrosion Protection. *Adv. Mater.* **2013**, *25*, 6980−6984.
(84) Small, L. J.; Wheeler, D. R.; Spoerke, E. D. Nanoporous Membranes with Electrochemically Switchable, Chemically Stabilized Ionic Selectivity. *Nanoscale* **2015**, *7*, 16909−16920.

Supporting Information for

Interfacial Charge Transfer Between Phenyl-capped Aniline Tetramer Films and Iron Oxide Surfaces.

Amirmasoud Mohtasebi,[1] Tanzina Chowdhury,[1] Leo H. H. Hsu,[2] Mark C. Biesinger,[3] Peter Kruse[1]*

[1]Department of Chemistry and Chemical Biology, McMaster University, 1280 Main Street West, Hamilton, Ontario, L8S 4M1, Canada

[2]Department of Mechanical Engineering, McMaster University, Hamilton L8S 4L8, Canada

[3]Surface Science Western, Room LL31, 999 Collip Circle, London, Ontario, N6G 0J3, Canada

Phenyl-capped aniline tetramer (PCAT) was synthesized and purified according to literature.[1] The as synthesized powder was characterized by high-resolution electrospray ionization mass spectrometry (Figure S1).

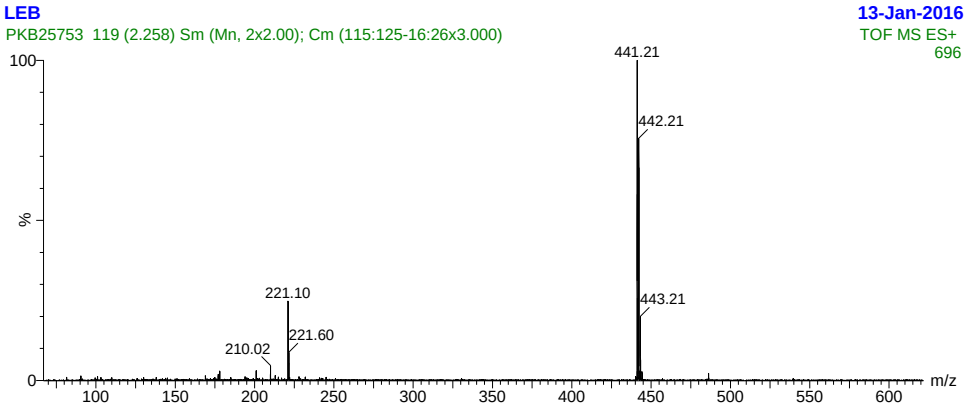

Figure S1. High-resolution electrospray ionization mass spectrometry of synthesized PCAT.

Each base form of PCAT was prepared using previously reported procedures[1] and characterized using Raman spectroscopy (Figure 6a, 9a, 9c) and UV-vis spectroscopy (Figure S2). The corresponding salt form of each base state was prepared by protonic doping using HCl. Figure S3 shows the UV-vis spectra of all the three salt forms of PCAT

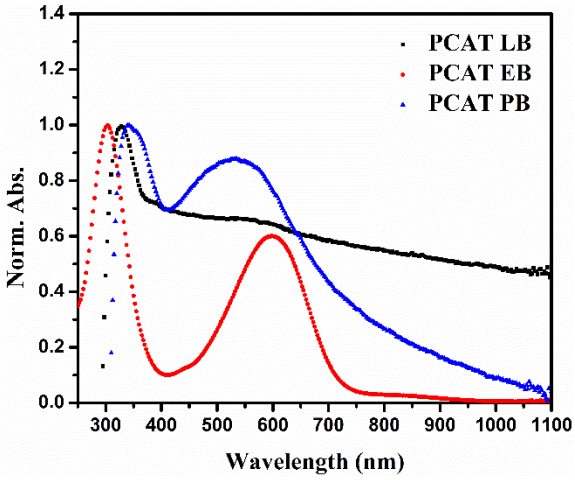

Figure S2. Normalized UV-Vis spectra of fully reduced PCAT base (LB), half-oxidized PCAT base (EB), fully oxidized PCAT base (PS).

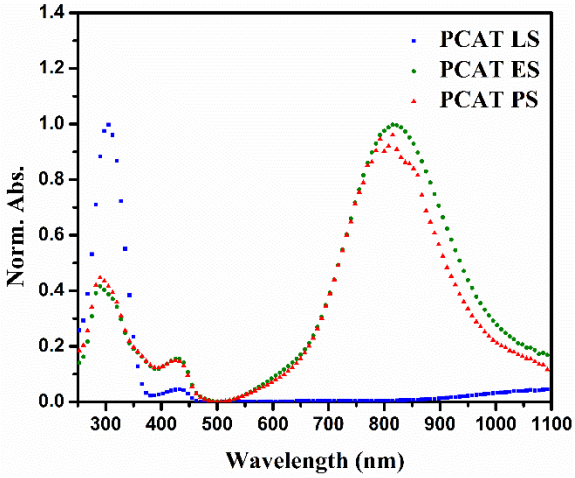

Figure S3. Normalized UV-Vis spectra of fully reduced PCAT salt (LS), half-oxidized PCAT salt (ES), and fully oxidized PCAT salt (PS).

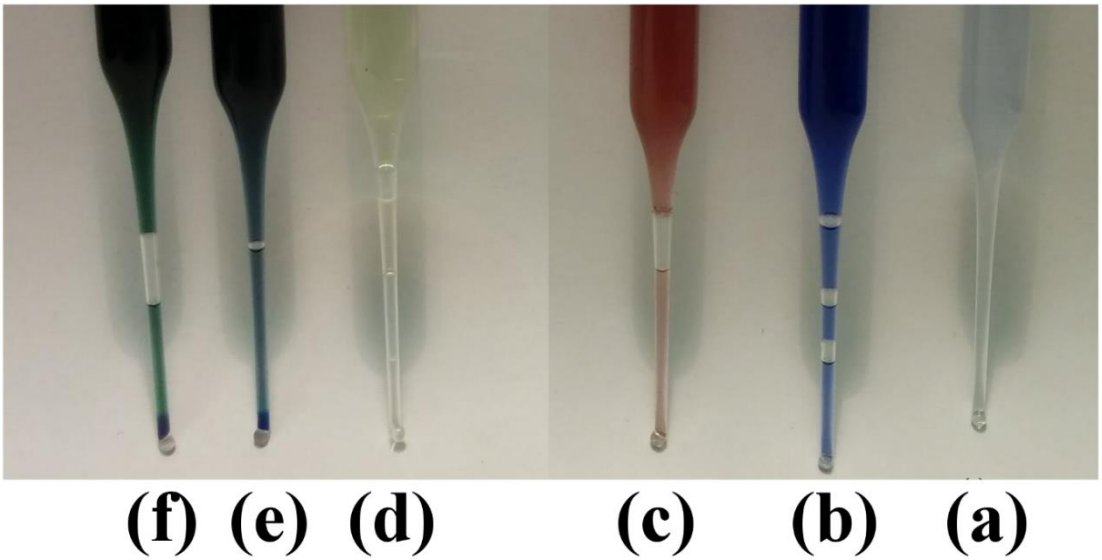

Figure S4. Color of methanolic solution of PCAT. (a) Fully reduced PCAT base, (b) half-oxidized PCAT base, (c) fully oxidized PCAT base, (d) fully reduced PCAT salt, (e) half-oxidized PCAT salt, and (f) fully oxidized PCAT salt.

The Raman spectrum of as-received particles (Figure S10a) shows the presence of intense peaks at 288 cm^{-1} (siderite), 371 cm^{-1} and 379 cm^{-1} (lepidocrocite), and 504 cm^{-1} (ferrihydrite) thus indicating that this sample consist of multiple phases of iron oxide and iron (oxy)hydroxide. This might be due to the storage of this sample for a long period of time in ambient conditions. After annealing this sample at 440 ºC for 14 hours, the Raman spectrum shows only the main hematite bands at 225, 245, 292, 409, 497, and 610 cm^{-1} (Figure S10b). [2,3] Scanning electron microscopy is used to confirm the monodispersity of these particles after the heat treatment (Figure S11).

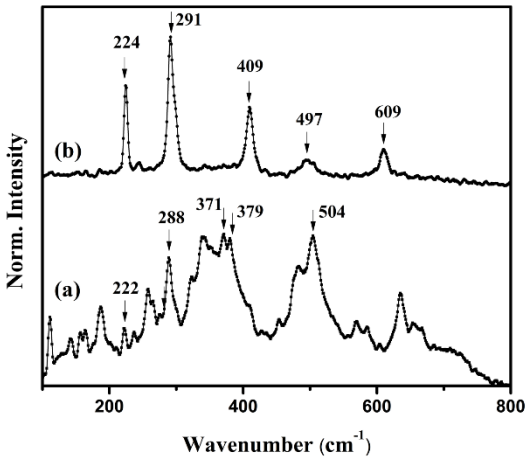

Figure S5. Raman spectra of iron oxide nanoparticle (a) as received, (b) annealed at 440ºC, showing hematite phase.

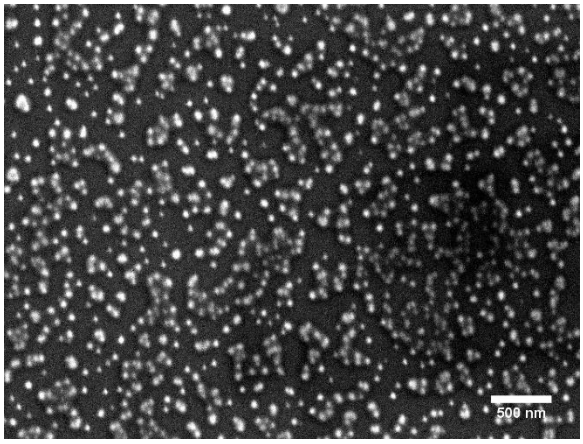

Figure S6. Scanning electron micrograph of hematite nanoparticles after annealing at 440ºC for 14 hours.

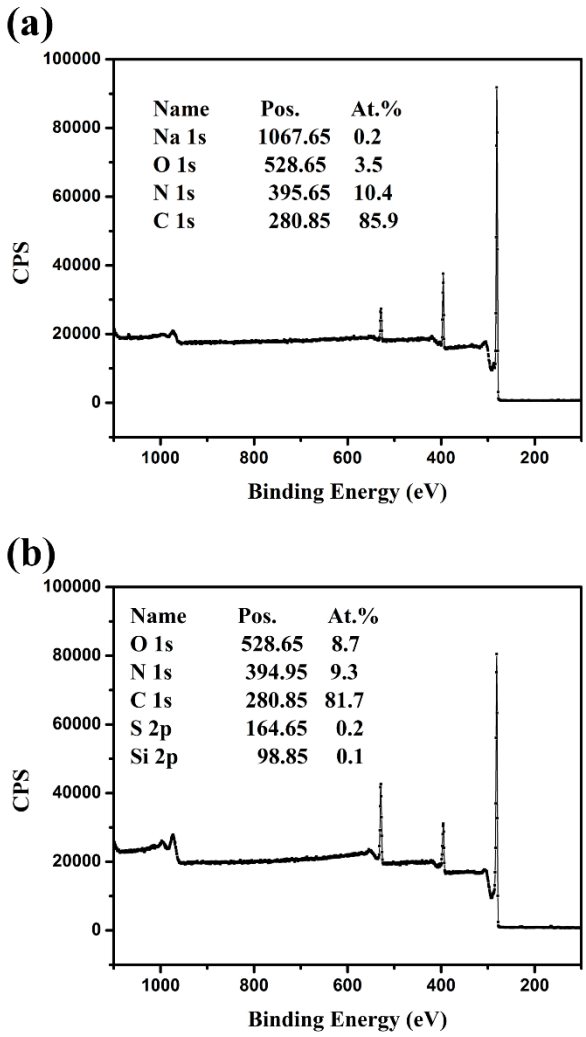

Figure S7. XPS survey spectra of (a) fully reduced PCAT base powder, (b) fully oxidized base PCAT powder.

Vacuum deposition of fully oxidized PCAT base on a hematite substrate at 25ºC leads to formation of two morphologies of islands: small globular islands and long sharp needle-shape islands.

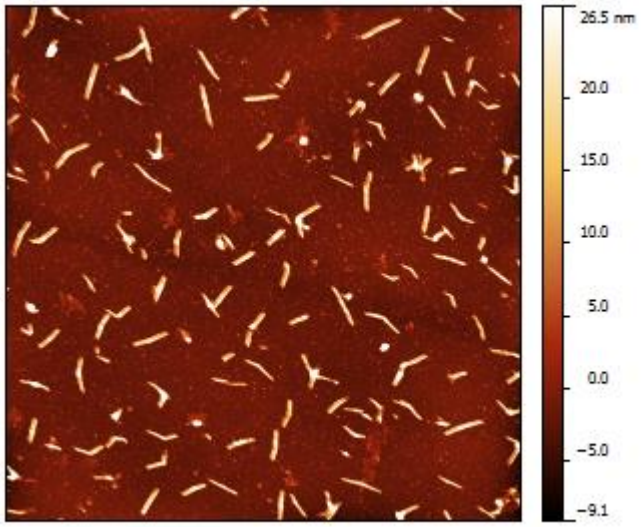

Figure S8. AFM of vacuum deposited fully oxidized PCAT base islands on hematite (1000) single crystal at 25ºC.

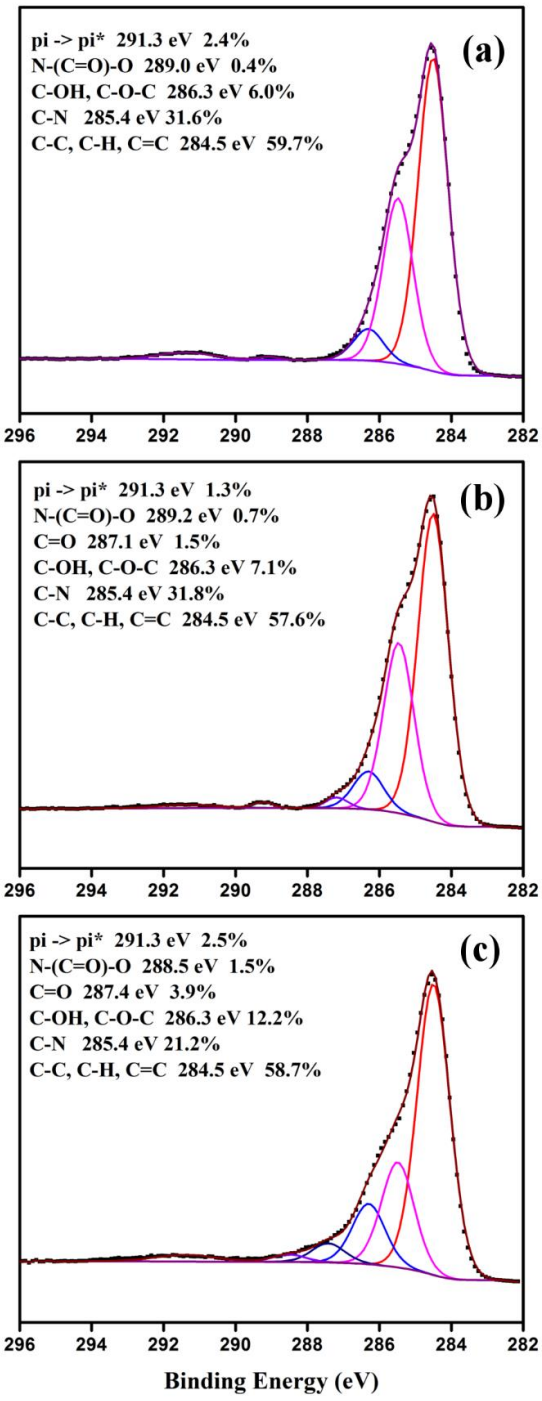

Figure S9. High-resolution C 1s XPS spectra of PCAT powders: (a) fully reduced PCAT base, (b) half-oxidized PCAT base, (c) fully oxidized PCAT base.

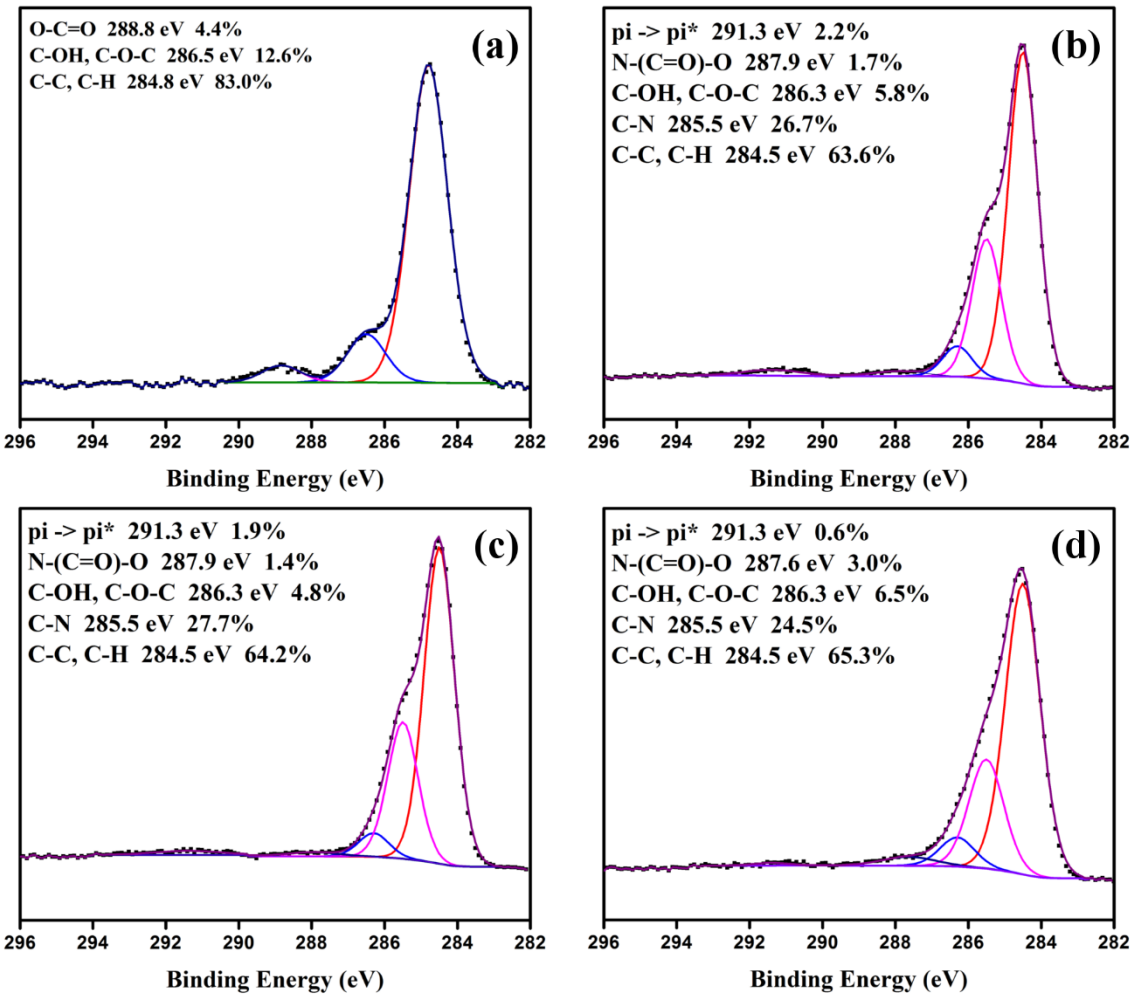

Figure S10. High-resolution C 1s XPS spectra of (a) a bare hematite single crystal prior to deposition of organic layers, (b) fully reduced PCAT base film deposited on hematite, (c) half-oxidized PCAT base film deposited on hematite, and (d) fully oxidized PCAT base film deposited on hematite.

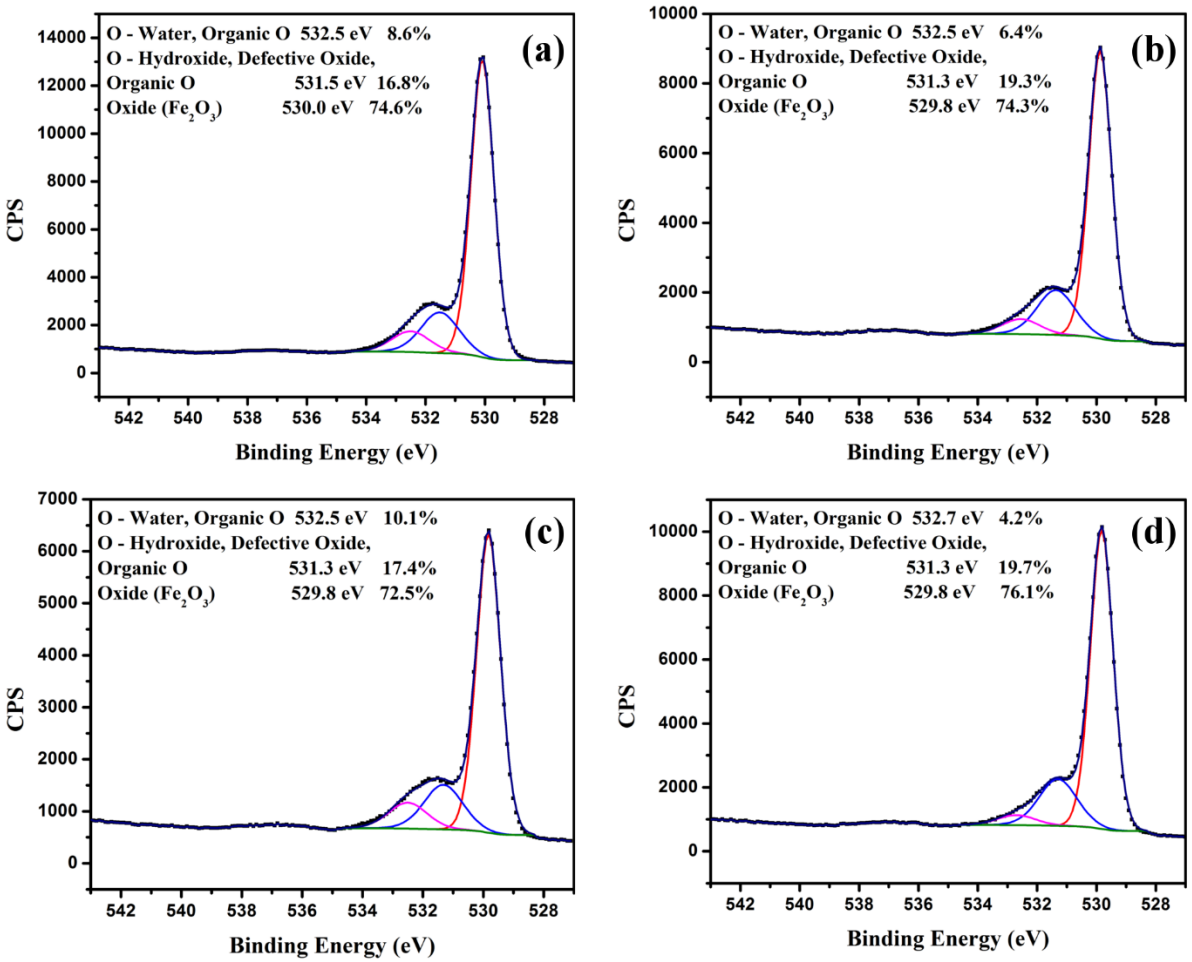

Figure S11. High-resolution O 1s XPS spectra of (a) a bare hematite (1000) surface, (b) fully reduced PCAT base on hematite (1000), (c) half-oxidized PCAT base on hematite (1000), (d) fully oxidized PCAT base on hematite (1000).

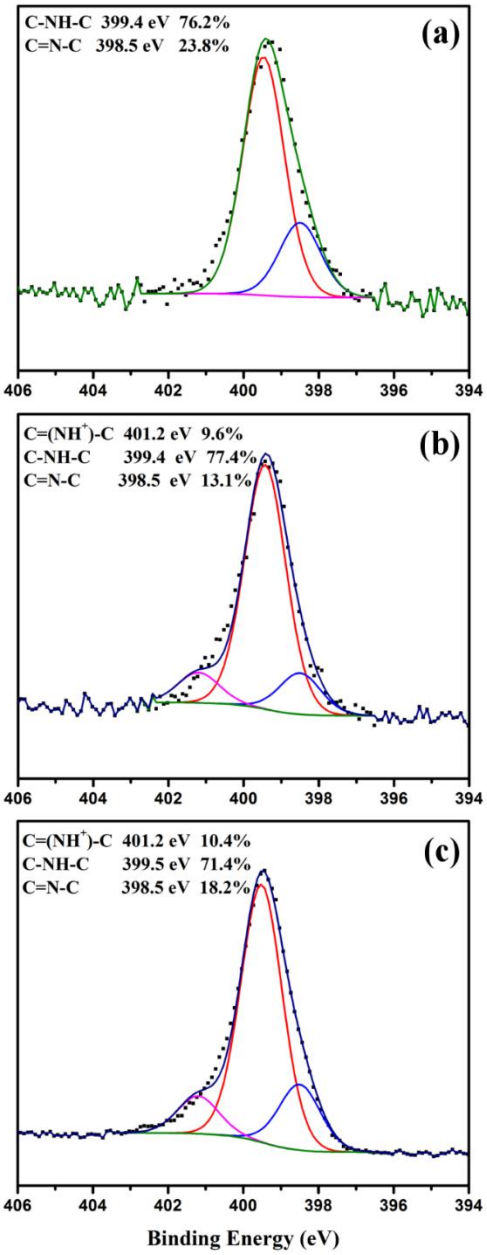

Figure S12. High-resolution N 1s XPS spectra of (a) fully reduced PCAT salt (LS) on glass, (b) half-oxidized PCAT salt (ES) on glass, and (c) fully oxidized PCAT salt (PS) on glass.

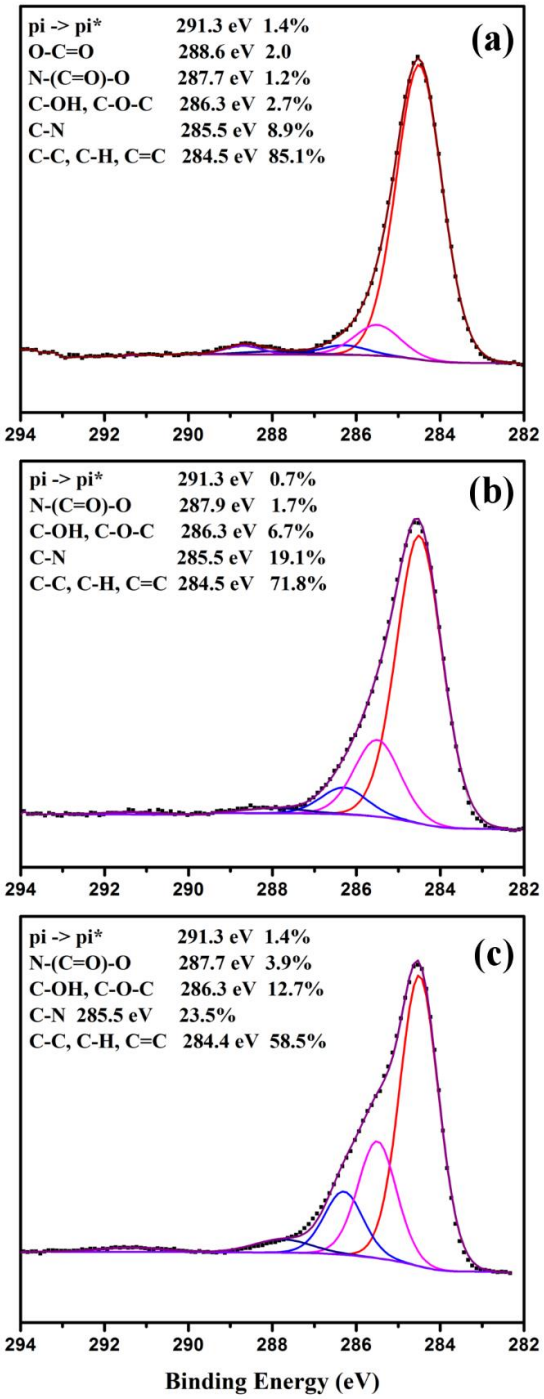

Figure S13. High-resolution C 1s XPS spectra of (a) fully reduced PCAT salt (LS) on glass, (b) half-oxidized PCAT salt (ES) on glass, and (c) fully oxidized PCAT salt (PS) on glass.

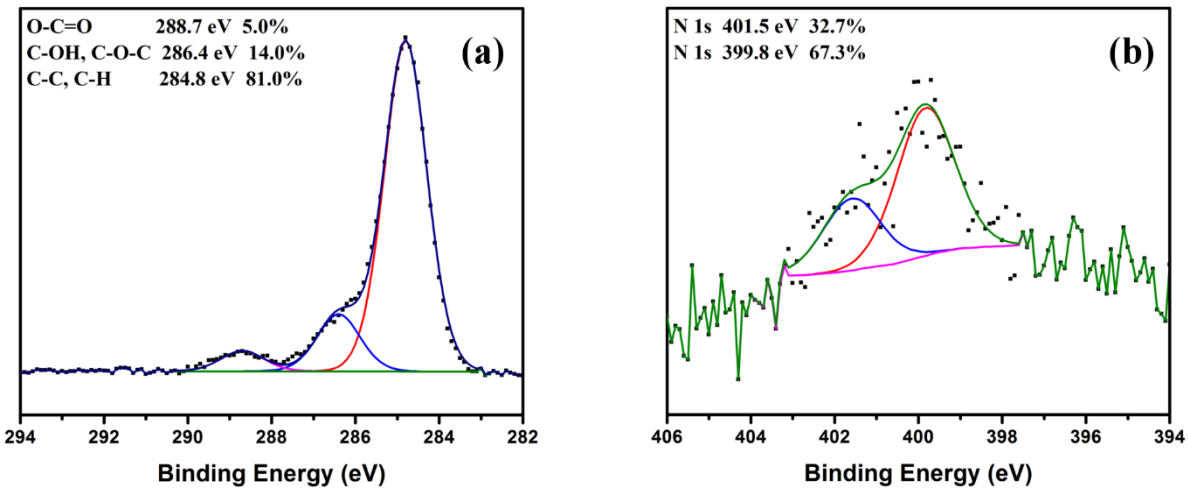

Figure S14. High-resolution (a) C 1s, and (b) N 1s XPS spectra of the bare hematite single crystal after exposure to HCl gas.

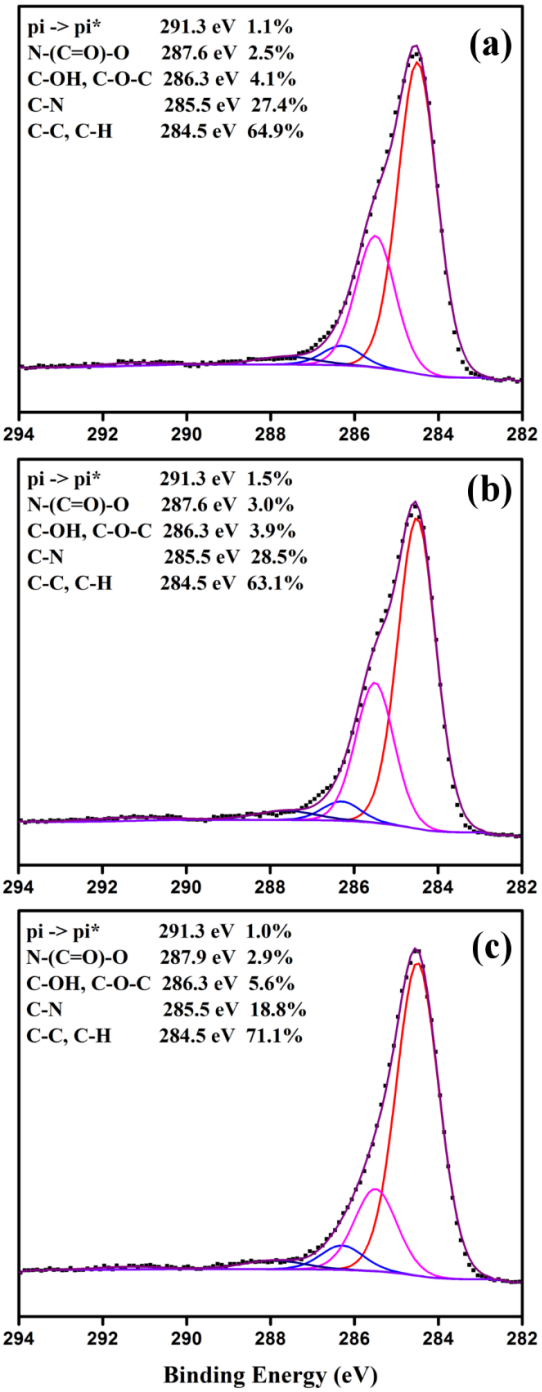

Figure S15. High-resolution C 1s XPS spectra of PCAT salt on hematite for (a) fully reduced, (b) half-oxidized, (c) fully oxidized forms.

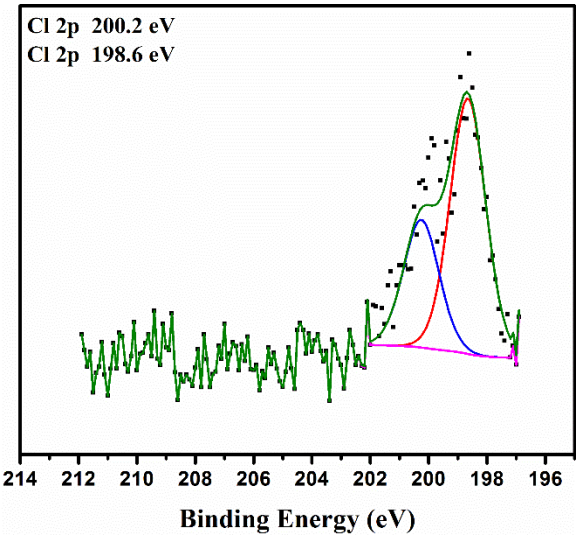

Figure S16. High-resolution Cl 2p XPS spectra of bare hematite single crystal exposed to HCl gas.

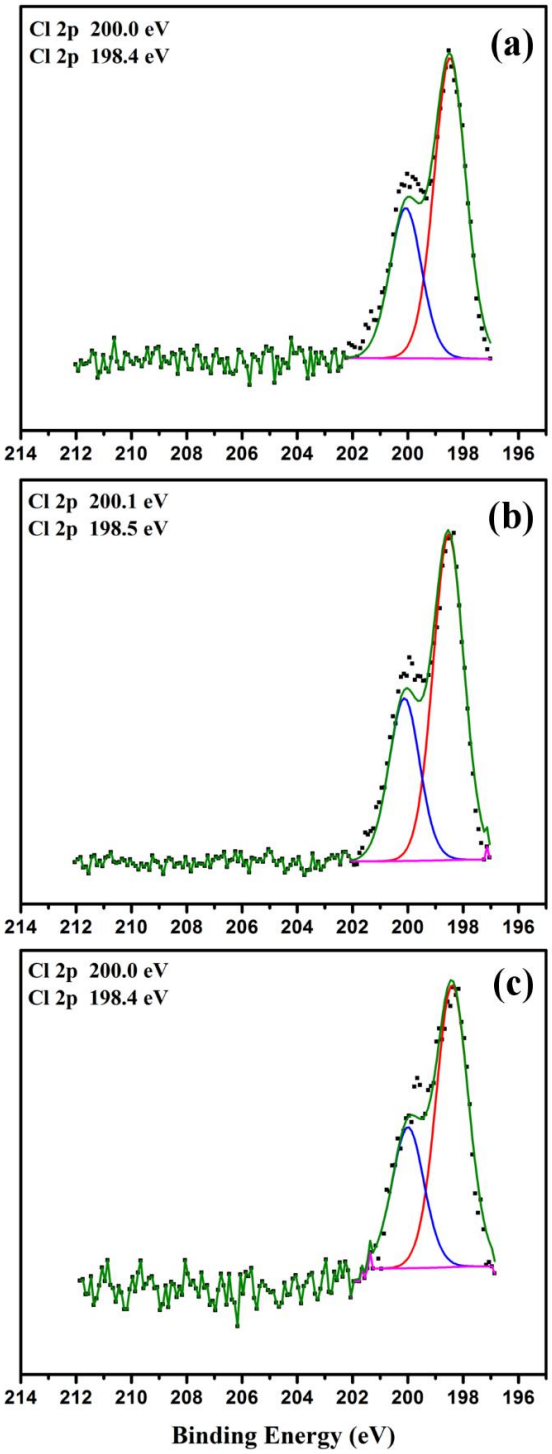

Figure S17. High-resolution Cl 2p XPS spectra of PCAT salt on hematite for (a) fully reduced, (b) half-oxidized, (c) fully oxidized forms.

A second microfluidic device consisting of interdigitated arrays of gold electrodes covered with a thin layer of iron oxide was prepared to verify the reproducibility of the experiment demonstrated in Figure 11. The same procedure described in the paper was repeated for the fabrication of the iron oxide thin film and the PDMS microfluidic device. The fabricated iron oxide film for this device had 14.2 nm thickness (measured by QCM). However, the film was not exposed to the vapor of hydrogen peroxide after the vacuum deposition. The higher defect density (Fe^{2+}) leads to higher conductivity of the film in comparison to the film used in the primary experiment. Nevertheless, it is still possible to see the increase in the measured current by exposing the iron oxide film to the fully reduced PCAT (LB) and decrease the measured conductivity by exposing the film to the fully oxidized PCAT (PB).

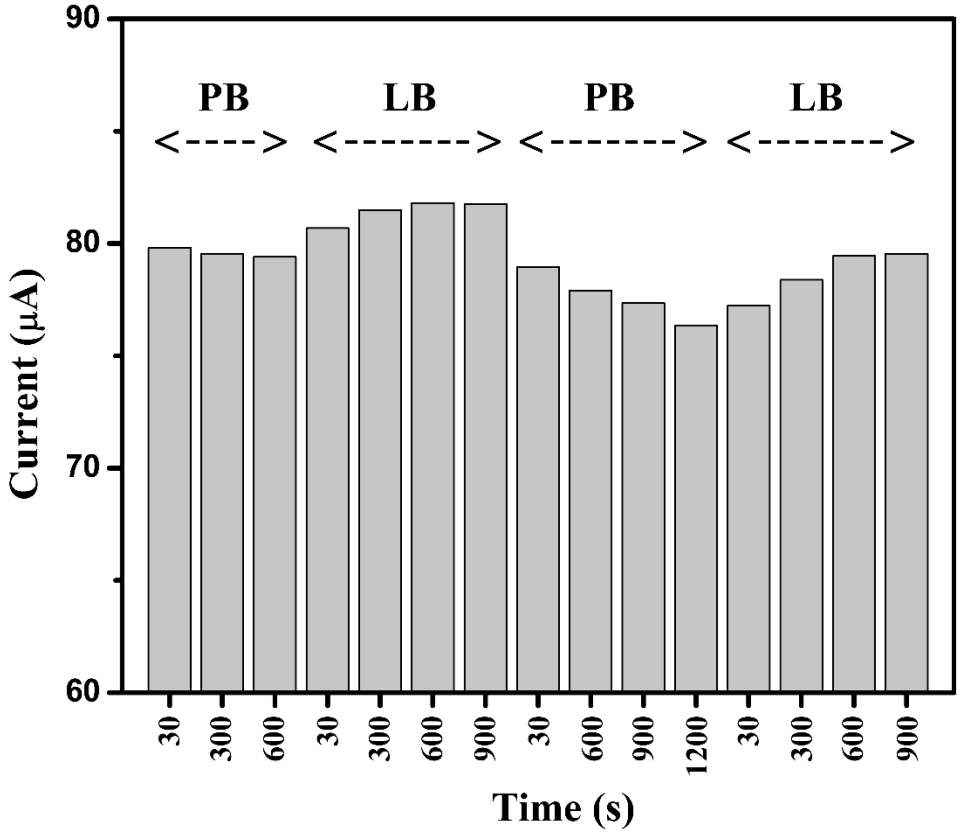

Figure S18. The plot of current as a function of time under allocation of constant bias voltage of 2.4 V to the iron oxide coated gold electrodes while PCAT LB in methanol, and PCAT PB in methanol in the microchannel for four consecutive measurements.

References

(1) Wang, W.; MacDiarmid, A. G. New Synthesis of Phenyl/phenyl End-Capped Tetraaniline in the Leucoemeraldine and Emeraldine Oxidation States. *Synth. Met.* **2002**, *129*, 199–205.

(2) Hanesch, M. Raman Spectroscopy of Iron Oxides and (oxy)hydroxides at Low Laser Power and Possible Applications in Environmental Magnetic Studies. *Geophys. J. Int.* **2009**, *177*, 941–948.

(3) de Faria, D. L. A.; Silva, S. V.; de Oliveira, M. T. Raman Microspectroscopy of Some Iron Oxides and Oxyhydroxides. *J. Raman Spectrosc.* **1997**, *28*, 873–878.

Chapter 6 Reagent-Free Quantification of Aqueous Free Chlorine via Electrical Readout of Colorimetrically Functionalized Pencil Lines

This chapter shows the application of the interface of phenyl-capped aniline tetramer (PCAT) and graphite film for the design of a simple chemiresistive sensor for quantification of free chlorine in drinking water. Using various spectroscopy and microscopy techniques, the sensing mechanism of the sensor is described. In addition, the effect of chlorine on PCAT film and its impact on the stability and sensing response of the sensor are demonstrates.

Reprinted with permission from the Journal of ACS Applied Materials & Interfaces, **2017**, 9, 20748-20761, Amirmasoud Mohtasebi, Andrew D. Broomfield, Tanzina Chowdhury, P. Ravi Selvaganapathy, and Peter Kruse. DOI: 10.1021/acsami.7b03968

ACS APPLIED MATERIALS & INTERFACES

Research Article

www.acsami.org

Reagent-Free Quantification of Aqueous Free Chlorine via Electrical Readout of Colorimetrically Functionalized Pencil Lines

Amirmasoud Mohtasebi,[†] Andrew D. Broomfield,[†] Tanzina Chowdhury,[†] P. Ravi Selvaganapathy,[‡] and Peter Kruse*[,†]

[†]Department of Chemistry and Chemical Biology, McMaster University, 1280 Main Street West, Hamilton, Ontario L8S 4M1, Canada

[‡]Department of Mechanical Engineering, McMaster University, 1280 Main Street West, Hamilton, Ontario L8S 4L7, Canada

Supporting Information

ABSTRACT: Colorimetric methods are commonly used to quantify free chlorine in drinking water. However, these methods are not suitable for reagent-free, continuous, and autonomous applications. Here, we demonstrate how functionalization of a pencil-drawn film with phenyl-capped aniline tetramer (PCAT) can be used for quantitative electric readout of free chlorine concentrations. The functionalized film can be implemented in a simple fluidic device for continuous sensing of aqueous free chlorine concentrations. The sensor is selective to free chlorine and can undergo a reagent-free reset for further measurements. Our sensor is superior to electrochemical methods in that it does not require a reference electrode. It is capable of quantification of free chlorine in the range of 0.1−12 ppm with higher precision than colorimetric (absorptivity) methods. The interactions of PCAT with the pencil-drawn film upon exposure to hypochlorite were characterized spectroscopically. A previously reported detection mechanism relied on the measurement of a baseline shift to quantify free chlorine concentrations. The new method demonstrated here measures initial spike size upon exposure to free chlorine. It relies on a fast charge built up on the sensor film due to intermittent PCAT salt formation. It has the advantage of being significantly faster than the measurement of baseline shift, but it cannot be used to detect gradual changes in free chlorine concentration without the use of frequent reset pulses. The stability of PCAT was examined in the presence of free chlorine as a function of pH. While most ions commonly present in drinking water do not interfere with the free chlorine detection, other oxidants may contribute to the signal. Our sensor is easy to fabricate and robust, operates reagent-free, and has very low power requirements and is thus suitable for remote deployment.

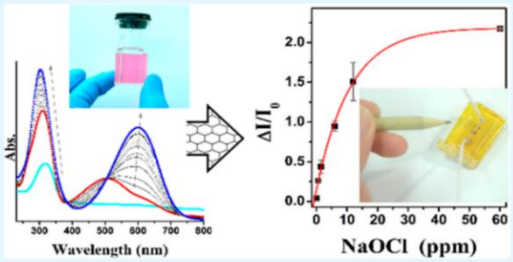

KEYWORDS: *water quality sensor, pencil lead, graphite, oligoaniline, PANI, free chlorine, chemiresistor, CHEMFET*

INTRODUCTION

Identification and quantification of chemicals present in gases and liquids are of great importance for healthcare, environmental monitoring, and industry. While, on occasion, offline analysis using lab-based equipment is warranted for quantification of a wide range of species, the ability to perform online and offline analysis in the field in (near) real time is crucial.[1,2] Consequently, there have been many efforts to miniaturize analytical equipment and automate the analysis process.[3] A chemical sensor creates a response upon exposure to a chemical stimulus and transduces it to a measurable physical quantity such as an electrochemical, optical, or electrical signal.[4] An important example is the quantification of free chlorine in drinking water. Electrochemical detection of free chlorine in solutions is often performed through voltammetric[5] or amperometric[6,7] measurements. Both methods are based on the oxidation of the analyte at a fixed or varying potential. A significant drawback of electrochemical methods is the need for a reference electrode.[8] An optical response can be measured through Raman scattering, fluorescence, surface plasmon resonance (SPR), or absorptivity (UV−vis−NIR).[9] The latter is also known as colorimetry, since the resulting color change in the visible region can also be judged by the eye. Free chlorine concentration can also be measured by an optical response to addition of an indicator reagent through methods such as colorimetry,[10] photoluminescence,[11] and chemiluminescence.[12] The indicator/analyte mixture resulting from these measurements cannot be disposed into the environment. In addition, they are often sensitive to the presence of other interfering ions in the solution (e.g., iron and manganese in colorimetry).[13]

Colorimetric methods are based on the color change of an indicator/reagent upon interaction with the analyte of interest. The method is simple, inexpensive, and does not require highly skilled personnel, making it popular, e.g., for the quantification

Received: March 20, 2017
Accepted: May 30, 2017
Published: June 7, 2017

of free chlorine content in drinking water using diethyl-*p*-phenylenediamine (DPD).[14] Oxidation of DPD leads to a change in its electronic structure and as a result to a change in the solution's color which can be quantified using a hand-held spectrophotometer.[13] Although this method is one of the most commonly employed techniques for quantification of free chlorine in drinking water, it requires several preparation steps and a spectrophotometer.[2] More importantly, it requires fresh chemicals for each measurement. This makes it difficult to be performed remotely and autonomously. Therefore, there have been efforts for developing chemical sensors which can be operated continuously and autonomously.[15]

Chemical sensors operating based on electrical transduction are particularly promising candidates for continuous monitoring of water quality due to their simplicity and robustness.[4] A variety of materials such as graphene,[16] carbon nanotubes (CNTs),[1] and organic compounds (e.g., polyaniline (PANI)) have been employed as the selective probe in chemical sensors.[4,15] One important class of such sensors are chemical field effect transistors (CHEMFETs) which are field effect transistors (FETs) in which the gate electrode is exposed to the environment.[17] Therefore, in CHEMFETs the modulation of the charge transport by the potential applied from the chemical stimulus at the gate can be used for sensing. The presence of an analyte modulates the charge carrier transport through the conductive channel by an applied potential and as a result leads to a shift in threshold voltage. Chemiresistors are another class of sensors based on electrical transduction in which a conductive material (often a semiconductor) is fabricated on an array of electrodes.[2] In chemiresistors, the analyte modulates the bulk electrical conductivity of the active material.[18] The simple design of chemiresistors makes them a robust and economical option for wide usage. CHEMFETs are somewhat more complex due to the need for a gate electrode and a dielectric. Gateless FETs are a variation of CHEMFETs in which the gate electrode and dielectrics are eliminated, and instead the direct interaction of the analyte with the surface layer on the conduction channel modulates the charge transport properties.[19]

Previously, it has been shown that CNTs integrated into a channel can be used for detection and quantification of sodium hypochlorite (NaOCl) present in a continuous flow of water.[20] The sensing response was attributed to the modulation of the CNTs electrical conductivity through charge transfer (donation of electrons) to hypochlorite. However, CNTs can produce similar responses to wide range of analytes such as SO_4^{2-}, dissolved oxygen, NH_3, and NO_2.[21,22] Recently, we have demonstrated the potential of immobilized oligoanilines on CNTs to increase the selectivity toward free chlorine.[15] It was shown that PCAT, an oligomer of PANI, will act as a selective probe of hypochlorite. PCAT in its base form has three oxidation states (fully reduced, half-oxidized, and fully oxidized) which are known to have differing abilities to dope CNTs.[23] It was proposed that the oxidation of PCAT by free chlorine leads to charge transfer from CNTs to oligoanilines.[15] This results in a change in the resistivity of the PCAT-CNTs film and can be used to quantify the concentration of free chlorine. The oxidized PCAT can be electrochemically recycled to its fully reduced form and used for further measurements. However, CNTs are expensive, and it can be challenging to create good electrical contacts between them and metal electrodes.[24]

Here we show that immobilization of oligoanilines on pencil lead, a cheap and chemically resistant material, can be used for detection and quantification of free chlorine in drinking water. This is a proof of principle for a simple approach in sensing, especially when the substrate (here a pencil-drawn film) does not show a significant and selective sensing response to analytes. We present the details of the mechanism and propose a new method for fast signal extraction. The sensitivity and selectivity of the device toward free chlorine were demonstrated and compared with colorimetric detection. Based on a study of the interaction of NaOCl with PCAT, and PCAT with graphite using X-ray photoelectron spectroscopy (XPS), Raman spectroscopy, and UV−vis spectroscopy, the operating principle of the device was elucidated. Conductivity measurements and atomic force microscopy (AFM) corroborate that the resistance modulation of the device is due to a change in conductivity of the graphitic film rather than any current flowing through the oligoaniline layer. In addition, the stability of the oligoaniline in the presence of free chlorine in both acidic and basic pHs was examined, and resettability of the device for repeated measurements was demonstrated. Electrical readout of colorimetric measurements is far from common in the field. The detection concept with respect to the sensing mechanism (transient peak detection vs baseline shift) described here is entirely novel. Furthermore, a new sensor film substrate material was demonstrated for this type of sensor. Therefore, we are demonstrating progress both in material/interface preparation and in detection concept.

EXPERIMENTAL SECTION

Materials Preparation. PCAT was synthesized and prepared in different oxidation states as previously reported in the literature.[25,26] Millipore water (18.2 MΩ cm) was obtained from a Simplicity UV purification system. The aqueous NaOCl solution (Reagent grade, 10−15%) was purchased from Sigma-Aldrich. All solutions of NaOCl were stored in polytetrafluoroethylene (PTFE) bottles in a fridge whenever not used. The 9B pencil was manufactured by Bruynzeel HOLLAND. The 9B pencil lead generally consists of around 95% graphite, the remainder being clay and wax.[27] The thermogravimetric analysis of the specific pencil lead used in this study indicates the presence of approximately 93% graphite (Figure S1). Highly ordered pyrolytic graphite (HOPG) samples were purchased from Alfa Aeser. A Sylgard 184 silicone elastomer kit (Dow Corning Corporation) was used to cast polydimethylsiloxane (PDMS) channels. The double-sided polyamide tape was purchased from Caplinq Corporation. The sodium hypobromite (NaOBr) solution was prepared by reaction of bromine solution (Sigma-Aldrich) with a stochiometric amount of sodium hydroxide (NaOH) solution. PCAT layers were vacuum deposited using a low-temperature Knudsen cell at a base pressure better than 5×10^{-6} Torr. During this process, the substrates were held at room temperature (20 °C). The thickness of the PCAT layer was monitored by quartz crystal microbalance (QCM).

Characterization. A Renishaw inVia laser Raman spectrometer was used to acquire Raman spectra with a spectral resolution of 2 cm^{-1} with an Ar^+ ion laser at 514 nm (2.41 eV). To obtain the Raman spectra of the powder samples, a methanolic solution of PCAT was cast and dried on a glass slide. Raman spectra were collected on multiple locations on each sample and recorded with a fully focused laser (10% or 5% laser power) with a 20× objective. A visible spectrophotometer (Ultraspec 100 pro) was used for absorptivity measurements. UV−vis spectra were collected using Cary 50 and Cary 300 spectrophotometers (Agilent Technologies) with quartz cuvettes. All electrical conductivity measurements were performed using a source measurement unit (Keithley).

A Kratos AXIS Nova XPS spectrometer with a monochromatic Al Kα X-ray source (15 mA, 1486.6 eV) was used to record the photoelectron spectra. XPS survey spectra and high-resolution spectra were obtained from an area of approximately 300×700 μm^2, using 160 and 20 eV pass energy, respectively. Only the sample with a glass

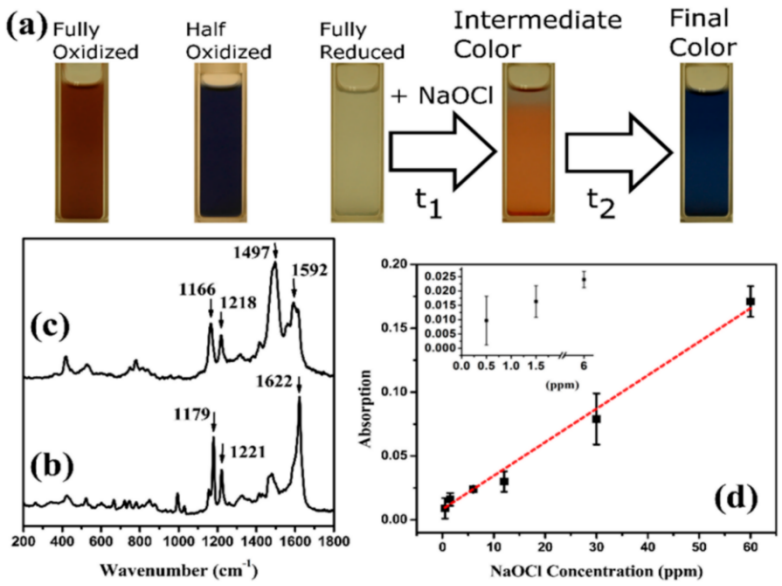

Figure 1. Colorimetric quantification of free chlorine. (a) Different colors of the methanolic solutions of fully oxidized, half-oxidized, and fully reduced PCAT. The intermediate color immediately after the introduction of NaOCl solution and the final color after approximately 20 min are also shown. (b) Raman spectrum of drop-cast pristine fully reduced PCAT and (c) Raman spectrum of drop-cast fully reduced PCAT after interaction with hypochlorite solution. (d) Calibration curve constructed based on the absorptivity measurement at 600 nm wavelength after the interaction of fully reduced PCAT with different concentrations of hypochlorite. The inset shows a closer look at the calibration curve at low concentrations of the analyte.

substrate was charge corrected. All XPS spectra were processed using CasaXPS software (version 2.3.17).[28] All peak integrations have been performed using a Shirley-type background and a line shape of GL(30), which is 30% Lorentzian and 70% Gaussian. ^{1}H nuclear magnetic resonance (NMR) spectra of PCAT powders were acquired using a 600 MHz spectrometer (AV 600, Bruker). In all NMR measurements, deuterated dimethyl sulfoxide (DMSO-d_6, Cambridge Isotope Laboratories, Inc.) was used as the solvent. pH measurements were carried out using a Delta 320 pH meter (Mettler Toledo) equipped with a Ag/AgCl electrode (Pasco Scientific). AFM was performed in tapping mode using a Veeco Enviroscope with a Nanoscope IIIa controller and antimony-doped Si cantilevers (Bruker, model NCHV-A). For all AFM images the background was subtracted.

Device Fabrication. The sensor device was fabricated by vacuum deposition of two parallel Au @ Cr (200 nm @ 20 nm) electrodes with a spacing of 2 mm on a frosted glass slide. Next, the pencil film is fabricated between these two electrodes. The effect of the number of pencil strokes on the frosted glass on the thickness and the electrical conductivity of the film is illustrated by comparison of two representative pencil films. The 1.8 μm thick film was fabricated by one hundred pencil strokes while a 0.9 μm thick film was fabricated using only four pencil strokes (Figure S2). It was found that the first few pencil strokes are responsible for the majority of the film's thickness and therefore its electrical conductivity. Therefore, the electrical conductivity of the film can be monitored and fine-tuned during writing. The width of the films was 2 mm. While we fabricated devices in different conductivity ranges, all data presented here was obtained from devices with a typical conductivity of about 1 mS (resistivity 1 kΩ). To obtain reproducible data, it is important to match the applied voltage to the conductivity in order to maintain a comparable current baseline. A PDMS channel (length:width:thickness = 15 mm:2 mm:2 mm) was fabricated by soft lithography and bonded on top of the pencil film using polyamide double-sided tape. It is of utmost importance that the aqueous analyte does not come in contact with the gold electrodes because it will short-circuit the device, as evidenced by a current increase by orders of magnitude due to ionic conduction through the analyte. At the relatively low voltages used during measurement, no such short circuit occurs between different portions of the carbon film. To this end, the channel geometry was imparted on the polyamide tape using an electronic cutting machine (Explore Air, Cricut).

Prior to the detection of free chlorine by this device a thin layer of PCAT was adsorbed on the graphite film. This step is performed by introducing a dilute solution of PCAT in methanol (0.5 mg/mL) to the channel over the course of 5 min using a syringe pump (0.2 mL/min). This step was followed by flowing Millipore water for 2 min to remove any oligoanilines not immobilized on the graphite film. The electrical conductivity measurement was performed by applying a constant bias voltage (typically between 0.1 and 10 mV to avoid causing electrochemistry) across the two gold electrodes using two alligator clamps while the analyte solution was flowing through the channel using the syringe pump (0.2 mL/min). Since PCAT is not soluble in water, no desorption of PCAT from the sensor film due to the exposure to the analyte is expected.[29] As a reference measurement, the free chlorine concentrations in the samples were evaluated using the DPD absorptivity method with a Pocket Chlorimeter II (Hach Company) and 5 mL free chlorine DPD reagent powder pillows. After calibration of the chlorimeter with 5 mL of analyte solution, one DPD powder pillow was added to the solution. The cell was flipped once, and the free chlorine concentration was quickly measured. For the interference experiment KCl was purchased form EMD Canada, NaCl, $NaNO_3$, and Na_2SO_4 were obtained from Caledon Laboratories Ltd., and $CaCl_2{\cdot}2H_2O$, $MgCl_2{\cdot}6H_2O$, and $AgNO_3$ were obtained from Sigma-Aldrich.

RESULTS AND DISCUSSION

Colorimetric Sensing of Free Chlorine. One of the characteristics of PCAT as a redox-active oligoaniline is the different color of its base and salt forms at different oxidation states (Figure S3).[26] In the basic pH regime, the solution of the

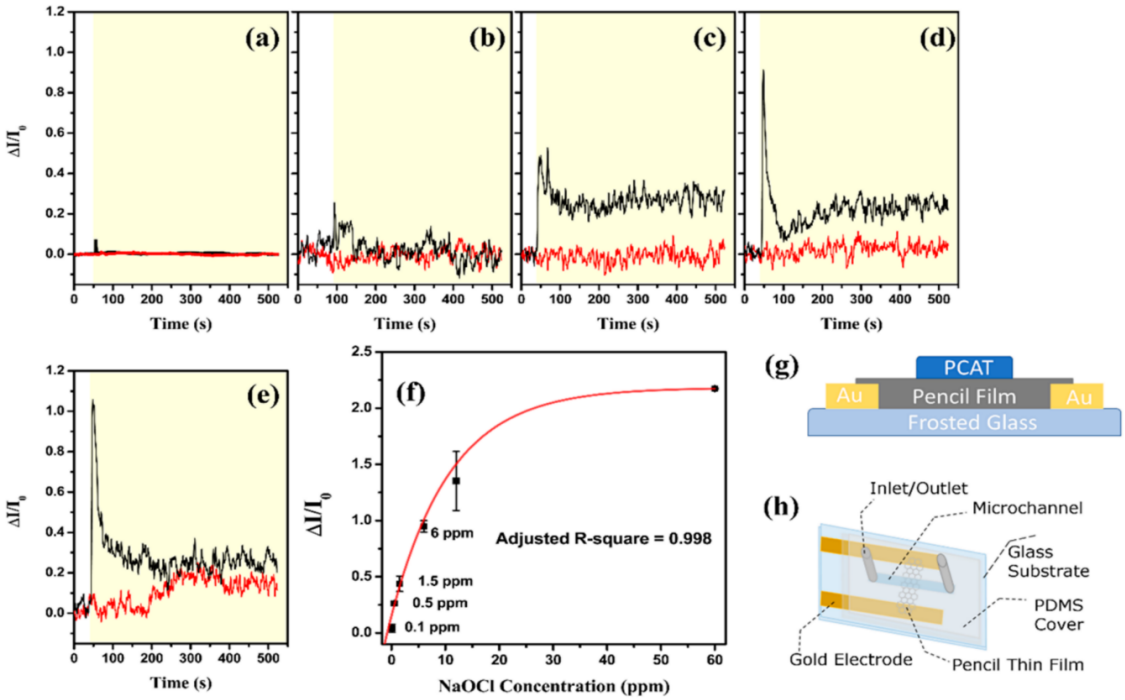

Figure 2. Sensing and quantification of free chlorine in water using PCAT-pencil film. Change in current ($\Delta I/I_0$) before (white area) and after (yellow area) exposure of the sensing film to aqueous solutions of NaOCl (black) and NaOBr (red) with concentrations of (a) 0.1, (b) 0.5, (c) 1.5, (d) 6, and (e) 12 ppm. (f) Calibration curve for NaOCl detection constructed using multiple measurements of $\Delta I/I_0$ for each concentration of the analyte. (g) The layer stack of sensing film. (h) Schematic of the sensor device.

fully oxidized PCAT in methanol is dark red, while its half-oxidized and fully reduced states are dark blue and pale blue, respectively (Figure 1a). Therefore, it is possible to follow the redox and protonation/deprotonation processes involving PCAT by eye. This makes PCAT a potential reagent for colorimetric measurements of free chlorine in solutions. NaOCl is a strong oxidizing agent which similarly to ammonium persulfate can be used for oxidation of PCAT.[15,26] Upon addition of hypochlorite solution (total concentration of 12 ppm) to the methanolic solution of fully reduced PCAT, it changes its color instantly to orange (Figure 1a, intermediate color). However, this color is not stable for more than a few tens of seconds and will convert to blue. After about 20 min, the color of the solution is dark blue and stable (Figure 1a, final color). This final color resembles the color of the base PCAT in its half-oxidized form. The oxidation state of this final product was examined using Raman spectroscopy. The Raman spectrum of the pristine fully reduced PCAT (Figure 1b) shows all three main bands of PCAT in its reduced form (1179, 1221, and 1622 cm^{-1}) while the spectrum of fully reduced PCAT after interaction with hypochlorite solution (Figure 1c) leads to appearance of new bands at 1165, 1219, 1497, 1592, and 1613 cm^{-1}.[30] These latter bands are associated with the PCAT in its half-oxidized state, indicating the oxidation of PCAT by hypochlorite.[30] Therefore, similar to DPD, fully reduced PCAT can be used as a probe in colorimetric sensing of free chlorine by comparing the color to a previously established color based calibration curve.[10] A more precise quantification can be performed by absorptivity measurement using a visible spectrophotometer. This way the changes in oxidation state of the molecular probe by free chlorine can be determined by monitoring the intensity of its absorption peak at a certain wavelength. Figure 1d shows the calibration curve constructed based on the absorption spectra of fully reduced PCAT at 600 nm after interaction with different concentrations of free chlorine. These data points can be fitted to a straight line with an adjusted *R*-square value of 0.827, which is a relatively low value for linearity (for 0.5−12 ppm). This shows the possibility to perform a quantification of free chlorine content in wide range of concentrations. However, a closer look at the calibration curve (Figure 1d, inset) shows a decrease in quantification's precision below 1.5 ppm of free chorine due to limited sensitivity of the spectrophotometer. One specific issue with PCAT is the somewhat long time required for achieving a final stable color (complete oxidation) after the introduction to the analyte solution. The reason behind this long response time will be discussed later. In addition, PCAT is not soluble in water and as a result not suitable for colorimetric measurements in water.[26] This issue could be solved through side chain engineering of the oligoanilines to increase their solubility.[31] More importantly, this method is not suitable for the in-line autonomous and continuous monitoring of free chlorine in water because it requires the introduction of a fresh reagent for each measurement. The reagent cannot be recovered after each measurement cycle.

Electric Readout of Aqueous Free Chlorine in Liquid Phase. To tackle these issues, a fluidic sensor based on a PCAT-modified graphite film was designed (Figure 2h). The

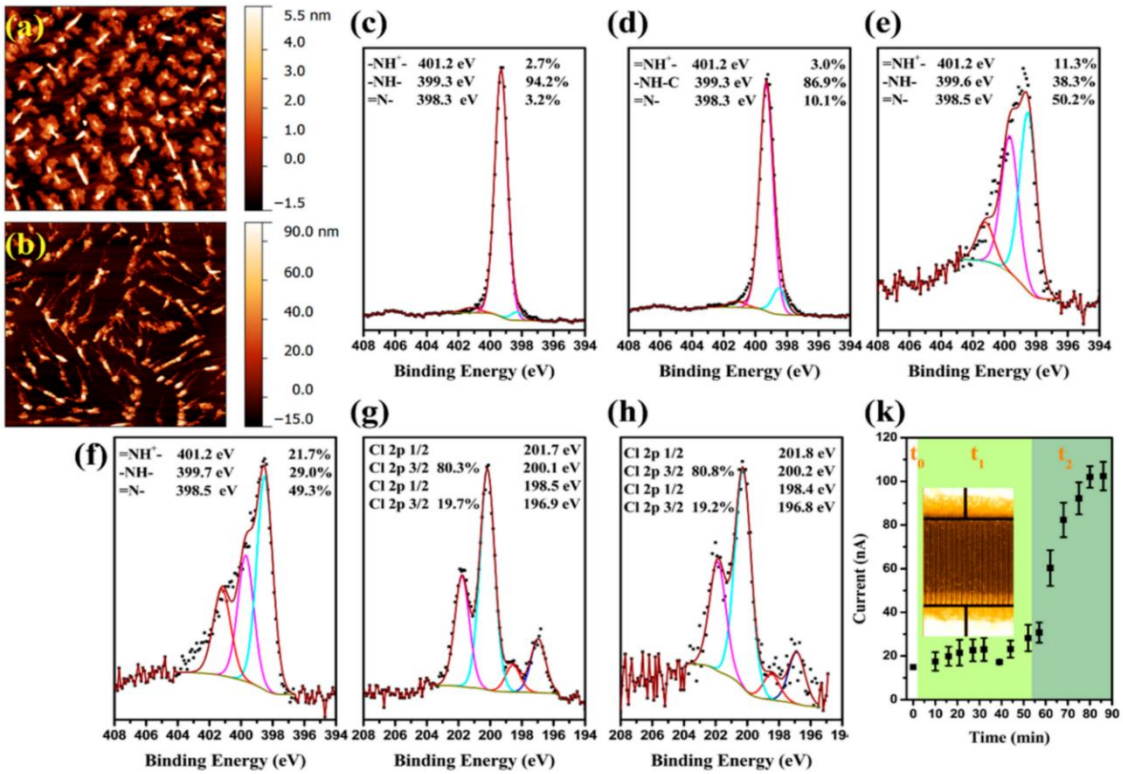

Figure 3. AFM of fully reduced (a) and half-oxidized (b) PCAT vacuum deposited on HOPG. N 1s XPS spectra of fully reduced and half-oxidized PCAT layers before (c and e, respectively) and after (d and f, respectively) exposure to bleach vapor. Cl 2p spectra of fully reduced (g) and half-oxidized (h) PCAT layers after exposure to bleach vapor. (k) Change in the electrical conductivity of the spin-coat film on an array of interdigitated gold electrodes, before (t_0) and after exposure to bleach vapor from 0.003% (t_1) and 3% (t_2) aqueous solutions. The measurement has been carried out under a constant bias voltage (+100 mV). The inset shows a photograph of the interdigitated electrodes before spin-coating PCAT on top.

graphite layer was used as a conductive channel between two gold leads. The oligoanilines were immobilized on the graphite film through noncovalent interactions (Figure 2g). First, the $\pi-\pi$ interaction between PCAT and graphite sheets leads to the adsorption of the first few layers of PCAT on the graphite film.[32] More layers of PCAT will accumulate on top of these layers through electrostatic interaction between PCAT molecules and by hydrogen bonding between the amine groups of the fully reduced PCAT state.[26] The source of graphite was 9B pencil lead. Pencil lead is conductive and cheap. It is resistant against numerous corrosive chemicals.[33] In addition, it can be fabricated by simple drawing on surfaces, such as a frosted glass slide, which results in a continuous thin film (Figure S2). The quantification of free chlorine through electric readout was performed using various concentrations of aqueous NaOCl solution. Figures 2a–e show the change in the normalized current of the PCAT-pencil film, $(I_p - I_0)/I_0 = \Delta I/I_0$ (where I_0 is the average of the measured current of the film prior to exposure and I_p is the maximum peak current after exposure to the analyte), prior to and after exposure to solutions of NaOCl at an applied voltage of 0.15 mV as a function of time. Upon exposure of the PCAT-pencil film to different concentrations of hypochlorite (0.1, 0.5, 1.5, 6, and 12 ppm), the current increases rapidly to a peak value followed by a drop to lower values (Figures 2a–e). No such peak was measured when only a bare graphite film was exposed to the analyte solution (Figure S5). This increase in the measured current was proportional to the increase in the concentration of the NaOCl. In addition to hypochlorite, hypobromite is also a common disinfectant for water treatment and as an antifoulant.[34−36] Depending on the pH, an aqueous solution of NaOCl consists of varying proportions of HOCl, OCl^-, and Cl_2 while the aqueous solution of NaOBr consists of HOBr, OBr^-, and Br_2.[36,37] Because of the chemical similarities between these two compounds, the response of the chemical sensor to different concentrations of hypobromite was determined for direct comparison. For this purpose, clean devices with similar characteristics were used. However, no significant change in current was observed when the device was exposed to 0.1, 0.5, and 1.5 NaOBr solutions (Figures 2a–c). The reason behind this result will be discussed later in this paper. Exposing the device to 12 ppm of NaOBr, above typical concentrations as disinfectant for drinking water, leads to a small increase in the measured current (Figure 2e). By further increasing the concentration of the analyte (60 and 240 ppm, Figure S6), the response was slightly amplified but still far weaker than when the device was exposed to similar concentrations of hypochlorite (Figure S7). The relative responses of the device demonstrate the sensitivity and selectivity of the sensor to free chlorine. Therefore, the device can be used as a selective sensor

for quantification of free chlorine in water treatment applications. Based on the responses of this device to free chlorine, a calibration curve was constructed (Figure 2f). Since the sensor starts saturating above 12 ppm of NaOCl and gets fully saturated at concentrations above 60 ppm (Figure S7), the calibration curve was fitted with an exponential decay function (eq S1). The adjusted *R*-square value of this fit was 0.998. The operational range of concentrations that can be measured with this selective sensor lies to be between 0.1 and 12 ppm.

Sensing Mechanism. Since the bare pencil film was not responsive to the analyte solutions (Figure S5), the key to understanding the sensing mechanism is the interaction of hypochlorite with oligoanilines and oligoanilines with the pencil film. XPS was used to better characterize the impact of bleach vapor on the oligoanilines. Vacuum deposition was employed to fabricate thin homogeneous layers of PCAT on graphite. The possibility of vacuum deposition of PCAT without altering its oxidation state has been previously demonstrated.[26] HOPG samples were used as model substrates of pencil film for this experiment. This is due to the ease of exposing a clean graphite surface by mechanically exfoliating HOPG with Scotch tape. Next, nominally 3 nm thick fully reduced and half-oxidized PCAT layers (measured by QCM) were deposited on two separate HOPG substrates. AFM of the fully reduced PCAT layer showed the formation of few nanometers thick (~1−8 nm), high-density dendritic islands (Figure 3a). The half-oxidized PCAT fabricated layer on HOPG (Figure 3b) led to the formation of low-density needle-shaped islands. The height of these islands is in the range of tens of nanometers (~10−110 nm). Both samples, along with a bare HOPG sample (as a reference substrate), were loaded into the XPS analysis chamber. For all three samples XPS survey spectra, C 1s, and N 1s spectra were acquired. Then, all samples were removed from the XPS vacuum chamber and exposed to the vapor of a 12.5% aqueous NaOCl solution for 7 min in ambient. All samples were loaded back in to the XPS analysis chamber. Changes in the structure of these samples were studied using their N 1s and Cl 2p XPS spectra. Figures 3c and 3d show the N 1s spectra of the fully reduced PCAT film deposited on HOPG before and after exposure to bleach vapor, respectively. Deconvoluted peaks at 398, 399, and 401 eV were assigned to imine, amine, and cationic nitrogen, respectively.[26] Comparison of the content of each structure before and after exposure to the vapor shows an oxidation of fully reduced PCAT (~7%, changes in amine and imine) while the contribution of cationic nitrogen remains almost unchanged (~0.3%). The species in the deconvoluted N 1s spectra of the half-oxidized state of PCAT before and after exposure to bleach vapor (Figures 3e and 3f, respectively) were assigned as for the fully reduced PCAT spectra (Figures 3c and 3d, respectively). Exposure of this sample to the vapor led to an increase in the amount of cationic nitrogen (~10%). Although no change in the imine content was observed, the transformation of −NH− to $-NH^{+}-$ (~9%) can be considered an oxidation event as well.[26] While the increase in the imine (decrease in amine) content is an indication of oxidation of the oligoanilines, the increase in the content of cationic nitrogen was previously assigned to their protonic doping, i.e., protonation.[26] The Cl 2p spectra of HOPG surfaces coated with both oligoanilines (fully reduced and half-oxidized PCAT) show peaks corresponding to two distinct species (Figures 3g and 3h, respectively). Since the Cl 2p spectrum of the bare HOPG surface does not show any peaks (Figure S13), all chlorine species are assigned to the PCAT films. The pair of peaks at higher binding energies in the Cl 2p spectra (Figures 3g and 3h) are assigned to chlorine which is covalently bonded to carbon (200.1 and 201.7 eV).[38] The peak pair at lower binding energies is due to ionic chloride species (196.9 and 198.5 eV), an indication of the protonic doping of PCAT by the vapor.[26] This is in agreement with the presence of cationic nitrogen in the N 1s spectra. While PCAT in its base form is almost nonconductive, protonic doping can significantly improve its electrical conductivity.[29] Therefore, although the NaOCl solution itself is basic, the absence of NaOH in the bleach vapor leads to both oxidation and protonic doping of the oligoanilines. The bleach vapor is mainly composed of chlorine gas, oxygen, and chlorine oxides.[39] The chemical reaction between chlorine and the water film physisorbed on the sensor film[40] results in the production of HCl and HOCl.[41] These acids cause protonic doping of PCAT, which can significantly increase its electrical conductivity.[29] This idea was examined by monitoring the electrical conductivity of a pristine fully reduced PCAT film during the exposure to bleach vapor. A continuous layer of fully reduced PCAT was spin-coated from methanolic solution onto an array of 100 planar interdigitated gold electrodes fabricated on a glass slide (Figure 3k, inset). The width of the electrodes was 20 μm with interelectrode spacing of 30 μm. The film was dried and exposed to bleach vapor (from 0.003% (Figure 3k, t_1) and 3% (Figure 3k, t_2) aqueous solutions) under ambient conditions. Exposure of this film to bleach vapor for approximately an hour lead to a nearly 5 times increase in the measured current as a result of protonic doping (Figure 3k, t_1 and t_2). In addition to doping, the partial oxidation of PCAT contributes to this significant increase in electrical conductivity. It was previously shown that protonic doping of the half-oxidized form of PCAT leads to the highest electrical conductivity among all of its states.[42]

As it was demonstrated above, the bleach vapor is acidic in nature while the solution of hypochlorite used in the sensing experiments is basic. In contrast to bleach vapor, the composition of the bleach solution at different pHs is well-known.[2] Therefore, to better understand the sensing mechanism of the sensor and the origin of the C−Cl bond, a sensor was exposed to a flow of aqueous NaOCl (6 ppm) for 15 min followed by a flow of Millipore water for 5 min. The PDMS channel was removed, and XPS N 1s, Cl 2p, and C 1s spectra were acquired from the PCAT-pencil sensor film (Figure 4b, Figure 4c, and Figure S14a, respectively). Figure 4d shows the topography of this PCAT-pencil film after exposure to the analyte. The absence of sodium in the XPS survey spectrum is an indication of successful washing of NaOCl from the channel with Millipore water (Figure S14b). The N 1s spectrum of the PCAT-pencil sensor film (Figure 4b) was deconvoluted to a cationic nitrogen peak (401.20 eV, 14.0%), amine nitrogen peak (399.6 eV, 37.7%), and a major imine nitrogen peak (398.5 eV, 48.3%).[26] A pristine fully reduced PCAT film drop-cast onto a gold substrate was used as a reference spectrum. The high-resolution N 1s spectrum of the pristine fully reduced PCAT (Figure 4a) can be deconvoluted into four peaks attributed to cationic nitrogen (401.2 eV, 15%), amine nitrogen (399.7 eV, 65.0%), imine nitrogen (398.5 eV, 13.8%), and an unknown nitrogen species (397.4 eV, 5.6%), possibly due to contamination of the substrate.[26] The presence of a small amount of imine nitrogen results from the oxidation of fully reduced PCAT during the fabrication process in ambient. The comparison between major nitrogen components

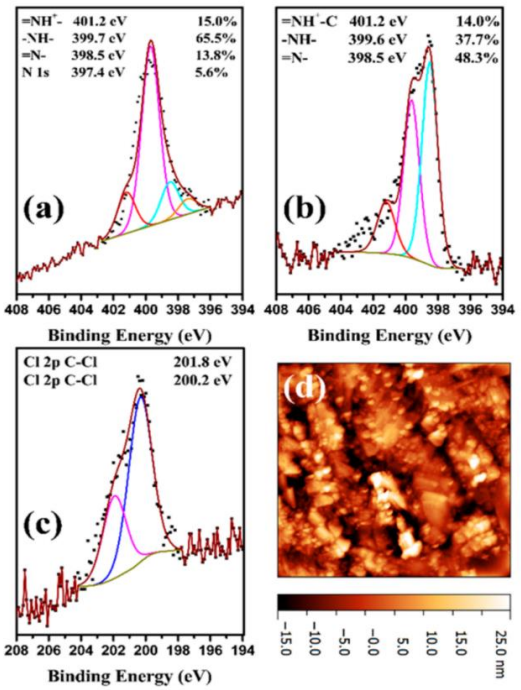

Figure 4. Characterization of the free chlorine sensor film. (a) N 1s spectra of pristine fully reduced PCAT film. (b) N 1s XPS spectra of fully reduced PCAT film adsorbed on a pencil-drawn film of the sensor after being exposed to aqueous solution of NaOCl (6 ppm) for 15 min. (c) Cl 2p spectrum of the sample in (b). (d) AFM image (2 μm × 2 μm) of the sensor film used in (b).

of the N 1s spectra of PCAT before and after exposure to the analyte show no change in the amount of cationic nitrogen. This confirms that the PCAT layer is still in its base form after exposure to an aqueous solution of NaOCl. The increase in the amount of imine (~50%) is a result of the transformation of fully reduced to half-oxidized PCAT after exposure to the analyte. The Cl 2p spectrum of the sensor film (Figure 4c) shows no sign of chloride species due to the absence of any peaks at 196.8 eV (Cl $2p_{3/2}$) and 198.4 eV (Cl $2p_{1/2}$). However, similar to the Cl 2p spectra of the oligoanilines exposed to bleach vapor (Figures 3g,h), the chlorine peaks at 200.2 eV (Cl $2p_{3/2}$) and 201.8 eV (Cl $2p_{1/2}$) are present.[38] The presence of covalently bonded chlorine is supported by a peak at 286.3 eV in the C 1s spectrum associated with C−Cl bonding (Figure S14a).[38] No chloramine (N−Cl) was detected, as confirmed by the absence of any peak at 197.8 eV in the Cl 2p spectrum.[43]

Recently, the presence of C−Cl bonds in the Cl 2p spectrum of PANI reacted with NaOCl has been attributed to the chlorination of the polymer.[44] While XPS of PCAT exposed to NaOCl solution mainly shows an oxidation reaction, UV−vis spectroscopy of the system hints at additional chemical reactions. The interaction between the oligoanilines and hypochlorite were monitored in situ with UV−vis spectroscopy. Figure 5a shows the change in the spectra of the fully reduced PCAT dispersed in methanol prior and after (over 20 min) the addition of aqueous solution of NaOCl (total concentration = 12 ppm). The spectrum of the fully reduced PCAT prior the reaction with the analyte (Figure 5a1) shows a sharp peak around 315 nm arising from the benzenoid $\pi-\pi^*$ transition.[42] Next, NaOCl was added to the cuvette and mixed thoroughly with the PCAT solution. This leads to an increase in the intensity of the benzenoid peak and appearance of two peaks at lower energies (Figure 5a2, ~504 and 596 nm). The latter peak is assigned to the benzenoid to quinoid ($\pi_B-\pi_Q$) excitonic transition, an indication of the oxidation of PCAT.[26,45] This step is in conjunction with the instant color change of the solution from pale blue to orange. However, the color will shift further to dark blue and the peak observed at ~504 nm disappears while the intensity of the quinoid peak increases. To the best of our knowledge, no data has been previously reported for this transition in UV−vis spectra of oligoanilines reacting with NaOCl. Over the course of 20 min, the intensities of both benzenoid and quinoid peaks increase (Figure 5a3). This long time required for completion of the oxidation reaction is what makes PCAT not suitable for colorimetric sensing. The same behavior was observed when PCAT was reacted with lower concentrations of NaOCl (Figure S15). To understand the nature of the short-lived peak at ~504 nm, a UV−vis measurement was conducted by fast cycling around this wavelength (390−550 nm, 10 nm/s, Figure 5c). NaOCl solution was carefully placed on top of the solution of PCAT, and no mixing was performed. Upon slow diffusion of the analyte in to the oligoaniline solution, a peak at 434 nm appears. Previously, this peak has been assigned to the polaron $\rightarrow \pi^*$ transition due to the protonic doping of PCAT with HCl.[45] The origin of this unexpected protonic doping in an alkaline NaOCl solution is explained by the reaction in Scheme 1.

At moderate basic pHs HOCl is a strong oxidant present in NaOCl aqueous solution.[2] It is, however, a weak acid and hence largely undissociated. Based on the reaction in Scheme 1, oxidation of the amine groups of PCAT by HOCl leads to the production of HCl. HCl is a strong acid and—in contrast to HOCl—will fully dissociate, causing a local drop in pH in proximity of the oligoanilines, resulting in their rapid protonation.[26] However, due to the basic pH of the overall NaOCl solution, the protons will eventually be stripped again from the oligoaniline, thus restoring its base form. The full spectrum of this sample (Figure 5b1, in red) shows the presence of a benzenoid peak (305 nm) in addition to the coexistence of peaks/shoulders at 434 nm (salt PCAT, polaron $\rightarrow \pi^*$), ~509 nm (intermediate peak, similar to Figure 5a2), 609 nm (base PCAT, $\pi_B \rightarrow \pi_Q$), and 824 nm (salt PCAT, $\pi \rightarrow$ polaron). Comparing this spectrum with a spectrum of half-oxidized PCAT protonated by HCl (Figure 5b2, in black), it shows the coexistence of peaks associated with base and salt half-oxidized PCAT in accordance with Scheme 1. This is in contrast with the spectrum of PCAT after being thoroughly mixed with NaOCl (Figure 5a3), where at the end only peaks associated with the half-oxidized oligoaniline base are present. This discrepancy originates from the differences in sample preparation in these two experiments (Figures 5a3 and 5b1). In the former experiment (Figure 5a3), NaOCl was thoroughly mixed with PCAT before the measurement, while in the latter experiment NaOCl slowly diffuses into the PCAT solution during the measurement. The photograph of the sample used in the latter measurement can be seen in the inset of Figure 5b, which shows the coexistence of both final product (blue, deprotonated) and the intermediate step (orange). Although the latter color might resemble the color of a methanolic

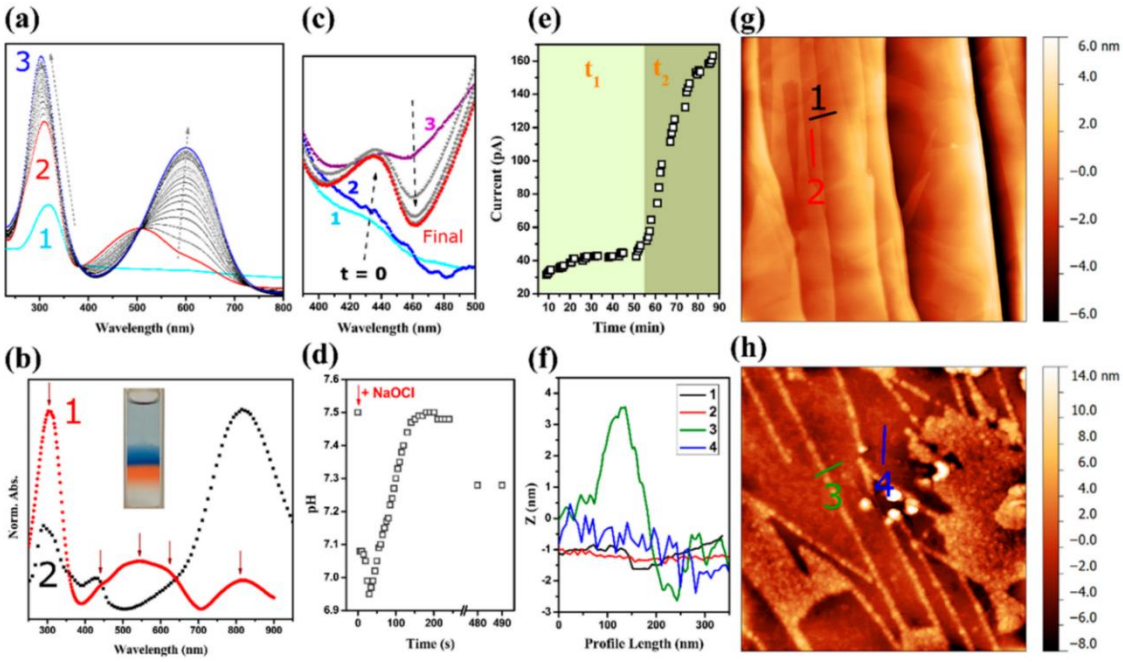

Figure 5. (a) UV−vis spectra of the pristine fully reduced PCAT before (1) and after (1 → 2 → 3, ~20 min) mixing with NaOCl solution (total concentration = 12 ppm). (b) UV−vis spectra of the diffusion of NaOCl solution into the fully reduced PCAT solution (1, red graph) and protonated half-oxidized PCAT (2, black graph). The inset shows the solution used for the former spectrum (c) monitoring the evolution of the polaron → π^* transition in (b1) over time. (d) pH change during the reaction of fully reduced PCAT with hypochlorite. (e) Current passing through a thick spin-coat fully reduced PCAT film exposed to the vapor of NaOCl solution (0.003% (t_1), 3% (t_2)) at 0.15 mV bias voltage obtained by extrapolation of $I-V$ curves used in Figure 3k. (f) Height profile of features in AFM of (g) and (h). AFM topography of bare HOPG surface (g, 4 μm × 4 μm) and HOPG surface coated with fully reduced PCAT via flowing PCAT solution through the channel (h, 4 μm × 4 μm).

Scheme 1. Reaction of a Fully Reduced Oligoaniline with Hypochlorous Acid

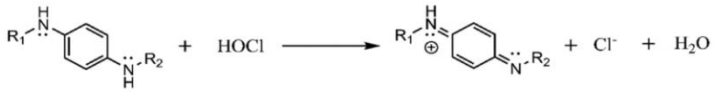

solution of fully oxidized PCAT, based on the spectra in Figure 5c, it contains the protonated form of oxidized PCAT.

The protonation and deprotonation of oligoanilines by NaOCl was also examined by monitoring the changes in the pH of the reaction. A magnetic stirrer bar was placed inside 5 mL of a solution of fully reduced PCAT. Up on addition of NaOCl solution (total concentration = 12 ppm) the pH rapidly decreased to values below 7, and a sudden change of color from pale blue to orange was observed (Figure 5d). This is followed by slowly ascending pH values and a shift of the solution's color to dark blue. This confirms the reaction mechanism suggested in Scheme 1 and the influence of mixing the solution on deprotonating the oligoanilines. The time required to reach a stable pH is comparable to the duration of the measured peak in current after exposure to the analyte in the sensing experiment (Figure 2a−e). Therefore, on the basis of the above results, it is expected that the temporary change in the pH contributes to the peak current response. It was shown earlier that the proton doping of oligoanilines makes them conductive (Figure 3k). Therefore, it is important to understand whether the immobilized oligoanilines on the pencil film can form a conductive network or not. The morphology of the PCAT-pencil film in the sensor exposed to NaOCl solution (6 ppm, Figure 4d) looks different from the bare pencil-drawn film (Figure S17). However, the irregular morphology of the pencil-drawn film hinders the assessment of the thickness of the adsorbed PCAT. On the other hand, HOPG is a graphite surface with well-known characteristics. Therefore, HOPG surfaces are used as a model system for the graphitic film to enable the assessment of the PCAT overlayer. A HOPG surface was placed in the channel, and fully reduced PCAT was immobilized on this surface based on the same procedure which was used in our sensors. Comparing the topography of this sample (Figure 5h) with a bare HOPG surface (Figure 5g) shows the step decoration of HOPG with PCAT (Figure 5f, profile 3). In addition, the morphology (Figure 5h) and the height profile of the terraces in this sample (Figures 5f and 5h, profile 4) show the existence of a very thin coverage (~1 nm) of fully reduced PCAT on HOPG. The current passing through a thick protonated PCAT film (Figure 5e) is in the range of pAs while the measured current at a similar bias voltage (0.15 mV) from the sensor device is in the range of tens to hundreds of nAs (Figure S19). Therefore, the current passing through the PCAT layer immobilized on pencil film does not make a

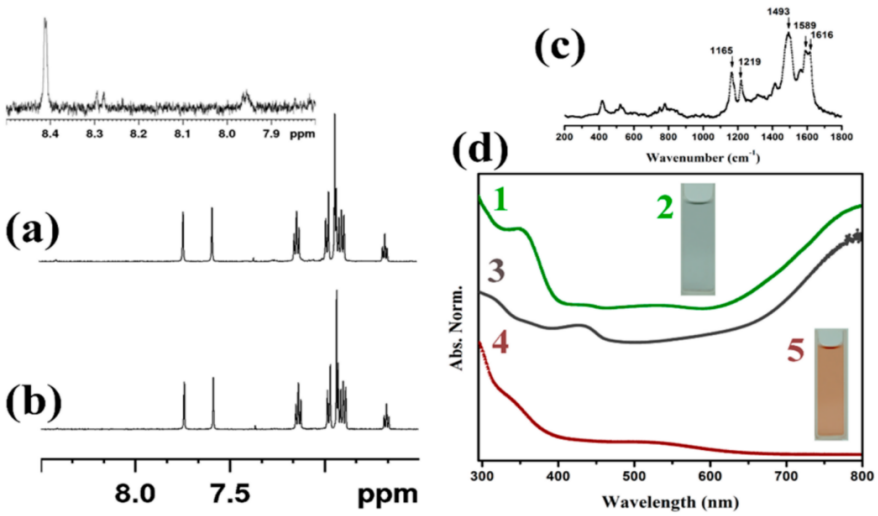

Figure 6. Chemical stability of PCAT against NaOCl in basic and acidic conditions. (a) ^{1}H NMR spectrum of fully reduced PCAT after reaction with the aqueous solution of hypochlorite (240 ppm) for 48 h. Inset figure depicts a closer look at 8.5−7 ppm of the spectrum. (b) ^{1}H NMR spectrum of pristine fully reduced PCAT. (c) Raman spectra of sample in (a). (d) UV−vis and color of the precipitate (1 and 2, respectively) and supernatant (4 and 5, respectively) of the reaction product of fully reduced PCAT and NaOCl in acidic condition. (3) UV−vis spectrum of protonated fully oxidized PCAT.

meaningful contribution to the sensing response of our sensor device. PCAT is not capable of creating a bypass electrical conduction channel on top of the graphite surface. Hence, our sensor deviates from the common design of a chemiresistive sensor in which the direct chemical changes to the bulk of the sensing material are the origin of the change in its conductivity.

An alternative method to change the conductivity of a material without inducing a direct chemical change in its structure is through modulation of the charge carrier density via one of two common pathways. The first path is based on chemical doping/polarity switching of the substrate by an adsorbed surface layer.[46] It has been previously shown that modification of p-type single-walled carbon nanotubes (SWCNTs) with fully reduced PANI will lead to them being switched from p-type to n-type.[23] Considering that PANI is a redox-active compound, this effect can be reversed (n-type to p-type) once the PANI coating is fully reduced chemically[23] or electrochemically.[15] On the basis of this idea, it has been previously shown that SWCNTs modified with fully reduced PCAT can be used for the sensing of oxidizing agents.[15] Another method to influence the charge transport in the sensing film is by imposing an electric field onto the conduction channel through charge built up from the adsorption of charged chemical species such as protons. The effective way of using this technique in chemical sensing is through modification of the sensing material (substrate) with chemical receptor groups selective to the analyte of interest. In addition to the selectivity, the extent of charging imposed on the conductive channel by the chemical receptors can be amplified by structural changes in the receptor molecules.[19] Therefore, our two-terminal device resembles the architecture of a gateless CHEMFET.[2,13] In such devices, the presence of certain groups of analytes leads to the modulation of the charge transport through the sensing film without any chemical alteration of it. Considering the coverage of the graphitic substrate with a thin layer of PCAT, the later mechanism based on the protonation of PCAT on the surface of the pencil film upon interaction with NaOCl fits with the data presented earlier in this paper (Figures 3f and 5c). Based on the UV−vis spectroscopy results (Figure 5c), upon interaction of fully reduced PCAT with NaOCl, molecules get both oxidized and protonated. As it was demonstrated by XPS, protonation of PCAT by the vapor of the NaOCl solution leads to appearance of cationic charges on the backbone of the oligoaniline. The same behavior is expected at the initial stages of the reaction of PCAT with a solution of NaOCl. Therefore, the thin film of oligoanilines imposes positive charges on the surface of the graphitic pencil film. The positive charges from cationic PCAT will lead to attraction of negative charge carriers into the graphitic conduction channel. This appears as a fast and sharp increase in the measured current ($\Delta I/I_0$). Upon deprotonation of the PCAT film due to the basic pH of the bulk of the NaOCl solution, the PCAT thin film loses its positive charge. Therefore, the accumulated charge carriers in the graphitic channel will be dispersed and the measured current drops to lower values, but not to the baseline values that existed before exposure to the NaOCl solution. In analogy to previous studies on carbon nanotubes,[15,23] the shift in the baseline can be associated with different doping interactions of different oxidation states of PCAT with the graphitic substrate.

The mechanism involving the effect of the electric field on the charge transport in the substrate can also be used to explain the higher sensitivity of the PCAT-pencil film to hypochlorite solution than to the hypobromite solution. At moderately basic pHs (7−8), HOCl and HOBr are the major oxidizing agents present in aqueous solutions of NaOCl and NaOBr, respectively.[36] They show similar redox reactions but they have different half-cell redox potentials (E_0, +1.49 for HOCl and +1.33 for HOBr).[47] The higher E_0 means that HOCl is a stronger oxidant in comparison to HOBr and as result can cause stronger oxidation of PCAT adsorbed on pencil film. Considering the proposed sensing mechanism and chemical reaction in Scheme 1, stronger oxidation of PCAT will lead to a

higher proton concentration, which will lead to stronger protonation of PCAT. The recommended amount of bromine as a disinfectant is double than when chlorine is employed.[47] The first distinct response of PCAT-pencil film to hypobromite solution is at 12 ppm and equal to $\Delta I/I_0 = 0.26$, equal to $\Delta I/I_0$ when the sensor film was exposed to 0.5 ppm of NaOCl solution.

Stability of the Oligoanilines. It is expected that the oxidation of fully reduced PCAT only leads to an increase in the intensity of its quinoid peak. However, the final spectrum of PCAT after reaction with hypochlorite indicates a significant increase in the intensity of both quinoid and benzenoid peaks (Figure 5a3). In addition, a red-shift of the quinoid peak (596 → 599 nm) and a blue-shift of the benzenoid peak (318 → 303 nm) were observed. Previously, a similar shift in the UV−vis spectrum of PANI after interaction with NaOCl was attributed to the chlorination of the polymer.[44] Although there have not been many studies on the chlorination of PANI or oligoanilines,[44] the chlorination of polyamides has been thoroughly investigated.[48] Chlorination of polyamide-based membranes used in desalination processes is known as the major reason behind their degradation.[48] The exposure of organic molecules containing primary or secondary amines to active free chlorine species is known to cause incorporation of chlorine at the aromatic ring.[38,48,49] This process includes a fast initial reaction of the amine group with free chlorine species followed by transfer of the chlorine to the aromatic ring,[38,50] known as Orton rearrangement.[51] At basic pHs no Cl_2 can be found in the solution. At pHs between 7 and 8 the ratio of $HOCl/OCl^-$ is close to 50:50.[37] The presence of chlorine in the +1 oxidation state in both HOCl and OCl^- is responsible for oxidizing properties of hypochlorite. In addition, Cl^+ is known to cause N-chlorination of amine groups.[50] The ring chlorination can eventually result in chain scission.[38,48] However, previous studies on chlorination of polyamides show that both N-chlorination and Orton rearrangement by hypochlorite are acid-catalyzed reactions.[48] The N-chlorinated polyamides can further undergo Orton rearrangement which results in a chloro-substituted aromatic moiety and degradation of the organic molecule. Assuming the same conditions apply to PANI and its oligomers, the intermediate decrease in pH from basic to acidic upon addition of NaOCl to the oligoanilines (Figure 5d) can create a suitable environment for chlorination. This is consistent with the detection of C−Cl bonds in the Cl 2p spectra of the sensor film (Figure 4c). In addition, it was previously suggested that immediate introduction of a basic solution can reverse the N-chlorination process.[48] Therefore, it is expected that the rise of the pH in Figure 5d will reverse the N-chlorination but cannot reverse the already chlorinated aromatic rings.

The stability of the oligoanilines against high concentrations of free chlorine species in basic conditions was examined. Figure 6b shows the ^{1}H NMR spectrum of pristine fully reduced PCAT.[52] The ^{1}H NMR spectrum of fully reduced PCAT after interaction with NaOCl (240 ppm) for 48 h shows the main characteristic peaks of PCAT in addition to three low-intensity peaks between 8.5 and 7.9 ppm (Figure 6a and its inset). These peaks were previously assigned to the N−H groups in half-oxidized forms of PCAT.[53] The peak at 8.4 ppm corresponds to the symmetric half-oxidized PCAT, and the peaks at 8.3 and 7.9 ppm correspond to the asymmetric half-oxidized PCAT. While it is difficult to identify the oxidation of fully reduced to half-oxidized PCAT using ^{1}H NMR spectroscopy, Raman spectroscopy of this sample indicates that the product is half-oxidized PCAT (Figure 6c).[30] No sign of degradation of PCAT by higher concentrations of NaOCl was observed (1750 ppm, Figure S20). These results indicate the stability of PCAT against degradation by NaOCl in basic conditions. The effect of NaOCl on oligoanilines in acidic conditions was also examined. Fully reduced PCAT (0.2 g) was dissolved in an excess amount of methanol. NaOCl solution (1000 ppm) was then added to the system. The pH of the solution was adjusted to ∼2 using HCl. After 20 h stirring of the reaction mixture (methanol/H_2O: 60/40) at room temperature, a small amount of precipitate was formed. It was soluble in methanol, similar to the pristine PCAT, but insoluble in water. Its green color (Figure 6d2) resembles the protonated PCAT by HCl.[26] UV−vis spectra of the precipitate show the main features at 342, 432, 530, and 800 nm (Figure 6d1). The peaks at 430 and 800 nm are in agreement with the main two peaks in UV−vis spectrum of protonated fully oxidized PCAT (Figure 6d3). However, the shoulder at 349 nm and the peak at 530 nm are absent in the spectrum of protonated fully oxidized form. On the other hand, the supernatant was red in color, soluble, and stable in water (Figure 6d5, unlike the pristine oligoanilines). The UV−vis spectrum of this solution (Figure 6d4) shows no similarity to the UV−vis spectra of base or salt PCAT in any oxidation states. However, the shoulder at 340 nm and a peak at 530 nm present in the spectrum of the precipitate sample are also present in this sample. Efforts to dedope or chemically reduce this sample were not successful (Figure S21). Therefore, similar to N-chlorination of polyamides, the N-chlorination of oligoanilines may be catalyzed in acidic conditions which led to their hydrolysis in solution. These compounds can undergo Orton rearrangement which leads to their eventual chain scissioning. It is concluded that the interaction of PCAT with very high concentrations of free chlorine in acidic conditions can significantly damage their structure. On the other hand, in spite of evidence of some degree of chlorination of PCAT by NaOCl (due to the drop in pH according to Scheme 1) in basic conditions, no indication of its degradation was found.

Electrochemical Resetting and Effect of Chlorination on the Sensing Response. It was previously shown that SWCNTs coated with fully reduced PCAT can be used for the measurement of free chlorine in drinking water.[15] The oxidized PCAT from this process can be electrochemically reduced back to its fully reduced form, and thus the device can be used for continuous measurement of chlorine concentrations. To examine such possibility in our device, after the first cycle of chlorine sensing (600 ppm) by pristine fully reduced PCAT, the channel was filled with an aqueous solution of NaCl (10 mM), and −0.8 V was applied between one of the gold electrodes and a stainless-steel tube inserted at the outlet of the channel for approximately 5 min. Since the resetting step is not a measurement, the reset potential does not have to be accurate. It merely has to be high enough (or higher) and long enough (or longer) in order to fully reduce PCAT, without causing undesirable side reactions. The cyclic voltammogram of PCAT (Figure S22) is a good starting point for the determination of the reset potential threshold, but one needs to take into account that it is measured against a reference potential (here ferrocene). In addition, the fluidic channel may cause a potential distribution due to the high impedance inside the channel. Therefore, the actual reset potential was determined iteratively to be safely high enough to ensure full

reduction of the entire PCAT film. Hence, no reference electrode is needed for any part of the sensor operation. Then, the channel was rinsed with Millipore water to remove any sodium chloride solution from it. In the second sensing cycle, +0.15 mV was applied between the two gold electrodes, and a 600 ppm solution of NaOCl was injected into the channel. Figure 7a shows the initial sensing cycle in addition to two

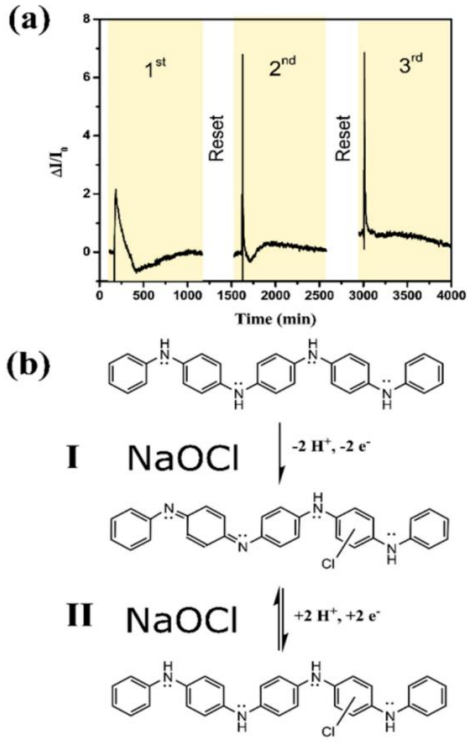

Figure 7. Electrochemical resetting of the chemical sensor. (a) Sensing measurement in aqueous solution of hypochlorite (600 ppm) using pristine fully reduced PCAT (1st cycle) and electrochemically reduced PCAT (2nd and 3rd cycles). (b) Proposed redox and chlorination of fully reduced PCAT (I), in addition to electrochemical reduction of chlorinated half-oxidized PCAT to fully reduced PCAT (II).

further sensing cycles after electrochemical resetting of the PCAT film. While $\Delta I/I_0$ for initial measurement using pristine fully reduced PCAT was 2.1, this value was approximately doubled after resetting (Figure 7a, second and third sensing cycles). This is an indication that the sensitivity of the device was increased after resetting. We attribute this change to the chlorination of PCAT during its first encounter with the NaOCl solution (Figure 7b, reaction I), in agreement with our XPS results (Figure 4c). It was previously demonstrated that chlorination of DPD which contains a primary amine can lead to a more pronounced reduction wave in its cyclic voltammogram.[49] This behavior was used for the detection of chlorine present in drinking water with higher sensitivity than the pristine DPD.[49] It should be noted that all four amine groups in the pristine fully reduced PCAT structure have equal possibility to be chlorinated by hypochlorite, and hence Cl may end up substituted on any of the five aromatic rings. The product of the electrochemical reduction of the oxidized PCAT is fully reduced, partially chlorinated PCAT and not pristine fully reduced PCAT. In further sensing cycles and electrochemical resetting cycles, the chlorinated fully reduced PCAT and the chlorinated half-oxidized PCAT will be transformed into each other (Figure 7b, reaction II). Even though, the chlorination might be beneficial for increasing the sensitivity of the device, it also requires recalibration of the device. However, based on our previous work,[15] the application of a low concentration of hypochlorite (<60 ppm) does not affect the sensing response possibly due to a negligible degree of chlorination.

Sensor Performance in the Presence of Interfering Ions. The response of the PCAT-pencil film based sensor device to interfering ions and real samples such as tap water was investigated. In addition, the selectivity of this device to free chlorine in the presence of other common ions or tap water was evaluated. Three of the most important metal ions present in drinking water are Na^+, Mg^{2+}, and Ca^{2+}.[54] Aqueous solutions of the respective chlorides were used as the source of Na^+, Mg^{2+}, and Ca^{2+}. As a typical scenario, the concentration of these ions in the drinking water of Toronto, Ontario, was reported as 12, 9, and 40 ppm, respectively.[54] Therefore, these concentrations were used for the selectivity experiment. Potassium is another mineral present in drinking water, mostly from water softeners. Its presence in drinking water is not a general health concern and therefore not a specific regulatory concentration has been mentioned for this mineral in most of the water quality guidelines.[55] A concentration of 10 ppm K^+ (from its chloride)[11] was used in this experiment. The regulatory limit for nitrate in drinking water is 45 ppm, and thus this concentration is used in this experiment,[55] with sodium as the counterion. In addition, the response of the sensor to 102 ppm of chloride ions (from $CaCl_2$) was measured. The solutions of each of these six ions were separately prepared in Millipore water. The free chlorine DPD method did not show any free chlorine content in any of these solutions. The PCAT-pencil based sensor response to each of these ions can be found in Figure 8. In all cases the response of the sensor ($\Delta I/I_0$) to these ions were below 6%. In another experiment, the sensor response to a solution containing all of these six analytes combined was measured but the highest response recorded for this sample was less than 8% (Figure 8, mixture). The average response of the sensor to the mixture containing all the interfering ions (Na^+, K^+, Ca^{2+}, Mg^{2+}, NO^{3-}, and Cl^-) is about 6% while its response to the individual solution of each ion is about 3–5%. This also demonstrates that the sensor is not affected by the conductivity of the solution. However, the presence of any leak to any or both gold leads cause an increase of the maximum measured current by about an order of magnitude due to a short circuit through the surroundings of the device.

In another experiment, the sensor response to a tap water sample (Hamilton, ON) was measured. The DPD test showed the presence of 0–0.1 ppm free chlorine in the tap water samples. The PCAT-pencil based sensor showed below 7% response to this sample. However, when the tap water samples were spiked with 0.5 ppm of NaOCl, a response of about 28% was achieved. This change in the conductivity is comparable to the response of the PCAT-pencil film to the Millipore water spiked with 0.5 ppm of NaOCl (Figure 8, about 26%). As it was shown earlier, the response of the sensor is mainly associated with the change in the pH of the solution surrounding the PCAT-pencil film upon oxidation of the oligoaniline film.

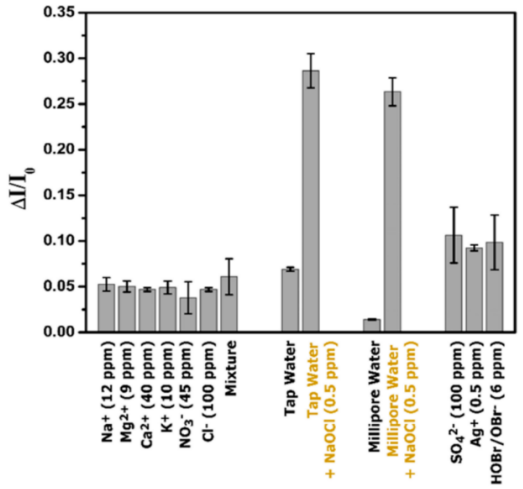

Figure 8. Selectivity of PCAT-pencil film based sensor for free chlorine over other interfering ions. The mixture solution consists of Na^+ (12 ppm), Mg^{2+} (9 ppm), Ca^{2+} (40 ppm), K^+ (10 ppm), NO_3^- (45 ppm), and Cl^- (100 ppm) ions.

Therefore, it is important to investigate the response of the sensor to common oxidants and dopants of PCAT present in natural waters or water treatment facilities. High level of sulfate ions can be found in water resources which can cause physiological effects on human body. The main sources of this ion are industrial wastes.[55] The response of the sensor to 100 ppm of SO_4^{2-} (from aqueous solution of Na_2SO_4) was measured which led to an average response below 11%. Silver is not a common metallic ion present in drinking water. The average concentration of this ion in drinking water is about 7.1 ppb with higher reported values between 20 and 80 ppb.[56] The exposure of the PCAT-pencil film to Ag^+ (0.5 ppm) caused a response of about 9%. Previously, it has been shown that silver nitrate can oxidize the fully reduced form of PANI through its reduction to metallic silver. The byproduct of this reaction is nitric acid which can protonate the oxidized PANI.[57] To this end, the silver nitrate solution used in the sensing experiment can cause both oxidization and protonation of the PCAT film. Finally, the response of the sensor film to $HOBr/OBr^-$, another important disinfectant used in water treatment facilities, was evaluated. As shown earlier (Figure 2 and Figure S8), both HOBr and OBr^- are oxidizing agents with different half-cell redox potential.[47] The recommended concentration of to $HOBr/OBr^-$ for water treatment is about double of the recommended concentration of $HOCl/OCl^-$.[34,36] Therefore, a solution of NaOBr (6 ppm) in Millipore water is used. The average response of the sensor film to this analyte was about 9%, which is less than half of the response measured when then sensor was exposed to NaOCl (0.5 ppm). The above measurement shows that common interfering ions present in drinking water do not have severe effects on the performance of the sensor. On the other hand, oxidizing agents and specifically dopants of PCAT can interfere with the measurement of very low (≤0.1 ppm) free chlorine concentrations.

CONCLUSION

We have demonstrated the quantification of free chlorine in aqueous solutions using a liquid flow sensor based on oligoanilines immobilized on a pencil film. The same oligoaniline was also used as a reagent in colorimetric (absorptivity) sensing of free chlorine. While the absorptivity measurement showed promising results for quantification of free chlorine at higher chlorine concentrations (1.5 to 60 ppm), it lacks resolution at low concentrations (below 6 ppm) and can also not be utilized in pure water due to low solubility of PCAT in water. On the other hand, the gateless sensor based on a PCAT-modified pencil film shows high sensitivity for detection of low concentrations of free chlorine (0.1−12 ppm) but will saturate at higher concentrations (>12 ppm). This range matches well with the requirements for monitoring of drinking water.[55] In addition, unlike colorimetric methods, the sensor can be regenerated electrochemically and operated reagent-free, continuously, and autonomously. The accuracy of this sensor depends on maintaining control over temperature, pH, and flow rate. Temperature and pH (6.5−8.5) are important quality parameters for drinking water which should be monitored simultaneously while flow rate is easily controlled in microfluidic devices.[55] The detection principle of the sensor is similar to the colorimetry in that it is based on a change in the electronic structure of organic molecules during redox reactions.

We have demonstrated that even free chlorine solutions at a basic pH can lead to the temporary protonation of oligoaniline molecules because the introduction of these solutions into the channel leads to fast oxidation of the oligoanilines by HOCl. The byproduct of this amine to imine transformation is HCl, a fully dissociated strong acid. In the absence of sufficient mixing, this will lead to a local drop in pH and protonation of the oligoanilines. However, the continuous flow of the basic solution into the channel will eventually reverse this process. Since by then the oligoanilines are partially or fully oxidized (depending on the analyte concentration), no further significant amount of oxidation will take place, and thus no additional high concentrations of HCl will be produced. While we have shown that PCAT cannot be degraded by exposure to free chlorine under basic conditions, this temporary drop in pH will lead to some degree of chlorination of the aromatic rings in PCAT when the sensor is exposed to high (>6 ppm) concentrations of free chlorine, as demonstrated by XPS. This process increases the sensitivity of the device to free chlorine, causing a shift in calibration.

Based on this reaction mechanism between PCAT and NaOCl solution, the working mechanism of the sensor can be explained. The protonation of PCAT upon interaction with the NaOCl solution, creates a blanket of positive charges on the surface of the pencil film. This results in an increase in the measured conductance. The followed deprotonation of PCAT due to rinsing with basic analyte, resets the state of the graphitic film to the initial situation, and appears as a drop in current values. A shift in the baseline current remains possibly due to differing degrees of doping of the graphitic film by the different oxidation states of PCAT, as demonstrated previously.[15,23] Since the concentration measurement itself is not electrochemical in nature, no reference electrode is needed for any part of the sensor operation. Even though we are sampling the outcome of a redox process, the redox reaction itself is not conducted under electrochemical control. The resetting step is

not a measurement and therefore does not require an accurate potential. It is just a brute-force reset which requires a "high enough" (or higher) potential for a "long enough" (or longer) time span. Therefore, our sensor is superior to electrochemical methods in that it does not require a reference electrode. To conclude, the use of inexpensive materials in our sensor makes it a suitable device for monitoring the water quality in remote areas. In addition, it can be fabricated and maintained by people without significant technical background due to its simple design.

■ ASSOCIATED CONTENT

Supporting Information

The Supporting Information is available free of charge on the ACS Publications website at DOI: 10.1021/acsami.7b03968.

Additional data (TGA, NMR, UV−vis spectra, AFM, SEM, XPS spectra, Raman spectroscopy, and interferometry) (PDF)

■ AUTHOR INFORMATION

Corresponding Author

*E-mail pkruse@mcmaster.ca; Ph (905) 525-9140 ext 23480; Fax (905) 522-2509.

ORCID

Peter Kruse: 0000-0003-4051-4375

Funding

The National Science and Engineering Research Council of Canada provided financial support through the Discovery Grant program.

Notes

The authors declare no competing financial interest.

■ ACKNOWLEDGMENTS

We acknowledge technical assistance from and helpful discussion with Mark C. Biesinger at Surface Science Western and Leo H. H. Hsu, Aditya Aryasomayajula, Md. Omar Sharif, and Enamul Hoque at McMaster University.

■ REFERENCES

(1) Meyyappan, M. Carbon Nanotube-Based Chemical Sensors. *Small* **2016**, *12*, 2118−2129.

(2) Qin, Y.; Kwon, H.-J.; Howlader, M. M. R.; Deen, M. J. Microfabricated Electrochemical pH and Free Chlorine Sensors for Water Quality Monitoring: Recent Advances and Research Challenges. *RSC Adv.* **2015**, *5*, 69086−69109.

(3) Chen, C. H.; Lin, Z.; Tian, R.; Shi, R.; Cooks, R. G.; Ouyang, Z. Real-Time Sample Analysis Using a Sampling Probe and Miniature Mass Spectrometer. *Anal. Chem.* **2015**, *87*, 8867−8873.

(4) Bobacka, J.; Ivaska, A.; Lewenstam, A. Potentiometric Ion Sensors Based on Conducting Polymers. *Electroanalysis* **2003**, *15*, 366−374.

(5) Jović, M.; Cortés-Salazar, F.; Lesch, A.; Amstutz, V.; Bi, H.; Girault, H. H. Electrochemical Detection of Free Chlorine at Inkjet Printed Silver Electrodes. *J. Electroanal. Chem.* **2015**, *756*, 171−178.

(6) Salazar, P.; Martín, M.; García-García, F. J.; González-Mora, J. L.; González-Elipe, A. R. A Novel and Improved Surfactant-Modified Prussian Blue Electrode for Amperometric Detection of Free Chlorine in Water. *Sens. Actuators, B* **2015**, *213*, 116−123.

(7) Salazar, P.; Martín, M.; González-Mora, J. L.; González-Elipe, A. R. Application of Prussian Blue Electrodes for Amperometric Detection of Free Chlorine in Water Samples Using Flow Injection Analysis. *Talanta* **2016**, *146*, 410−416.

(8) Olivé-Monllau, R.; Orozco, J.; Fernández-Sánchez, C.; Baeza, M.; Bartrolí, J.; Jimenez-Jorquera, C.; Céspedes, F. Flow Injection Analysis System Based on Amperometric Thin-Film Transducers for Free Chlorine Detection in Swimming Pool Waters. *Talanta* **2009**, *77*, 1739−1744.

(9) Lange, U.; Roznyatovskaya, N. V.; Mirsky, V. M. Conducting Polymers in Chemical Sensors and Arrays. *Anal. Chim. Acta* **2008**, *614*, 1−26.

(10) Palin, A. T. The Determination of Free and Combined Chlorine in Water by the Use of Diethyl-*p*-Phenylene Diamine. *J. - Am. Water Works Assoc.* **1957**, *49*, 873−880.

(11) Fang, Q.; Wang, Q.; Lin, W.; You, X.; Dong, Y.; Chi, Y. Chemical High Photoluminescent TPA and the Ratiometric Sensor for Free Chlorine. *Sens. Actuators, B* **2017**, *244*, 771−776.

(12) Tang, Y.; Su, Y.; Yang, N.; Zhang, L.; Lv, Y. Carbon Nitride Quantum Dots: A Novel Chemiluminescence System for Selective Detection of Free Chlorine in Water. *Anal. Chem.* **2014**, *86*, 4528−4535.

(13) Moberg, L.; Karlberg, B. An Improved *N, N′*-Diethyl-*p*-Phenylenediamine (DPD) Method for the Determination of Free Chlorine Based on Multiple Wavelength Detection. *Anal. Chim. Acta* **2000**, *407*, 127−133.

(14) Banna, M. H.; Imran, S.; Francisque, A.; Najjaran, H.; Sadiq, R.; Rodriguez, M.; Hoorfar, M. Online Drinking Water Quality Monitoring: Review on Available and Emerging Technologies. *Crit. Rev. Environ. Sci. Technol.* **2014**, *44*, 1370−1421.

(15) Hsu, L. H. H.; Hoque, E.; Kruse, P.; Selvaganapathy, P. R. A Carbon Nanotube Based Resettable Sensor for Measuring Free Chlorine in Drinking Water. *Appl. Phys. Lett.* **2015**, *106*, 063102.

(16) Ang, P. K.; Chen, W.; Wee, A. T. S.; Loh, K. P. Solution-Gated Epitaxial Graphene as pH Sensor. *J. Am. Chem. Soc.* **2008**, *130*, 14392−14393.

(17) Janata, J. Thirty Years of CHEMFETs - A Personal View. *Electroanalysis* **2004**, *16*, 1831−1835.

(18) Wohltjen, H.; Snow, A. W. Colloidal Metal−Insulator−Metal Ensemble Chemiresistor Sensor. *Anal. Chem.* **1998**, *70*, 2856−2859.

(19) Ng, A. L.; Chen, C. F.; Kwon, H.; Peng, Z.; Lee, C. S.; Wang, Y. Chemical Gating of a Synthetic Tube-in-a-Tube Semiconductor. *J. Am. Chem. Soc.* **2017**, *139*, 3045−3051.

(20) Yang, L.; Li, M.; Qu, Y.; Dong, Z.; Li, W. J. Carbon Nanotube-Sensor-Integrated Microfluidic Platform for Real-Time Chemical Concentration Detection. *Electrophoresis* **2009**, *30*, 3198−3205.

(21) Moonoosawmy, K. R.; Kruse, P. Cause and Consequences of Carbon Nanotube Doping in Water and Aqueous Media. *J. Am. Chem. Soc.* **2010**, *132*, 1572−1577.

(22) Kong, J.; Franklin, N. R.; Zhou, C.; Chapline, M. G.; Peng, S.; Cho, K.; Dai, H. Nanotube Molecular Wires as Sensors. *Science* **2000**, *287*, 622−625.

(23) Klinke, C.; Chen, J.; Afzali, A.; Avouris, P. Charge Transfer Induced Polarity Switching in Carbon Nanotube Transistors. *Nano Lett.* **2005**, *5*, 555−558.

(24) Cao, Q.; Han, S.; Tersoff, J.; Franklin, A. D.; Zhu, Y.; Zhang, Z. End-Bonded Contacts for Carbon Nanotube Transistors with Low, Size-Independent Resistance. *Science* **2015**, *350*, 68−72.

(25) Wang, W.; MacDiarmid, A. G. New Synthesis of Phenyl/Phenyl End-Capped Tetraaniline in the Leucoemeraldine and Emeraldine Oxidation States. *Synth. Met.* **2002**, *129*, 199−205.

(26) Mohtasebi, A.; Chowdhury, T.; Hsu, L. H. H.; Biesinger, M. C.; Kruse, P. Interfacial Charge Transfer between Phenyl-Capped Aniline Tetramer Films and Iron Oxide Surfaces. *J. Phys. Chem. C* **2016**, *120*, 29248−29263.

(27) Sousa, M. C.; Buchanan, J. W. Observational Models of Graphite Pencil Materials. *Comput. Graphic Forum* **2000**, *19*, 27−49.

(28) Fairley, N. *CasaXPS, Revision 2.3.17*; Casa Software Ltd.: Teignmouth, Devon, 2016.

(29) Wang, Y.; Torres, J. A.; Stieg, A. Z.; Jiang, S.; Yeung, M. T.; Rubin, Y.; Chaudhuri, S.; Duan, X.; Kaner, R. B. Graphene-Assisted Solution Growth of Vertically Oriented Organic Semiconducting Single Crystals. *ACS Nano* **2015**, *9*, 9486−9496.

(30) Boyer, M.-I.; Quillard, S.; Rebourt, E.; Louarn, G.; Buisson, J. P.; Monkman, A.; Lefrant, S. Vibrational Analysis of Polyaniline: A Model Compound Approach. *J. Phys. Chem. B* **1998**, *102*, 7382−7392.
(31) Mei, J.; Bao, Z. Side Chain Engineering in Solution-Processable Conjugated Polymers. *Chem. Mater.* **2014**, *26*, 604−615.
(32) Wei, W.; Wang, G.; Yang, S.; Feng, X.; Müllen, K. Efficient Coupling of Nanoparticles to Electrochemically Exfoliated Graphene. *J. Am. Chem. Soc.* **2015**, *137*, 5576−5581.
(33) Kurra, N.; Kulkarni, G. U. Pencil-on-Paper; Electronic Devices. *Lab Chip* **2013**, *13*, 2866−2873.
(34) Kolios, G.; Johann, J.; Bissen, M.; Müller, A. Treatment of Water with Hypobromite Solution. U.S. Patent 8496830 B2, July 30, 2013.
(35) Glater, J.; Zachariah, M. R.; McCray, S. B.; McCutchan, J. W. Reverse Osmosis Membrane Sensitivity to Ozone and Halogen Disinfectants. *Desalination* **1983**, *48*, 1−16.
(36) Debiemme-Chouvy, C.; Hua, Y.; Hui, F.; Duval, J. L.; Cachet, H. Electrochemical Treatments Using Tin Oxide Anode to Prevent Biofouling. *Electrochim. Acta* **2011**, *56*, 10364−10370.
(37) Aoki, T.; Munemori, M. Continuous Flow Determination of Free Chlorine in Water. *Anal. Chem.* **1983**, *55*, 209−212.
(38) Do, V. T.; Tang, C. Y.; Reinhard, M.; Leckie, J. O. Degradation of Polyamide Nanofiltration and Reverse Osmosis Membranes by Hypochlorite. *Environ. Sci. Technol.* **2012**, *46*, 852−859.
(39) Young, J. A. Sodium Hypochlorite Solution. *J. Chem. Educ.* **2002**, *79*, 1196.
(40) Vilkman, M.; Lehtinen, K.; Mäkelä, T.; Rannou, P.; Ikkala, O. Poly(aniline) Doped with 5-Formyl-2-Furansulfonic Acid: A Humidity Memory. *Org. Electron.* **2010**, *11*, 472−478.
(41) Gibbs, H. D. The Production of Hydrochloric Acid from Chlorine and Water. *J. Ind. Eng. Chem.* **1920**, *12*, 538−541.
(42) Wang, Y.; Tran, H. D.; Liao, L.; Duan, X.; Kaner, R. B. Nanoscale Morphology, Dimensional Control, and Electrical Properties of Oligoanilines. *J. Am. Chem. Soc.* **2010**, *132*, 10365−10373.
(43) Ettori, A.; Gaudichet-Maurin, E.; Schrotter, J. C.; Aimar, P.; Causserand, C. Permeability and Chemical Analysis of Aromatic Polyamide Based Membranes Exposed to Sodium Hypochlorite. *J. Membr. Sci.* **2011**, *375*, 220−230.
(44) Huang, X.; McVerry, B. T.; Marambio-Jones, C.; Wong, M. C. Y.; Hoek, E. M. V.; Kaner, R. B. Novel Chlorine Resistant Low-Fouling Ultrafiltration Membrane Based on a Hydrophilic Polyaniline Derivative. *J. Mater. Chem. A* **2015**, *3*, 8725−8733.
(45) Lyu, W.; Feng, J.; Yan, W.; Faul, C. F. Self-Assembly of Tetra(aniline) Nanowires in Acidic Aqueous Media with Ultrasonic Irradiation. *J. Mater. Chem. C* **2015**, *3*, 11945−11952.
(46) Kim, K. K.; Kim, S. M.; Lee, Y. H. Chemically Conjugated Carbon Nanotubes and Graphene for Carrier Modulation. *Acc. Chem. Res.* **2016**, *49*, 390−399.
(47) World Health Organization, Disinfectants & Disinfectants By-Products: Environmental Health Criteria Series No. 216; Geneva, 2000.
(48) Barassi, G.; Borrmann, T. N-Chlorination and Orton Rearrangement of Aromatic Polyamides, Revisited. *J. Membr. Sci. Technol.* **2012**, *2*, 2−4.
(49) Seymour, E. H.; Lawrence, N. S.; Compton, R. G. Reaction with N, N-Diethyl-p-Phenylenediamine: A Procedure for the Sensitive Square-Wave Voltammetric Detection of Chlorine. *Electroanalysis* **2003**, *15*, 689−694.
(50) Gabelich, C. J.; Frankin, J. C.; Gerringer, F. W.; Ishida, K. P.; Suffet, I. H. Enhanced Oxidation of Polyamide Membranes Using Monochloramine and Ferrous Iron. *J. Membr. Sci.* **2005**, *258*, 64−70.
(51) Orton, K. J. P.; Jones, W. J. CLXIII.-Primary Interaction of Chlorine and Acetanilides. *J. Chem. Soc., Trans.* **1909**, *95*, 1456−1465.
(52) Shao, Z.; Rannou, P.; Sadki, S.; Fey, N.; Lindsay, D. M.; Faul, C. F. J. Delineating Poly(Aniline) Redox Chemistry by Using Tailored Oligo(Aryleneamine)s: Towards Oligo(Aniline)-Based Organic Semiconductors with Tunable Optoelectronic Properties. *Chem. - Eur. J.* **2011**, *17*, 12512−12521.
(53) Rebourt, E.; Joule, J. A.; Monkman, A. P. Polyaniline Oligomers; Synthesis and Characterization. *Synth. Met.* **1997**, *84*, 65−66.
(54) Azoulay, A.; Garzon, P.; Eisenberg, M. J. Comparison of the Mineral Content of Tap Water and Bottled Waters. *J. Gen. Int. Med.* **2001**, *16*, 168−175.
(55) Guidelines for Canadian Drinking Water Quality Summary Table; Federal-Provincial Committee on Drinking Water of the Federal-Provincial-Territorial Committee on Health and the Environment, Health Canada, Ottawa, ON, 2017.
(56) World Health Organization. *Guidelines for Drinking-Water Quality*, 2nd ed.; Geneva, 1996.
(57) Šeděnková, I.; Trchová, M.; Stejskal, J.; Prokeš, J. Solid-State Reduction of Silver Nitrate with Polyaniline Base Leading to Conducting Materials. *ACS Appl. Mater. Interfaces* **2009**, *1*, 1906−1912.

Supporting Information

Reagent-Free Quantification of Aqueous Free Chlorine via Electrical Read-Out of Colorimetrically Functionalized Pencil Lines

Amirmasoud Mohtasebi,[1] Andrew D. Broomfield,[1] Tanzina Chowdhury,[1] P. Ravi Selvaganapathy,[2] Peter Kruse[1]*

[1]Department of Chemistry and Chemical Biology, McMaster University, 1280 Main Street West, Hamilton, Ontario, L8S 4M1, Canada

[2]Department of Mechanical Engineering, McMaster University, 1280 Main Street West, Hamilton, Ontario, L8S 4L7, Canada

Corresponding Author*

E-mail: pkruse@mcmaster.ca. Phone: (905) 525-9140 ext23480. Fax: (905) 522-2509.

Thermogravimetric Analysis of 9B Pencil Lead

9B pencil lead generally consists of about 95% graphite and 5% clay and wax.[1]

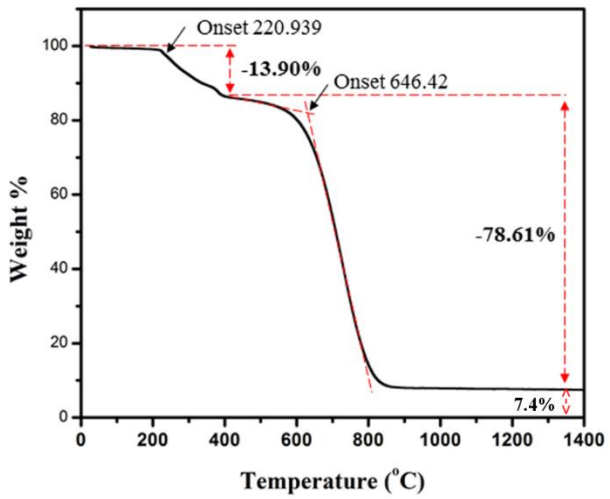

Figure S1. Thermogravimetric analysis of 9B pencil lead from room temperature to 1400 °C acquired under pure oxygen atmosphere. The analysis indicates the presence of approximately 7.4% additive to the graphite particles.

Device Fabrication

The effect of the number of the pencil strokes on the thickness and electrical conductivity of the fabricated pencil films was evaluated by fabrication of two samples with equal surface areas on two frosted glass slides. The areas were marked by indention on the frosted glass slides before fabrication of the pencil films. The first sample was fabricated by 100 pencil strokes while the other sample was fabricated by 4 pencil strokes. The optical microscopy and height measurement of the pencil films fabricated on frosted glass slides were performed using Nikon Eclipse LV100ND microscope with NIS-Elements imaging software. This microscope can reconstruct 3D images of the sample by scanning the height of the focal plane and reconstructing the sample topography via software algorithms. Figures S2a and S2b show the optical microscopy (reflection geometry) of the former and the latter samples at the interface between the pencil films (reflective portion) and the frosted glass substrates (dull portion). Figures S2c and S2d show the three-dimensional view of these two samples, respectively. Figure S2e shows the height profile along the blue line in the sample in Figure S2a. The boundary region indicated in this sample is a result of the indentation marks created prior to the fabrication of the pencil film to define the exact area of the pencil film. Figure S2f shows the height profile along the blue line in Figure S2b for the film fabricated by four pencil strokes. The average thickness of the pencil films fabricated by 100 pencil strokes and four pencil strokes were evaluated to be about 1.81 μm and 0.85 μm, respectively. This indicates that most of the thickness of the pencil films fabricated on frosted glass slides is formed by the first few pencil strokes. The electrical conductivity of each sample was evaluated by four-

probe conductivity measurement at three different spots of each sample. The electrical conductivity of pencil films fabricated by 100 and 4 pencil strokes were measured to be about 0.0107 and 0.0047 mS, respectively (Figure S2g). The 2.25 times higher electrical conductivity of the former pencil film is proportional to its 2.12 times higher thickness in comparison to the latter pencil film. Therefore, it is concluded that fabrication of pencil films with identical surface area and identical number of pencil strokes can lead to fabrication of the reproducible sensor devices based on pencil films on frosted glass.

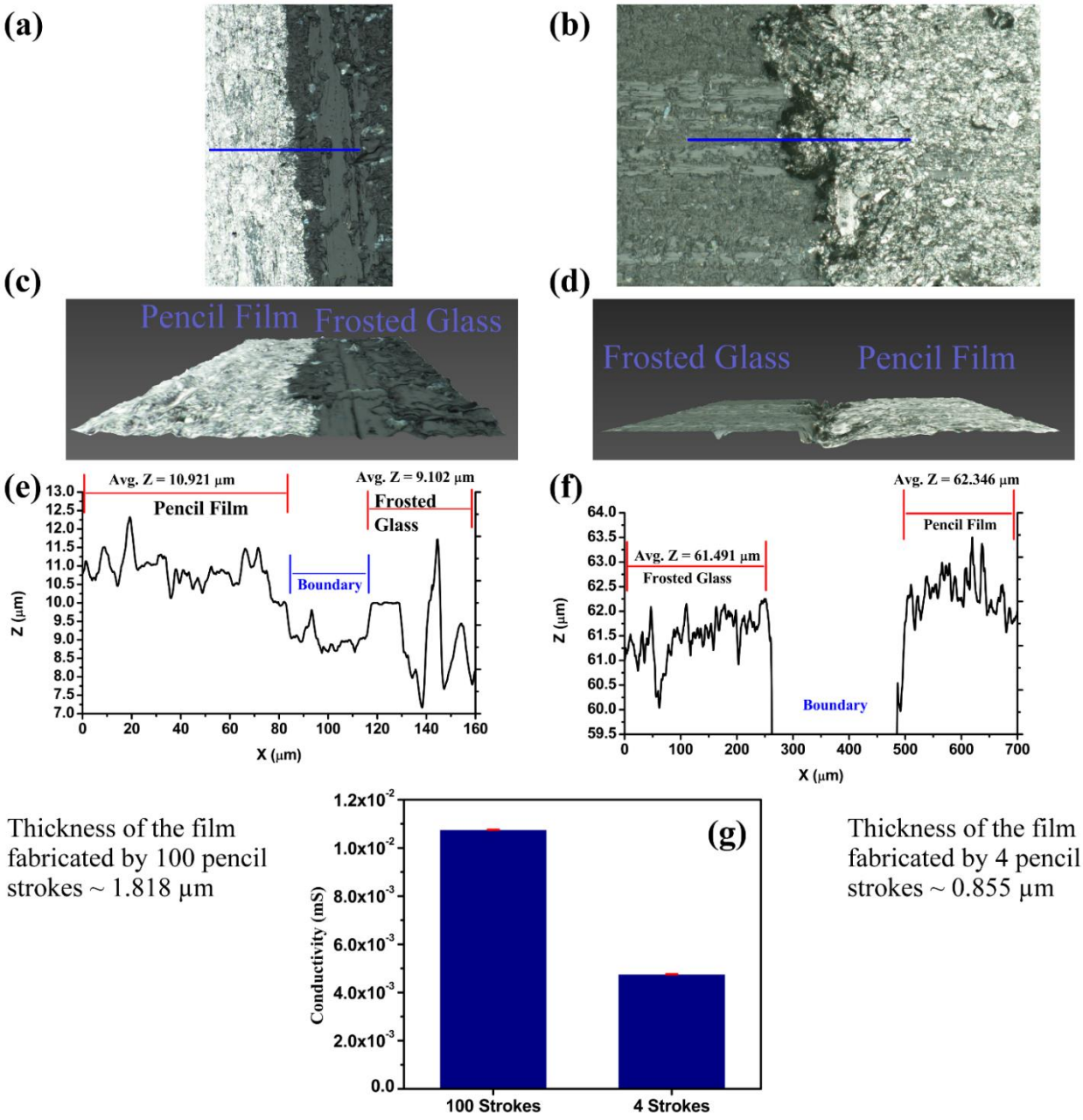

Figure S2. Optical microscopy of the pencil films fabricated on frosted glass slides by 100 pencil strokes (a) and four pencil strokes (b). (c) and (d) the three-dimensional view of the interface in (a) and (b), respectively. (e) and (f) the height profile along the blue lines in (a) and (b), respectively. (g) Four probe conductivity measurement of the film in (a) and (b).

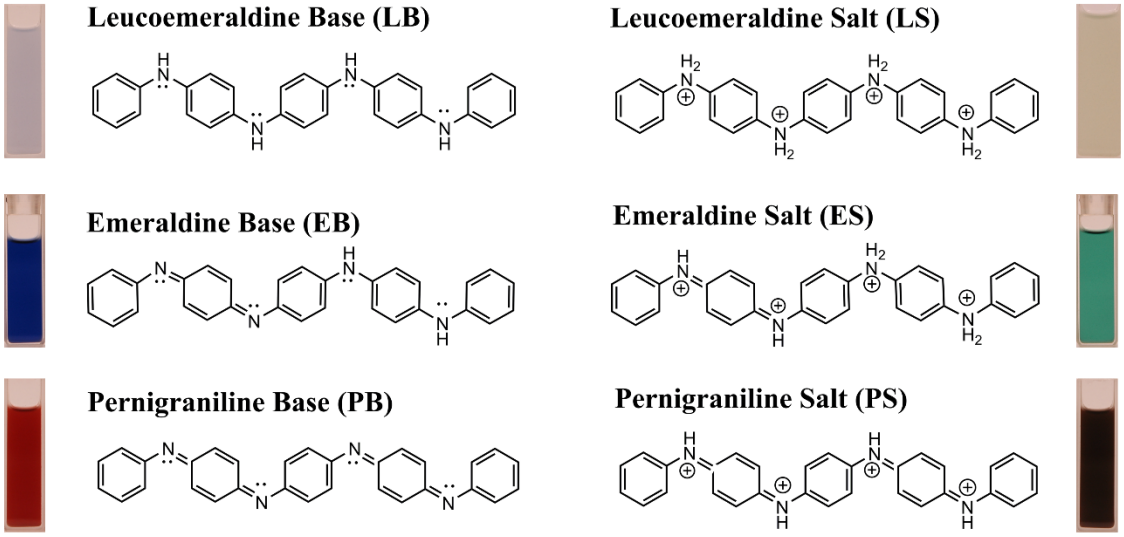

Figure S3. Molecular structure of different oxidation states of PCAT in base and salt (doped by HCl) in addition to their color in methanolic solution.

Chemical Sensing Setup

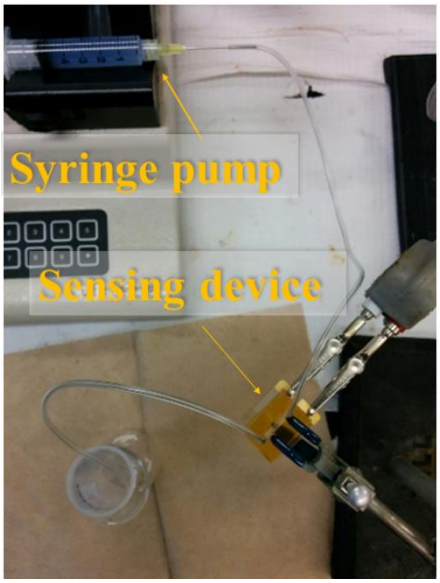

Figure S4. Photograph of the set up used for sensing measurement. The setup includes a syringe and a syringe pump (for circulating the analyte), the sensor device, a waste container, and two alligator clips connected to the two gold electrodes on one side and to a source measure unit on the other side. The above photograph shows the process of introducing fully-reduced PCAT (LB) to the pencil film to immobilize oligoanilines on top of the graphite surface. A methanolic solution of fully reduced PCAT (0.5 mg/ml) was introduced to the channel (0.2 ml/min) for five minutes. Then a stream of Millipore water (0.2 ml/min) was introduced to the channel for two minutes to remove any oligoanilines not adsorbed on the surface of the pencil film.

Sensing with Bare Pencil Drawn Film

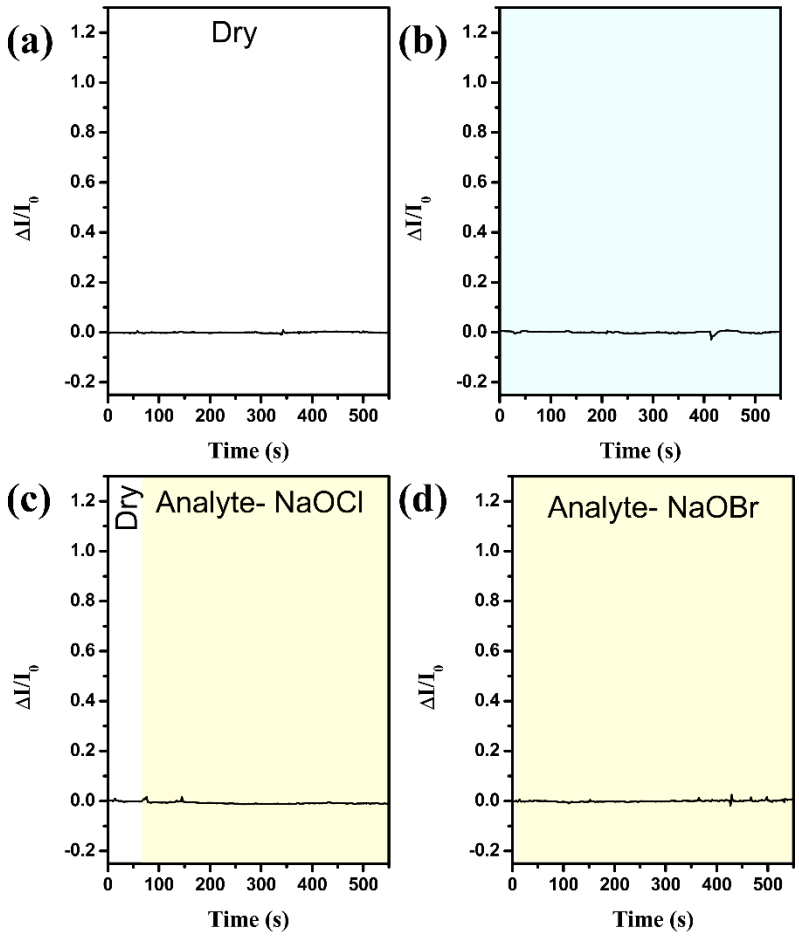

Figure S5. Normalized current as a function of time under application of a constant bias voltage of 0.15 mV for the bare sensor (without immobilized PCAT) in dry condition (a), while exposed to Millipore water (b), exposed to aqueous NaOCl solution (1.5 ppm) from dry state (c), and exposed to aqueous NaOBr solution with the concentration of 1.5 ppm (d).

Sensing of High Concentration of Aqueous Hypobromite Solutions

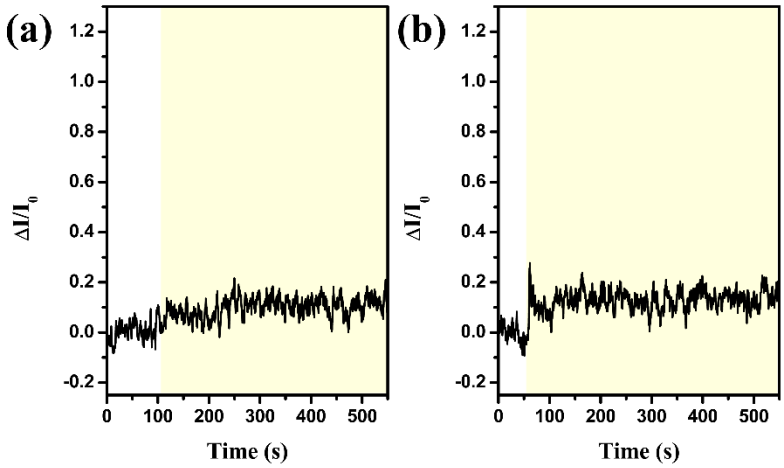

Figure S6. Change in the measured current of PCAT-pencil electrode as a function of time (constant bias measurement, 0.15 mV), prior and after exposure (white area and yellow area, respectively) to 60 ppm (a), 240 ppm (b) of aqueous solution of NaOBr.

Calibration Curve Obtained After Sensing of Different Concentrations of Hypochlorite with the PCAT-Pencil Drawn Sensor

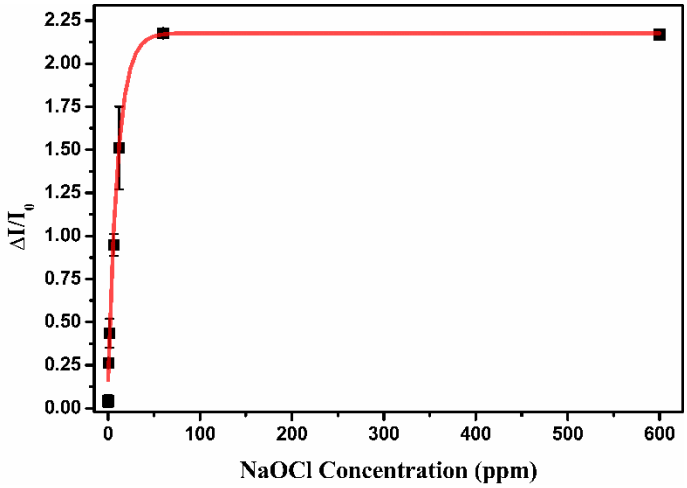

Figure S7. $\Delta I/I_0$ values for 0.1, 0.5, 1.5, 12, 60, 600 ppm aqueous solutions of NaOCl.

The $\Delta I/I_0$ values were fitted by an exponential decay function with the following formula.

$$y = A_{1\times} \exp\left(-\frac{x}{b}\right) + y_0 \qquad (S1)$$

The adjusted R-squared value for the fit was 0.998.

The A_1, b, and y_0 values for this fit are shown in the Table S1.

Table S1. Fitting parameters of the exponential decay function used for fitting in Figure S7.

	Value	**Standard Deviation**
$\mathbf{y_0}$	2.176	0.013
$\mathbf{A_1}$	-2.031	0.036
B	10.596	2.048

UV-vis Spectra of PCAT Before and After (over 20 minutes) Interaction with Different Concentration of Hypobromite

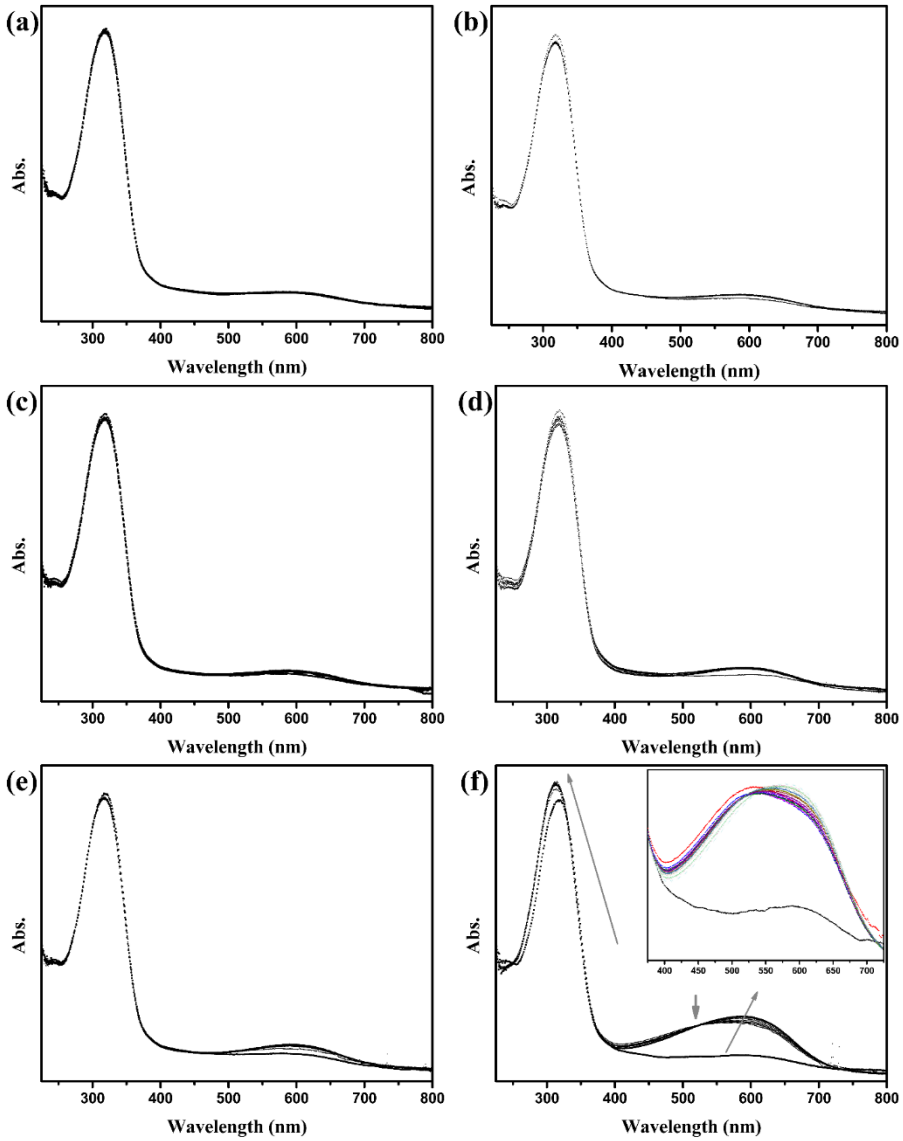

Figure S8. UV-vis spectra of fully reduced PCAT as a function of time (over 20 min) before and after interaction with different concentrations of aqueous solution of NaOBr; (a) 1.5 ppm, (b) 6 ppm, (c) 12 ppm, (d) 60 ppm, (e) 240 ppm, (f) 1598 ppm. Inset of (f) is a zoom-in.

In Situ Raman Spectroscopy of The Interaction of PCAT with Bleach Vapor.

The in situ cell for Raman spectroscopy was fabricated using a PDMS substrate with a channel (Length: width: thickness = 15 mm: 3 mm: 4 mm). A 3 × 10 mm silicon wafer with a 200 nm top gold electrode (coated in PCAT) was placed inside the channel to intensify the Raman signal. The compartment was sealed using a glass slide as a top transparent cover. This top cover was bonded to the PDMS substrate using polyamide double-sided tape. Two PTFE tubes (Cole Parmer Canada) were used as the inlet and the outlet of the cell. To isolate the cell from the Raman spectrometer device, the inlet was connected to a PTFE compartment filled with a high concentration of sodium hypochlorite (12.5%). The outlet was connected to a compartment filled with water.

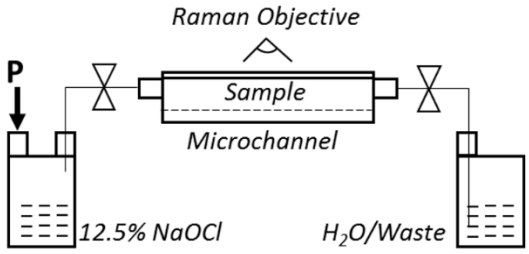

Figure S9. Schematic diagram of set-up used for performing in situ Raman spectroscopy on a PCAT film.

First the redox chemistry of PCAT under the bleach vapor was studied using in situ Raman spectroscopy. A film of reduced PCAT was coated on a gold substrate placed in an

in situ cell (Figure S9) using the same procedure as for the liquid phase sensor. The cell was placed under the objective lens of the Raman spectrometer and the film was exposed to a flow of bleach vapor while Raman spectra of the film were acquired continually for approximately 15 minutes. Figure S10 shows a selection of these spectra. Before the exposure to bleach vapor (t=0), the Raman spectrum shows all three main bands of reduced PCAT. The band at 1480 cm^{-1} is a sign of oxidation of PCAT. The presence of this peak is associated with the partial oxidation of PCAT due to the aging of the pristine powder. After less than a minute exposure to the vapor (t=38 s), the intensity of the oxidation peak at 1480 cm^{-1} is increased in addition to the appearance of a shoulder at 1587 cm^{-1}. These bands represent the half-oxidized PCAT. The intensity of these two bands increase during the second and third minute of exposure, while the intensity of the main reduction band at 1620 cm^{-1} decreased. Two further reduction bands at 1178 cm^{-1} and 1220 cm^{-1} shift to lower frequencies (1164, 1216 cm^{-1}) which indicates the complete conversion of reduced to half-oxidized PCAT. Finally, at t=212 s, no band of reduced PCAT can be found in the spectra. This result indicates that not only is the aqueous solution of bleach a strong oxidizer of the oligoanilines, but also its vapor can cause the oxidation of PCAT to higher oxidations states (EB or PB). It was reported that an intermediate level of protonic doping leads to evolution of a small band at around 1377 cm^{-1}.[2] However, this band will disappear at higher levels of doping. In our case, after approximately two minutes of exposure to this vapor (t=115 s), a low intensity band at around 1377 cm^{-1} is observed. This band remained present after approximately ten minutes of exposure.

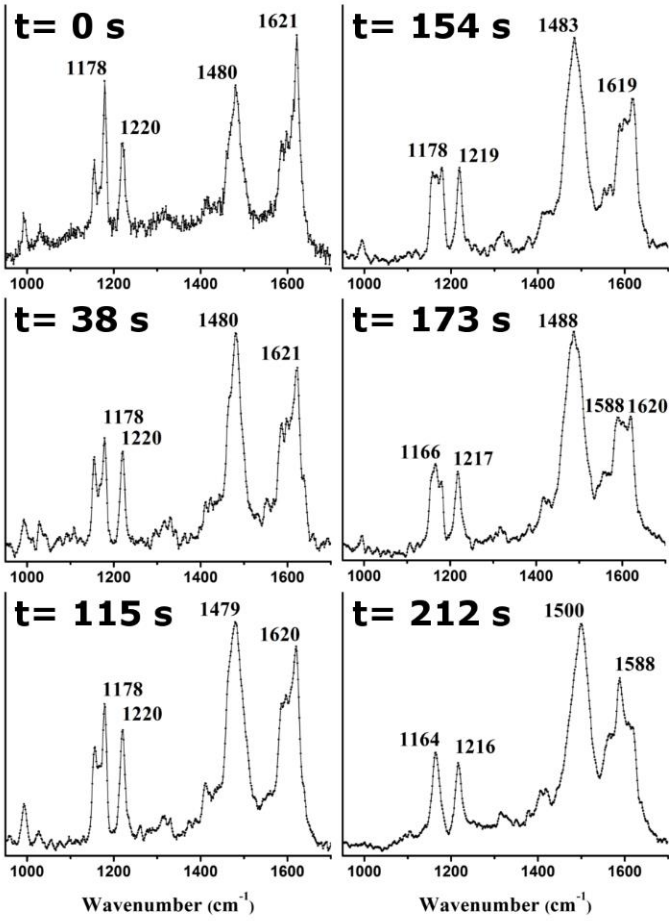

Figure S10. In situ Raman spectroscopy of LB film exposed to the bleach vapor as a function of time.

XPS Spectroscopy of PCAT Films

First, the possibility of vacuum deposition of reduced and half-oxidized PCAT was examined by deposition on clean polycrystalline gold substrates. Using the survey spectra of oligoaniline coated gold substrates, the C/N elemental ratio is equal to 7.4, and 11.0 for the reduced and half-oxidized films, respectively (Figures S11a and S11b, respectively). These values are close to the ratio of C/N=7.5 in PCAT ($C_{30}H_{22}N_4$, $C_{30}H_{20}N_4$). The deviation of experimental C/N values from the theoretical value increases for the half-oxidized state because the half-oxidized form of PCAT wets the surface less than its reduced form. This leads to a higher contribution from the adventitious carbons on the gold substrates in the C 1s spectrum and therefore a higher C/N ratio.

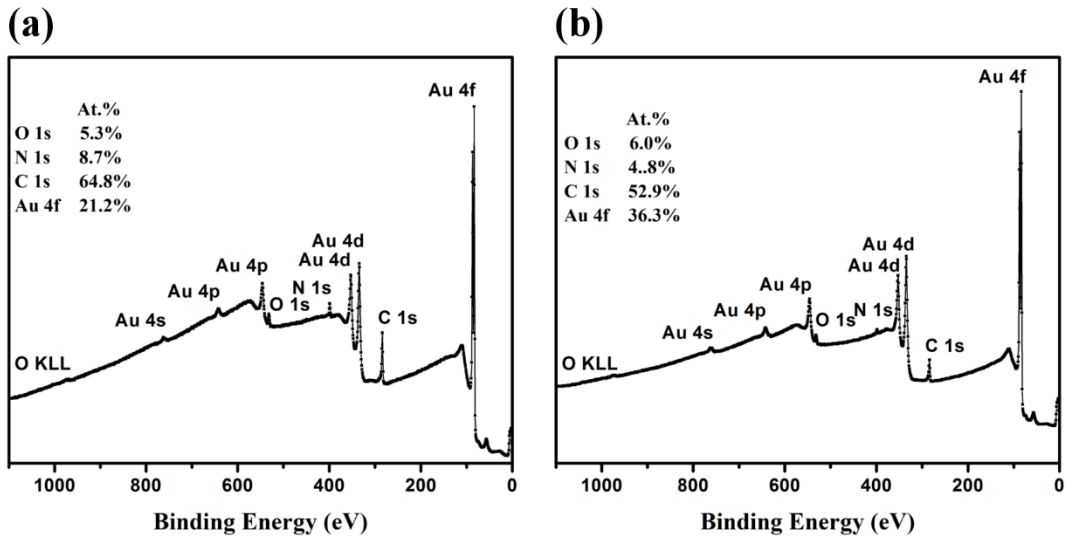

Figure S11. XPS survey spectra of vacuum deposited reduced (a) and half-oxidized (b) PCAT on gold substrates.

Based on the ratio of Cl/C and Cl/N extracted from the survey spectra, a maximum 16% of reduced and 25% of half-oxidized molecules are chlorinated.

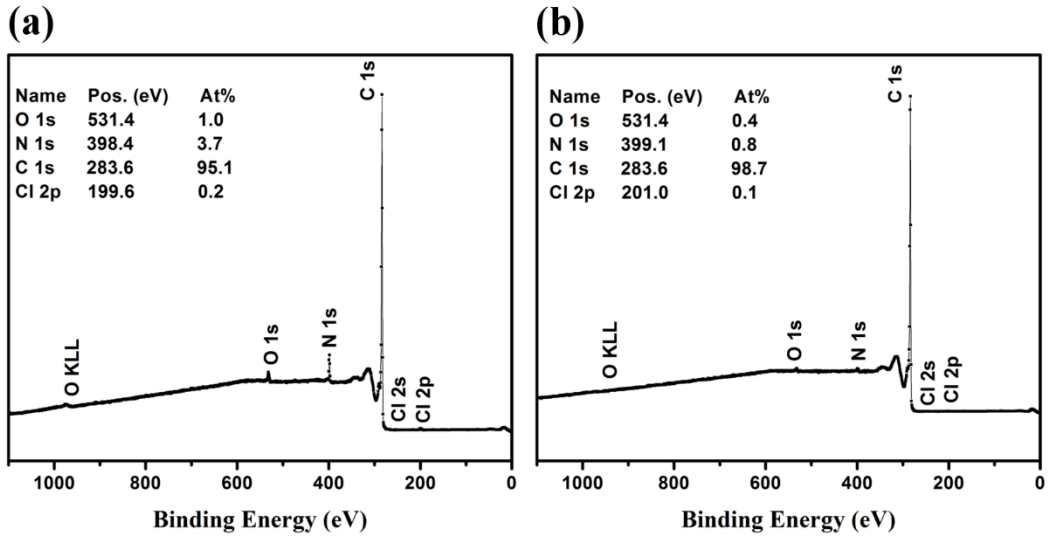

Figure S12. XPS survey spectra of vacuum deposited reduced (a) and half-oxidized (b) PCAT on HOPG after exposure to bleach vapor.

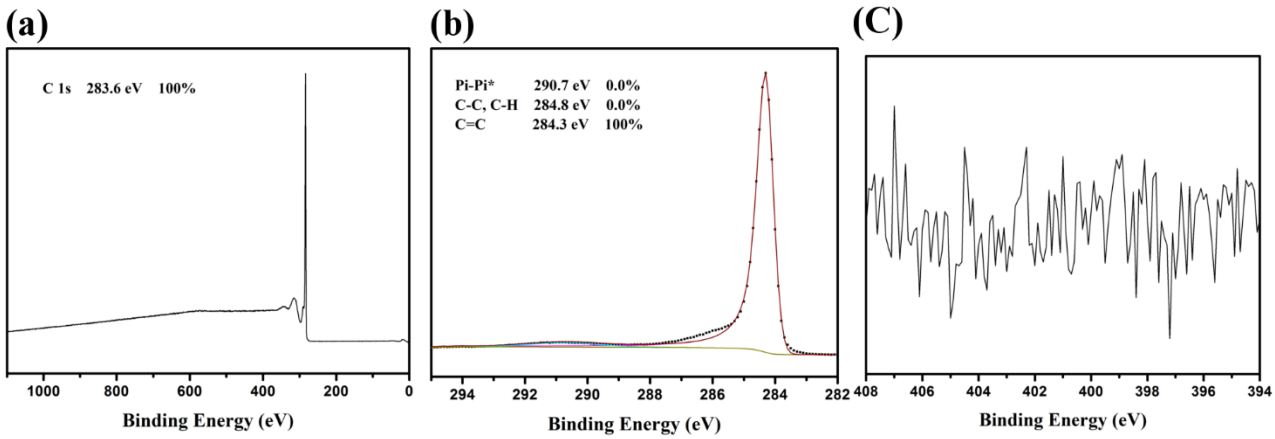

Figure S13. XPS survey, C 1s, and N 1s spectra of bare HOPG.

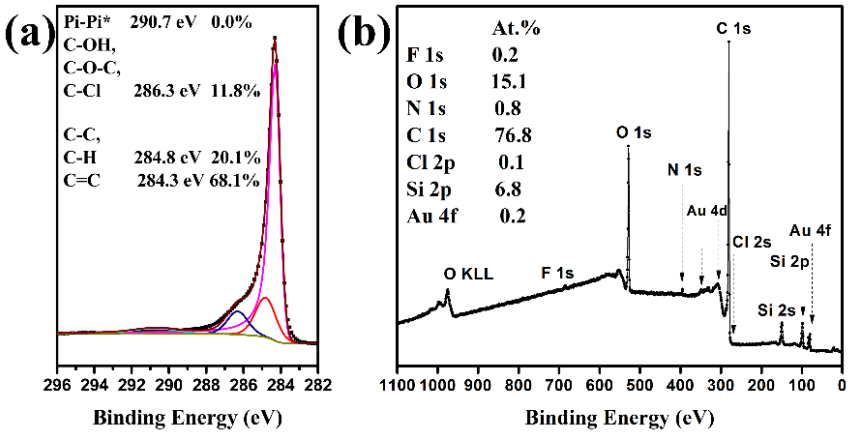

Figure S14. XPS C 1s (a) and survey spectra (b) of the PCAT-pencil film exposed to an aqueous flow of NaOCl (6 ppm), depicted in Figure 4. The presence of silicon in the survey spectra may be due to detached glass particles created during writing on glass, residue of the PDMS channel, or the glass substrate itself under the thin graphite film.

UV-vis Spectra of PCAT Before and After (Over 20 Minutes) Interaction with Different Concentrations of Sodium Hypochlorite

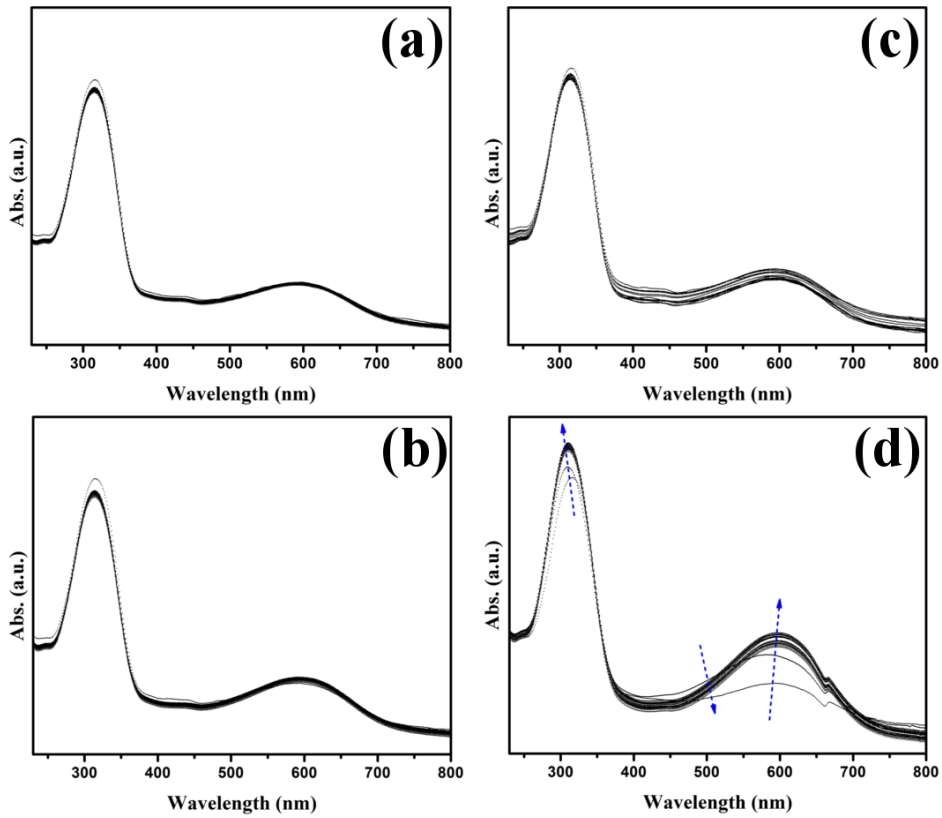

Figure S15. UV-vis characterization of the interaction between reduced PCAT and NaOCl solution. UV-vis spectra of pristine reduced PCAT after interaction with 60 µl of (a) 1.5 ppm, (b) 6 ppm, (c) 12, and (d) 60 ppm.

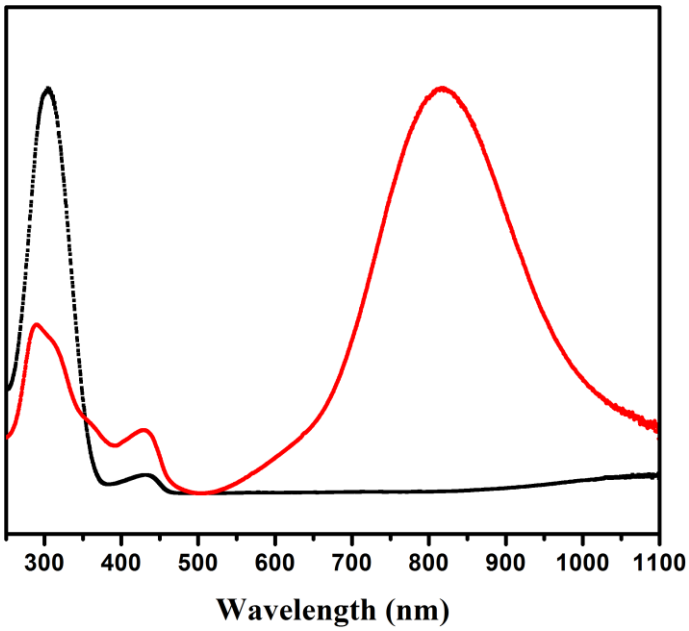

Figure S16. UV-vis spectra of salt form of the fully reduced (black spectrum) and half-oxidized (red spectrum) PCAT. In both cases HCl solution was used for protonic doping.

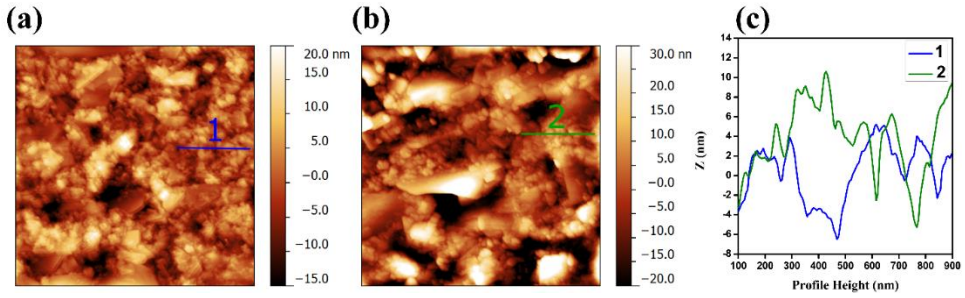

Figure S17. (a) Atomic force microscopy (AFM) of pencil-drawn film on frosted glass slide. (b) AFM of a PCAT-pencil film used in the sensor used for XPS spectroscopy (Figures 4b and 4c) after exposure to aqueous solution of NaOCl (6 ppm). (c) height profile along the lines shown in (a) and (b).

A JEOL JSM-7000F scanning electron microscope (SEM) was used to investigate the morphology of the 9B pencil lead electrode (Figure S18a) and the adsorbed oligoanilines on it, prior and after exposure to an aqueous flow of NaOCl (6 ppm, 0.2 ml/min).

The investigation of the oligoaniline-9B pencil thin film of the sensor using SEM only shows the presence of organic patches on the surface of graphite (Figures S18b and S18c). However, comparison of AFM data of a HOPG surface coated with PCAT using the same procedure as used in the sensor device (Figure S18d) with a bare HOPG surface (Figure S18e) shows thin and continuous coverage of PCAT on the graphitic substrate.

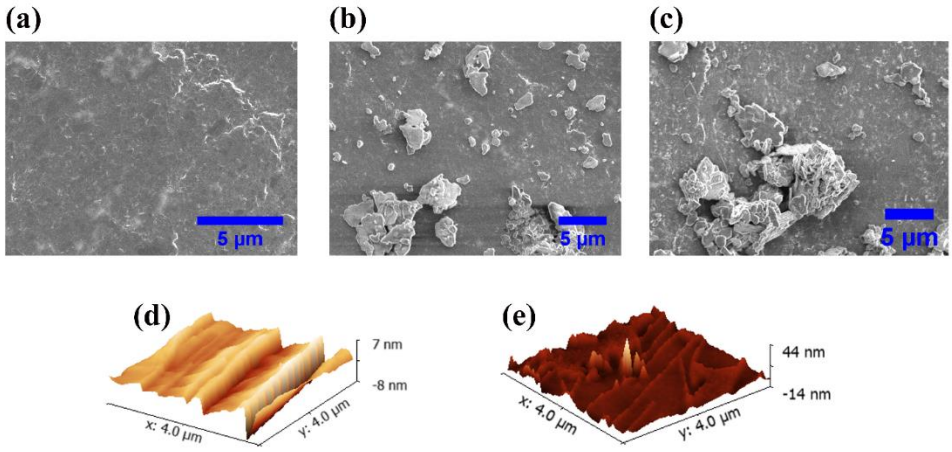

Figure S18. SEM micrograph of; (a) bare pencil film fabricated on frosted glass, (b) PCAT immobilized on pencil film before reaction with NaOCl solution (6 ppm), and (c) after reaction with NaOCl (6 ppm). (d) AFM on a bare HOPG surface. (e) AFM on a HOPG surface which was placed in the channel of the sensor device and introduced to the flow of LB based on the same procedure used for pencil films.

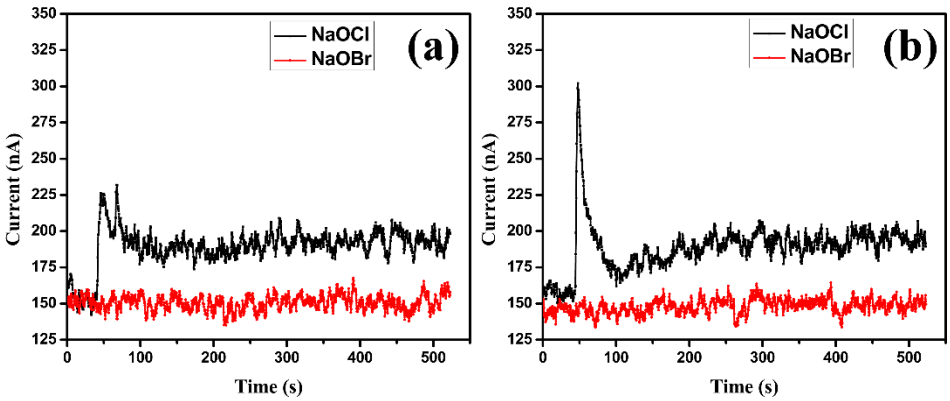

Figure S19. I-t graph of the sensor device exposed to different concentrations of aqueous solutions of NaOCl and NaOBr with the concentrations of 1.5 ppm (a), 6 ppm (b).

Interaction of PCAT with High Concentration of Sodium Hypochlorite in Basic pHs

Reduced PCAT was reacted with a high concentration of NaOCl (1750 ppm) for two days. The 1H NMR on this sample does not show any peaks. However, Raman spectroscopy on this powder showed that the oligoanilines are fully-oxidized. The 1H NMR of fully oxidized PCAT is elusive because of the high concentration of delocalized charge. Although it is not possible to determine whether some of the PCAT is degraded by exposure to hypochlorite, it shows that the PCAT can resist degradation in presence of high concentration of hypochlorite in basic regime.

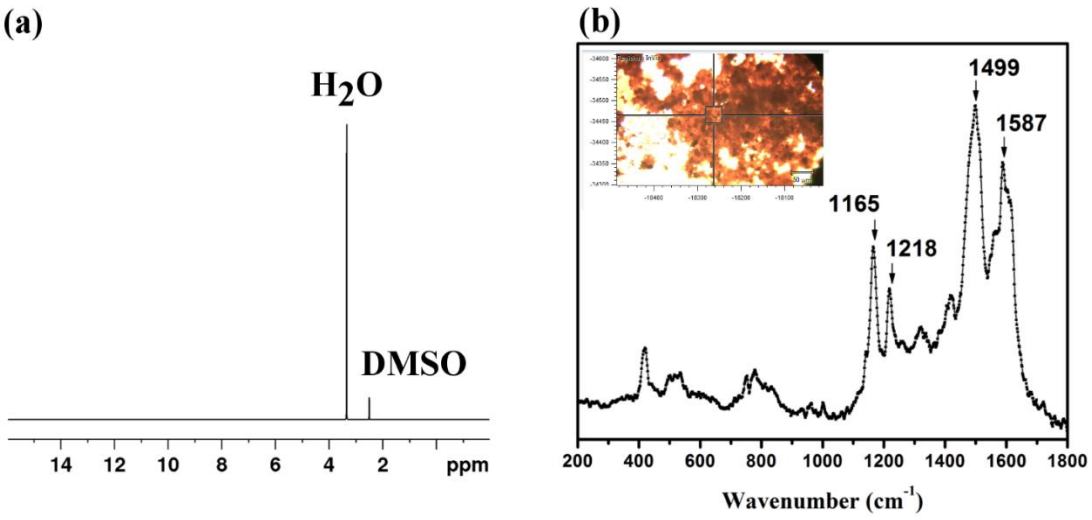

Figure S20. (a) ^{1}H NMR spectrum of fully reduced PCAT after reaction with 1750 ppm NaOCl solution. (b) Raman spectrum of the same sample in (a), after drop casting on a gold substrate. The inset shows an image of this sample under the Raman spectrometer objective lens.

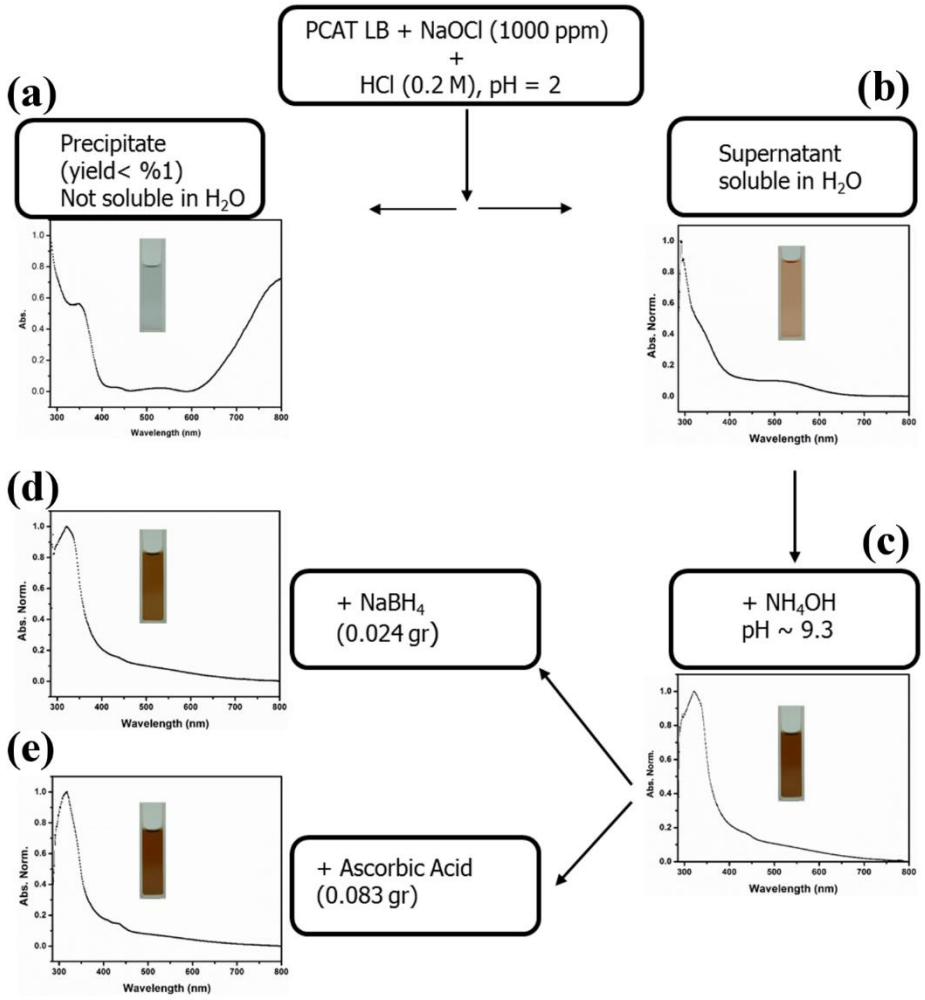

Figure S21. Interaction of PCAT with NaOCl (1000 ppm) for 20 hours in acidic conditions (pH ~ 2). (a) Precipitate obtained from the reaction mixture. (b) Supernatant of the reaction mixture. (c) Increase in the pH of the supernatant by addition of NH_4OH. Addition of $NaBH_4$ (d) and ascorbic acid (e) to the sample in (c) to chemically reduce this solution.

Cyclic Voltammetry of PCAT

Cyclic voltammetry of PCAT was performed using a Emstat potentiostat (PalmSens). The measurements were performed in a Faraday cage equipped with argon purging to avoid interference due to air oxidation of PCAT during the experiment. The CV measurement were carried out in non-aqueous medium of acetonitrile in which 0.1 M tertbutyl ammonium perchlorate (TBAP) supporting electrolyte and 0.02 M diphenyl phosphate proton source were dissolved. The working electrode was a platinum disk (0.785 mm^2 in diameter) and the counter electrode was a platinum wire. The reference electrode was a non-aqueous electrode of $Ag/AgNO_3$ which was prepared by dipping a Ag wire into $AgNO_3$ (10 mM) and TBAP (0.1 M) base electrolyte in acetonitrile solution. The Ag wire was placed and sealed into a glass tube equipped with a porous Teflon tip and filled with $AgNO_3$ electrolyte solution. The scan rate in CV measurement was 100 mV/s and the experimental window was -1.5 V to 1.5 V. To calculate the CV of PCAT versus redox potentials of ferrocene (FC/FC+), the same experiment procedure described above was carried out when ferrocene molecules were dissolved in the electrolyte. The concentration of ferrocene was 0.1 mM ad the scan rate was 100 mV/s.

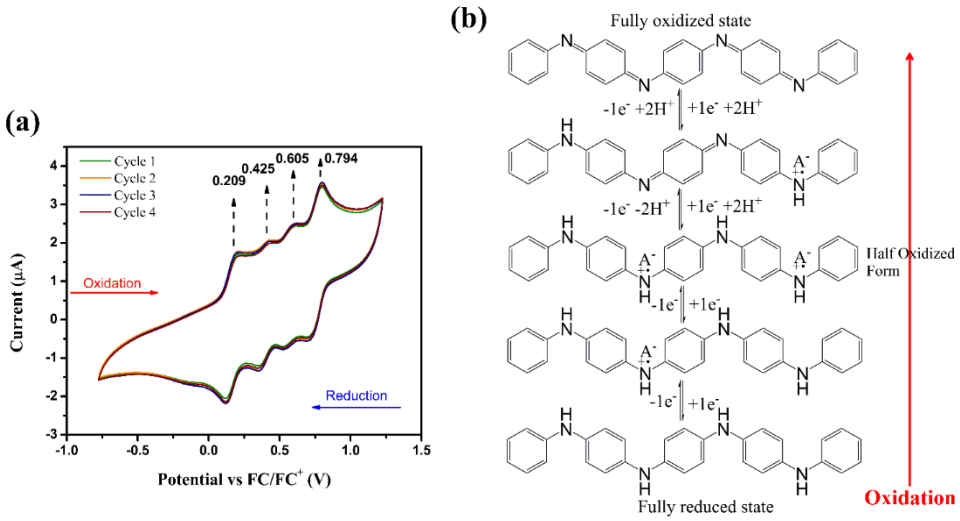

Figure S22. (a) CV measurement of PCAT versus ferrocene redox potentials. Each of the four arrow/peaks marked in the oxidation scan of PCAT shows a single electron transfer process. (b) Schematic diagram of oxidation of fully reduced PCAT to its fully oxidized form in four consecutive oxidation steps.

Figure S22a shows four sets of CVs of PCAT, demonstrating the complete reversible oxidation/reduction of PCAT. The oxidation wave of each scan contains four distinct oxidations peaks. This is in agreement with previous reports on CV of PCAT which attributes these peaks to electron-electron and electron-proton reactions.[3] The schematic diagram of these four oxidation/reduction reactions is depicted in Figure S22b. Starting from the fully reduced states of PCAT, the first two oxidation reactions are mediated by electron-electron reactions, while the two conversions from the half-oxidized state to fully oxidized state is mediated by two electron-proton reactions.[3]

References

(1) Sousa, M. C.; Buchanan, J. W. Observational Models of Graphite Pencil Materials. *Comput. Graphic Forum* **2000**, *19*, 27–49.

(2) Cochet, M.; Louarn, G.; Quillard, S.; Buisson, J. P.; Lefrant, S. Theoritical and Experimental Vibrational Study of Emeraldine in Salt Form. *J. Raman Spectrosc.* **2000**, *31*, 1041-1049.

(3) Shao, Z.; Rannou, P.; Sadki, S.; Fey, N.; Lindsay, D. M.; Faul, C. F. J. Delineating Poly(Aniline) Redox Chemistry by Using Tailored Oligo(Aryleneamine)s: Towards Oligo(Aniline)-Based Organic Semiconductors with Tunable Optoelectronic Properties. *Chem. Eur. J.* **2011**, 17, 12512–12521.

Chapter 7 Conclusions and Outlook

The interfacial interactions of a redox-active organic molecular layer with a metal oxide surface and a graphitic surface are investigated. The concept of this study is based on the idea introduced by Herbert Kroemer who considered each interface as a device on its own.1 In this thesis, initially, the thin film formation of a redox-active small molecule, phenyl-capped aniline tetramer (PCAT) on its fully reduced and fully oxidized base forms on iron oxide surfaces were studied. This aim has been achieved by examining the applicability of a dynamic scaling model (scaling island size distribution)2 on nucleation and growth of submonolayer PCAT islands on hematite surface. The complete description of this study can be found in chapter 4. The main findings of this part of the thesis can be summarized as

- The demonstration of the different morphology of the reduced PCAT islands from the oxidized PCAT islands on hematite single crystal surfaces fabricated through vacuum deposition. The reduced PCAT islands are few nanometers in thickness while the oxidized PCAT islands fabricated under similar conditions are more than hundred nanometers in thickness. At moderate substrate temperatures (293 K-338 K) the rescued islands are dendritic while the oxidized islands are more globular in shape. In addition, at any temperature in this range, the density of the reduced islands is significantly higher than the density of the oxidized islands.

- Optimization of vacuum deposition of different oxidation states of PCAT on iron oxide substrate as a function of substrate temperature.
- The successful application of the scaling island size distribution on the reduced and the oxidized islands which can be used for estimation of the critical island size of the reduced and the oxidized PCAT nuclei.
- Estimation of the surface barrier energy and the diffusion prefactor for the reduced and the oxidized islands which shows that even small changes in the structure of a small molecule may significantly affect its intramolecular interactions as well as its interaction with surfaces. This can directly affect the nucleation and growth of the islands and the ability to fabricate thin homogeneous organic films.
- The demonstration that moderate changes in the oxidation states of the substrate do not cause discernable changes in the nucleation and growth of the reduced and the oxidized PCAT.

In the 5th chapter of this thesis the charge transfer at the interface of the PCAT-iron oxide which is introduced in previous chapter was studied. The motivation behind this part of the study is the application of redox-active organic compounds such as polyaniline (PANI) for corrosion inhibition of iron oxide.3 It has been argued that PANI at its oxidized form can cause formation of a passive oxide layer on the surface of iron oxide while the polymer itself will become reduced.4 In addition, the reoxidation of PANI by ambient is necessary for the continuity of this cycle and thus prolonged protection of the substrate. The main findings of this part are

- Demonstrating the partial reduction of half-oxidized and fully oxidized PCAT on the surface of hematite single crystal. For the first-time demonstration of partial oxidation of the fully reduced PCAT through interaction with hematite surface. Therefore, it was argued that among all oxidation states of PCAT at the interface with iron oxide, the half-oxidation state of PCAT is closest to an equilibrium.
- Showing the charge transfer and mutual doping between PCAT and hematite through appearance or increase in the charged nitrogen species appeared in the N 1s x-ray photoelectron spectroscopy (XPS) of PCAT.
- Demonstrating the possibility to detect the effect of reduced and oxidized PCAT on the oxidation state of iron oxide film through conductivity measurements of a thin iron oxide film imbedded in a microfluidic channel.

Finally, in the 6th chapter the further application of PCAT and solid surfaces in electronic devices is shown. The fabrication of a microfluidic sensor based on the interface of the reduced PCAT-graphite was illustrated. The procedure and the quality of the PCAT film on graphite surface was demonstrated. Pencil lead was used as the surface of graphite. The sensor was used for detection and quantification of free chlorine in water. It was shown that the sensor is sensitive and selective to free chlorine in comparison to other common disinfectant present in drinking water. Using several spectroscopy methods such as XPS, Raman spectroscopy, and UV-vis spectroscopy the reaction mechanism behind the reaction of PCAT and free chlorine was described. To this end, the sensing mechanism of the sensor was thoroughly discussed. The summary of the findings of this study, the novelties, and its contributions to the field of interface science and sensing are

- Demonstrating the fabrication and the performance of a reagent-free, resettable microfluidic sensor based on electrical transduction mechanism (chemiresistive) for detection and quantification of free chlorine in drinking water based on the interface of a pencil film and a fully reduced PCAT thin film.
- Showing that the interaction of PCAT with the vapor of sodium hypochlorite solution leads to the chlorination, oxidation, and protonic doping of PCAT.
- Demonstrating that the interaction of PCAT and sodium hypochlorite leads to a drop in pH, the chemical doping and chlorination of PCAT.
- Proposing that the electrostatically charged PCAT film forms up on the interaction with sodium hypochlorite solution can affect the charge transport in the thin pencil film and responsible for the signal in the sensing measurement. The intensity of this signal is scaled with the concentration of sodium hypochlorite (below 60 ppm).
- Increase in the intensity of the sensing measurements for the highly chlorinated PCAT films.

As it was demonstrated in this thesis, the interface of redox-active organic molecules and solid surfaces can offer new possibilities for various applications from smart coatings to electronic devices. In the following, some of the future research projects than can unlock more of the possibilities of such interfaces are introduced.

1. **Switchable surface morphology.** We have demonstrated that different oxidation states of a redox-active oligoaniline lead to the formation of different islands morphologies on surfaces. First, the possibility of the reversible switching of the

morphologies of the reduced islands to the oxidized islands through redox reactions (preferably, chemical redox reactions) should be investigated. Up on success of this step, thin films of PCAT on solid surfaces can be used in applications in which the switching of the surface morphologies are desirable. One potential application can be the development of surfaces with switchable optical properties (absorptivity, refractive index),5 for example for detection of chemical species in gases or liquids through the change in the optical properties of PCAT coated solid surfaces.

2. **Elecromigration and surface mobility.** Based on the surface diffusion parameters calculated in this work, the effect of electric field and joule heating on the reduced and the oxidized islands can be studied.6 While iron oxide was used in our study due to the application of PCAT film for inhibition of corrosion of such surface, two dimensional surfaces with high charge mobility such as graphene are preferred for electromigration studies. This is because in contrast to majority of materials in which charge carrier flow inside their bulk, in graphene the charge carriers flow on its surface producing a sufficient electric field for electromigration of islands. In addition, the effect of joule heating on the mobility of the reduced and the oxidized islands is worth studying. This energy can be applied either as a local heat (e.g. through laser beam) or through temperature gradient.
3. **Switchable charge transfer between oligoanilines and other surfaces.** While investigating the charge transfer between hematite and PCAT is of importance for understanding the passivation mechanism of iron oxide surfaces against corrosion, iron oxide is not a desirable material for electronic devices. This is mainly due to

fast oxidation and rusting in ambient and its various interchangeable phases with various bandgaps from semimetallic to high bandgaps.7 Therefore, investigating the possibility of switchable doping of other surfaces such as MoS_2, WS_2, and graphene can be useful for future electronic devices considering the difficulty of p-doping of majority of semiconductors. The same mechanism has been previously demonstrated for the carbon nanotube-PANI system and was used for fabrication of polarity switchable carbon nanotube transistors.8

4. **Chlorination of oligoaniline.** More research should be carried out to evaluate the impact of chlorination of PCAT on its structure and stability. It is important to evaluate the effect of pH on the extent of chlorination and possible degradation of PCAT.9 Based on our result on the impact of chlorination of the sensing response of PCAT in our chemical sensing experiments, other substituted PCAT derivatives (e.g. fluorine substitute PCAT) should be synthesized and be tested in our chemical sensor.
5. **Biosensors**. While the detection of free chlorine in drinking water is important for water quality monitoring, the presented sensing mechanism in this thesis can be used for the detection of other analytes such as biomolecules.10 For this purpose, PCAT should be replaced with biomolecules for selective detection of analytes such as specific sequences of DNA.

References

(1) Kroemer, H. Quasi-Electric Fields and Band Offset: Teaching Electrons New Tricks. *Rev. Mod. Phys.* **2000**, *73*, 449–469.

(2) Ruiz, R.; Nickel, B.; Koch, N.; Feldman, L. C.; Haglund, R. F.; Kahn, A. Dynamic Scaling, Island Size Distribution, and Morphology in the Aggregation Regime of Submonolayer Pentacene Films. **2003**, 1–4.

(3) Rohwerder, M. Conducting Polymers for Corrosion Protection: A Critical View. *Int. J. Mat. Res.* **2009**, *219*, 1331–1342.

(4) DeBerry, D. W. Modification of the Electrochemical and Corrosion Behavior of Stainless Steels with an Electroactive Coating. *J. Electrochem. Soc.* **1985**, *132*, 1022–1026.

(5) Li, X.; Gao, Y.; Serpe, M. J. Reductant-Responsive Poly(N -Isopropylacrylamide) Microgels and Microgel-Based Optical Materials. *Can. J. Chem* **2015**, *93*, 685–689.

(6) Barreiro, A.; Rurali, R.; Hernández, E. R.; Bachtold, A. Structured Graphene Devices for Mass Transport. *Small* **2011**, *7*, 775–780.

(7) Maschhoffr, B. L.; Armstrong, N. R. Thin Oxide Layers on Clean Iron Surfaces: Formation under Vacuum and Characterization by Photoelectron Spectroscopy and Electrochemical Reactions of Probe Molecules at the Oxide / Electrolyte Interface. *Langmuir* **1991**, 693–703.

(8) Klinke, C.; Chen, J.; Afzali, A.; Avouris, P. Charge Transfer Induced Polarity Switching in Carbon Nanotube Transistors. *Nano Lett.* **2005**, *5*, 555–558.

(9) Mohtasebi, A.; Broomfield, A. D.; Chowdhury, T.; Selvaganapathy, P. R.; Kruse, P. Reagent-Free Quantification of Aqueous Free Chlorine via Electrical Readout of Colorimetrically Functionalized Pencil Lines. *ACS Appl. Mater. Interfaces* **2017**, *9*, 20748–20761.

(10) Ng, A. L.; Chen, C.; Kwon, H.; Peng, Z.; Lee, C. S.; Wang, Y. Chemical Gating of a Synthetic Tube-in-a-Tube Semiconductor. *JACS* **2017**, *139*, 3045–3051.